12-2021

Dynamic Modeling of a Three Degree of Freedom Reaction Sphere

Joshua Michael Byron

Dynamic Modeling of a Three Degree of Freedom Reaction Sphere

by

Joshua Michael Byron

B.S., Kettering University, 2009

A thesis submitted to the College of Engineering and Science of
Florida Institute of Technology
in partial fulfillment of the requirements
for the degree of

Master of Science
in
Mechanical Engineering

Melbourne, Florida
December, 2021

We the undersigned committee hereby approve the attached thesis,
“Dynamic Modeling of a Three Degree of Freedom Reaction Sphere.”
by
Joshua Michael Byron

Hector Gutierrez, Ph.D.
Professor, Mechanical and Civil Engineering
Major Advisor

Weinan Gao, Ph.D.
Associate Professor
Mechanical and Civil Engineering

Tariel Kiguradze, Ph.D.
Associate Professor
Mathematical Sciences

Ashok Pandit, Ph.D.
Professor and Department Head
Mechanical and Civil Engineering

Abstract

Title: Dynamic Modeling of a Three Degree of Freedom Reaction Sphere

Author: Joshua Michael Byron

Advisor: Hector Gutierrez, Ph.D.

This thesis presents a method to simulate the dynamics of a three degree of freedom, electromagnetically suspended Northrop Grumman Corporation Reaction Sphere (NGCRS) in MATLAB Simulink® by computing the magnetic force and torque relations offline, using COMSOL® Multiphysics. The goal of the thesis is firstly to demonstrate through Finite Element Magnetic Modeling (FEM) that magnetic field interactions between a stator levitation electromagnet (EM) and the rotor permanent magnets (PM) are limited to a single EM-PM pair and that all other PMs can be considered decoupled from the EM. Secondly, this thesis aims to demonstrate that a set of generalized magnetic force and torque relations can be derived for single EM-PM pair using a COMSOL Multiphysics®.

The NGCRS geometry was selected for analysis due to its relative simplicity and design maturity. The NGCRS consists of a stator which houses eight EMs and a rotor with 12 PMs. The NGCRS stator was modified to include six additional EMs to levitate the rotor within the stator and reject external disturbances. The levitation EMs were designed to ensure magnetic field interactions were restricted to a single EM-PM pair for any given rotor orientation and for varying excitation currents. The rotor was modified to be made of iron material and copper inserts were added to decouple the PM fields from the iron, allowing the principle of superposition to be utilized.

The geometric and kinematic relations of the NGCRS were derived and then implemented in a COMSOL Multiphysics® model. Simulations were performed to predict the forces and torques between a single levitation EM, rotor PM, and the iron rotor for varying coil excitation currents of 0.5 to 5.0 amperes in 0.5 amp increments and for angular distances of 0 degrees to 31.717 degrees in one-degree increments. Regression analysis is utilized to obtain relations for the forces and torques. Then a series of coordinate

transformations are applied to obtain the forces and torques for any orientation of the levitation EM-PM pair. These relations and coordinate transformations are programmed into a dynamic model developed in MATLAB Simulink®.

Table of Contents

List of Figures

List of Tables

List of Appendices

Acknowledgement

I would like to express my sincerest gratitude to Professor Hector Gutierrez, whose guidance was instrumental in the completion of this thesis, and whose passion and enthusiasm for engineering helped motivate me throughout the pursuit of my degree.

Chapter 1 Introduction and Motivation

Attitude control of spacecraft is usually performed by Momentum Exchange Devices (MED), such as Reaction Wheels (RW) or a Control Moment Gyros (CMG). Reaction wheels impart momentum to the spacecraft during a pointing maneuver by adding or removing energy from a flywheel, while also providing attitude stability by maintaining a constant momentum and rejecting external disturbances (Markley, et al., 2014). In contrast, a CMG contains a gimbaled fly-wheel with a constant angular momentum. The momentum can be vectored by gimballing the flywheel to provide the desired torque. A single RW or a single CMG (with a single gimbal) can only rotate and stabilize a spacecraft on a single axis, thus a minimum of three devices are required for full attitude control and stability. Both types of MEDs are mature technologies, but are susceptible to a phenomenon known as gimbal lock, which occurs when two of the three MEDs rotational speeds become saturated, which prevents the spacecraft from rotating to the desired orientation. Typically, four to five devices are implemented to provide redundancy (Sidi, 2000). Recovery from a saturation condition requires maneuvering using the on-board propulsion system to re-orient the spacecraft, which is undesirable due to the limited fuel on-board the spacecraft (Markley, et al., 2014). Prevention of gimbal lock is typically achieved through steering logic or by the inclusion of a fourth device with the CMGs arranged into a pyramid, or a combination of the two solutions. Successful implementation of RS technology could reduce the number MED devices from four to two, thus providing a significant weight savings. Figure 1 provides an illustration of the benefit of RS technology and that three one-degree of freedom reaction wheels can be replaced by a single RS.

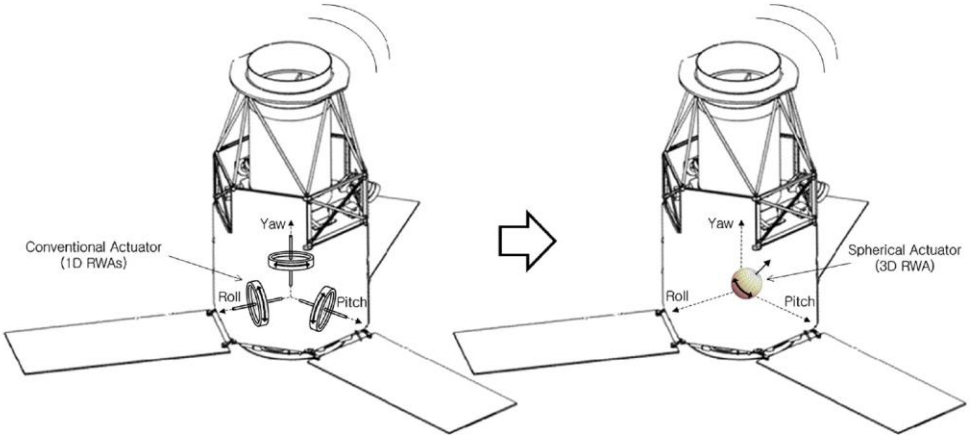

Figure 1: Reaction Wheel Arrangement vs. a Single Reaction Sphere (Kim, et al., 2014)

Recently, significant research has been devoted to development of Reaction Sphere (RS) technologies. If three reaction wheels are superimposed on top of one another, then it becomes clear the optimal solution is a RS capable of rotating in any direction. One of the earliest embodiments of the RS was contrived by Walter Haeussermann, a NASA engineer working under the famed Verner Von Braun. The design was filed for patent in October 1960 under United States Patent US 3,017,777 and was granted patent in 1962. Haeussermann developed the reaction sphere as a solution to the issue of reaction wheel coupling effects. Haeussermann proposed suspending the spherical rotor by either pneumatic or electromagnetic means as shown in Figure 2.

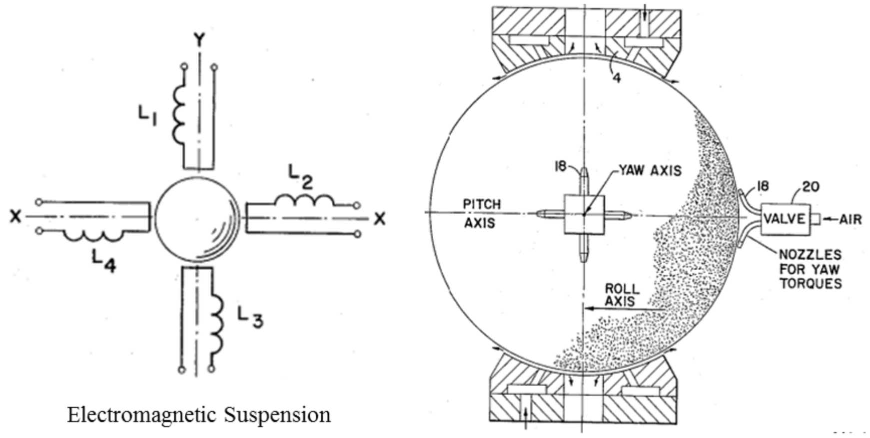

Electromagnetic Suspension

Pneumatic Suspension

Figure 2: Space Vehicle Attitude Control System (Haeussermann, 1962)

Over 60 years have passed since the inception of the RS, but none have been successfully used in commercial or military satellites, based on the available public data searched while researching this thesis. This is due primarily to the complication of suspending the spherical rotor within the stator in a reliable manner. Various solutions to the suspension problem have been proposed such as, mechanical, pneumatic, liquid, magnetic, and electromagnetic, but none have been able to meet the service life, reliability, and power consumption requirements. The engineering challenge that a reaction sphere designer must overcome, is how to suspend the rotor within the stator reliably.

Chapter 2 Prior Art

A brief overview of the technologies currently utilized within reaction spheres and spherical motors will be discussed in the subsequent sections. Discussion points will include operating principles, architecture, and performance. The merits and demerits of each technology are discussed in Section 2.6.

2.1 Alternating Current Induction Reaction Sphere

2.1.1 Design Overview

An alternating current (AC) induction RS functions by creating a rotating magnetic field around a conductive sphere, which induces an electric current (e.g. an eddy current) on the surface of the sphere (Kim, et al., 2014). The induced current then interacts with the rotating magnetic field which results in a Lorentz force on the sphere's surface causing the rotational torque to spin the spherical rotor (Iwakura, et al., 2008). Figure 3 depicts the operating principle of an AC induction RS.

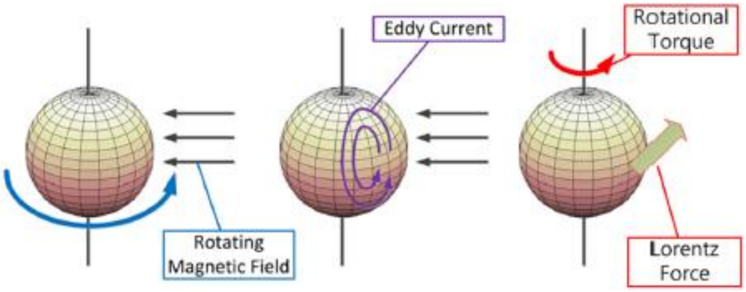

Figure 3: Operating Principle of an AC Induction Reaction Sphere (Kim, et al., 2014)

2.1.2 Architecture

The architecture of a typical AC Induction RS includes a stator assembly, a rotor assembly, power supply, and a control system. The rotor assembly is comprised of a hollow spherical shell with two or more layers (Kim, et al., 2014, Yuan, et al., 2014). The outer layer of the rotor is typically made of copper because it provides a higher level of conductivity than iron. Higher conductivity reduces the losses associated with the formation of eddy currents, leading to higher torque levels than if a single iron layer were used (Kim, et al., 2014). The second, or innermost layer of the rotor, is made of iron and is needed to provide a complete the magnetic circuit with the stator poles (Yuan, et al., 2019). A hollow rotor is also desirable because it provides a larger moment of inertia than a solid sphere for a given mass (Yuan, et al., 2019). A typical two-layered rotor is depicted in Figure 4.

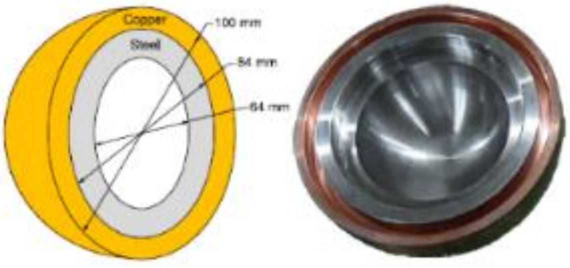

Figure 4: AC Induction RS Rotor Design (Kim, et al., 2014)

The stator assembly includes the stator housing, position sensing components, and the electromagnets that generate magnetic flux needed for rotor levitation and rotor torque transmission. The stator housing is wholly or partially made of a magnetic material with curved stator and levitation cores around the periphery of the rotor. In the model developed by Yuan, et al., 2019, four levitation cores were used to reduce the field interactions between levitation and drive electromagnets. The stator core geometry developed by Yuan, et al., 2019, uses a curved pole geometry with three orthogonal circles of poles arranged with a symmetric structure. Each circle is composed of 4 curved segments that allows sphere to rotate about axis orthogonal to the circle. Torque can be applied around an arbitrary axis by combining the torques generated by the three circles. The drive coils are arranged in three-phase windings to enable self-starting of the actuator (Yuan, et al., 2019). This architecture is depicted in Figure 5.

The reaction spheres developed by Kim, et al., 2014 and Iwakura, et al., 2008 only allowed rotation in one axis, which was achieved using a 2-phase, 2-pole (per phase) configuration with the excitation signals 90 degrees out of phase, and a single levitation electromagnet positioned above the rotor to counteract gravity. The architecture developed by Kim, et al., is shown in Figure 6.

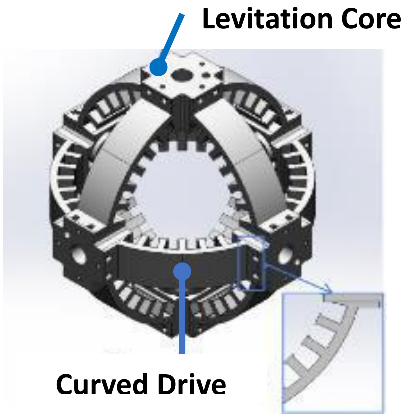

Figure 5: AC Induction RS Stator Construction (Yuan, et al., 2019)

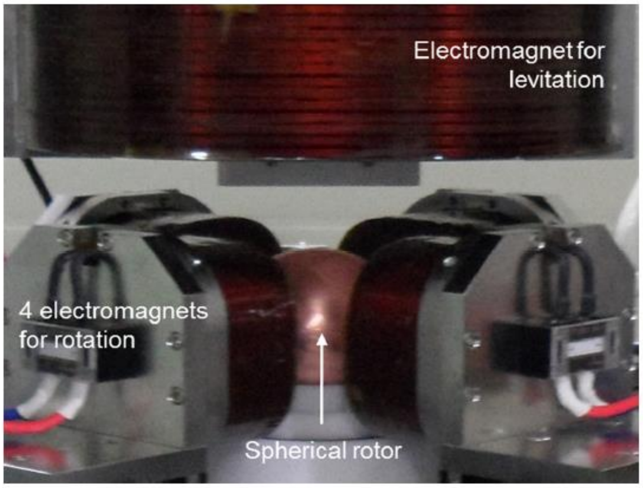

Figure 6: Architecture used in feasibility Study of AC Induction Sphere (Kim, et al., 2014)

The desired rotational speeds and direction is achieved by controlling the velocity, magnitude, and direction of the magnetic fields generated by the levitation and drive cores (Kim, et al., 2014). The angular velocity of the rotor can be modulated by varying the frequency of the rotating magnetic field or its intensity similar to that of conventional induction motors (Iwakura, et al., 2008).

2.1.3 Measurement and Control

A laser tachometer, in conjunction with a laser reflector attached to the rotor, measured the angular velocity of the rotor in the experiments performed by the Iwakura, et al., (2008) and by Kim et al., (2014). The resolution of the measurement device was one pulse per revolution in both experiments. Position control (e.g. levitation) of the rotor was achieved through a PID control loop with position feedback provided by an LED and photo-diode positioned near the side of the rotor. Speed was measured in a similar manner by Yuan, et. al., but position was measured by eddy current displacement sensors placed at the center of each levitation coil. The position of the rotor was controlled by PID control algorithms in the experiments performed by Kim, et al., 2014. Iwakura, et al., 2008, while Yuan, et al., used a PD controller for levitation.

Kim et al., 2014 considered the magnetic fields generated by the levitation electromagnet to be decoupled from the driving electromagnets during development of the analytical models and control loops, however Iwakura, et al., 2008 did not. The research performed by Yuan et al., 2019 did not directly discuss the potential interactions between the levitation and stator electromagnets. A block diagram of the control algorithm for the developed by Kim et al., (2014) is shown in Figure 7 and the experimental setups for the reaction spheres are shown in Figure 8 and Figure 9.

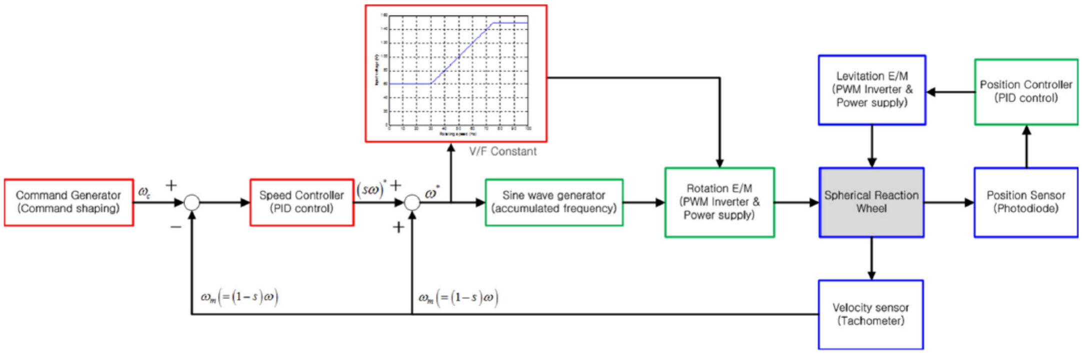

Figure 7: AC RS Velocity and Levitation Control Algorithm (Kim, et al., 2014)

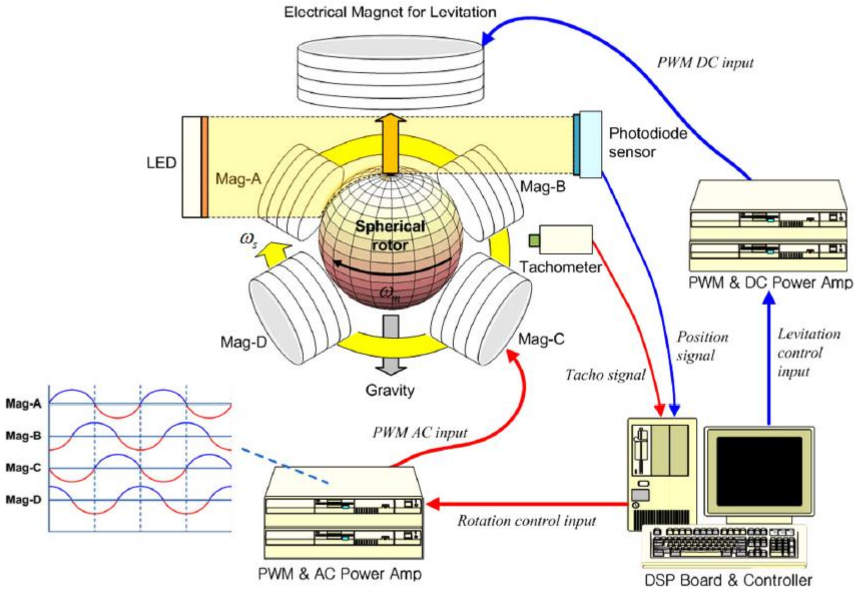

Figure 8: Experimental setup for feasibility Study of AC Induction RS (Kim, et al., 2014)

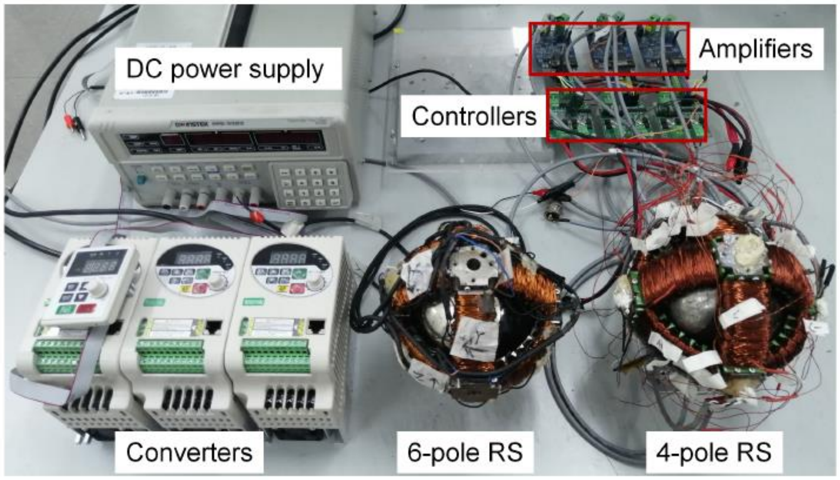

Figure 9: Experimental setup for Design Study of AC Induction RS (Yuan et al., 2019)

2.1.4 Performance

If a variable frequency power supply is used, then the maximum rotational speed occurs when the torque generated by the magnetic field is equal to the air resistance drag torque. The maximum speed achievable with a fixed frequency power supply is the synchronous speed. In satellite applications, the reaction sphere could be housed in a vacuum, which would allow for rotational speeds limited by the power supply frequency, structural strength, and the manufacturing precision of the reaction sphere rotor and stator.

The maximum speeds achieved by Yuan, et al., 2019 was approximately 800 RPM for the 4-pole stator design and roughly 400 RPM for the 6-pole stator design, which are both well below the synchronous speed of 1800 RPM for a 60Hz excitation signal. According, to Yuan, et al., 2019 the speed limitation was attributed to manufacturing quality of the prototypes, which causes the rotor to become unstable and strike the stator housing. The maximum speed achieved by the experiments performed by Kim, et al., 2014 was 13,500 RPM, and the maximum torque was 0.7 Nm. The experiments performed by Iwakura, et al., 2008 achieved a maximum speed of approximately 1000 RPM. However, these speeds were only achieved for a uni-axial rotation of the rotor.

2.2 ELSA Reaction Sphere

The European Levitated Spherical Actuator (ELSA) is a European Union funded research and development project aimed toward maturation of reaction sphere technology for utilization in space craft attitude control systems (CORDIS, 2014).

2.2.1 Design Overview

The ELSA is a Permanent Magnet (PM) synchronous spherical actuator that is designed to allow rotation about any axis. Torque and levitation (magnetic bearing) forces are produced by the attraction and repulsion of the magnetic fields formed by twenty (20) air-core stator electromagnets (EMs) and eight (8) rotor permanent magnets (PM). A control algorithm constructs the position and orientation of the rotor assembly using magnetic flux sensors and laser optical sensors. The control algorithm generates a vector of currents to the stator EMs to develop the levitation and rotational fields simultaneously (Rossini, 2014).

2.2.2 Architecture

The ELSA is comprised by a stator assembly, rotor assembly, and a control system. The rotor assembly is composed of eight (8) PMs arranged into a cubic polyhedron. The PMs are mounted to a hollow iron sphere, and are arranged such that the opposing spherical faces of the rotor have opposite polarity as shown in Figure 10. The stator assembly consists of two hemispherical shells of non-magnetic material, with a total of 20 air-core electromagnets which serve to levitate and rotate the rotor assembly. The stator also includes the magnetic flux sensors and optical sensors that detect the position and angular velocity of the rotor, as well as hard stops to prevent the rotor from striking and damaging the EMs. The general architectures of the rotor and stator assemblies are shown in Figure 10.

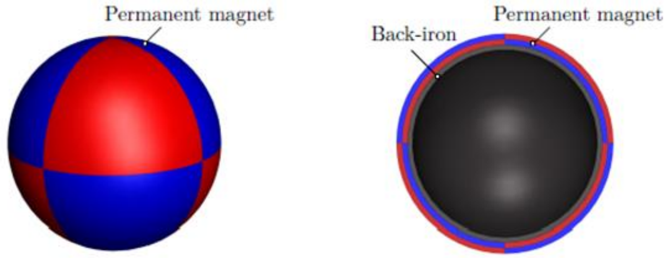

(a) Rotor. (b) Rotor section view.

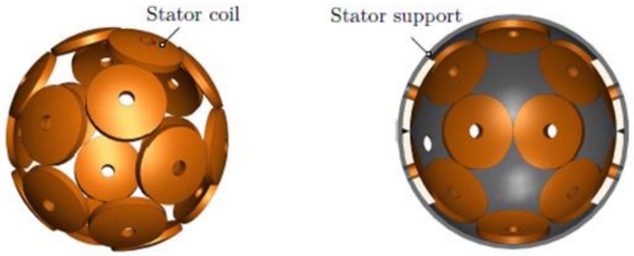

(c) Stator coils. (d) Stator section view.

(e) Rotor and a half stator assembled. (f) Rotor and stator assembled in section view.

Figure 10: Architecture of ELSA Reaction Sphere (Rossini, 2014)

The permanent magnet rotor was conceived as an ideal rotor with fundamental octupole spherical harmonic (spherically shaped PMs). However, manufacturing curved permanent magnets would be cost prohibitive, so an approximate rotor was developed, which used a mosaic of 728 cylindrically shaped, Neodymium Iron Boron (NdFeB) permanent magnets with a remanence of 1.4 Tesla (Rossini, 2014). The PMs were adhered to the hollow iron sphere using a pattern of pre-machined supports composed of non-magnetic ABS plastic material. The rotor was then surrounded by a non-magnetic cover to protect the PMs and to obtain a smooth spherical surface, which is necessary to measure the position of the rotor inside the stator. This configuration is shown in Figure 11.

Figure 11: Prototype ELSA Rotor Assembly (Rossini, 2014)

A more recent rotor configuration includes truncated, spherically shaped permanent magnets to better approximate the magnetic field of a magnetic octupole. Additionally, balancing mechanisms were integrated into the rotor in order to improve the stability of the rotor at higher rotational speeds. This architecture is shown in Figure 12.

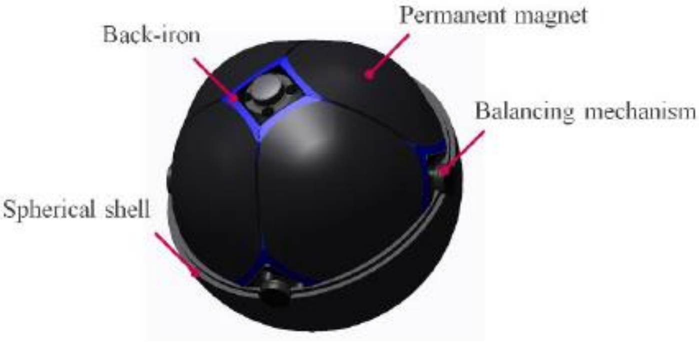

Figure 12: Elegant breadboard Rotor Assembly (Rossini, et al., 2017)

The stator assembly contains 20 rigidly mounted, air-core electromagnets located at the vertices of a dodecahedron, as shown in Figure 13.

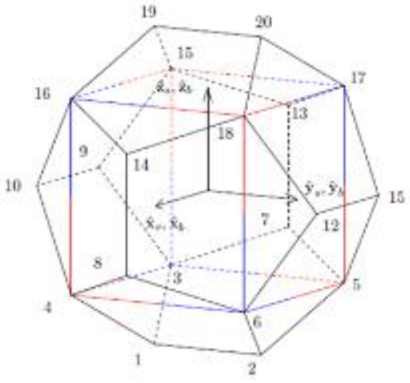

Figure 13: ELSA Electromagnet Positions at Vertices of a Dodecahedron

The spherical shell of the stator was initially manufactured using a magnetic material (iron) to benefit from a higher magnetic flux density in the airgap and to provide shielding from outside magnetic fields, however, this configuration resulted in a tendency of the rotor to contact the stator due to strong reluctant forces that occur when the rotor is eccentric to the stator (Rossini, 2014). For this reason, the stator shells were manufactured out of a non-magnetic ABS plastic, but at the expense of lower torque output. A section view of the stator is shown in Figure 14.

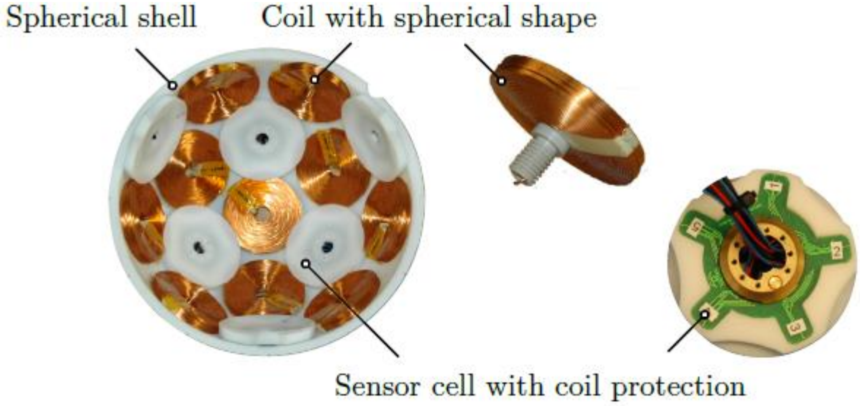

Figure 14: ELSA Stator Assembly (Rossini, 2014)

2.2.3 Position Sensing and Control

Levitation and rotation of the rotor assembly are achieved by two independent closed-loop control laws. The levitation, or magnetic bearing, control loop positions the rotor inside the stator, and is a state-feedback controller with integral control (Rossini, 2014). Rotor position feedback is provided by three optical linear displacement sensors positioned around the sphere in a tetrahedral arrangement (Rossini, 2014). The angular velocity control loop is a simple proportional controller with an angular velocity estimator. The angular velocity of the rotor is estimated using an array of fifteen (15) magnetic flux sensors, optimally positioned around a number of the stator electromagnets (Rossini, et. al., 2015). The fields generated by the levitation force fields and the torque fields were considered decoupled in the control algorithm, but coupling will occur when the rotor is not centered within the stator, but the strength of the coupling was not analyzed (Rossini, 2014). The angular velocity is estimated by the spherical harmonic coefficients, which are calculated from the magnetic flux density sensor measurements (Rossini, 2014). The levitation controller develops a vector of currents based on the desired force output, and the velocity controller develops a vector of currents based on the desired torque. The simplified control scheme is provided in Figure 15.

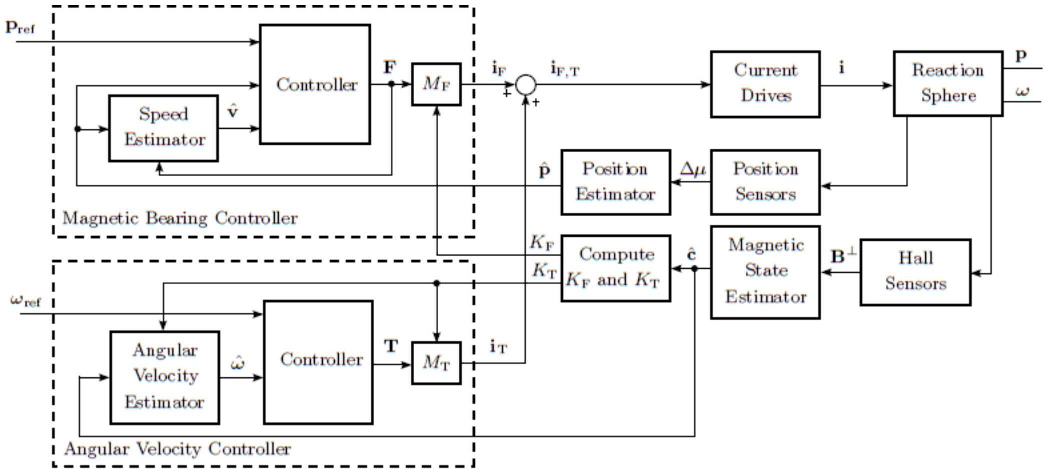

Figure 15: ELSA Levitation and Rotation Control Algorithms

2.2.4 Performance

Experimental bench tests of the “Elegant Breadboard” ELSA design was able to achieve rotation about any axis at rotation velocities of 300 RPM (CORDIS, 2014). However, in order to achieve the desired angular momentum, the sphere is required to rotate at an angular velocity of 3190 rpm.

2.3 Hysteresis Reaction Sphere

2.3.1 Design Overview

A hysteresis motor, also referred to as an asynchronous/synchronous AC motor, generates torque by utilizing the magnetic hysteresis of a ferro-magnetic rotor and eddy currents (Zhou, 2014). The stator generates a rotating magnetic field with an angular velocity ω, which passes passes through the airgap into the rotor, and due to the hysteresis of the rotor material, induces a spatial lag between the rotor and stator fields. This lag causes the rotor magnetic field to interact with the stator field within the airgap and create a torque (Zhou, 2014). During transient startup and acceleration states, torque is also induced by eddy currents in a manner similar to the AC induction RS. Once the synchronous speed is reached, torque production is only attributable to hysteresis (Zhou, 2014). The strength of the hysteresis torque correlates to both the magnetic field strength H and the lag angle δ. (Zhou, 2014). The operating principle is shown in Figure 16.

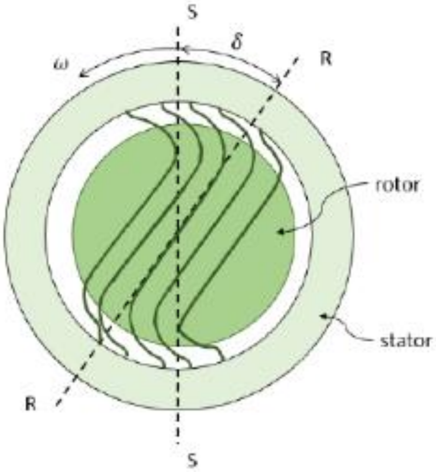

Figure 16: Operating Principle of Hysteresis Motor (Zhou, 2014)

2.3.2 Architecture

`The architecture of the Hysteresis RS is fairly simple. The hysteresis RS developed by Zhou, et al., 2017, consists of a stator, rotor, levitation electromagnet, power supply and amplifiers, position and speed sensors, and controller. The rotor is a solid sphere made of a material with a large magnetic hysteresis loop such as iron. The stator consists of a laminated core and windings. The stator windings are arranged into 4-pole windings for rotation and 2-pole windings to provide lateral bearing. Three-phase excitation signals are supplied to the 4-pole windings to achieve rotation. Additionally, a single bipolar, iron core electromagnetic with an integral permanent magnet is used to provide vertical suspension of the rotor. The permanent magnet provides flux to the magnetic circuit in addition to the electromagnet, which reduces the power demands on the power supply. The architecture of the reaction sphere studied by Zhou, et al., 2017 is shown in Figure 17.

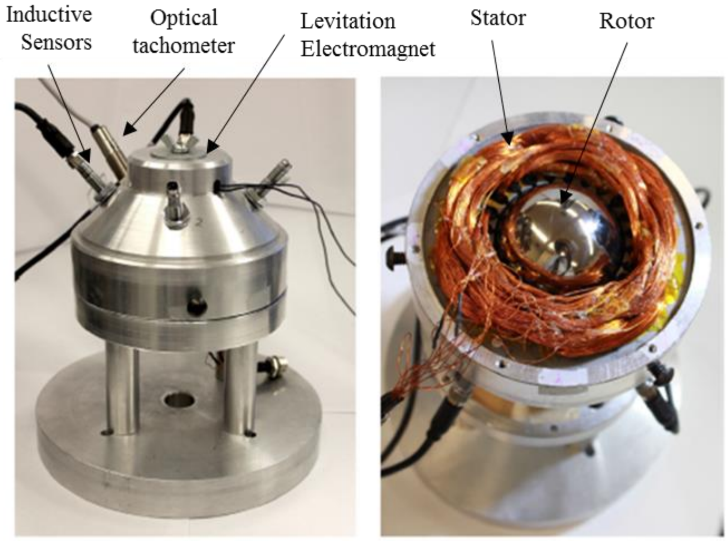

Figure 17: Hysteresis Reaction Sphere Architecture (Zhou, et al., 2017)

2.3.3 Position Sensing and Control

The vertical position of the sphere is controlled by a single iron-core, permanent magnet biased, electromagnet positioned directly above the rotor. Position control is achieved by a lead-lag PID controller with position feedback provided by inductive proximity sensors. The transfer function of the vertical suspension system is inherently unstable and thus requires position feedback. Control of the lateral position of the rotor in both the x and y directions was accomplished by two independent lead-lag PID controllers with position feedback provided by inductive proximity sensors (Zhou, 2014).

Rotor speed was sensed using an optical tachometer with binary markings applied to the rotor (Zhou, 2014). Speed control was achieved using a PD controller with parameters developed around the hunting dynamics. When speed hunting is detected the control algorithm will switch to a lead filter to suppress the speed hunting (Zhou, 2014). Speed hunting is a phenomenon associated with hysteresis motors, wherein the motor speed will fluctuate above and below the commanded speed when the motor is operating at the synchronous speed (Zhou, 2014).

2.3.4 Performance

High rotational speeds on the order of 12,000 RPM were achieved in the experiments performed by Zhou, et al., 2017. At higher synchronous speeds the hysteresis RS suffered from the phenomenon referred to as “speed hunting” which induces sporadic oscillations around reference speed, which would lead to undesirable vibrations within the spacecraft. However, Zhou, et al., 2017 mitigated the issue through careful design of the speed control loop. Zhou et al., 2017 compared the performance of the 1-D Hysteresis RS to the specification of an MW200 reaction wheel manufactured by Microsat Systems® Canada. The torque and angular momentum capacity of the MW200 is 30 mNm and 0.18 Nm-sec respectively, while the 1D Hysteresis RS provided a torque capacity of 8.15 mNm and an angular momentum capacity of 0.23 Nm-sec at 9,000 RPM.

2.4 Ultrasonic and Friction Drive Reaction Spheres

Ultrasonic motors have been successfully implemented in numerous commercial and industrial applications, specifically those that require high torque in a small form factor. Within the last 20-30 years researchers, such as Toyama, et al., 1991, have developed and tested multi-degree of freedom ultrasonic motors for use in robotic manipulators. And more recently, Paku, H., et al., 2016, proposed the use of ultrasonic motors within reaction spheres.

2.4.1 Design Overview

Ultrasonic motors generate linear or rotary motion through piezoelectric resonant vibrations. The vibrations are typically categorized as one of two waveforms: stationary (standing) wave or traveling (propagating) wave (Toyama, et al., 1991). The standing wave method is not studied in multi-degree of freedom motors / actuators due to the inability to reverse the direction of motion (Toyama, et al., 1991). The propagating-wave method of operation combines two standing waves with a 90-degree phase difference in both time and space (Uchino, 1997, Toyama et al., 1991). Propagating waves are generated by applying alternating voltages 90° out of phase to two pieces of piezoelectric strips attached to an elastic body. A surface particle of the elastic body draws an elliptical locus due to the coupling of longitudinal and transverse waves (Uchino, 1997, Toyama et al., 1991). The operating principle is illustrated in Figure 18.

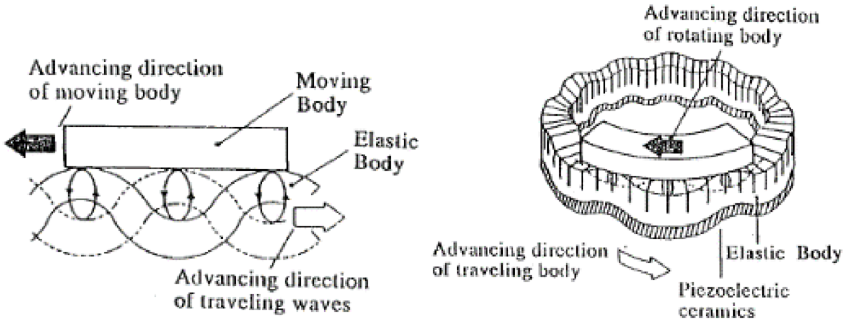

Figure 18: Principle of Propagating Wave Ultrasonic Motor (Toyama, et al., 1991).

Paku, et al., 2016 developed two types of reactions spheres that utilize friction to actuate the spherical rotor. In one design, piezo-electric actuators impart momentum to the rotor while simultaneously providing support to the rotor. The second design also uses friction to drive the rotor, but uses small uni-axial motors to impart momentum. The actuation methods are shown in Figure 19 and Figure 20.

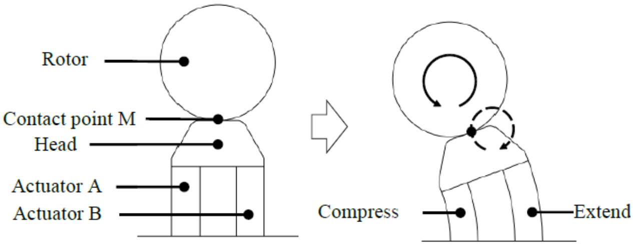

Figure 19: Piezo-electric Actuated RS (Paku, et al., 2016)

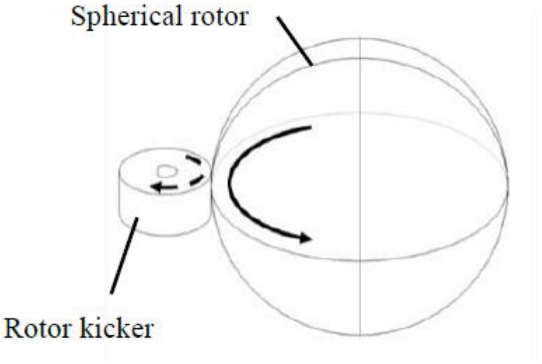

Figure 20: Motor Actuated RS (Paku, et al., 2016)

2.4.2 Architecture

Spherical ultrasonic motors, and similarly ultrasonic reaction spheres, typically consist of a spherical rotor and a minimum of three stators. The rotor is made of aluminum, steel, or an engineering plastic and may be laminated with a friction material. Ceramics are typically used as the Piezo-electric material (stator) as they have high conversion efficiency and long life. An example spherical ultrasonic motor architecture developed by Toyama, et al., is shown in Figure 21.

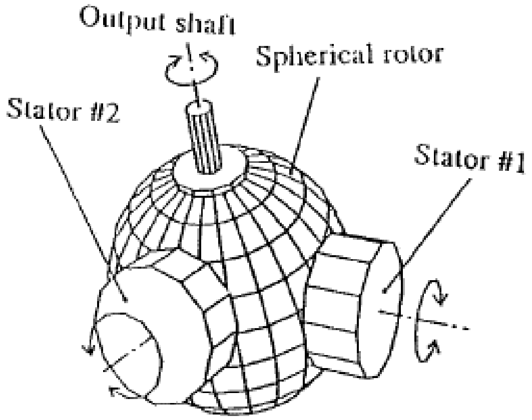

Figure 21: Construction of a Spherical Ultrasonic Motor (Toyama, et al., 1991)

The architecture of the two types of piezo-electric reaction spheres developed by Paku, et al., 2016 are depicted in Figure 22 and Figure 23.

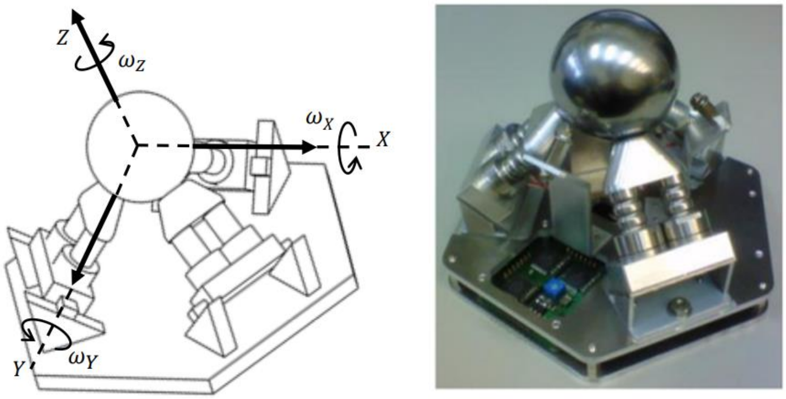

Figure 22: Piezo-electric Driven Reaction Sphere (Paku, et al., 2016)

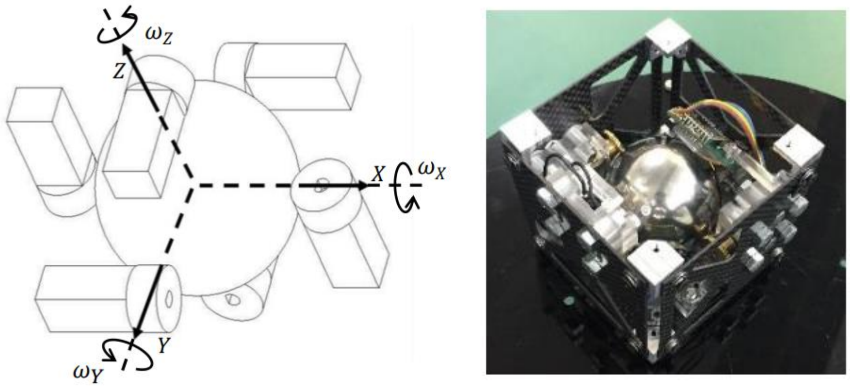

Figure 23: Motor Driven Reaction Sphere (Paku, et al., 2016)

2.4.3 Position Sensing and Control

Lateral position sensing of the rotor is not required because it is in physical contact with the actuators. Paku et. al., 2016 measured the velocity of the sphere using three optical sensors that acquire sequential images of the surface of the rotor and can detect changes in position by that identifying surface roughness patterns on the rotor. The velocity of the rotor was controlled by a Sliding Mode Control (SMC) algorithm with high-speed switched feedback. Sliding mode control (SMC) is a robust, nonlinear control technique that drives the state variables of the system to a surface in the state space, and once reached the controller maintains plant state trajectory on or near the surface. SMC control allows for control of nonlinear systems with large model uncertainties as well as large external disturbances.

2.4.4 Performance

The ultrasonic motor tested by Toyama, et al., 1991, was able to achieve speeds up to approximately 100 RPM, which is well below the rates of 3,000 – 10,000 RPM typically required to produce angular momentum on par with that produced by a micro-satellite reaction wheel. Similarly, the two types of reaction spheres developed by Paku et. al., 2016 were operated at low speeds. The motor driven system was tested to a rotational speed for 5.66 rad/s with controller saturation at 54%.

2.5 Northrop Grumman Corporation Reaction Sphere

2.5.1 Design Overview

The Northrop Grumman Corporation Reaction Sphere (NGCRS) can be described as a multi-degree of freedom, “free-flying” stepper motor (Stagmer, 2016). In this arrangement, short duration pulses of current are delivered to electromagnets in order to accelerate the rotor and thus the stator assembly in order to orient the spacecraft into the desired position. The electromagnets are energized by an Electronic Control Module (ECM) when the corresponding sensor pod detects the rotor permanent magnet is in the correct control wedge to achieve the desired rotation. Further details of the control algorithm are discussed in Section 2.5.3.

2.5.2 Architecture

The spherical motor system is comprised of a spherical rotor, a spherical stator, and a control system. The spherical rotor contains 12 permanent magnets (PM) arranged into anti-podal pairs which are evenly distributed around the circumference of a non-ferrous sphere, with each PM oriented with a common polarity (Stagmer, 2016). Any arrangement of PMs can be realized, but each PM must have another PM on the opposite side, or anti-podal to it. Two thin hemispherical shells surround the rotor and PMs to provide a smooth bearing surface for the mechanical bearings. The stator assembly includes a non-magnetic, non-conductive structural housing with the six evenly spaced mechanical bearings to support the rotor during rotation. Eight electromagnets (EM) are arranged into anti-podal pairs and are positioned around the circumference of the rotor to form two equilateral tetrahedrons. The vertices of the two tetrahedrons inscribes a cube, whose vertices are inscribed by a sphere. The vertices of one tetrahedron represents the location of the EMs in the upper hemisphere and the vertices of the other tetrahedron represents the location of the EMs in the lower hemisphere. (Stagmer, 2016). This arrangement is shown in Figure 24.

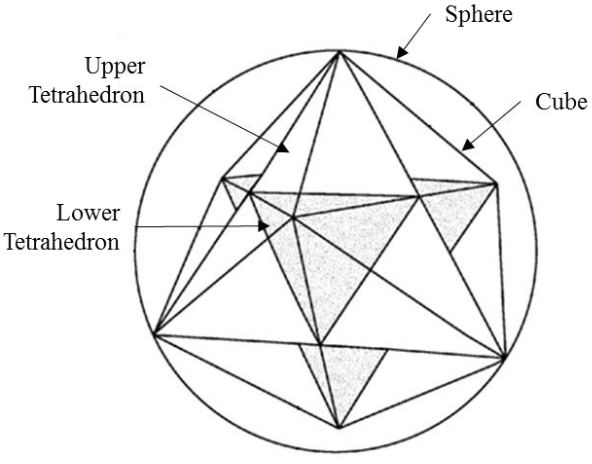

Figure 24: Tetrahedral Arrangement of EMs in the Outer Sphere

The rotational position of the rotor is detected by magnetic sensors arranged around the periphery of the EM and is referred to as a "sensor pod" (Stagmer, 2016). The vertex positions of the EMs also describe the location of the sensor pods. A minimum of four sensor pods is required to achieve control with one sensor pod surrounding one of the EMs in each anti-podal arrangement. Any number of EMs and sensor pod arrangements can be realized, with the restriction that the sensor pod is arranged such that only a single sensor pod can detect the presence of a single rotor PM for a given rotor / stator orientation. However, more than one sensor array can detect the presence of a rotor PM at one time (Stagmer, 2016). An NGC proprietary control algorithm controls the timing and duration of the excitation current to the electromagnets that transmit angular momentum to the rotor, which reacts with the stator assembly, allowing the satellite to positioned in the desired attitude. An illustration of the overall NGCRS architecture is provided in Figure 25.

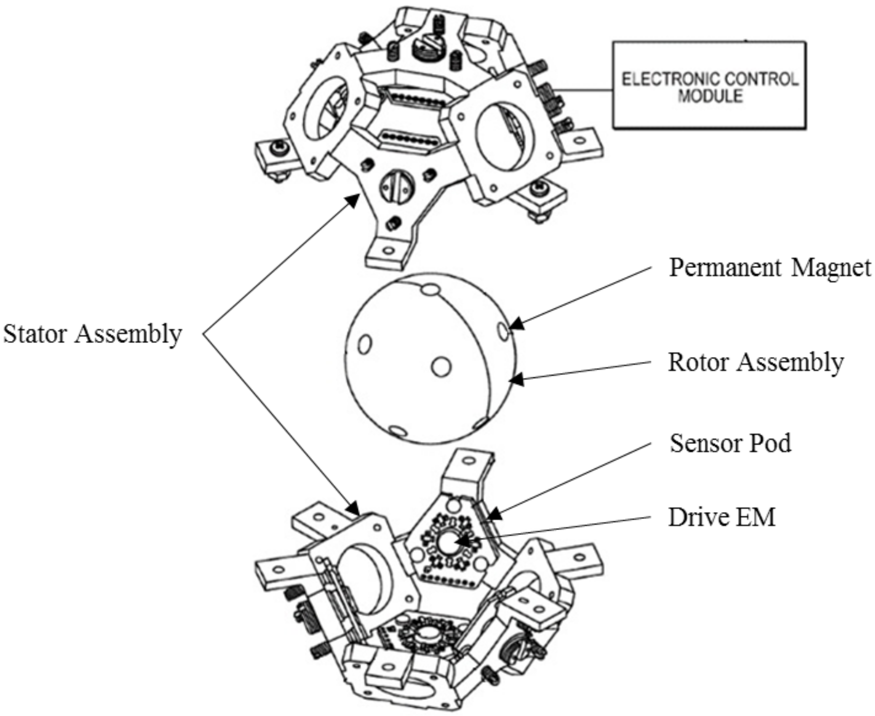

Figure 25: Northrop Grumman Corporation Reaction Sphere System (Stagmer, 2016)

2.5.3 Position Sensing and Control

The control algorithm determines the current rotational axis and speed, as well as the desired rotational direction and speed, referred to as the control axis henceforth. This is achieved via sensor pods mounted to the stator of the reaction sphere. Each sensor pod contains six (6) magnetic sensors arranged around the periphery of the drive EM, so that the field of view (FOV) of each sensor overlaps one another. The sensor field of view is then formulated into control “wedges”, as the primary means for command and control of the satellite attitude. The sensor implementation is depicted in Figure 26. The lateral position of the sphere is not measured in the architecture presented herein. However, this could be achieved using a one of sensing methods presented in the foregoing RS architectures.

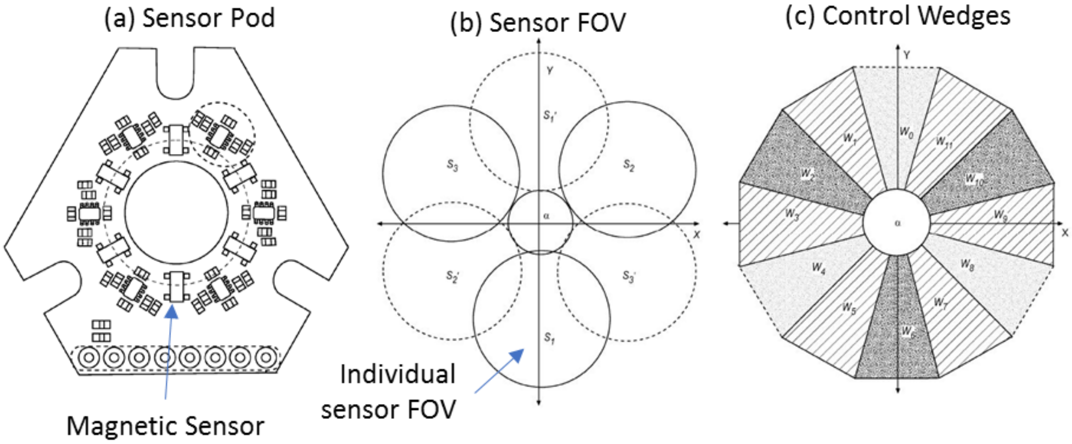

Figure 26:Sensor Architecture: (a) Sensor Pod (b) Sensor FOV (c) Control Wedges (Stagmer, 2016)

Implementation of the control wedges into the control algorithm is achieved by firstly defining basis vectors in terms of a coordinate system in which the x-y plane is tangent to the sphere at each vertex of the tetrahedron containing a sensor pod. The i and j basis vectors of each tangent plane are aligned with the x and y axes of the RS coordinate system, and these basis vectors form a total of four orthonormal bases, where one basis is located at each vertex vector (Stagmer, 2016). The desired rotational direction at each sensor vertex is then determined from the control quaternion which defines the desired rotational direction and speed. The rotational direction is specified as the control axis, which is projected onto the tangent planes of the sensor pods. The control axis is therefore expressed in terms of the two-dimensional rings of sensors, as shown in Figure 26.

Rotation of the rotor occurs on the plane perpendicular to the vector representing the control axis. The cross product of the rotation vector and the vertex position vector is another vector perpendicular to the plane containing the vertex and rotation vectors. The resulting vector represents the desired spin direction in terms of the sensor plane tangent to the sphere (Stagmer, 2016). The directional vectors are translated from the sphere coordinate space to the two-dimensional coordinate space of the tangent plane at each sensor vertex so the directional vector is coplanar with the basis vectors of the tangent plane. The necessary translation matrices are derived from the basis vectors at each vertex (Stagmer, 2016).

The current axis of rotation of is determined from the inverse of the operations used to determine the control axis in terms of the sensor vertices and the corresponding wedges (Stagmer, 2016). As the rotor rotates no sensor pods will be active and at other times all four could be active. However, in order to determine the current rotation axis, a minimum of two sensor pods must be actively detecting the presence of a rotor PM. The resulting rotation axis will be within conical tolerance zone of ± 15 degrees which is a constraint of the sensor pod resolution. The control algorithm determines the amount of angular momentum to transfer to the sphere based on the rotational velocity specified by the control axis, and by projecting the instantaneous angular velocity of the rotor onto the tangent planes of each sensor pod. The controller will activate the EM, if the magnet is in a wedge that can pull the rotor in the desired direction of rotation. The wedge aft (π radians away) of the directional wedge is “active” in order to “react” and rotate the spacecraft in the desired direction.

2.5.4 Performance

No published performance data exists for the NGCRS. Any performance data in existence is NGC proprietary and will not discussed herein.

2.6 Concluding Remarks

The AC induction RS has several attractive features, including simple architecture, small form factor, high reliability, and high operational speeds. The major drawbacks associated with this design, are the complexity of the pole design, strong propensity for levitation and rotational field coupling, and lower efficiencies in comparison to DC motors. For these reasons, AC induction architectures were not considered for this thesis.

The most notable merits of a hysteresis RS are its simple structure, potential for low vibration operation at high speeds, and the ability to self-start. Some disadvantages of the hysteresis RS include low torque generation, which is only 30% the torque of a similarly sized reaction wheel, non-linearity of the torque production, speed hunting behavior, and added weight due to the solid sphere requirement. The hysteresis RS was not selected for study because of the complexities related to the magnetic pole design as well as the non-linear torque generation which complicates the modeling and control algorithm, and no three degree of freedom hysteresis motor configurations have been developed (Zhou, et al., 2017).

The ELSA RS has high torque density and high efficiency and appears to be one of the most mature reaction sphere architectures in existence. However, its architecture is highly complex and costly. The rotor assembly contains custom manufactured, rare-earth permanent magnets and also requires balancing mechanisms to maintain stability. During prototype testing Rossini et al., were able to achieve rotational velocities of approximately 300 RPM, but a rotational speed of 3,190 RPM was required to reach the required angular momentum output. The complexity of the ELSA design was the primary reason for not selecting this architecture for study herein.

Ultrasonic motor performance can be characterized as low-speed, high-torque allowing for direct drive systems with fast response times and high torque densities within a compact envelope (Uchino, 1997). However, ultrasonic motors also exhibit several disadvantages, including operational life limitations due to mechanical wear, high heat generation due to friction, high levels of vibrations, variations in frictional coefficient over life, low rotational speeds, and lower efficiencies and lower reliabilities with respect to traditional DC motors (Uchino, 1997, Toyama et al., 1991). For these reasons, this operating method was not selected for this thesis.

The NGCRS was selected as the basis for this thesis over the other designs for several reasons. Firstly, it is capable of operating at high speeds (> 5,000 RPM), but with higher efficiencies than the AC induction, hysteresis, and ultrasonic / frictional RS designs. Secondly, its architecture is simpler and more cost-effective than the ELSA design. And thirdly, its operating principle and architecture allows integration of levitation coils without significant modifications to the existing architecture.

The majority of the RS prototypes studied herein demonstrated the ability to generate angular momentum equivalent to similarly sized reaction wheel, but ultimately, all the designs suffer from the complication of suspending the rotor within the stator in a reliable and stable manner. Mechanical, electromagnetic, and fluidic suspensions have been attempted. To date, none have been successfully suspended a three degree of freedom rotor while still meeting the desired performance and life requirements.

Chapter 3 Proposed Approach

3.1 Modeling Approach

This thesis presents a method to simulate the dynamics of a three degree of freedom (3-DOF), Northrop Grumman Corporation Reaction Sphere (NGCRS) in MATLAB Simulink®, using force and torque relations derived from a Finite Element Magnetic (FEM) model. Development of a model using the strategies presented herein, allows for high fidelity plant modeling, rapid iteration of design configurations, and a relatively simple implementation into the Simulink® model.

The RS architecture and modeling approach presented herein ensures that the magnetic fields between the levitation EMs and adjacent PMs are decoupled (e.g. only one EM-PM pair are interacting at one time). Moreover, one of the pitfalls of other reaction sphere designs is that the levitation EMs are sized to levitate the rotor in a gravity environment. This increases the propensity for the levitation and driving magnetic fields to couple and increase the disturbances on the rotor leading to instabilities. The approach taken herein, is to use low output EMs as a starting point for future controller designs. The EM coil design can be modified until a satisfactory level of disturbance rejection is achieved.

3.2 Contribution to State of the Art

The NGCRS is an innovative design that has potential to become the first commercially adopted RS in spacecraft applications. However, suspending the rotor in the stator has been a significant engineering challenge. Development of a 3-DOF NGC RS model with integrated levitation EMs is a first step in assessing the feasibility of magnetic levitation as a means to suspend the rotor and reject external disturbances (also a starting point for a 6-DOF model). The dynamic model presented in 5.7 and 5.8 can be implemented in a control algorithm to evaluate the disturbances the levitation electromagnets have on the spacecraft attitude controller. The state-space formulation is a convenient way to represent a multi-input, multi-output (MIMO) system, such as the NGC RS.

The characteristics of the reaction sphere dynamics are coupled and non-linear for the condition of a non-homogenous sphere. In that case, it may be possible to linearize the system around an operating point where the system behaves linearly. One such possibility is considering the stator and rotor to be in equilibrium. Other constraints, such as the rotational axes may be necessary.

However, as shown in Section 5.7, the inertia tensor can be diagonalized and the principal inertias considered equal. The state-space equations for this case are given below, where x is the state vector of the system, u is the input vector, and y is the output vector. The state matrix A relates the states to the state derivatives, the input matrix B relates the inputs to the derivatives of the states, the output matrix C relates the states to the outputs, and the feedthrough matrix D relates the input to the output. The rotational motion of the 3-DOF RS is completely described by the body-fixed angular velocity components and the angular position of the sphere in terms of the Euler angle kinematic relations (Section 5.4.2). Therefore, there are six state variables for the 3-DOF system and are given in equation (2).

$$\dot{x}(t) = A(t)x(t) + Bu(t) \tag{1}$$

$$\begin{bmatrix} \dot{\omega}_x \\ \dot{\omega}_y \\ \dot{\omega}_z \\ \dot{\psi} \\ \dot{\theta} \\ \dot{\phi} \end{bmatrix} = \begin{bmatrix} 0 & 0 & 0 & 0 & 0 & 0 \\ 0 & 0 & 0 & 0 & 0 & 0 \\ 0 & 0 & 0 & 0 & 0 & 0 \\ 0 & sec\theta sin\phi & sec\theta cos\phi & 0 & 0 & 0 \\ 0 & cos\phi & -sin\phi & 0 & 0 & 0 \\ 1 & tan\theta sin\phi & tan\theta cos\phi & 0 & 0 & 0 \end{bmatrix} \begin{bmatrix} \omega_x \\ \omega_y \\ \omega_z \\ \psi \\ \theta \\ \phi \end{bmatrix} + \begin{bmatrix} {I_x}^{-1} & 0 & 0 \\ 0 & {I_y}^{-1} & 0 \\ 0 & 0 & {I_z}^{-1} \\ 0 & 0 & 0 \\ 0 & 0 & 0 \\ 0 & 0 & 0 \end{bmatrix} \begin{bmatrix} \tau_x \\ \tau_y \\ \tau_z \end{bmatrix} \tag{2}$$

The output equation is given below, where the outputs of the system are the body angular velocity components and the orientation of the sphere in terms of the Euler angles.

$$y(t) = Cx(t) + Du(t) \tag{3}$$

$$\begin{bmatrix} \omega_x \\ \omega_y \\ \omega_z \\ \psi \\ \theta \\ \phi \end{bmatrix} = \begin{bmatrix} 1 & 0 & 0 & 0 & 0 & 0 \\ 0 & 1 & 0 & 0 & 0 & 0 \\ 0 & 0 & 1 & 0 & 0 & 0 \\ 0 & 0 & 0 & 1 & 0 & 0 \\ 0 & 0 & 0 & 0 & 1 & 0 \\ 0 & 0 & 0 & 0 & 0 & 1 \end{bmatrix} \begin{bmatrix} \omega_x \\ \omega_y \\ \omega_z \\ \psi \\ \theta \\ \phi \end{bmatrix} + \begin{bmatrix} 0 & 0 & 0 \\ 0 & 0 & 0 \\ 0 & 0 & 0 \\ 0 & 0 & 0 \\ 0 & 0 & 0 \\ 0 & 0 & 0 \end{bmatrix} \begin{bmatrix} \tau_x \\ \tau_y \\ \tau_z \end{bmatrix} \tag{4}$$

The RS system has three inputs and six outputs. The transfer functions relating the each input to the each output of the system can be derived.

In addition to supporting controller development, the FEM model also provides the inverse force and torque relations, derived in Section 5.6, which allow the controller to output the appropriate current to develop the desired force and torque.

Chapter 4 Objectives

The objectives of this thesis are fivefold:

1. Design and integrate levitation EMs into the NGCRS. The EMs should have fast response times, negligible field interactions with adjacent EMs, and field interactions decoupled from all but one Permanent Magnet (PM)
2. Demonstrate through FEM modeling that the EM and PM field interactions are limited to a single EM-PM pair.
3. Derive a generalized set of force and torque relations from the FEM model data, that can describe the force and torque for any arbitrary orientation of the rotor/stator, and for any EM-PM pair.
4. Develop an algorithm which determines the appropriate force and torque relations to use for the instantaneous rotor / stator orientation, levitation coil current.
5. Develop a three-degree of freedom (3-DOF) rotational dynamic model of the RS using the force and torque relations derived from the FEM model

The work performed to achieve these objectives is detailed in the sections that follow.

Chapter 5 Methods and Work Performed

After selecting the NGCRS architecture as the basis for this thesis, a trade study was performed to evaluate the suitability of iron-core and air-core electromagnets (EM) for rotor levitation (magnetic bearing). Ultimately, an air-core EM was down-selected as a result of the trade study for reasons detailed in the sections 5.1.

The RS dynamic model was developed using both traditional and novel design methodologies. Firstly, the coordinates of the rotor permanent magnets (PM) and stator electromagnets (EM) were derived using geometric and trigonometric relations. Then, the kinematic relations between each rotor PM and each stator EM was established using principles of linear algebra.

From there, the ground rules and assumptions were established for the modeling of the magnetic forces and torques between the rotor PMs and stator EMs. The principle of superposition was utilized in this analysis because development of a physical RS prototype was beyond the scope and budget of the thesis project. The lack of any hardware testing required conservatism in the modeling approach. Superposition models were developed alongside "integrated" models, which include the PM and iron in the same FEM model. Decoupling inserts were introduced into the integrated model and the insert geometry was altered until the superposition and integrated models were in close agreement. Additionally, a comparative study of linear and non-linear FEM models was also performed in order assess the need to include material non-linearities. After a complete set of data was gathered from the FEM models, regression analysis was performed to establish the force relations as a function of current and angular distance from the EM / PM pair. The results of these studies are detailed in Section 0.

An algorithm that computes the forces and torques acting on the rotor due to the six electromagnets was implemented in MATLAB Simulink®. The forces are computed from curve and surface plots obtained from regression analysis of the forces computed by the generalized FEM model. A coordinate transformation is applied to the generalized forces to transform them into the RS stator coordinates, and then the applicable torques are calculated.

Finally, the equations of motion of the 3-DOF RS were implemented in a MATLAB Simulink® model, which is discussed in detail in Section 5.8.

5.1 Levitation Electromagnet Trade Study

5.1.1 Iron Core Electromagnet

A bi-polar, iron-core EM configuration was studied due to its higher power density relative to single pole design with the same magneto-motive force (MMF) (Roters, 1941). The EM was designed to fit within the dimensions of the existing NGCRS stator cage, and are positioned in the stator assembly as well as the dimensions of the EM are shown in Figure 27. The core material was modeled as low carbon steel – soft iron material. The BH curve data for the material was extracted from the COMSOL® material library, and the normal DC magnetization curve of the material is plotted in Figure 57. The coil has 300 turns of 34 AWG magnet wire, and was sized to provide an MMF sufficient to drive the core material into saturation level of approximately 1.2 Tesla for airgaps ranging from 20 to 40 mils (1 mil = 0.001 inch).

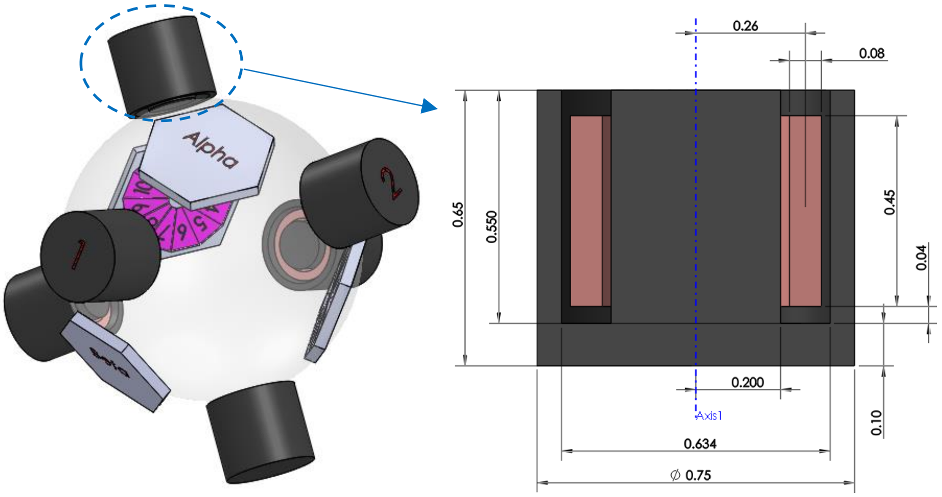

Figure 27: Dimensions (inches) of Bi-Polar Levitation Electromagnet

The curvature of the spherical rotor was ignored and instead was considered as a flat plate with one translational degree of freedom in order to simplify the analysis. The analysis also assumed the following:

- Magnetic fringing and leakage flux effects are negligible
- Inductance is a function only of rotor position
- Core permeability follows the $B = \mu H$ relation (e.g. μ is not a function of B)
- Joule heating of the coil is negligible

An abstraction of the magnetic circuit of the iron-core electromagnet is depicted in Figure 28. The electrical circuit is analyzed first, followed by the magnetic circuit. The equations derived from the electrical and magnetic circuit analyses were implemented in a Simulink® model. The magnetic forces predicted by the magnetic circuit analysis were then compared to a FEM model.

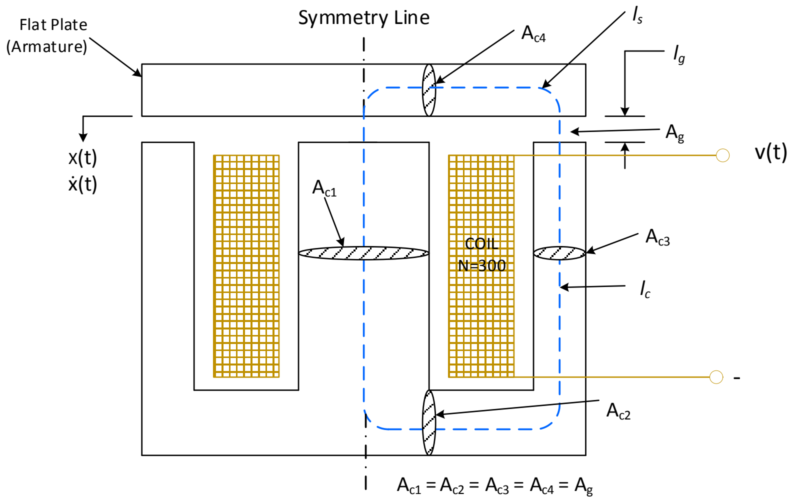

Figure 28: Iron-core Electromagnet with Optimal Geometry

The relation describing the current in the coil is derived by considering it as an RL circuit with a ferrous core surrounding the coil. An abstraction of the circuit is shown in Figure 29.

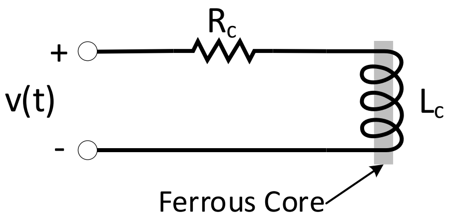

Figure 29: Electrical Circuit of the Iron-core Levitation Electromagnet

Applying the Kirchhoff Voltage Law to the circuit yields a first order differential equation, where $v(t)$ is the voltage in the coil, R is the resistance of the coil, N is the number of turns in the coil, x is the displacement of the core from the designated null position, or in this case the displacement of the flat rotor, and ϕ is the flux in the ferrous core (Roters, 1941).

$$v(t) = Ri + N\frac{d\phi(i,x)}{dt} \tag{5}$$

Insertion of the flux linkage relation λ yields:

$$\lambda(i,x) = N\phi(i,x) = L(x)i \tag{6}$$

And the relation for magnetic flux:

$$\phi(i,x) = \frac{L(x)i}{N} \tag{7}$$

Inserting equation (6) into equation (5) and applying the chain and product rules of differentiation yields:

$$v(t) = Ri + L(x)\frac{di}{dt} + i\frac{dL(x)}{dx}\frac{dx}{dt} \tag{8}$$

The terms (from left to right) in equation (8) represent the resistive voltage, inductive voltage due to changing current, and the back-emf caused by movement of the rotor. The self-inductance L of an iron-core EM is determined by the material and geometry of the core and is given by the equation (9), where A_c is the cross sectional area of the coil, μ is the relative permeability of the core material, l is the mean length of the magnetic circuit path. This relation shows that the inductance can be written in terms of magnetic reluctance, as will be shown in the magnetic circuit analysis that follows.

$$L = \frac{N\phi(i,x)}{i} = \frac{N(Ni\mu A_c)}{il} = N^2\frac{\mu A_c}{l} \tag{9}$$

The performance of the EM can be analyzed by treating it as a series of magnetic circuit elements. A magnetic circuit is analogous to an electrical circuit, where the magneto-motive force (MMF) is analogous to electrical voltage v, reluctance $\mathcal{R}$ is analogous to the electrical resistance R, and magnetic flux ϕ is analogous to electrical current i (Sen, 1996). The magnetic circuit for the bipolar electromagnet is shown in Figure 30.

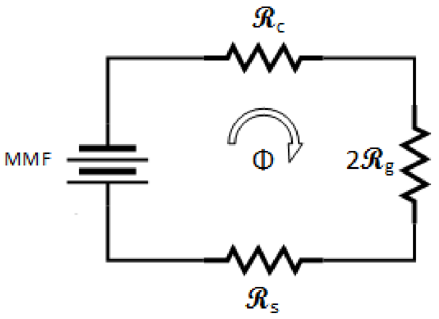

=

Figure 30: Magnetic Circuit of Iron-core Electromagnet

The MMF is the driving force in the magnetic circuit and is equal to the number of turns in the coil N multiplied by the current i in the coil. The total MMF in the circuit is given below where l_c is the mean length of the path of a magnetic line through the core material, l_r is the length of the magnetic path within the flat rotor, l_g is the length of the airgap, and x is the displacement of the rotor, and H_c, H_r, and H_g are the magnetic field intensities within the core, rotor, and the airgap respectively.

$$Ni = l_c H_c + l_r H_r + 2(l_g - x)H_g \tag{10}$$

The BH relationship can be used to express equation (10) in terms of flux density (Sen, 1996):

$$B = \mu H = \mu_r \mu_0 H \tag{11}$$

$$Ni = l_c \frac{B_c}{\mu_r \mu_0} + l_r \frac{B_r}{\mu_r \mu_0} + 2(l_g - x)\frac{B_g}{\mu_0} \tag{12}$$

Equation (12) can also be expressed in terms of magnetic flux:

$$Ni = \phi\left(\frac{l_c}{\mu_r \mu_0 A_c} + \frac{l_r}{\mu_r \mu_0 A_r} + \frac{2(l_g - x)}{\mu_0 A_g}\right) \tag{13}$$

The reluctance of a magnetic circuit is given by equation (14).

$$\mathcal{R} = \frac{l}{\mu A} \tag{14}$$

Equation (13) can be expressed in terms of series reluctances using equation (14). The resulting relation is again analogous to an electrical circuit with series resistances:

$$Ni = \phi(i,x)\left(\mathcal{R}_c + \mathcal{R}_r + 2\mathcal{R}_g(x)\right) \tag{15}$$

An expression for the inductance of the inductance of the electromagnet can be obtained by inserting the flux linkage relation given in equation (6) into equation (15):

$$Ni = \frac{L(x)i}{N}\left(\mathcal{R}_c + \mathcal{R}_r + 2\mathcal{R}_g(x)\right) \tag{16}$$

Solving for the inductance and simplifying terms yields:

$$L(x) = \frac{N^2}{\mathcal{R}_{total}} = \frac{N^2}{\mathcal{R}_c + \mathcal{R}_r + 2\mathcal{R}_g(x)} = \frac{N^2}{\dfrac{l_c}{\mu_r\mu_0 A_c} + \dfrac{l_r}{\mu_r\mu_0 A_r} + \dfrac{2\left(l_g - x\right)}{\mu_0 A_g}} \tag{17}$$

$$L(x) = \frac{N^2\mu_r\mu_0 A_c A_r A_g}{A_g(A_r l_c + A_c l_r) + 2\left[\mu_r A_c A_r\left(l_g - x\right)\right]} \tag{18}$$

The derivative of inductance with respect to the rotor displacement x is:

$$\frac{dL(x)}{dx} = -\frac{N^2\mu_r\mu_0 A_c A_r A_g}{A_g(A_r l_c + A_c l_r) + 2\left[\mu_r A_c A_r\left(l_g - x\right)\right]} \cdot \frac{2\mu_r A_c A_r}{1} \tag{19}$$

$$\frac{dL(x)}{dx} = -\frac{2\mu_0 A_g (N\mu_r A_c A_r)^2}{\left(A_g(A_r l_c + A_c l_r) + 2\left[\mu_r A_c A_r\left(l_g - x\right)\right]\right)^2} \tag{20}$$

The magnetic force between the core and flat rotor can be approximated by assuming the majority of the field energy W_f is stored within the airgaps of the magnet, and that the flux linkage - current (λ-i) relation is linear as given in equation (6) (Sen, 1996). With this simplifying assumption, the field energy relation given in equation (21) can be used to derive the magnetic force of the EM in terms of coil current and differential inductance (Sen, 1996).

$$W_f = \int_0^{\lambda} i \, d\lambda = \int_0^{\lambda} \frac{\lambda}{L(x)} \, d\lambda = \frac{\lambda^2}{2L(x)} \tag{21}$$

Substituting for flux linkage λ using equation (6) gives a relation for the magnetic force:

$$F_{em}(i,x) = \frac{1}{2} \frac{dL(x)}{dx} i^2 \tag{22}$$

The force equation then becomes:

$$F_{em}(i,x) = -i^2 \frac{\mu_0 A_g (N \mu_r A_c A_r)^2}{\left(A_g (A_r l_c + A_c l_r) + 2\left[\mu_r A_c A_r \left(l_g - x\right)\right]\right)^2} \tag{23}$$

The EM system (considering a single EM) will have three state variables: the coil current i, the rotor velocity $\dot{x}$, and the rotor displacement x. The three non-linear state equations of the electromagnet are given below. Note that the term multiplied by rotor velocity in equation (24) represents the back emf generated by the rotor movement.

$$\frac{di}{dt} = \frac{\left(v(t) - Ri + i \dfrac{2\mu_0 A_g (N \mu_r A_c A_r)^2}{\left(A_g (A_r l_c + A_c l_r) + 2\left[\mu_r A_c A_r \left(l_g - x\right)\right]\right)^2} \dot{x}\right)}{\left(\dfrac{N^2 \mu A_c A_r A_g}{A_g (A_r l_c + A_c l_r) + 2\left[\mu_r A_c A_r \left(l_g - x\right)\right]}\right)} \tag{24}$$

$$\frac{dx}{dt} = \dot{x} \tag{25}$$

$$\frac{d^2 x}{dt^2} = -\frac{F_{em}(i,x)}{m_r} = -\frac{i^2}{m_r} \frac{\mu_0 A_g (N \mu_r A_c A_r)^2}{\left(A_g (A_r l_c + A_c l_r) + 2\left[\mu_r A_c A_r \left(l_g - x\right)\right]\right)^2} \tag{26}$$

The airgap reluctance is linear, but the reluctance of the magnetic core is non-linear. Consequently, the load-line graphical method was used to approximate the permeability of the iron core. Recalling equation (10), except the airgap relation is expressed in the form of equation (12), and re-arranging in terms airgap density B_g gives equation (28).

$$Ni = l_c H_c + l_r H_r + 2\left(l_g - x\right)\frac{B_g}{\mu_0} \rightarrow B_g = \frac{Ni\mu_0}{2\left(l_g - x\right)} - \frac{\mu_0(l_c H_c + l_r H_r)}{2\left(l_g - x\right)} \tag{27}$$

Equation (28) is the load-line, which is a straight line of the form $y = mz + c$ where y represent flux density B and z represents the field intensity H (Sen, 1996). The y-intercept of the load-line is computed by assuming all of the field energy acts on the airgap (H_c and $H_r = 0$) (Sen, 1996). Note that the airgap length is multiplied by two in equation (28) because there are two airgaps in a bi-polar EM.

$$c = B_g = \frac{Ni\mu_0}{2\left(l_g - x\right)} \tag{28}$$

The x-intercept is calculated based on the assumption that all the MMF acts on the iron and that the flux density in the airgap is zero. Considering the airgap as zero, the iron of the EM can be treated as one piece of iron.

$$x_{int} = H_{iron} = -\frac{Ni}{l_c + l_r} \tag{29}$$

The slope of the load-line can be determined from equations (28) and (29):

$$m = \frac{y_2 - y_1}{x_2 - x_1} = \frac{y_2 - 0}{x_2 - 0} = \frac{y_{int}}{x_{int}} = -\frac{Ni\mu_0}{2l_g}\left(\frac{Ni}{l_c + l_r}\right)^{-1} = -\mu_0 \frac{l_c + l_r}{2l_g} \tag{30}$$

The load-line intersects the BH curve at the operating point of the magnetic circuit, which gives approximate values for the flux density and field intensity in the core of the material, which in turn allows the permeability to be approximated using the $B = \mu H$ relation. The load-line method was implemented in the Simulink® model as a MATLAB® Level-2 S-function. At every time step, the S-function constructs the BH curve as a series of line segments and checks each line segment for intersection with the load line. The resulting H and B values at the point of intersection are then used to determine the permeability of the iron in the circuit. An example plot is shown in Figure 31.

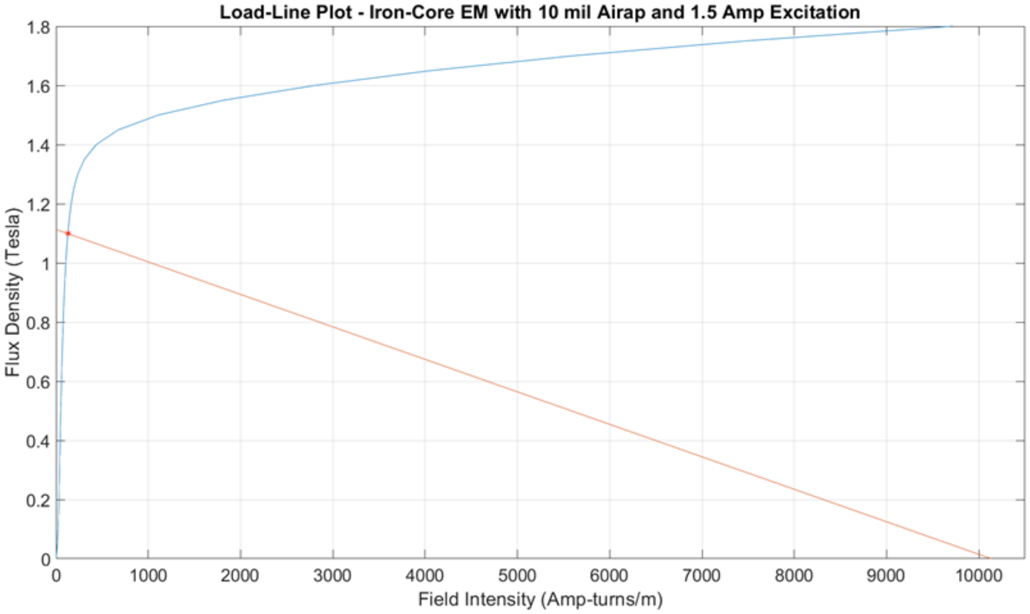

Figure 31: Load-Line Intersection with BH Curve

The Simulink® model was evaluated against a FEM model of the EM using David Meeker's Finite Element Method Magnetics software (FEMM 4.2). The model was implemented as an axisymmetric, magnetostatic problem using a non-linear BH curve for low carbon steel – soft iron material. This material BH curve was used in both the Simulink® and the FEMM model and was obtained from the COMSOL® material library. The excitation current was fixed at 1.5 amperes, and airgaps ranging from 1 mil to 40 mils were simulated in 1 mil increments. The simulations were programmed into FEMM 4.2 using a Lua script to automatically solve for magnetic force over the specified range of airgaps. The forces predicted by the Simulink® and FEMM models are plotted in Figure 32. The Simulink® model is shown in Figure 33 and the FEMM model (with mesh) is shown in Figure 34.

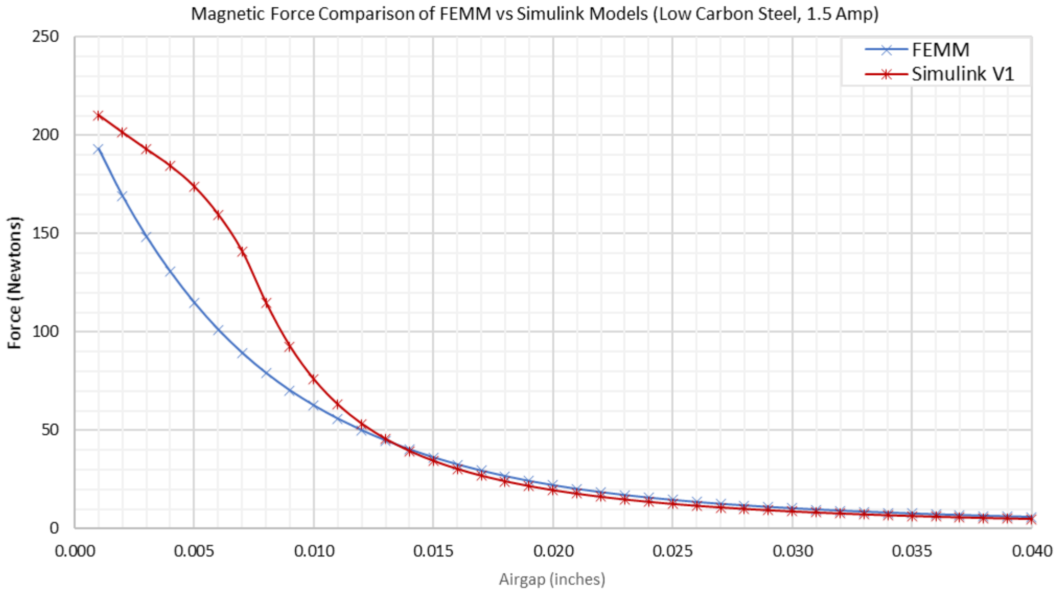

Figure 32: Iron-Core EM Force Comparison – FEMM vs. Simulink® Models

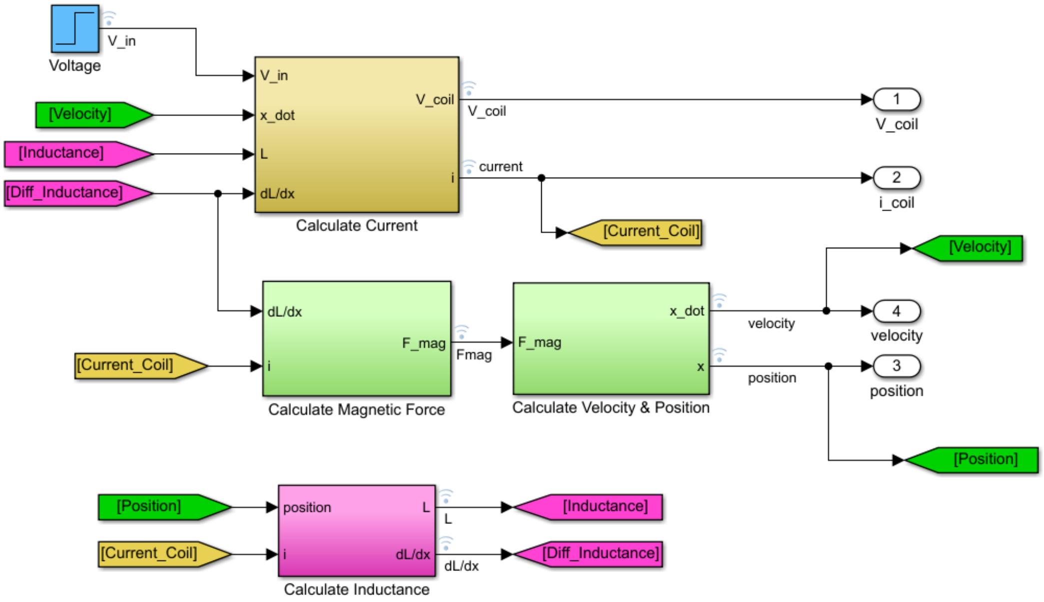

Figure 33: Simulink® Model of Iron-Core EM

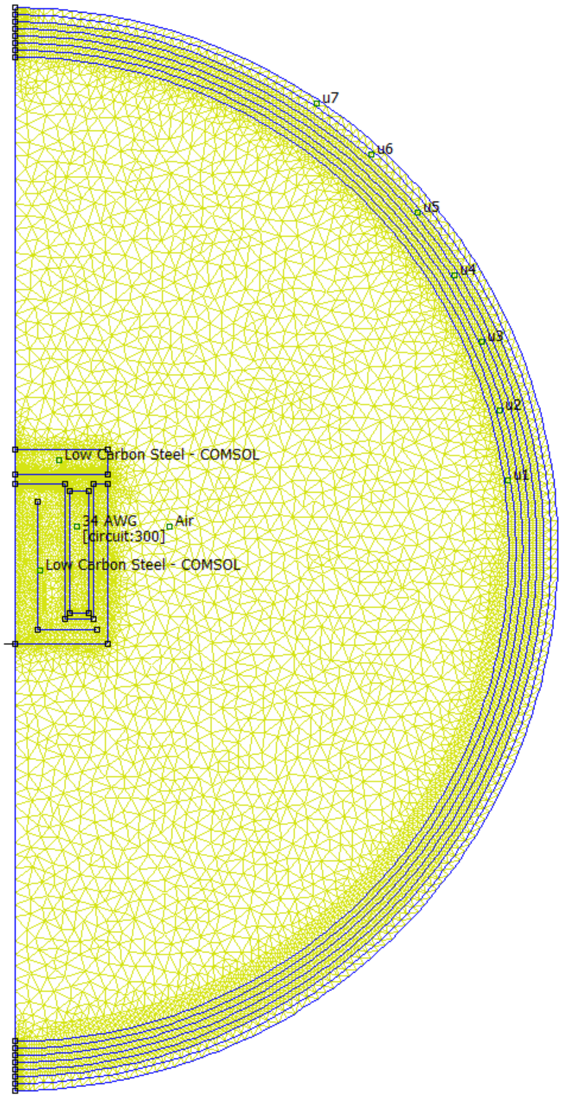

Figure 34: Axisymmetric FEMM Model of Iron-Core EM

The discrepancy between the forces predicted by the Simulink® and FEMM models is caused by several factors. Firstly, the magnetic circuit analysis calculates an average flux density for the iron core and the permeability for the iron portion of magnetic circuit using the load-line method, which is an approximation. The behavior of the force vs. stroke curve of the Simulink® model for airgap ranges of 5 to 10 mils is due to the load-line intersecting the BH curve in the non-linear region, or “knee” of the BH curve. This effect is not observed in the FEMM model because FEMM 4.2 computes the permeability at every node using the relation in equation (31), where the permeability is a function of B (Meeker, 2018):

$$\mu = \frac{B}{H(B)} \tag{31}$$

Secondly, the FEMM model predicted differing levels of induction for the inner and outer poles, while the magnetic circuit analysis assumed an average flux density for both poles. At larger airgaps, the average flux density of each pole was nearly equal to the value computed in the magnetic circuit analysis, however, at smaller gaps, the values diverged. Figure 35 shows two plots of the flux density within the airgap of the electromagnet poles for gaps of 20 mils and 10 mils respectively. The FEMM model predicted an average airgap flux density of 0.545T for a 20-mil airgap, which is close to the 0.55T value predicted by the magnetic circuit analysis. However, FEMM predicts an average value of 0.91T for an airgap of 10 mils, which is 17% less than the flux density predicted by the magnetic circuit analysis.

Plot of Flux Density within 0.020 inch airgap at Inner and Outer Pole

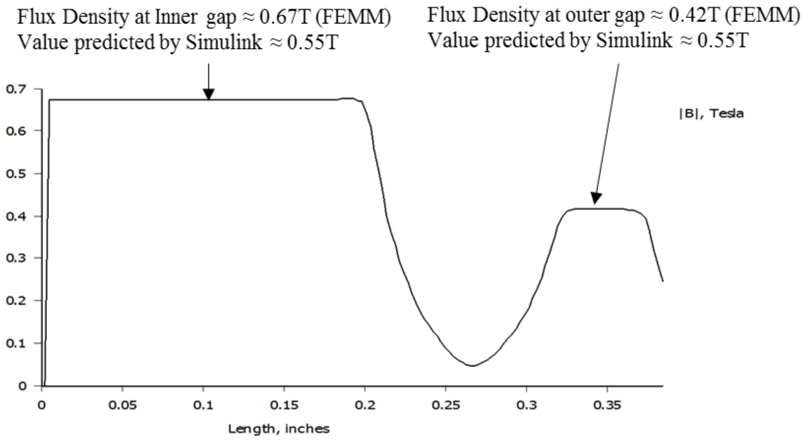
Flux Density at Inner gap ≈ 0.67T (FEMM)
Value predicted by Simulink ≈ 0.55T

Flux Density at outer gap ≈ 0.42T (FEMM)
Value predicted by Simulink ≈ 0.55T

Plot of Flux Density within 0.010 inch airgap at Inner and Outer Pole

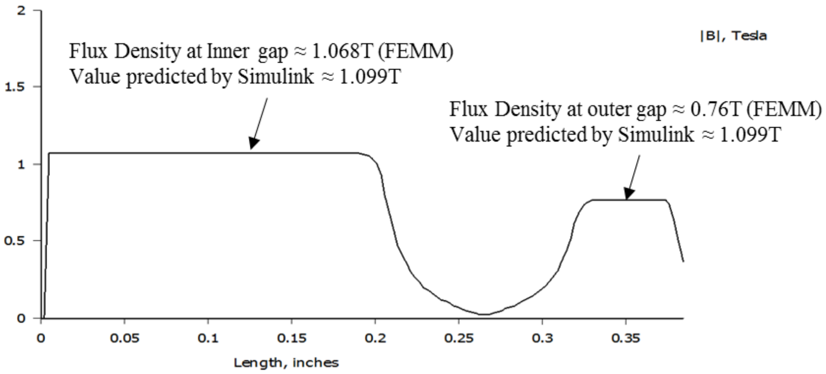
Flux Density at Inner gap ≈ 1.068T (FEMM)
Value predicted by Simulink ≈ 1.099T

Flux Density at outer gap ≈ 0.76T (FEMM)
Value predicted by Simulink ≈ 1.099T

Figure 35: Flux Density Plot in Airgap of Inner and Output Poles of Electromagnet

Lastly, the magnetic circuit analysis does not account for magnetic fringing or leakage flux, which is illustrated by a flux density plot of the FEMM model shown in Figure 36. Magnetic fringing is a phenomenon observed in magnetic circuits with airgaps, and is caused by variations in reluctance (Roters, 1941). Leakage flux bypasses the airgap altogether and does not contribute to work done and fringing flux contributes little to no work to the system and in some cases can actually decrease the amount of work done (Roters, 1941).

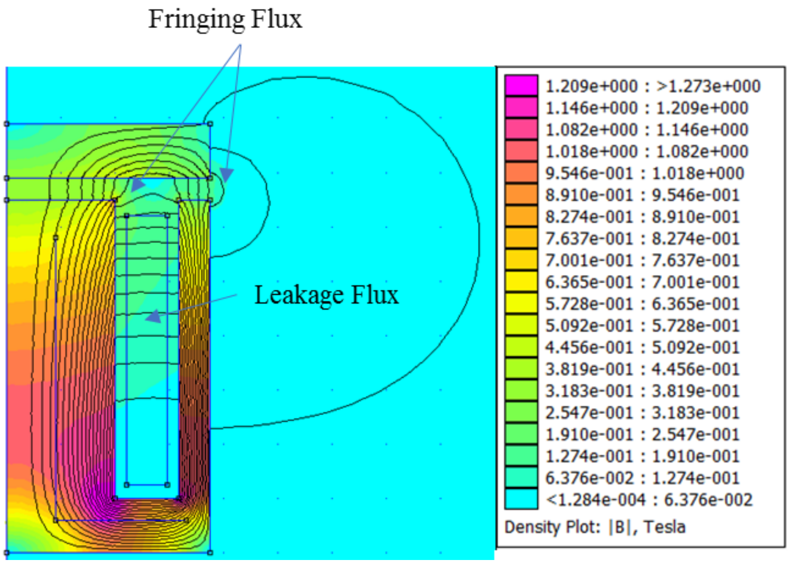

Figure 36: Flux Density Plot – FEMM Model of Iron-Core Electromagnet

Based on the results of the comparison, FEM modeling should be utilized to perform further investigation of the iron-core EM. Nevertheless, the magnetic circuit analysis does provide greater confidence in the forces predicted by the FEM model. Dr. Hector Gutierrez and a number of Florida Institute of Technology students performed additional research using this model, and modeled the iron-core EM in COMSOL®. They concluded that the iron-core EM has several drawbacks, one of which is slow response times, large disturbance forces when the rotor is eccentric to the stator, and disturbances due to the attraction of the PM to the iron core even if the EM is de-energized. (Gutierrez, 2020).

Consider a rotor with adjacent PMs separated by an angular distance of 1.10715 radians (63.435 degrees) and an angular velocity of 5,000 RPM (523.6 rad/sec). This condition gives less than 2.114 milliseconds for the EM to de-energize to avoid interacting with the PM. As shown in Figure 37, the rise and fall times of the iron-core EM are approximately 15 milliseconds, which is too slow to fully de-energize prior interacting with a passing rotor PM.

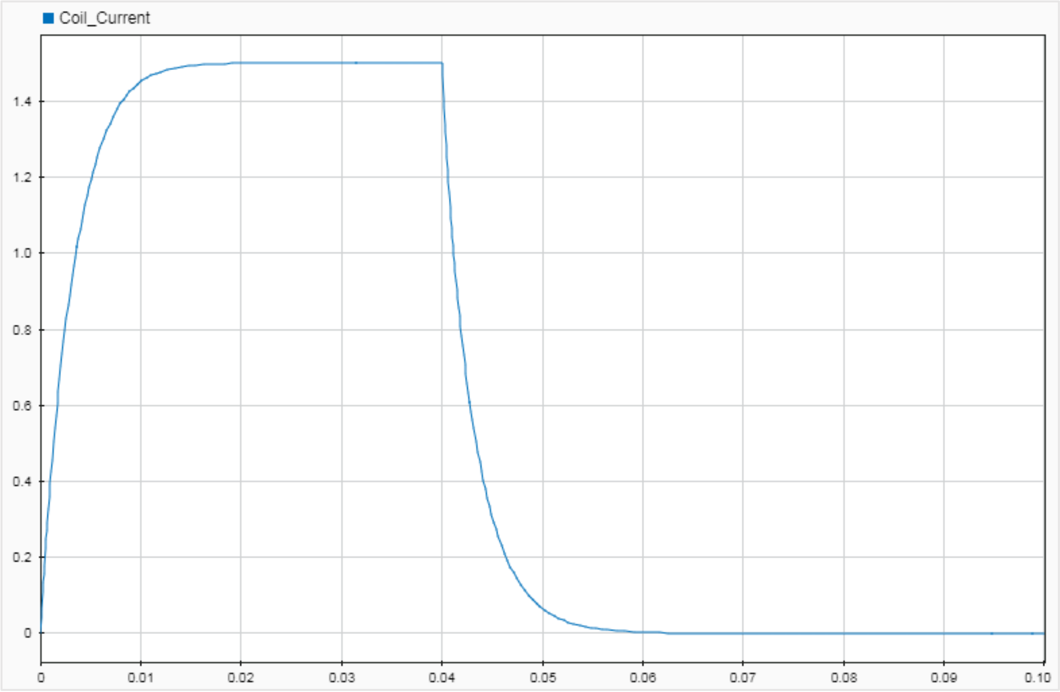

Figure 37: Iron-core EM Coil Current Rise / Fall Time - 15 Volt Step, Fixed 5 mil airgap

5.1.2 Air Core Electromagnet

The air-core EM could not be modeled using the magnetic circuit approach due to the inability to precisely estimate the mean flux path between the rotor and the electromagnet. The inductance of the coil and its response time were estimated in Simulink® and compared to the iron-core electromagnet. The inductance of an air-core electromagnet can be approximated by equation (32), where, N is the number of turns in the coil, μ_0 is the absolute permeability of medium surrounding the core, l_c is the length of solenoid, and A_c is the cross-sectional area of the coil with r_i and r_o being the inner and outer radius of the solenoid respectively.

$$L = \frac{N^2 \mu_o A_c}{l_c} = \frac{N^2 \mu_o \pi \left(r_o^2 - r_i^2\right)}{l_c} \tag{32}$$

However, equation (32) is only accurate for long, slender solenoids. A more accurate empirical formula, derived by Wheeler, 1928 for a multi-layer, air-core solenoid is given by equation (33), where r_m is the mean radius of the coil in meters winding and L is given in micro-Henries (Wheeler, 1928).

$$L = 31.6 \cdot \frac{N^2 r_m^2}{6r_m + 9l_c + 10(r_o - r_i)} \tag{33}$$

This formula predicts an inductance of 0.526 mH using the values provided in Table 3, and is in close agreement with the COMSOL® prediction of 0.51 mH. The EM was modeled in Simulink® using the relations given in equations (34) and (35).

$$v(t) = L\frac{di(t)}{dt} + Ri(t) \tag{34}$$

Expressing in normalized form gives:

$$\frac{di(t)}{dt} = \frac{1}{L}[V - Ri(t)] \tag{35}$$

The time constant of an LR circuit is given by equation (36).

$$\tau_c = \frac{L}{R} = \frac{0.526\ \mathrm{mH}}{4.271\ \mathrm{Ohms}} = 1.232 \cdot 10^{-4} sec \tag{36}$$

And the steady-state current is reached in five time constants, and the complete response of the air-core EM to a 15 volt step input is plotted in Figure 38.

$$5\tau_c = 5(1.232 \cdot 10^{-4}) = 6.158 \cdot 10^{-4} sec \tag{37}$$

The air-core EM exhibits response times more than an order of magnitude faster that the iron-core EM, which is expected due to the increased inductance associated with iron-core EMs. Based on the results of the EM trade study, the air-core EM configuration was selected for the levitation.

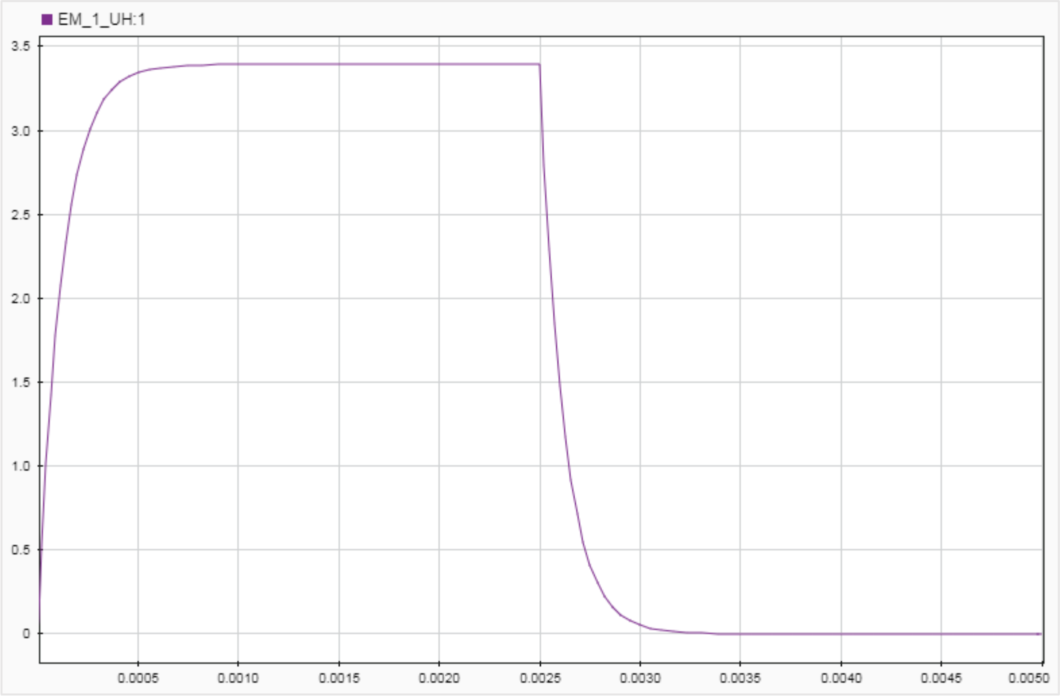

Figure 38: Air-core EM Response (Coil Current vs. Time) – 15 Volt Step Input

5.2 NGCRS Design Modifications

The Reaction Sphere (RS) geometry studied herein is essentially that of the NGCRS architecture, described in Section 2.5.2, but with modifications to the stator and rotor as described below in Sections 5.2.1 and 5.2.2.

5.2.1 Stator Modifications

The NGCRS stator is modified to include six levitation electromagnets (EM). The EMs are positioned as antipodal pairs and are located such that they are equally spaced between the sensor pods and drive EMs. The drive EMs are located at the center of the sensor pods that detect the presence of the PMs. The position of the levitation EMs relative to the sensor pods is depicted in Figure 39. The characteristics of the levitation EMs, including the geometry, are discussed in Section 5.8.1.

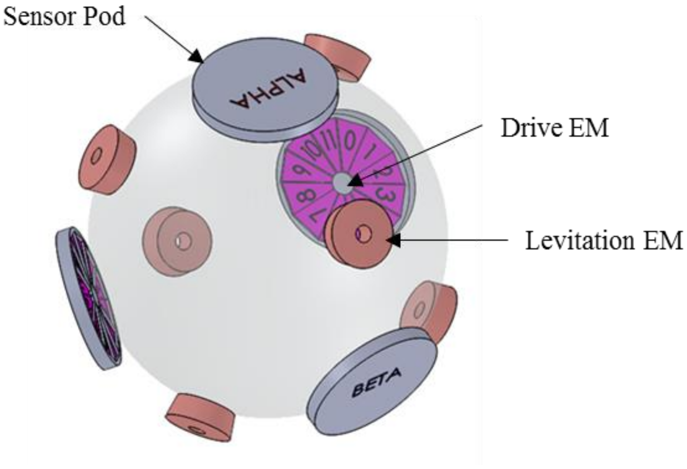

Figure 39: Stator Modifications with Levitation EMs

5.2.2 Rotor Modifications

The proposed rotor is a solid sphere made of a ferrous material and encompasses 12 N52 grade Neodymium PMs of 0.25-inch diameter and 0.50-inch length. The rotor includes features to accommodate decoupling inserts made of a non-magnetic material. The diameter of the sphere is 2.5 inches. This value was selected to prevent the holes that accommodate the decoupling inserts from interfering. The geometry of the rotor is discussed in detail in Section 5.3 and an image of the proposed rotor assembly is shown in Figure 41. The dimensions of the decoupling inserts are shown in Figure 58.

5.3 Reaction Sphere Geometry

This section discusses the rotor and stator geometries and derives the coordinates of the rotor PMs and levitation EMs in terms of position vectors. The kinematic relations between the levitation EM position vectors the rotor PM position vectors are then derived and expressed in terms of Euler Angles.

The Reaction Sphere (RS) geometry is treated in a manner similar to the original NGCRS, where the RS comprises two geometric regions: the inner sphere (rotor) and outer sphere (stator). An illustration of the RS configuration is shown in Figure 40 with the stator structural elements, stator drive coils, position sensors, and control circuitry omitted.

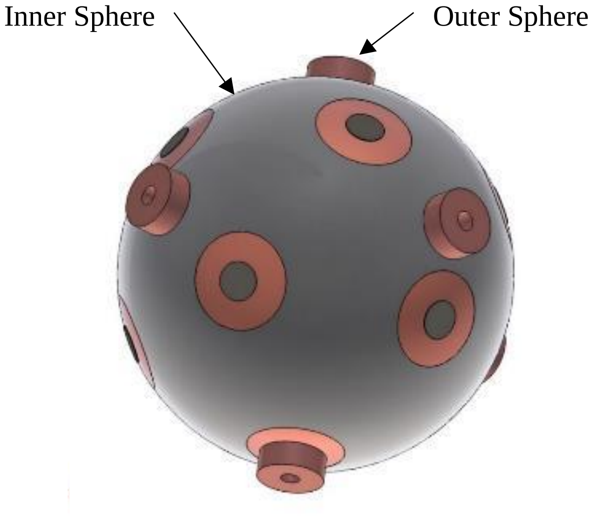

Figure 40: Reaction Sphere Geometry

5.3.1 Geometry of the Inner Sphere

The inner sphere, or rotor assembly, consists of a solid ferrous metal sphere, copper inserts to decouple the PM field from the iron sphere, and 12 permanent magnets (PM) as depicted in Figure 41.

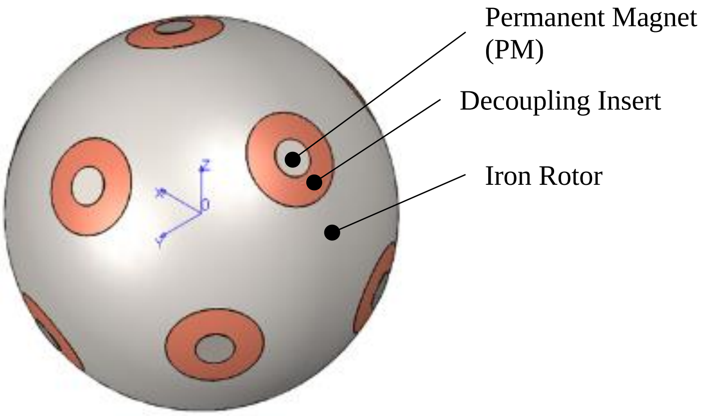

Figure 41: Reaction Sphere Rotor Assembly

The locations of the PMs are arranged along the vertex vectors of an icosahedron, which is a regular polyhedron comprised of 30 edges, 20 equilateral triangular faces, and 12 vertices.

The vertices are equi-spaced around the sphere and coincident with the surface of spherical rotor and the surface of each PM. From Leonard Euler's famed Polyhedral Formula, it can be shown that the arrangement of the PMs forms a convex, or regular, polyhedron where V is the number of vertices, F is the number of faces, and E represents the number of edges.

$$V + F - E = 2 \rightarrow 12 + 20 - 30 = 2 \tag{38}$$

Since the vertices are equally distributed around the rotors circumference, the magnets can be paired into six antipodal pairs of PMs with six (6) in the upper hemisphere of the sphere designated by subscripts: M_{Un} and the corresponding six (6) antipodal magnets in the lower hemisphere designated as M_{Ln}, where n represents magnets 1 through 6, where the upper and lower hemispheres are bisected by the XY plane. The spatial coordinates of each PM are described in terms of a position vector relative to a fixed coordinate frame located at the center of both the inner and outer spheres. The position vectors are derived by analyzing the geometry of an icosahedron circumscribed by a sphere of radius *r*, as shown in Figure 42.

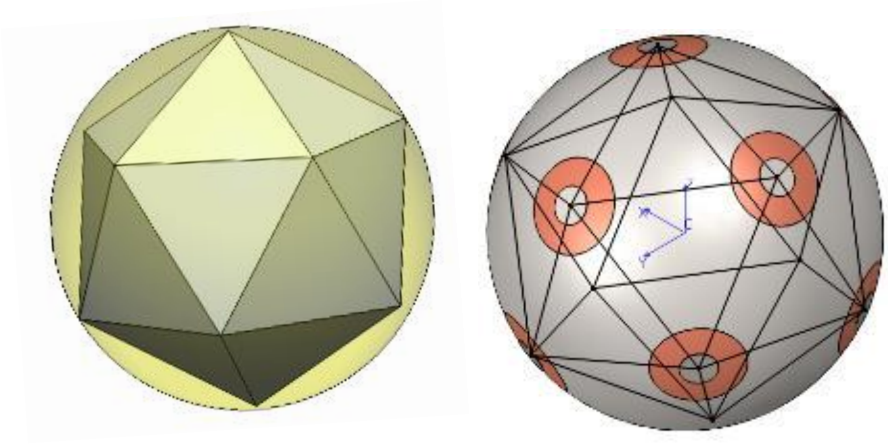

Figure 42: Inner Sphere Geometry with Inscribed Icosahedron

Considering the surface area of a sphere with a radius equal to unity:

$$A_s = 4\pi r^2 = 4\pi \tag{39}$$

Now dividing the surface area of the sphere by the number of faces gives the area of each triangular face in the elliptical plane.

$$A_f = \frac{A_s}{N_f} = \frac{4\pi}{20} = \frac{\pi}{5}\ steradians \tag{40}$$

The area of a polygon in the elliptical plane is equal to the spherical excess E_s of its angle sum over the angle sum of the polygon in the Euclidean plane (Coxeter, 1961). The spherical excess is computed using the Girard spherical excess formula, where A, B, and C are the angles of the spherical triangle in the elliptic plane and a, b, and c are the angles of the triangle in the Euclidean plane (Coxeter, 1961). The spherical excess is given by equation (41) and the geometry of a single face is illustrated in Figure 43.

$$E_s = A_f = (A + B + C) - (a + b + c) \tag{41}$$

The triangles are all equilateral and so $A = B = C$, and for an equilateral triangle in the Euclidean plane $a + b + c = \pi$.

Simplifying yields:

$$E_s = \frac{\pi}{5} = 3A - \pi \tag{42}$$

Solving for A gives the angle of each triangular face:

$$A = B = C = \frac{\pi}{15} + \frac{\pi}{3} = \frac{2\pi}{5} \tag{43}$$

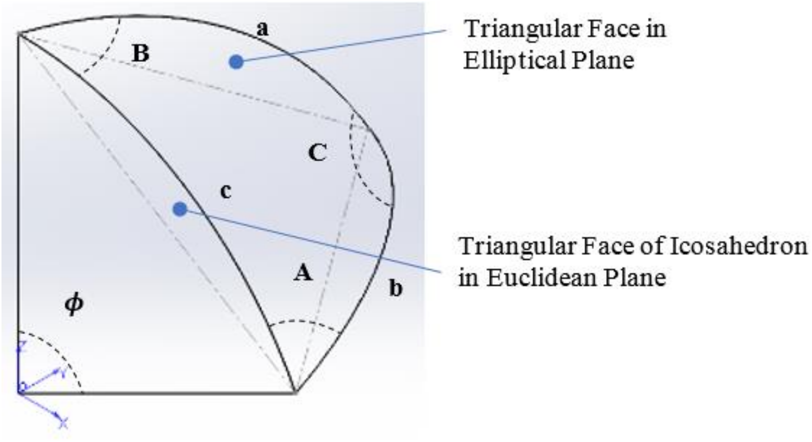

Figure 43: Geometry of an Equilateral Spherical Triangle

The angle subtended by each side is determined from the Second Spherical Law of Cosines. Recalling that the lower-case letters represent the angles between the edges of the triangle in the Euclidean plane and the upper case denotes the elliptic plane:

$$\cos(C) = -\cos(A)\cos(B) + \sin(A)\sin(B)\cos(c) \tag{44}$$

Rearranging equation (44) in terms of $cos(c)$:

$$\cos(c) = \frac{\cos(C) + \cos(A)\cos(B)}{\sin(A)\sin(B)} \tag{45}$$

And since:

$$\cos(A) = \cos(B) = \cos(C) = \cos\left(\frac{2\pi}{5}\right) = \frac{-1+\sqrt{5}}{4} \tag{46}$$

$$\sin(A) = \sin(B) = \sin(C) = \sin\left(\frac{2\pi}{5}\right) = \sqrt{\frac{5+\sqrt{5}}{8}} \tag{47}$$

Substituting equations (46) and (47) into the equation (45) yields:

$$cos(c) = cos\,(\phi) = \frac{\frac{-1+\sqrt{5}}{4} + \left(\frac{-1+\sqrt{5}}{4}\right)^2}{\left(\sqrt{\frac{5+\sqrt{5}}{8}}\right)^2} = \frac{1}{\sqrt{5}} \tag{48}$$

The arc length of the side of the spherical triangle is equal to the angle subtended by the edge of the Euclidean triangle:

$$cos(c) = cos\,(\phi) \tag{49}$$

Which leads to:

$$\phi = \cos^{-1}\left(\frac{1}{\sqrt{5}}\right) \approx 1.10714871779409050301706546 01\,radians \tag{50}$$

As shown in Figure 42, the icosahedron is oriented with two vertices coincident with the Z axis. The other five vertices in the upper hemisphere are each offset from the Z-axis by angle ϕ and are equally spaced around the circumference by the angle $\theta = 72\text{ degrees} = \frac{2\pi}{5}\text{ radians}$. Note that the golden ratio could also have been utilized to derive the coordinates of the position vectors. The position vectors of the PMs in the upper hemisphere can now be expressed in spherical coordinates as column vectors $[r \quad \theta \quad \phi]^T$. Henceforth, vectors are denoted with an arrow symbol $\vec{P}$ and unit vectors are denoted with the hat symbol $\hat{P}$.

$$\vec{P}_{Mu_1} = [r_s \quad 0 \quad 0]^T \tag{51}$$

$$\vec{P}_{Mu_2} = \left[r_s \quad 0 \quad \cos^{-1}\left(\frac{1}{\sqrt{5}}\right)\right]^T \tag{52}$$

$$\vec{P}_{Mu_3} = \left[r_s \quad \frac{2\pi}{5} \quad \cos^{-1}\left(\frac{1}{\sqrt{5}}\right)\right]^T \tag{53}$$

$$\vec{P}_{Mu_4} = \left[r_s \quad \frac{4\pi}{5} \quad \cos^{-1}\left(\frac{1}{\sqrt{5}}\right)\right]^T \tag{54}$$

$$\vec{P}_{Mu_5} = \left[r_s \quad \frac{6\pi}{5} \quad \cos^{-1}\left(\frac{1}{\sqrt{5}}\right)\right]^T \tag{55}$$

$$\vec{P}_{Mu_6} = \left[r_s \quad \frac{8\pi}{5} \quad \cos^{-1}\left(\frac{1}{\sqrt{5}}\right)\right]^T \tag{56}$$

The PM position vectors in the lower hemisphere are offset from the upper hemisphere position vectors by an angle π radians due to the antipodal arrangement (i.e. $\hat{P}_{ML_1}$ is antipodal to $\hat{P}_{Mu_1}$).

$$\vec{P}_{ML_1} = [r_s \quad 0 \quad \pi]^T \tag{57}$$

$$\vec{P}_{ML_2} = \left[r_s \quad \pi \quad \pi - \cos^{-1}\left(\frac{1}{\sqrt{5}}\right)\right]^T \tag{58}$$

$$\vec{P}_{ML_3} = \begin{bmatrix} r_s & \frac{7\pi}{5} & \pi - \cos^{-1}\left(\frac{1}{\sqrt{5}}\right) \end{bmatrix}^T \tag{59}$$

$$\vec{P}_{ML_4} = \begin{bmatrix} r_s & \frac{9\pi}{5} & \pi - \cos^{-1}\left(\frac{1}{\sqrt{5}}\right) \end{bmatrix}^T \tag{60}$$

$$\vec{P}_{ML_5} = \begin{bmatrix} r_s & \frac{11\pi}{5} & \pi - \cos^{-1}\left(\frac{1}{\sqrt{5}}\right) \end{bmatrix}^T \tag{61}$$

$$\vec{P}_{ML_6} = \begin{bmatrix} r_s & \frac{13\pi}{5} & \pi - \cos^{-1}\left(\frac{1}{\sqrt{5}}\right) \end{bmatrix}^T \tag{62}$$

The PM position vectors are now converted to from spherical coordinates into cartesian coordinates to facilitate kinematic analysis and to take advantage of vector operations such as addition, the scalar product, and the cross product. The converted coordinates are shown below using the well-known conversion factors: $x = r\sin(\phi)\cos(\theta)$, $y = r\sin(\phi)\sin(\theta)$, and $z = r\cos(\phi)$.

$$\vec{P}_{Muc_1} = r_s[0 \quad 0 \quad 1]^T \tag{63}$$

$$\vec{P}_{Muc_2} = r_s\begin{bmatrix} \frac{2}{\sqrt{5}} & 0 & \frac{1}{\sqrt{5}} \end{bmatrix}^T \tag{64}$$

$$\vec{P}_{Muc_3} = r_s\begin{bmatrix} \frac{5-\sqrt{5}}{10} & \sqrt{\frac{5+\sqrt{5}}{10}} & \frac{1}{\sqrt{5}} \end{bmatrix}^T \tag{65}$$

$$\vec{P}_{Muc_4} = r_s\begin{bmatrix} \frac{-5-\sqrt{5}}{10} & \sqrt{\frac{5-\sqrt{5}}{10}} & \frac{1}{\sqrt{5}} \end{bmatrix}^T \tag{66}$$

$$\vec{P}_{Muc_5} = r_s\begin{bmatrix} \frac{-5-\sqrt{5}}{10} & -\sqrt{\frac{5-\sqrt{5}}{10}} & \frac{1}{\sqrt{5}} \end{bmatrix}^T \tag{67}$$

$$\vec{P}_{Muc_6} = r_s\left[\frac{5-\sqrt{5}}{10} \quad -\sqrt{\frac{5+\sqrt{5}}{10}} \quad \frac{1}{\sqrt{5}}\right]^T \tag{68}$$

Again, due to the anti-podal arrangement, the position vectors of the lower hemisphere PMs are simply the negative of the upper hemisphere coordinates:

$$\vec{P}_{MLc_1} = r_s[0 \quad 0 \quad -1]^T \tag{69}$$

$$\vec{P}_{MLc_2} = r_s\left[-\frac{2}{\sqrt{5}} \quad 0 \quad -\frac{1}{\sqrt{5}}\right]^T \tag{70}$$

$$\vec{P}_{MLc_3} = r_s\left[\frac{-5+\sqrt{5}}{10} \quad -\sqrt{\frac{5+\sqrt{5}}{10}} \quad -\frac{1}{\sqrt{5}}\right]^T \tag{71}$$

$$\vec{P}_{MLc_4} = r_s\left[\frac{5+\sqrt{5}}{10} \quad -\sqrt{\frac{5-\sqrt{5}}{10}} \quad -\frac{1}{\sqrt{5}}\right]^T \tag{72}$$

$$\vec{P}_{MLc_5} = r_s\left[\frac{5+\sqrt{5}}{10} \quad \sqrt{\frac{5-\sqrt{5}}{10}} \quad -\frac{1}{\sqrt{5}}\right]^T \tag{73}$$

$$\vec{P}_{MLc_6} = r_s\left[\frac{-5+\sqrt{5}}{10} \quad \sqrt{\frac{5+\sqrt{5}}{10}} \quad -\frac{1}{\sqrt{5}}\right]^T \tag{74}$$

All twelve position vectors can be expressed in a single matrix, where the rows equal the x, y, z components of each vector, in descending order, and columns one through six represent the PMs in upper hemisphere and columns seven through twelve represent the PMs in the lower hemisphere. The vectors are given as unit vectors and can be scaled to coincide with the surface of a sphere of an arbitrary radius r_s.

$$\vec{P}_M = r_s \begin{bmatrix} 0 & \frac{2}{\sqrt{5}} & \frac{5-\sqrt{5}}{10} & \frac{-5-\sqrt{5}}{10} & \frac{-5-\sqrt{5}}{10} & \frac{5-\sqrt{5}}{10} & 0 & -\frac{2}{\sqrt{5}} & \frac{-5+\sqrt{5}}{10} & \frac{5+\sqrt{5}}{10} & \frac{5+\sqrt{5}}{10} & \frac{-5+\sqrt{5}}{10} \\ 0 & 0 & \sqrt{\frac{5+\sqrt{5}}{10}} & \sqrt{\frac{5-\sqrt{5}}{10}} & -\sqrt{\frac{5-\sqrt{5}}{10}} & -\sqrt{\frac{5+\sqrt{5}}{10}} & 0 & 0 & -\sqrt{\frac{5+\sqrt{5}}{10}} & -\sqrt{\frac{5-\sqrt{5}}{10}} & \sqrt{\frac{5-\sqrt{5}}{10}} & \sqrt{\frac{5+\sqrt{5}}{10}} \\ 1 & \frac{1}{\sqrt{5}} & \frac{1}{\sqrt{5}} & \frac{1}{\sqrt{5}} & \frac{1}{\sqrt{5}} & \frac{1}{\sqrt{5}} & -1 & -\frac{1}{\sqrt{5}} & -\frac{1}{\sqrt{5}} & -\frac{1}{\sqrt{5}} & -\frac{1}{\sqrt{5}} & -\frac{1}{\sqrt{5}} \end{bmatrix}$$

5.3.2 Outer Sphere Geometry

Six (6) air-core electromagnets (EM) are utilized to provide the forces necessary reject external disturbances acting on the sphere and thus stabilize the rotor position with the stator housing during satellite positioning. The EMs are positioned to form two equilateral, triangular tetrahedrons arranged such that the three (3) EMs in the upper hemisphere are antipodal to the three (3) EMs in the lower hemisphere. The upper and lower hemispheres are separated by the XY plane. The EMs are also geometrically constrained due to the position sensors and drive EMs, and consequently, are offset from the Z-axis by an angle $\varphi = \cos^{-1}\left(\frac{1}{\sqrt{3}}\right)$ radians. The EMs are equally spaced by an angle $\theta = \frac{2\pi}{3}$ radians round the sphere with one EM in the upper and lower hemispheres coincident on the ZY plane. This geometry forms two triangular tetrahedrons with the apexes located at the origin of the fixed global coordinate system as shown in Figure 44.

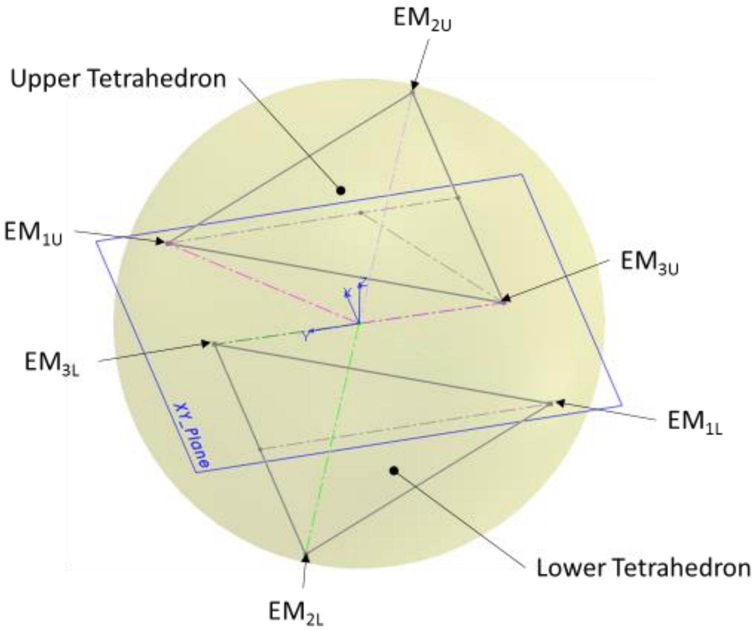

Figure 44: Geometry of the Outer Sphere

The position vectors of the EMs are given in spherical coordinates below:

$$\vec{P}_{EMu_1} = \begin{bmatrix} r_{EM} & \frac{\pi}{2} & \cos^{-1}\left(\frac{1}{\sqrt{3}}\right) \end{bmatrix}^T \tag{75}$$

$$\vec{P}_{EMu_2} = \begin{bmatrix} r_{EM} & \frac{7\pi}{6} & \cos^{-1}\left(\frac{1}{\sqrt{3}}\right) \end{bmatrix}^T \tag{76}$$

$$\vec{P}_{EMu_3} = \begin{bmatrix} r_{EM} & \frac{11\pi}{6} & \cos^{-1}\left(\frac{1}{\sqrt{3}}\right) \end{bmatrix}^T \tag{77}$$

$$\vec{P}_{EML_1} = \begin{bmatrix} r_{EM} & \frac{3\pi}{2} & \pi - \cos^{-1}\left(\frac{1}{\sqrt{3}}\right) \end{bmatrix}^T \tag{78}$$

$$\vec{P}_{EML_2} = \begin{bmatrix} r_{EM} & \frac{\pi}{6} & \pi - \cos^{-1}\left(\frac{1}{\sqrt{3}}\right) \end{bmatrix}^T \tag{79}$$

$$\vec{P}_{EML_3} = \begin{bmatrix} r_{EM} & \frac{5\pi}{6} & \pi - \cos^{-1}\left(\frac{1}{\sqrt{3}}\right) \end{bmatrix}^T \tag{80}$$

The EM position vectors converted to cartesian coordinates and are given below:

$$\vec{P}_{EMu_1} = r_{EM} \begin{bmatrix} 0 & \frac{\sqrt{2}}{\sqrt{3}} & \frac{1}{\sqrt{3}} \end{bmatrix}^T \tag{81}$$

$$\vec{P}_{EMuc_2} = r_{EM} \begin{bmatrix} -\frac{\sqrt{2}}{2} & -\frac{\sqrt{2}}{2\sqrt{3}} & \frac{1}{\sqrt{3}} \end{bmatrix}^T \tag{82}$$

$$\vec{P}_{EMuc_3} = r_{EM} \begin{bmatrix} \frac{\sqrt{2}}{2} & -\frac{\sqrt{2}}{2\sqrt{3}} & \frac{1}{\sqrt{3}} \end{bmatrix}^T \tag{83}$$

$$\vec{P}_{EMLc_1} = r_{EM} \begin{bmatrix} 0 & -\frac{\sqrt{2}}{\sqrt{3}} & -\frac{1}{\sqrt{3}} \end{bmatrix}^T \tag{84}$$

$$\vec{P}_{EMLc_2} = r_{EM}\begin{bmatrix}\frac{\sqrt{2}}{2} & \frac{\sqrt{2}}{2\sqrt{3}} & -\frac{1}{\sqrt{3}}\end{bmatrix}^T \tag{85}$$

$$\vec{P}_{EMLc_3} = r_{EM}\begin{bmatrix}-\frac{\sqrt{2}}{2} & \frac{\sqrt{2}}{2\sqrt{3}} & -\frac{1}{\sqrt{3}}\end{bmatrix}^T \tag{86}$$

The position vectors can be expressed as a single matrix where the rows represent the $x, y, and\ z$ components of each EM position vector, in descending order. The matrix is arranged such that columns one, two, and three represent the upper hemisphere EM position vectors and columns four, five, and six represent the lower hemisphere position vectors with the column one in the left most column of the matrix order. The vectors are given as unit vectors and can be scaled to coincide with the surface of an outer sphere of an arbitrary radius r_{EM}.

$$\vec{P}_{EM} = r_{EM}\begin{bmatrix}0 & -\frac{\sqrt{2}}{2} & \frac{\sqrt{2}}{2} & 0 & \frac{\sqrt{2}}{2} & -\frac{\sqrt{2}}{2} \\ \frac{\sqrt{2}}{\sqrt{3}} & -\frac{\sqrt{2}}{2\sqrt{3}} & -\frac{\sqrt{2}}{2\sqrt{3}} & -\frac{\sqrt{2}}{\sqrt{3}} & \frac{\sqrt{2}}{2\sqrt{3}} & \frac{\sqrt{2}}{2\sqrt{3}} \\ \frac{1}{\sqrt{3}} & \frac{1}{\sqrt{3}} & \frac{1}{\sqrt{3}} & -\frac{1}{\sqrt{3}} & -\frac{1}{\sqrt{3}} & -\frac{1}{\sqrt{3}}\end{bmatrix} \tag{87}$$

The coordinates of the eight drive EMs, $\vec{P}_{DM}$, are provided below as column vectors for reference, but are not included in the dynamic model simulation. These position vectors were derived by Stagmer in the NGCRS patent (U.S. Patent No. 9,475,592 B2).

$$\vec{P}_{DM} = r_{DM}\begin{bmatrix}0 & 0 & -\frac{\sqrt{2}}{\sqrt{3}} & \frac{\sqrt{2}}{\sqrt{3}} & 0 & 0 & \frac{\sqrt{2}}{\sqrt{3}} & -\frac{\sqrt{2}}{\sqrt{3}} \\ 0 & \frac{2\sqrt{2}}{3} & -\frac{\sqrt{2}}{3} & -\frac{\sqrt{2}}{3} & 0 & -\frac{2\sqrt{2}}{3} & \frac{\sqrt{2}}{3} & \frac{\sqrt{2}}{3} \\ 1 & \frac{1}{3} & -\frac{1}{3} & -\frac{1}{3} & -1 & \frac{1}{3} & \frac{1}{3} & \frac{1}{3}\end{bmatrix} \tag{88}$$

5.4 Kinematics of Reaction Sphere

The RS dynamic model described herein is a 3-DOF with the spherical rotor free to rotate about the $X, Y,$ and Z axes, but it is fixed translationally in the axial directions. Thus, the orientation, or attitude, of each PM attached to the spherical rotor can be described by as a position vector in terms of the basis vectors located at the origin of the fixed outer sphere (Stator) coordinate system.

5.4.1 Euler Angles and Rotation Matrices

The Euler Angle rotations are applied to the rotor PMs following the *Z-Y-X* attitude sequence which is commonplace in aerospace applications. All rotations follow the right-hand rule, where the thumb points in the directions of the positive axis and the fingers curl around the axis in the positive angular direction (Greenwood, 2003). The rotation sequence is depicted in Figure 45.

1. Rotation angle ψ about the original (principal) Z-Axis (Yaw Rotation)
2. Rotation angle θ about the intermediate Y-Axis (Pitch Rotation)
3. Rotation angle ϕ about the intermediate X-Axis (Roll Rotation)

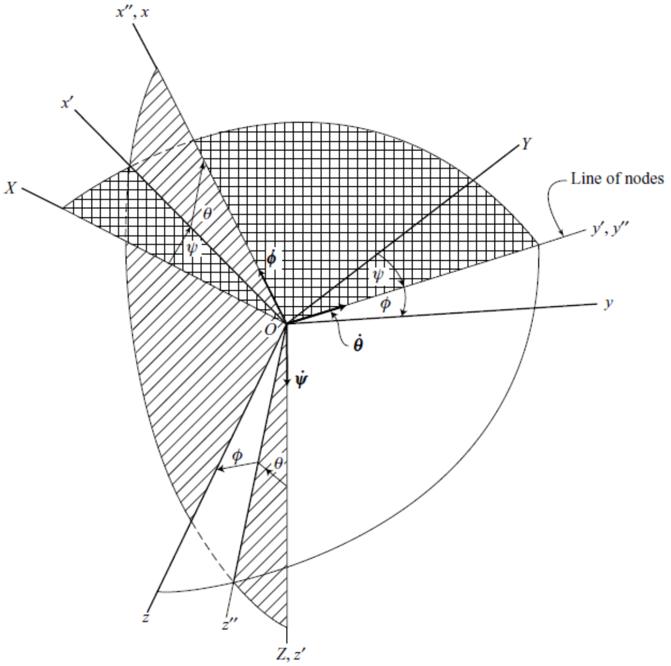

Figure 45: Euler Angle Rotation Sequence (Greenwood, 2003)

The reference frame and associated basis vectors of the stator F_S is denoted by Z, Y, X in Figure 45. The successive body rotations of the rotor are expressed symbolically by following the convention above, and considering the basis vectors where Z, Y, X represents the initial un-rotated reference frame F_1 of the rotor, and z', y', z' and z'', y'', z'' represent intermediate rotations of the rotor, and x, y, z represents the final rotated position of the rotor denoted below by F_2.

$$F'_1 = [R_\psi]\, F_1 \tag{89}$$

$$F''_1 = [R_\theta]\, F'_1 \tag{90}$$

$$F_2 = [R_\phi] F''_1 \tag{91}$$

$$[R_\psi]\begin{bmatrix} X_1 \\ Y_1 \\ Z_1 \end{bmatrix} = \begin{bmatrix} \cos\psi & \sin\psi & 0 \\ -\sin\psi & \cos\psi & 0 \\ 0 & 0 & 1 \end{bmatrix} \begin{bmatrix} X_1 \\ Y_1 \\ Z_1 \end{bmatrix} = \begin{bmatrix} x'_1 \\ y'_1 \\ z'_1 \end{bmatrix} \tag{92}$$

$$[R_\theta]\begin{bmatrix} x'_1 \\ y'_1 \\ z'_1 \end{bmatrix} = \begin{bmatrix} \cos\theta & 0 & -\sin\theta \\ 0 & 1 & 0 \\ \sin\theta & 0 & \cos\theta \end{bmatrix} \begin{bmatrix} x'_1 \\ y'_1 \\ z'_1 \end{bmatrix} = \begin{bmatrix} x''_1 \\ y''_1 \\ z''_1 \end{bmatrix} \tag{93}$$

$$[R_\phi]\begin{bmatrix} x''_1 \\ y''_1 \\ z''_1 \end{bmatrix} = \begin{bmatrix} 1 & 0 & 0 \\ 0 & \cos\phi & \sin\phi \\ 0 & -\sin\phi & \cos\phi \end{bmatrix} \begin{bmatrix} x''_1 \\ y''_1 \\ z''_1 \end{bmatrix} = \begin{bmatrix} x_2 \\ y_2 \\ z_2 \end{bmatrix} \tag{94}$$

Pre-multiplying the column position vectors by the three Euler Angle rotation matrices, following the order in which the rotations were applied, will produce a matrix for the complete rotation of reference frame F_1 to reference frame F_2 with respect to the fixed stator reference frame. The final rotation matrix is shown below. The multiplication and simplification steps are not shown.

$$[R_M] = [R_\phi][R_\theta][R_\psi] \tag{95}$$

$$[R_M] = \begin{bmatrix} \cos\psi\cos\theta & \sin\psi\cos\theta & -\sin\theta \\ -\sin\psi\cos\phi + \cos\psi\sin\theta\sin\phi & \cos\psi\cos\phi + \sin\psi\sin\theta\sin\phi & \cos\theta\sin\phi \\ \sin\psi\sin\phi + \cos\psi\sin\theta\cos\phi & -\cos\psi\sin\phi + \sin\psi\sin\theta\cos\phi & \cos\theta\cos\phi \end{bmatrix}$$

Pre-multiplying the column PM position vectors by the transpose of the Euler rotation matrix R_M will yield the rotated position vector in terms of the basis vectors at the stator coordinate system. The rotation matrix is transposed to output the coordinates of the PM position vectors as a column vector.

$$\vec{P}_{Rot} = [R_M]^T \vec{P}_M \tag{96}$$

5.4.2 Euler Angle Rates

The absolute angular velocity of rotor, in terms of the x, y, z body-axis frame is given by noting that the vectors $\dot{\psi}$ and $\dot{\phi}$ are not orthogonal (Greenwood, 2003).

$$\omega = \dot{\psi} + \dot{\theta} + \dot{\phi} \tag{97}$$

The velocity can also be expressed in terms of the body-axis components and is given below, where $\omega_x, \omega_y, \omega_z$ represent the respective roll, pitch, and yaw rates (Greenwood, 2003).

$$\omega = \omega_x \hat{\imath} + \omega_y \hat{\jmath} + \omega_z \hat{k} \tag{98}$$

The body-axis components of the angular velocity in terms of the absolute Euler Angle rates are given below (Greenwood, 2003).

$$\omega_x = \dot{\phi} - \mathit{sin}\,\theta \tag{99}$$

$$\omega_y = \dot{\psi}\,\mathit{cos}\,\theta\,\mathit{sin}\,\phi + \dot{\theta}\,\mathit{cos}\,\phi \tag{100}$$

$$\omega_z = \dot{\psi}\,\mathit{cos}\,\theta\,\cos\phi - \dot{\theta}\,\mathit{sin}\,\phi \tag{101}$$

$$\omega = \left(\dot{\phi} - \mathit{sin}\,\theta\right)\hat{\boldsymbol{\imath}} + \left(\dot{\psi}\,\mathit{cos}\,\theta\,\mathit{sin}\,\phi + \dot{\theta}\,\mathit{cos}\,\phi\right)\hat{\boldsymbol{\jmath}} + \left(\dot{\psi}\,\mathit{cos}\,\theta\,\cos\phi - \dot{\theta}\,\mathit{sin}\,\phi\right)\hat{\boldsymbol{k}} \tag{102}$$

And the absolute Euler Angle rates expressed in terms of the body-axis components of the angular velocity are given below (Greenwood, 2003).

$$\dot{\psi} = \sec\theta\left(\omega_y\,\mathit{sin}\,\phi + \omega_z \cos\phi\right) \tag{103}$$

$$\dot{\theta} = \omega_y \cos\phi - \omega_z\,\mathit{sin}\,\phi \tag{104}$$

$$\dot{\phi} = \omega_x + \dot{\psi}\sin\theta = \omega_x + \omega_y\, tan\theta sin\,\phi + \omega_z tan\theta\cos\phi \tag{105}$$

5.5 Finite Element Magnetic Modeling

One of the objectives of the FEM modeling effort is determine if a generalized FEM model of the NGCRS could be developed to model the forces and torques acting on the rotor assembly with reasonable accuracy when compared to a fully integrated model with all twelve PMs and all six levitation EMs. The advantage of using a generalized model is that a single set of relations can be derived for the forces and torques acting on the rotor iron and rotor PM. The generalized relation can then be used to determine the forces and torques acting on the rotor / stator for any EM-PM pair and for any arbitrary orientation. Additionally, changes to the design can be rapidly developed and simulated. The generalized model of the NGCRS is shown in Figure 46. The feasibility of a generalized model was investigated by the following modeling approach:

1. Evaluate the need to include non-linearities in the model
2. Apply the principle of superposition to evaluate the extent of magnetic field coupling between the EM and PM through the rotor iron
3. Demonstrate that the generalized model of a single EM-PM pair accurately models the magnetic forces and torques relative to a complete model with all 12 rotor PMs
4. Verify the coordinate transformations applied to the forces, predicted by the generalized model, are correct for any arbitrary orientation of the rotor and stator

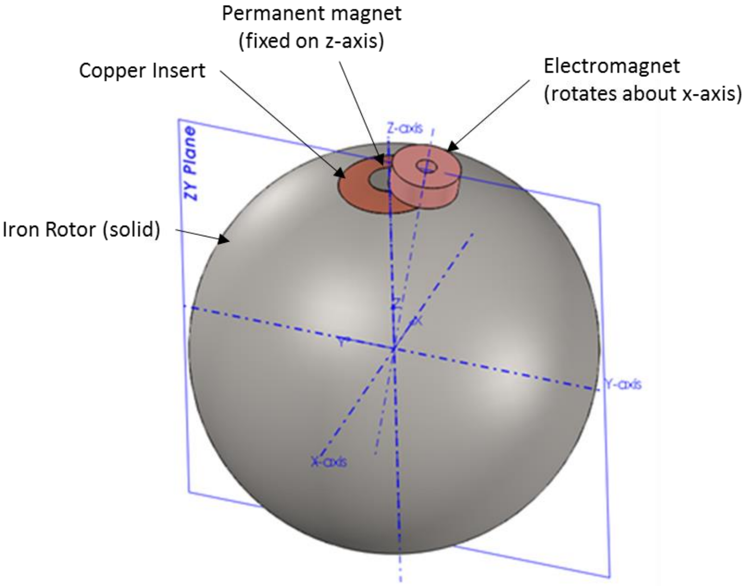

Figure 46: Generalized model of the NGCRS

The influence of material non-linearities was evaluated by developing models that used linear and non-linear constitutive relations for the magnetic fields. The results of this study are detailed in Section 5.5.8. The extent of the magnetic field coupling was evaluated by developing superposition models of the generalized NGCRS as well as an integrated model, which contained the rotor iron, EM, PM, and decoupling insert as shown in Figure 46. The superposition modeling approach is detailed in Section 5.5.1. The setup of the FEM model is discussed in Sections 5.5.2 and the modeling approach for the reaction sphere components are described in Sections 5.5.3, 5.5.4, 5.5.5, and 5.5.6. Each section includes discussion of the applicable constitutive relations. The FEM model mesh and the results of a convergence study are presented in Section 5.5.11.

Finite Element Magnetic (FEM) modeling of the reaction sphere was performed using COMSOL version 5.6. A three-dimensional FEM model was required due to the asymmetry of the reaction sphere geometry. The magnetic forces obtained from the superposition models were used to derive the generalized force and torque relations which were programmed into the Simulink® dynamic model. Implementation of the force and torque relations in Simulink® dynamic model are discussed in Section 5.6. Simulations were performed with coil excitation levels of 0.2, 0.3, 0.4 amperes and from 0.5 to 5.0 amperes in

0.5 ampere increments and angular distances between the EM and PM centerlines ranging from 0 to 31.7175 in 1-degree increments, with the exception of the final increment. Note that the angular distance of 31.7175 degrees represents half the distance between adjacent PMs in the rotor assembly. All combinations of coil excitation levels and angular distances were simulated. The radial airgap between the rotor and the EMs was fixed to 30 mils (7.62×10^{-4} meter) for all simulations.

5.5.1 Principle of Superposition

The scope of this thesis project did not include development of a physical prototype to verify the forces and torques predicted by the FEM model. Consequently, a conservative FEM modeling approach was implemented that relied on the principle of superposition to increase confidence in the predicted forces and torques.

In order to apply the principle of superposition, non-linearities must be removed from the system. In this system, the PM will tend to drive the rotor iron into the non-linear region of the magnetization curve when it is in close proximity to the rotor iron. Decoupling was achieved by introducing a high reluctance path between the PM and the iron sphere. The gap between the PM and the sphere was filled by an insert made of copper, which has a permeability close to that of a vacuum ($\mu_r \approx 1$), but in practice, the insert could be made of any non-magnetic material. Simulations were performed with decoupling inserts with varying thicknesses until sufficient decoupling could be achieved. The results of this study are detailed in section 5.5.7.

The superposition model consists of two separate FEM models. The magnetic forces predicted by each model are then summed together to obtain the overall force acting on the stator EM. The two superposition models of the generalized NGCRS model are described below and illustrated in Figure 47. Note that the model of the iron rotor includes the recess to house the copper insert.

1. A model of a single EM and a single PM with the iron rotor omitted
2. A model of a single EM and the iron rotor with the PM omitted

The forces predicted by the superposition models are summed to obtain the total force.

$$\vec{F}_{total} = \vec{F}_{PM} + \vec{F}_{Iron} \tag{106}$$

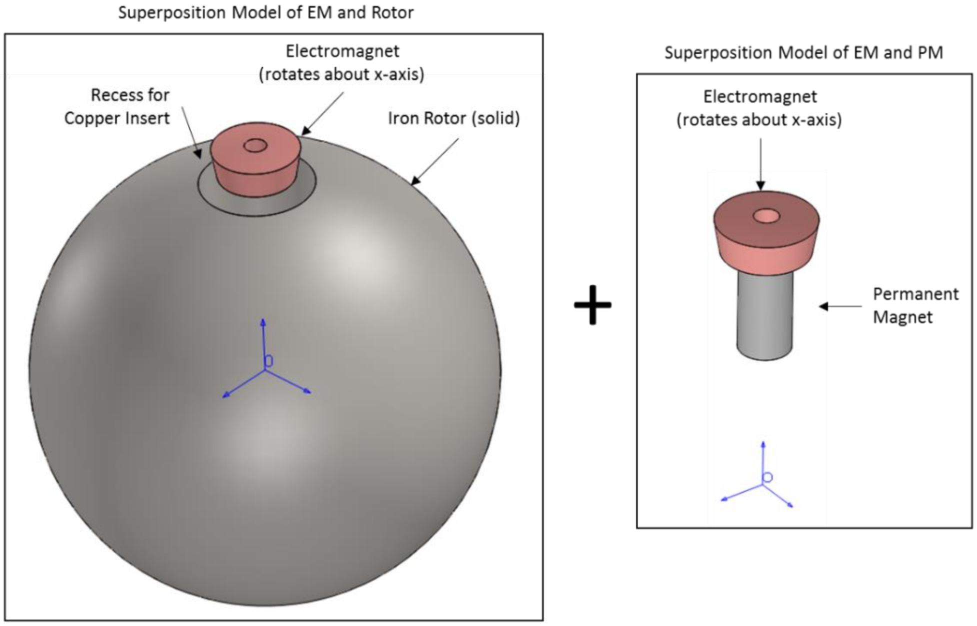

Figure 47: Superposition FEM Models of Generalized RS

5.5.2 Problem Setup and Pre-Processing

The reaction sphere was simulated using the COMSOL® Multiphysics AC/DC Module version 5.6, and was defined as a three-dimensional problem due to the asymmetric geometry. The magnetic fields interface was used to define the problem, which is the recommended interface for solving physics problems with magnetic fields, induced current distributions in and around coils, conductors and magnets (COMSOL, 2019). The reaction sphere components and component boundaries are stationary, and as such, the problem was implemented as a magnetostatic problem which uses the stationary solver. The COMSOL® interface solves the Maxwell's equations for the defined boundary condition and the selected constitutive relations (COMSOL, 2019).

Ampère's Law nodes were added for each material domain in the simulation. The Ampère's Law node adds the equation for the magnetic vector potential and provides an interface to define the constitutive relations associated with the magnetic and electric properties (COMSOL, 2019). Magnetostatics problems are solved by COMSOL® using a magnetostatic equation derived from the Ampère's Law, where J is the total volume current density, H is the magnetic field intensity, and μ_0 is the magnetic permeability of a vacuum.

$$\nabla \times H = J \tag{107}$$

The total volume current density J is defined by equation (113)(113), where, v is the velocity in the conductor, σ is the electrical conductivity, B is the magnetic flux density, $V$is the electric scalar potential, and J_e is an externally generated current density (COMSOL, 2019).

$$J = \sigma v \times B - \sigma \nabla V + J_e \tag{108}$$

Using the definitions for magnetic vector potential A given by equation (109) and the constitutive relation for the magnetic field given by equation (110), and substituting into equation (107), the magnetostatics equation is obtained in the form of equation (111) (COMSOL, 2019).

$$B = \nabla \times \mathrm{A} \tag{109}$$

$$B = \mu_0 (H + M) \tag{110}$$

$$\nabla \times (\mu_0^{-1} \nabla \times \mathrm{A} - \mathrm{M}) - \sigma v \times (\nabla \times \mathrm{A}) = J_e \tag{111}$$

The constitutive relations used within the FEM models of the reaction sphere are described in the subsequent sections.

5.5.3 Electromagnet Modeling

The electromagnet was modeled as a homogenous multi-turn, circular coil with 360 turns of 32 AWG copper magnet wire. An image of the EM geometry is shown in Figure 48 with applicable dimensions. The surface of the EM nearest the rotor is curved to maintain a constant radial airgap of 0.030 inches (7.62×10^{-4} m). The coil model uses current excitation with currents ranging from 0.2, 0.3, 0.4, and from 0.5 to 5.0 amperes in 0.5 ampere increments. The default values for length and area were overridden, because the edges selected to represent coil axis is taken to be the average coil length in the domain (COMSOL®, 2019). The average coil circumference was approximated from the coil geometry, and is given below.

$$L_{edges} = 2\pi r_m = 0.0228 \text{ m} \tag{112}$$

The coil cross-sectional area of coil was measured from the Solidworks® CAD model geometry. The computed value is provided below:

$$A_{domain} = 1.824 \times 10^{-5}\, m^2 \tag{113}$$

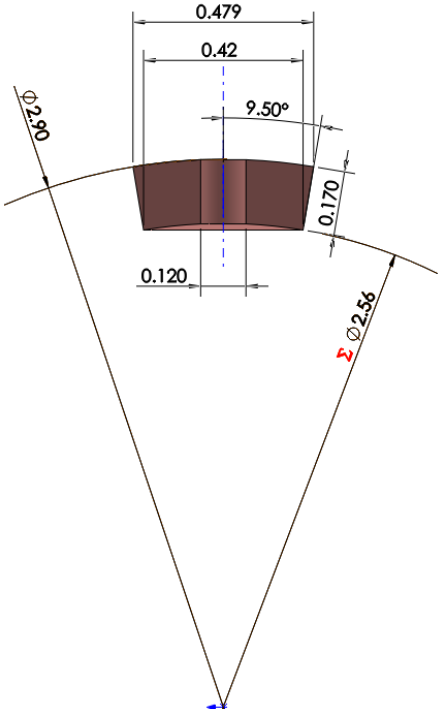

Figure 48: Electromagnet Geometry (Dimensions in Inches)

The relative permeability constitutive relation was used to model the magnetic field of the coil because copper has a relative permeability $\mu_r \approx 1$. The relation is given below, where B is the magnetic flux density, H is the magnetic field intensity, μ_r is the relative permeability given by the COMSOL® material library for copper material, and μ_0 is the permeability of vacuum ($4\pi \cdot 10^{-7} N \cdot A^{-2}$) (COMSOL®, 2019).

$$B = \mu_0 \mu_r H \tag{114}$$

COMSOL® calculates the current density of the coil J_e using the following equation, where N is the number of turns in the coil, I_{coil}, is the coil current, A is the sectional area of the coil, and e_{coil} is a vector field representing the local direction of the current flow in the wires (COMSOL®, 2019).

$$J_e = \frac{NI_{coil}}{A} e_{coil} \tag{115}$$

The model of the EM was the same for both the linear and non-linear FEM models.

5.5.4 Permanent Magnet Modeling

COMSOL Multiphysics® provides the several constitutive relations for modeling the behavior of permanent magnets. These relations include magnetization, remnant flux density, BH non-linear permanent magnet, and the Jiles-Atherton hysteresis model. The Jiles-Atherton hysteresis model is used to model circuits where permanent magnets are subjected to alternating magnetic fields, which is not the case for this reaction sphere model because it has magnetic fields of constant polarity. The BH non-linear permanent magnet relation is essentially a mix of the magnetization and material BH curve relations (COMSOL, 2019). This constitutive relation was used in reaction sphere simulations for two purposes. The first was to evaluate the need to include PM non-linearities and the second was to evaluate the effect of introducing a decoupling insert into the reaction sphere. The magnetization relation was not used in the FEM model because remnant flux density relation is a generalized form of the magnetization relation and is better suited to modeling magnets in the second quadrant of the magnetization curve (Tozzo, 2018). The remnant flux density relation is often used in place of the magnetization relation because the recoil permeabilities, remnant flux density, and coercivity are more readily available from manufacturers than magnetization data (Tozzo, 2018). The constitutive relation for remnant flux density is given by equation (116).

$$B = \mu_0 \mu_r H + B_r \tag{116}$$

The remnant flux density was specified as 1.45T and the relative permeability was specified as 1.05 for all simulations. This information was extracted from the Arnold Magnetic Technologies® data sheet for an N52 sintered neodymium iron boron (NdFeB) magnet data sheet. The remnant flux density relation is used in the generalized reaction sphere model, and is justified by examination of the open circuit operating point of the PM, and by the results of a COMSOL® simulations.

The remnant flux density B_r is the residual permanent magnetism in the material when the externally applied magnetizing field is reduced to zero after saturating the material (MMPA, 1998) and is the consequence of hysteresis (or memory) of the PM material. If the magnet is placed in a circuit with an airgap or a demagnetizing field is applied, then the PM will operate somewhere in the second quadrant of the demagnetization curve (Meeker, 2007). A special case is when a PM is in an open circuit condition, where it is surrounded by air with no external magnetic field present. In this scenario the PM forms free poles and a self-demagnetizing field potential H_d forms (MMPA, 1998). This self-demagnetization field can be expressed as a demagnetizing flux density B_d and is related to related to B_r by the PM geometry by a demagnetization factor N. Meeker proposed N based on a numeric computation of the ratio of PM energy to PM coenergy. Meeker's method determines a value of N over the entire volume of the PM and is similar to the magnetometric factor, and Meeker defined N in terms of a reluctance coefficient c which is a function of the PM geometry (Meeker, 2007). Meeker also proposed energy methods (e.g. Magnetic field energy and co-energy) to calculate the open circuit operating point of a PM using his previously derived magnetization factor N (Meeker, 2007). Following the method developed by Meeker, the operating point of the N52 PM was calculated and then plotted against the demagnetization curve from the Arnold Magnetics N52 data sheet, as shown in Figure 49. The operating point of the magnet was calculated to be approximately 1.34 $Tesla$, which agrees with the COMSOL output for the same N52 magnet, which is plotted in Figure 52 and Figure 53. Note: this is the BH curve using in COMSOL to model the N52 PM.

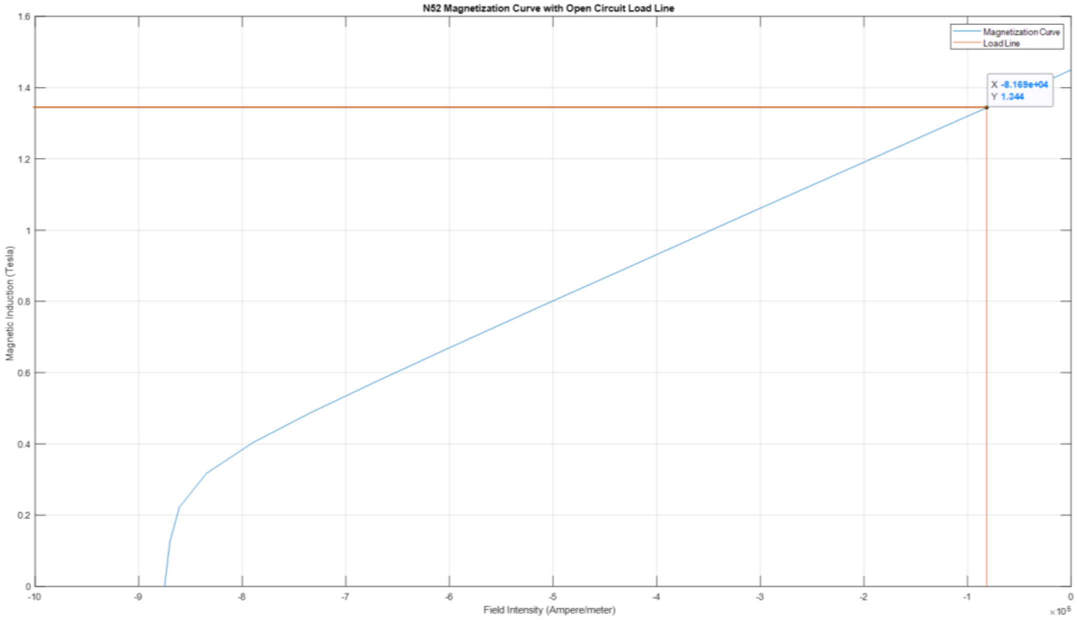

Figure 49: Open Circuit Operating Point of N52 Permanent Magnet

The remnant flux density relation was selected to model the PM because the PM operates in only the 2nd quadrant of the demagnetization curve, which is substantiated by the simulations results. Figure 53 depicts the normalized magnetic flux density on the outside of the PM, adjacent to an EM excited by 5 amperes, and Figure 52 shows a line plot of the normalized magnetic flux density over the length of the PM and along the centerline. The maximum and minimum flux densities are 1.35 Tesla and 0.71 Tesla respectively, both of which are located on the linear region of the N52 demagnetization curve, which is presented in Figure 53. Also observe that the EM is polarized so that its magnetic field does not tend to demagnetize the PM.

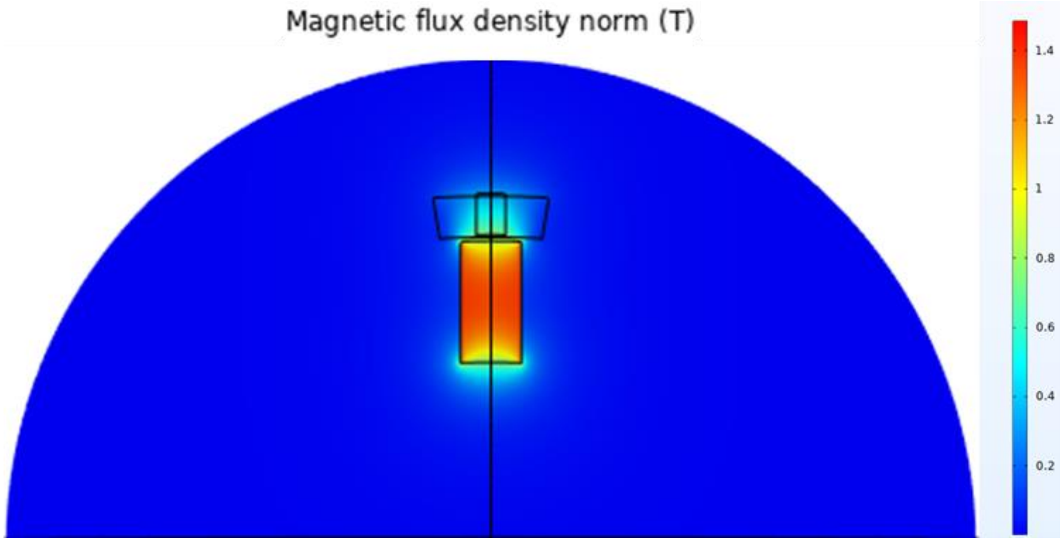

Figure 50: Magnetic Flux Density Norm for N52 PM, EM current at 5.0 Amp

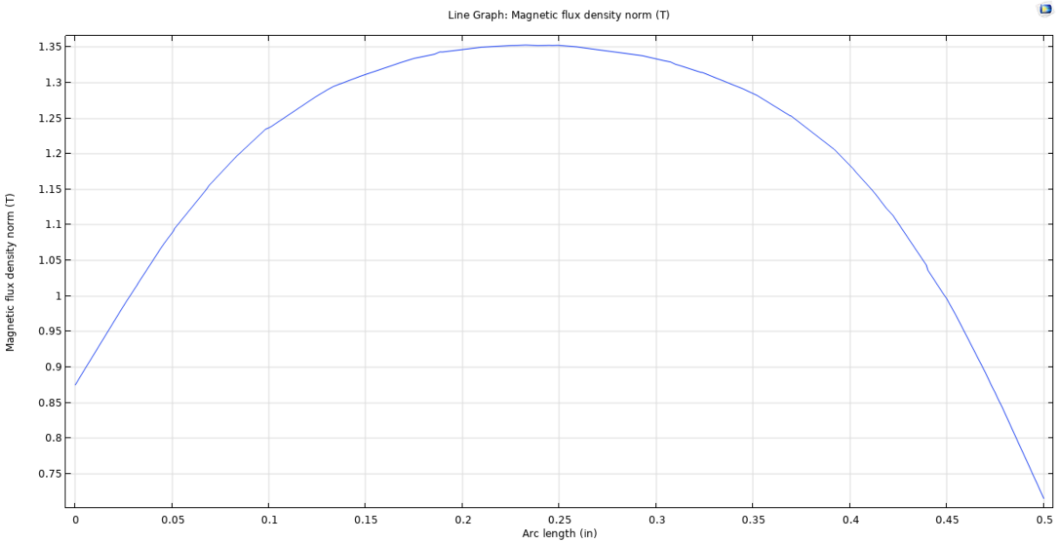

Figure 51: Magnetic Flux Density Norm along center of PM, EM current at 5.0 Ampere

In three dimensional simulations B_r must be expressed in terms of x, y, and z components, which for the generalized model is simply: $B_r = B_{rz}$ and $B_{ry} = B_{rx} = 0$. However, in the case of the validation model that contained all twelve PMs, the components were expressed by multiplying B_r value by the components of the unit position vector of each PM. All PMs were all assigned dimensions of 0.5 inches in length and 0.25 inch in diameter for all simulations as shown in Figure 52, and all PMs were oriented with the north pole normal to the surface of the rotor.

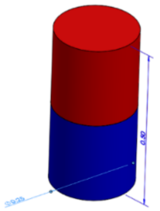

Figure 52: Permanent Magnet Geometry

The permanent magnet is modeled after an Arnold Magnetic Technologies® N52 sintered NdFeB magnet. The material properties and magnetization curve data were extracted from the manufacturer data sheet and input into COMSOL®. The magnetization curve data was extracted from the data sheet data using the Automeris Web Plot Digitizer software. The demagnetization curve of the PM is plotted in Figure 53.

The intrinsic magnetization curve was not considered in the COMSOL® modeling of the permanent magnet. This is because the intrinsic curve is used to understand the effect of an external field on the magnetization within the PM, whereas the normal magnetization curve is used primarily to determine the amount of flux density and energy the magnet is capable of producing outside the magnet volume – the latter is of interest in this model (MMPA, 1998).

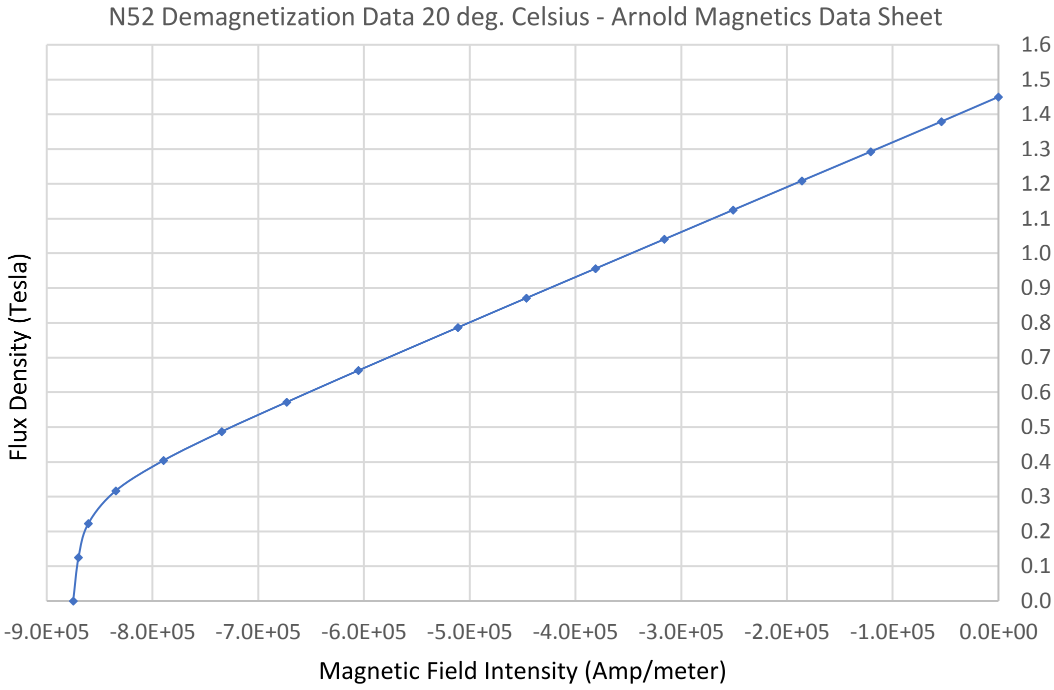

Figure 53: N52 PM Normal Demagnetization Curve (Arnold Magnetic Technologies®)

5.5.5 Iron Sphere Modeling

The iron sphere was simulated in COMSOL® using two constitutive relations. The first was the non-linear BH curve and the second relation was the relative permeability relation which treats the BH relation as a linear relationship. The rotor material was modeled using low carbon steel – soft iron, which has a comprehensive set of properties defined in the COMSOL® material library, including the normal magnetization curve. The geometry of the iron sphere is shown in Figure 54 and remained unchanged for all models studied herein. Note that the iron sphere model includes a pocket to accommodate a decoupling insert of the dimensions shown in Figure 58. The diameter of the iron sphere is 2.5 inches (0.0635 meter).

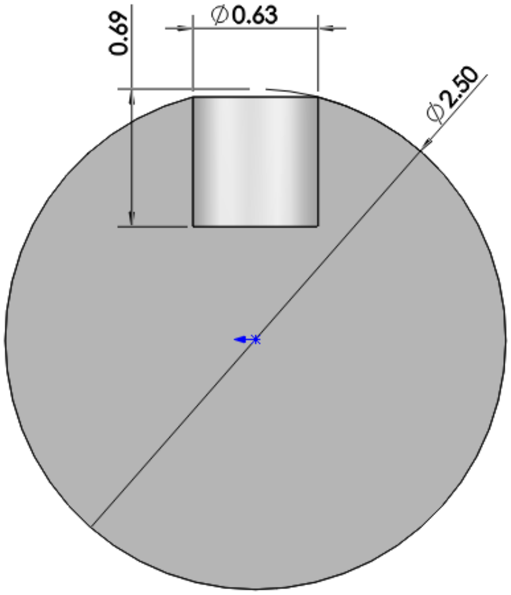

Figure 54: Generalized Model of the NGCRS Iron Rotor

The constitutive relation computed by COMSOL® for the non-linear BH curve is given by equation (117), where $\|H\|$ is the magnetic field norm and $f(\|H\|)$ is a function relating the flux density to the magnetic field of the material as a function of the magnetic field norm. The BH curve for the low carbon steel – soft iron material is plotted in Figure 57.

$$B = f(\|H\|)\frac{H}{\|H\|} \tag{117}$$

Several simulations were performed using the non-linear BH relation in order to assess the need to include the material non-linearities. The first series of simulations considered only the interactions between an electromagnet and the iron sphere for varying levels of current excitation and EM positions. The maximum flux density induced in the sphere with an EM excited with 5.0 amperes of electrical current, which is the highest level of excitation considered herein, was approximately 0.35 Tesla. The flux density plot for this condition is shown in Figure 55.

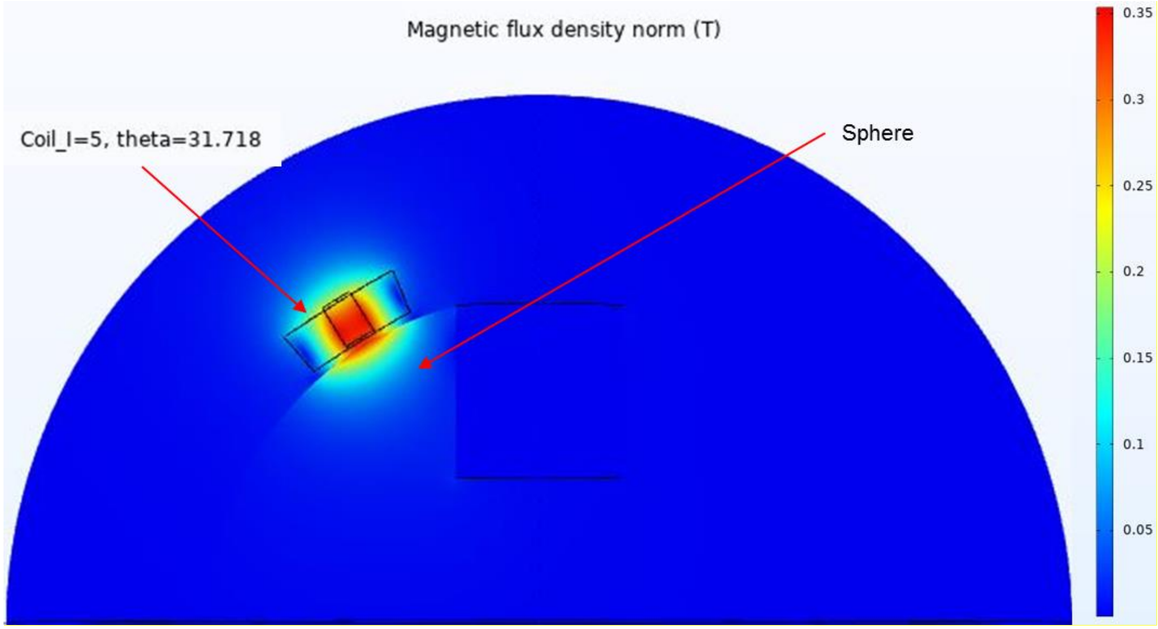

Figure 55: Magnetic Induction in iron rotor due to the EM

Additional simulations were performed with a PM included in the model. The maximum level of induction within the iron due to the PM field was limited to approximately 0.2 Tesla. The low level of induction is attributable to the large reluctance that the walls of the decoupling insert introduce into the magnetic circuit of the PM and rotor iron. Figure 56 shows the magnetic flux density in the iron due to the PM, which is less than that of the EM.

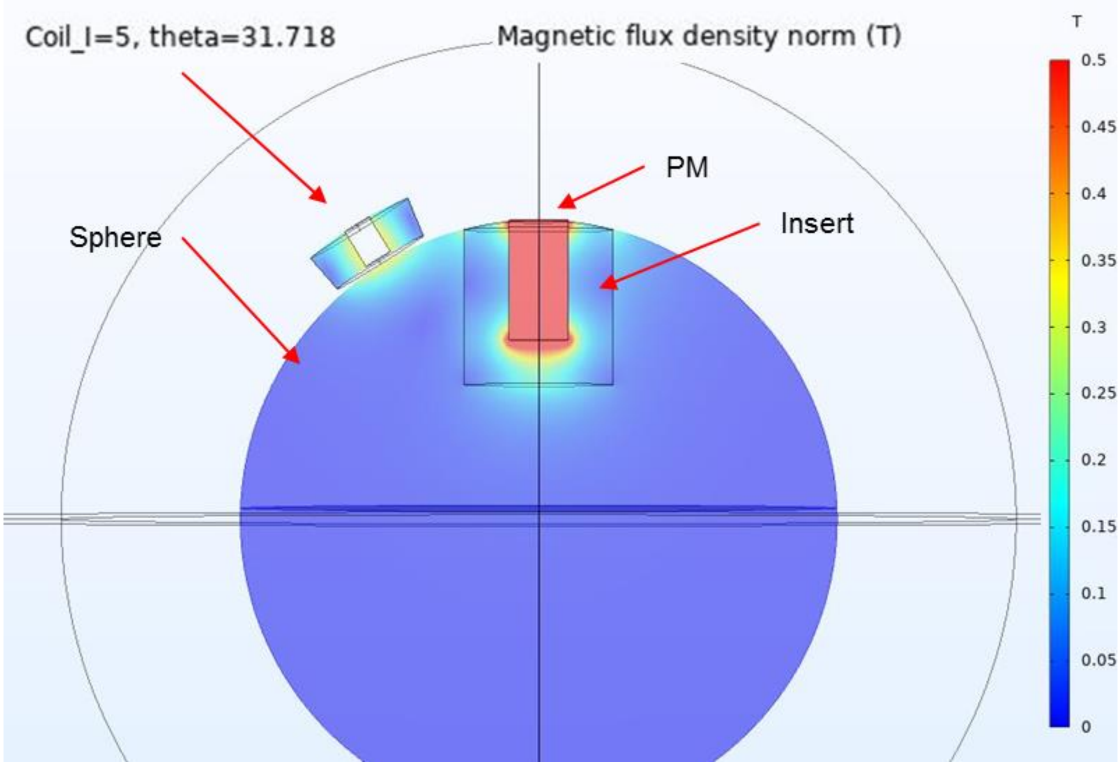

Figure 56: Magnetic Induction in Iron Rotor due to the PM

The relative permeability relation for the magnetic field of the iron sphere is given below, where B is the flux density, or induction, H is the magnetic field strength, μ_0 is the permeability of air, and μ_r represents the relative permeability of the iron sphere.

$$B = \mu_0 \mu_r H \tag{118}$$

COMSOL® requires the user to input a relative permeability when a library material is assigned to the problem domain. A relative permeability of *3,720* was selected based on the flux density plots in Figure 55 and Figure 56, which were generated from the non-linear constitutive relations. The relative permeability was obtained by taking the average permeability of three points along the linear region of the BH curve using the following relation:

$$\mu_r = \frac{B}{H\mu_0} \tag{119}$$

The data points used to approximate the relative permeability μ_r are provided in Table 1. The corresponding portion of the material BH curve is shown in red in Figure 57.

Table 1: Derivation of Relative Permeability for Iron Sphere

H	B	μ_r
47.02	0.22	3758.13
92.85	0.43	3727.48
136.30	0.63	3674.61
Average $\mu_r \sim 3720$		

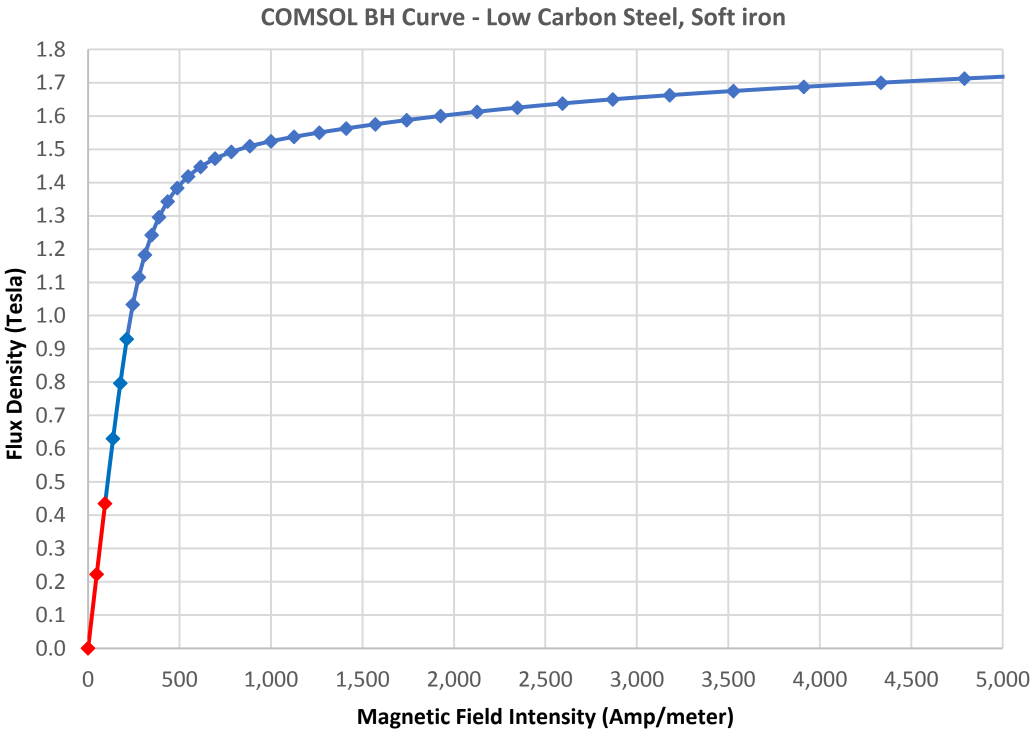

Figure 57: BH Curve for COMSOL® Low Carbon Steel – Soft Iron

The magnetic forces predicted by COMSOL® for the non-linear BH and relative permeability models have a negligible difference, the details of which are presented in section 5.5.8.

5.5.6 Decoupling Insert Modeling

A decoupling insert was introduced into the model to decouple the magnetic field of the PM from rotor iron such that the magnetic induction in the rotor iron was restricted to the linear region of the material magnetization curve as shown in Figure 57. This allowed the superposition principle to be applied with minimal error, and allowed the sphere to be modeled using the relative permeability constitutive relation without introducing significant inaccuracies and reducing the computation times of the simulations.

The decoupling effect is attributable to the walls of the insert, which introduce a large reluctance into the magnetic circuit of the rotor iron and PM which causes a significant reduction of magnetic flux within the rotor. Ideally, the insert would be made of a lightweight non-magnetic and non-conducting material. However, copper was used in the model because its relative permeability is close to one and material properties are available in the COMSOL® material library. The insert was modeled in COMSOL® as a region of constant permeability ($\mu_r = 1$). The decoupling insert geometry shown in Figure 58.

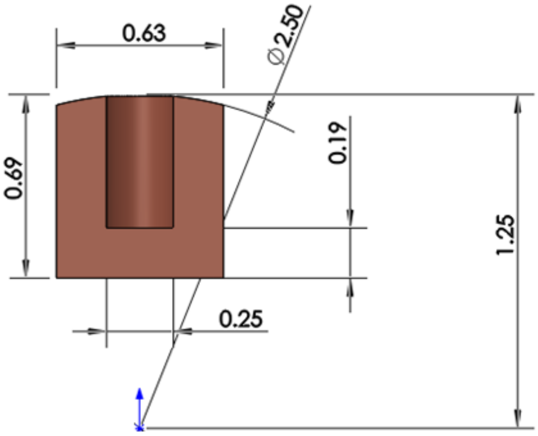

Figure 58: Decoupling Insert Geometry

The insert dimensions needed to adequately decouple the magnetic fields were determined by performing a plurality of simulations with increasing wall thickness. Insert wall thicknesses of 1/64 inch, 1/32 inch, 1/16inch, 1/8 inch, and 3/16 inch were studied using the non-linear BH relation with the PM modeled using the Remnant Flux Density constitutive relations. The details of this study are detailed in Section 5.5.7.

5.5.7 Comparison of Superposition and Integrated Models

The Lorentz forces obtained from the individual superposition models are summed to obtain the total force acting on the EM. These forces are compared to the forces obtained from an integrated model with varying decoupling insert thicknesses. The results of the study are shown in Figure 59. The plots show that wall thicknesses below 3/16 inch do not provide sufficient decoupling between the PM and rotor iron, but the plot with for the 3/16-inch insert shows good agreement between the superposition and coupled model. However, the coupled model predicts a drop in magnetic force between angular distances of 12 and 22 degrees with the maximum drop occurring at approximately 16 degrees. These angular distances encompass the area where the EM overlaps with the high reluctance gap between the PM and rotor, and the maximum drop occurs when the centerline of the EM is located at the sharp edge of the rotor iron as shown in the flux density plots in Figure 63. It is apparent that the magnetic field is not fully decoupled in this region.

Additional plots of the magnitude of the Lorentz forces for the 3/16-inch decoupling insert with increasing current levels are provided in Figure 60, Figure 61, and Figure 62. At 0.5 ampere coil excitation the drop in forces is not apparent, however once the current is increased to 1 ampere the drop in force appears and the effect increases in severity up to the maximum of 5 amperes. This behavior will not be accounted for in the dynamic model discussed herein, and will be rejected as a disturbance by the ensuring controller implementation. Refer to Section 5.6.1 for detailed discussion of the implementation of the forces in the dynamic model.

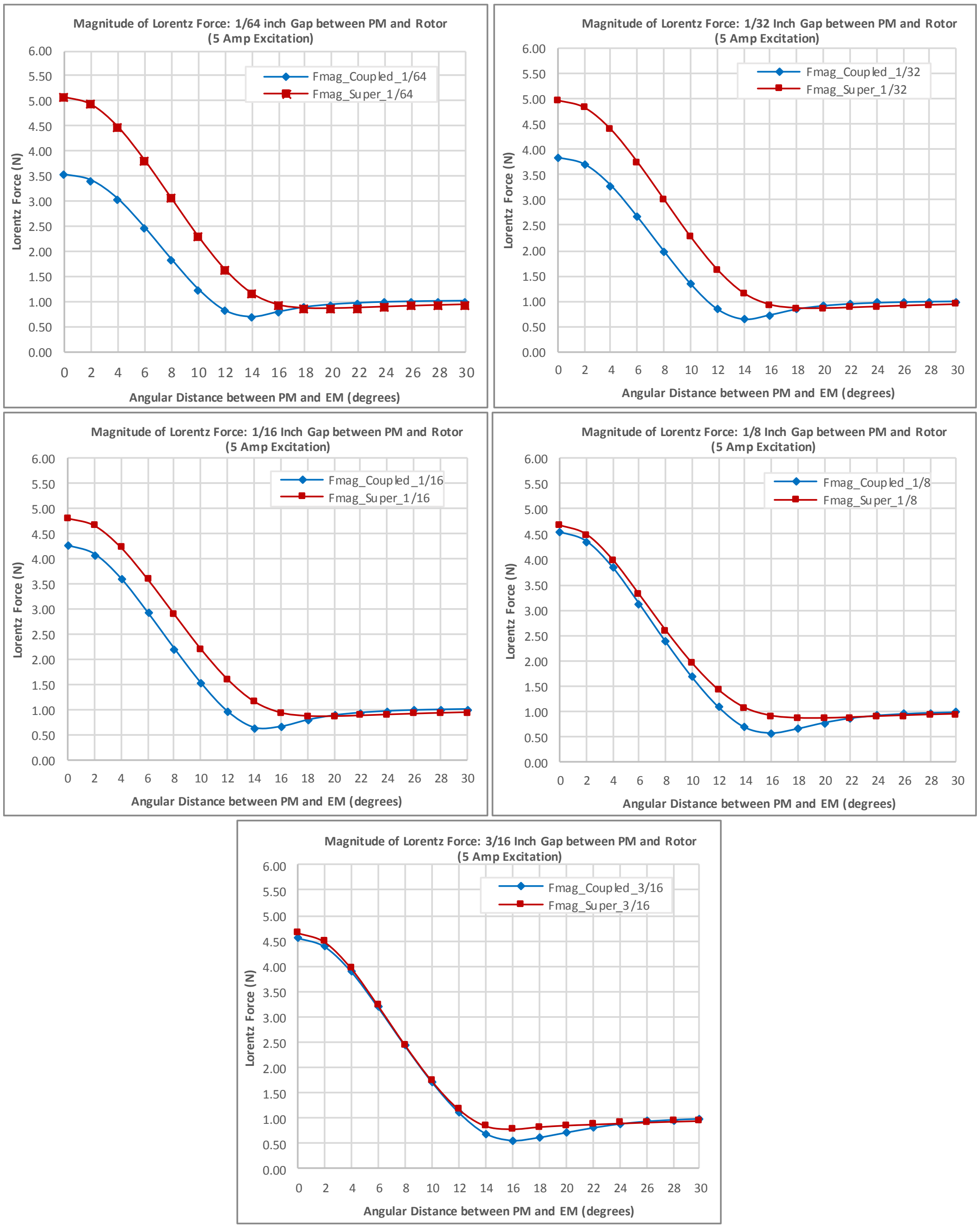

Figure 59: Comparison of Magnetic Force for Varying Gap Width – Integrated & Superposition Models

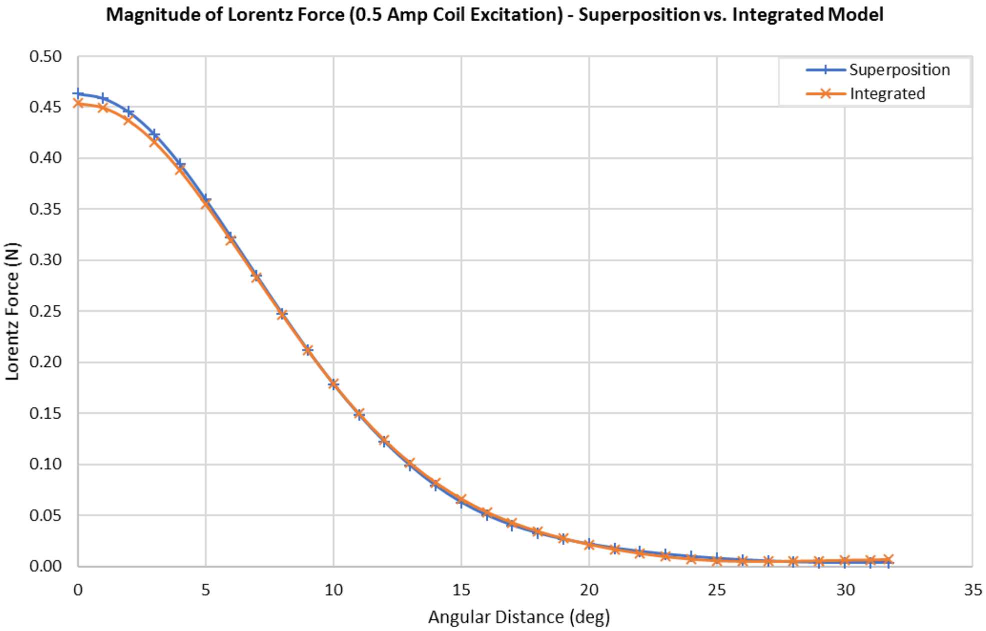

Figure 60: Magnitude of Lorentz Force: Integrated vs. Superposition Model (0.5 amp)

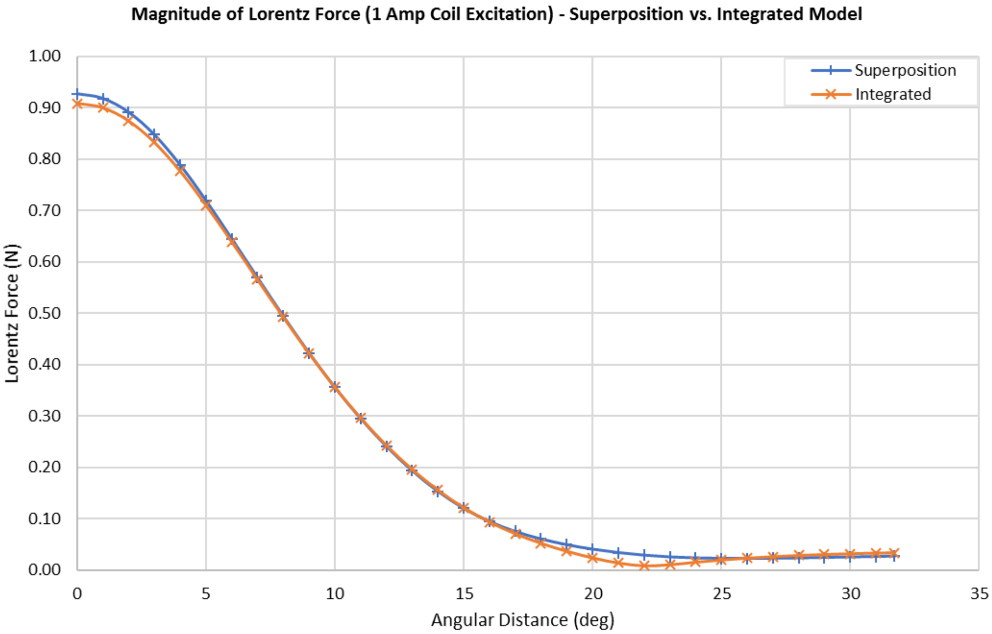

Figure 61: Magnitude of Lorentz Force: Integrated vs. Superposition Model (1 amp)

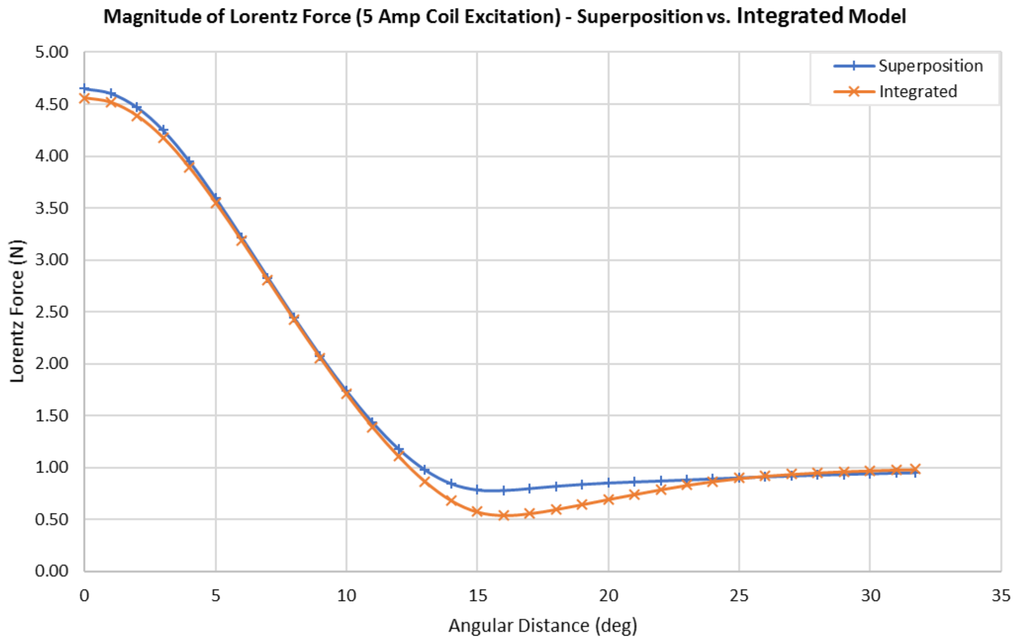

Figure 62: Magnitude of Lorentz Force: Integrated vs. Superposition Model (5 amps)

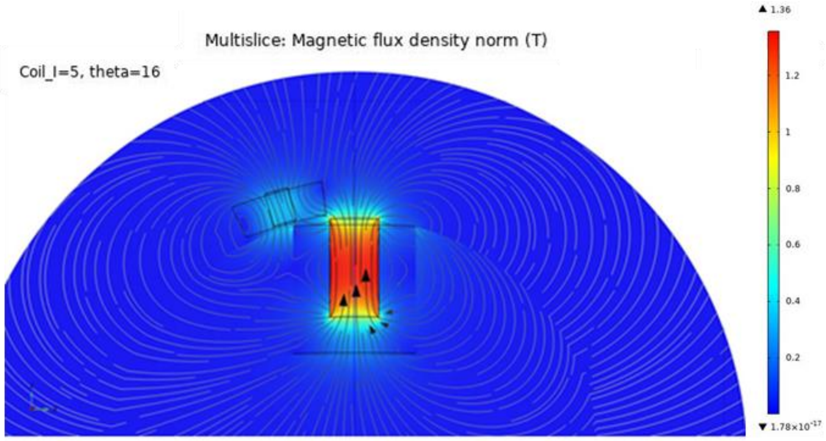

(a) Coupled Model

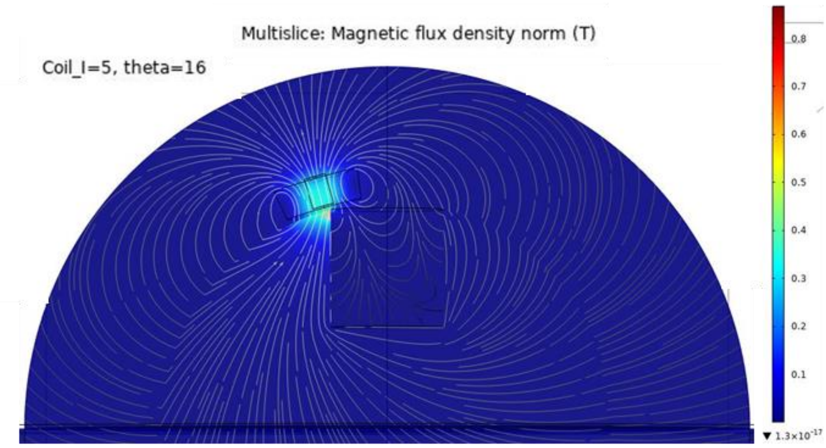

(b) Superposition Model (Rotor)

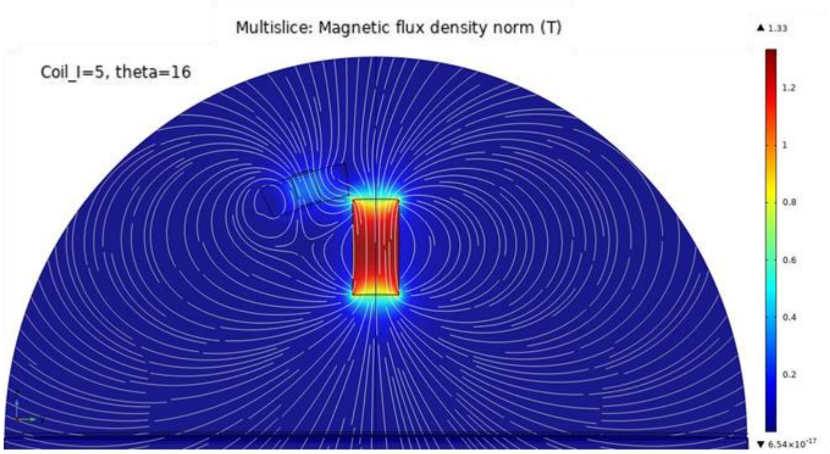

(c) Superposition Model (PM)

Figure 63: Flux Density Plots of Superposition and Integrated Models (16 Deg Angle)

5.5.8 Comparison of Linear and Non-Linear FEM Models

This section presents comparative results of the models listed below which were simulated using both linear and non-linear constitutive relations. Typically, only the cases with an EM excited by 5.0 amperes of electrical current are examined since this results in the highest magnetic field intensities and exhibit the non-linear behavior.

1. The generalized superposition model of the EM and Sphere
2. The generalized superposition model of the EM and PM
3. The generalized integrated model of the RS (EM, PM, and Sphere)

The magnetic forces predicted by COMSOL® for the linear and non-linear relations of the generalized superposition model of the EM and Sphere are plotted in Figure 64. The results show that the linear model predicts forces very close to that of the non-linear model. The closeness of the results is due to the fact that the non-linear BH curve relation in COMSOL® behaves as the relative permeability relation if the magnetic fields are small (Tozzo, 2018). The largest percent difference in the magnitude of the force was 0.005%, while the average percent difference between the computed forces was less than 0.001%. Based on these results, the inclusion of material non-linearities is not warranted.

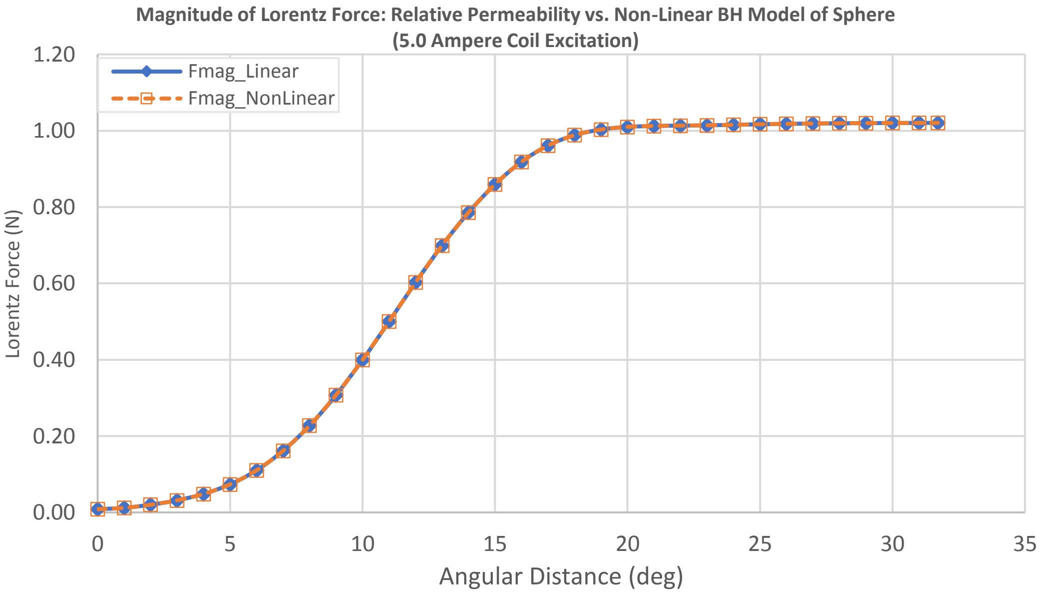

Figure 64: Magnitude of Lorentz Force: Relative Permeability vs. BH Curve of Sphere

The y and z components of the Lorentz forces predicted by COMSOL® for the PM superposition model using the remnant flux density (linear) and non-linear (BH, non-linear PM) relations of are plotted in Figure 65, and the magnitude of the Lorentz force is shown in Figure 66. The results show that the remnant flux density model predicts forces close to that of the non-linear PM model. The largest percent difference in the magnitude of the force was 1.58%, while the average percent difference between the computed forces was less than 1%. Based on these results, the inclusion of material non-linearities is not warranted.

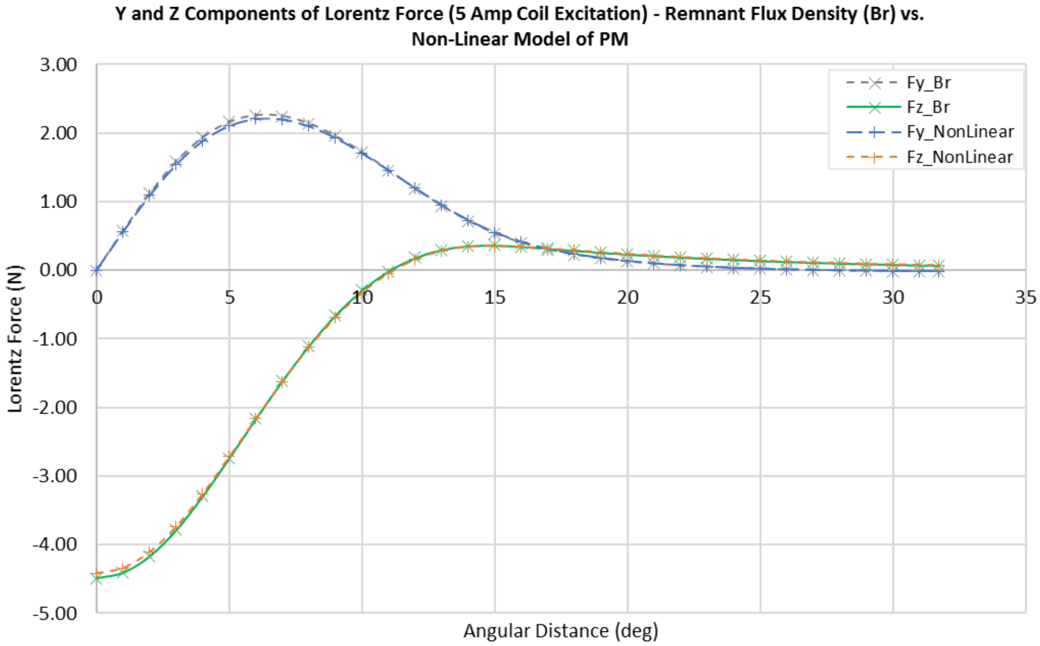

Figure 65: Y, Z Components of Lorentz Force: Remnant Flux vs. Non-linear PM

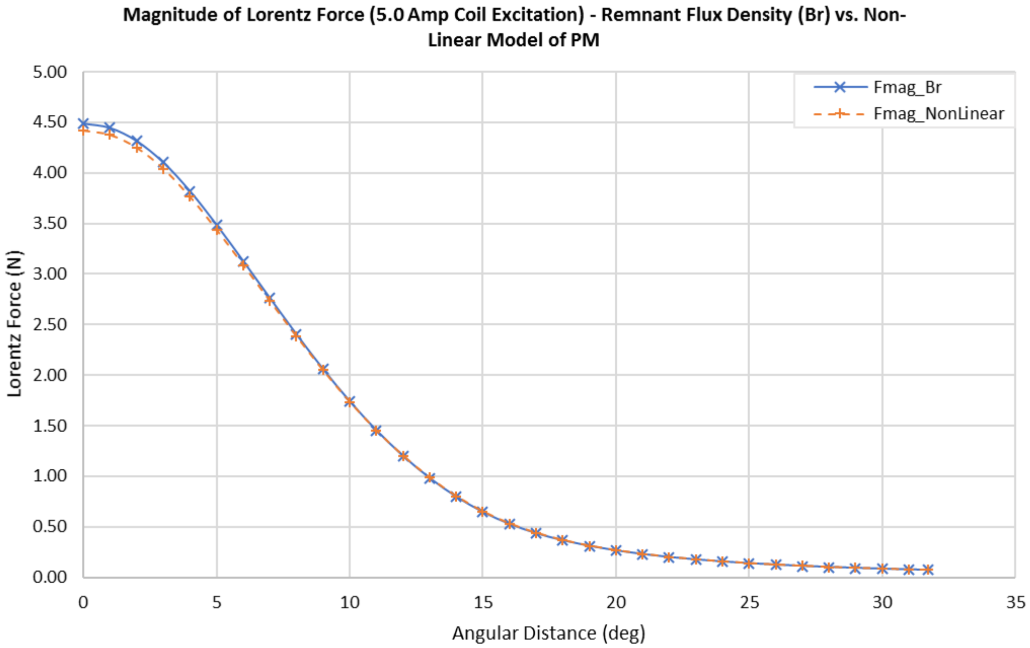

Figure 66: Magnitude of Lorentz Force: Remnant Flux vs. Non-linear PM

The generalized, integrated model with the 3/16-inch insert (see Figure 46) was also simulated using linear and non-linear relations to ensure the linear relations could be used without inducing significant errors. A comparison of the magnetic forces generated by these two models is presented in Figure 67. The results show the linear model is in close agreement with the non-linear model, and justifies using linear continuative relations in COMSOL®. The largest percent difference in the magnitude of the force was 1.94%, while the average percent difference between the forces was less than 0.66%. The results again show that the non-linear constitutive relations do not provide any significant improvement in accuracy over the linear relations.

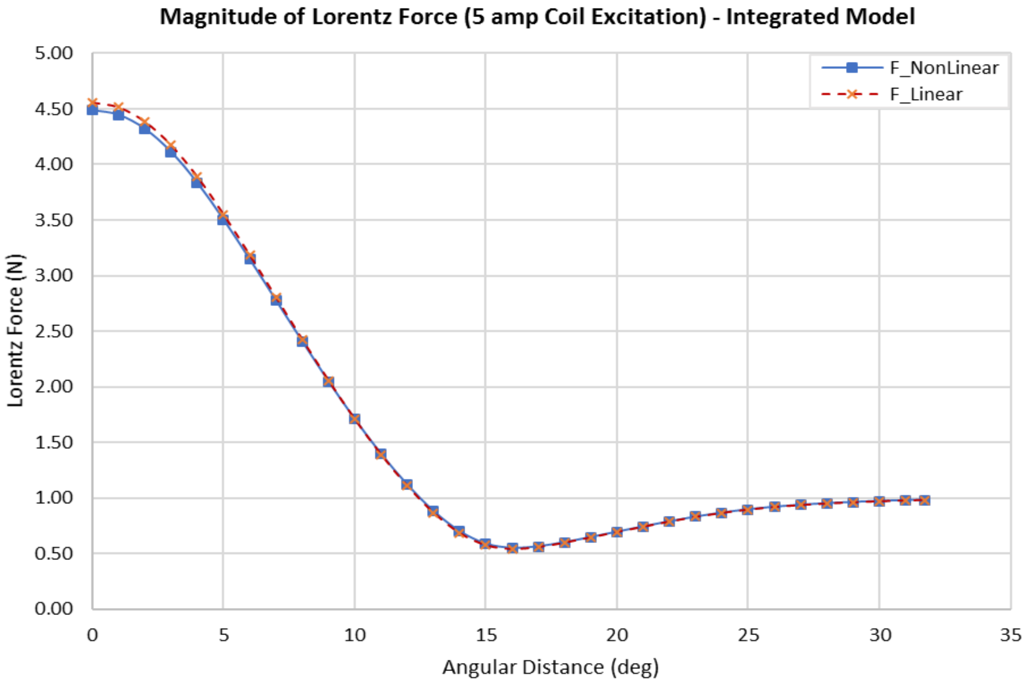

Figure 67: Magnitude of Lorentz Force: Linear vs. Nonlinear Integrated Model

5.5.9 Comparison of Generalized Model to Complete Model

Simulations were performed for a rotor model complete with all twelve PMs and all twelve decoupling inserts. The forces predicted by this model were compared against the forces predicted by the generalized superposition model and the generalized integrated model. Two conditions were simulated using the complete model and are listed below, and illustrated in Figure 68.

1. The EM is rotated through a trajectory with one PM adjacent to the path
2. The EM is rotated through a trajectory with two PMs adjacent to the path

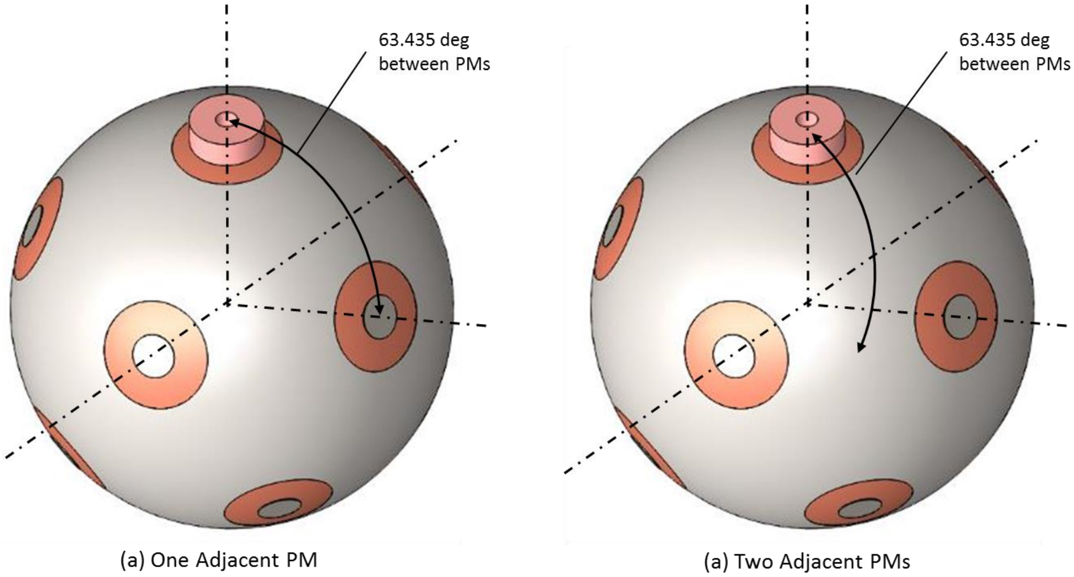

Figure 68: EM Rotation: (a) One Adjacent PM and (b) Two Adjacent PMs

The forces predicted by COMSOL® for the complete model of the rotor assembly are compared to the forces for the generalized integrated model and the superposition models in Figure 69. This plot is for the condition of one adjacent PM (shown in Figure 68) with a coil excitation of 0.5 ampere. The plot shows close agreement between all the models. Similarly, the plot in Figure 70 compares the forces predicted by the three models, but for a coil excitation current of 5.0 amperes. The complete rotor model and generalized (integrated) model show close agreement, but the superposition model does not account for the coupling between the EM and PM in the region near the decoupling insert as discussed previously in Section 5.5.7.

The plots for the condition with two adjacent PMs are provided in Figure 71 and Figure 72. Again, the plots show close agreement amongst the models. However, in contrast to the condition with one adjacent PM, the force is approximately equal to the force the EM exerts on the iron only because the magnetic fields of the two PMs largely cancel one another and the force between the iron and EM dominates. The force plot for any arbitrary trajectory would be between these two extremes.

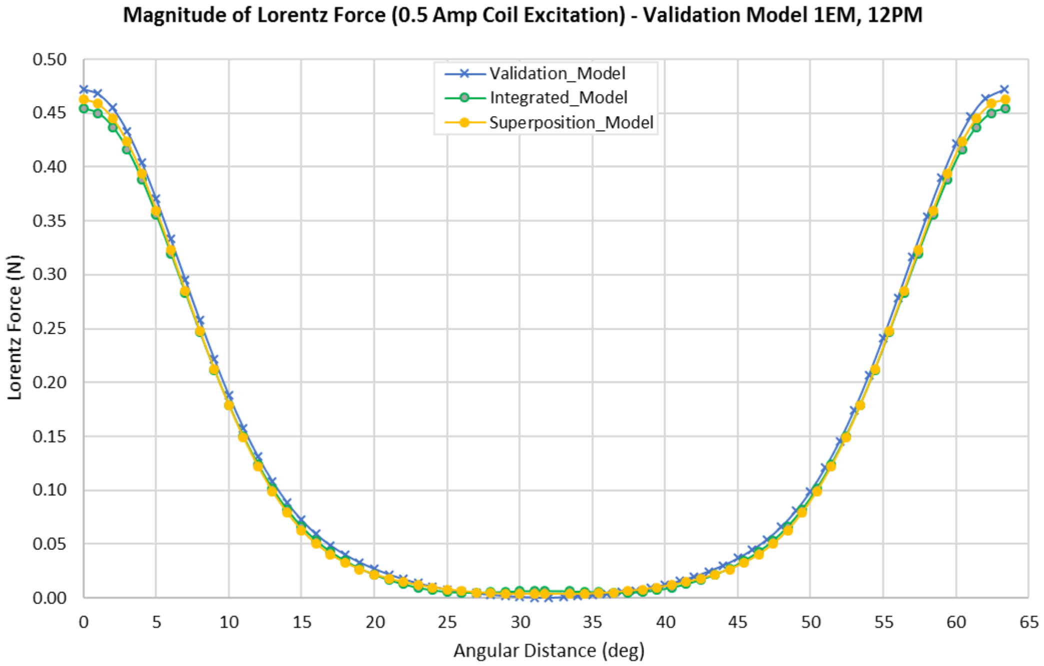

Figure 69: Forces for Generalized vs. Complete Rotor Assembly 1 Adjacent PM (0.5 Amp)

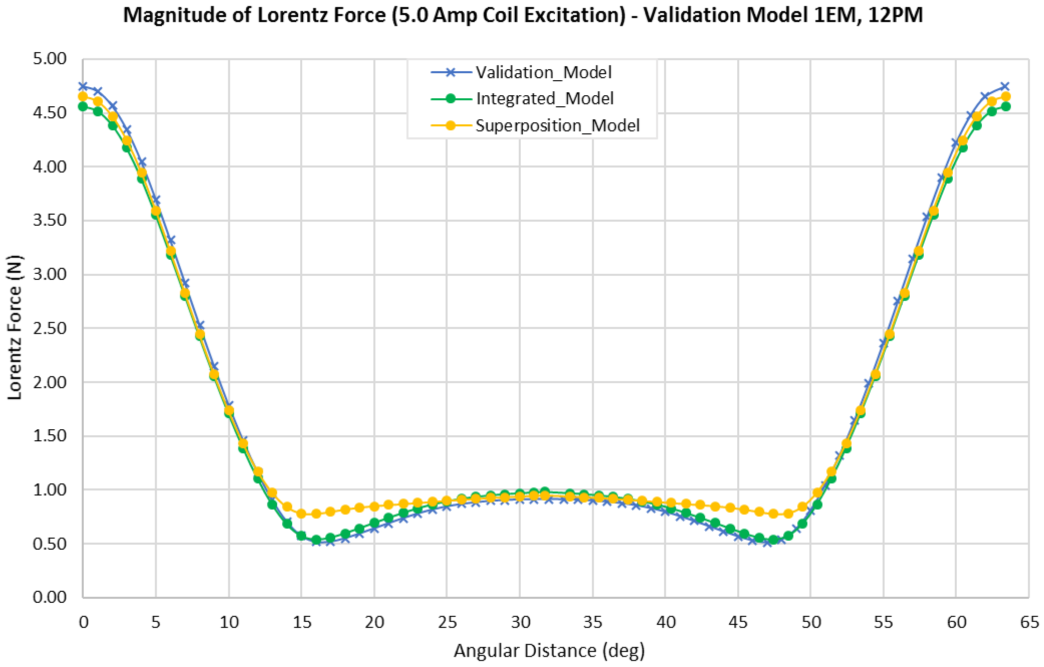

Figure 70: Forces for Generalized vs. Complete Rotor Assembly 1 Adjacent PM (5 Amps)

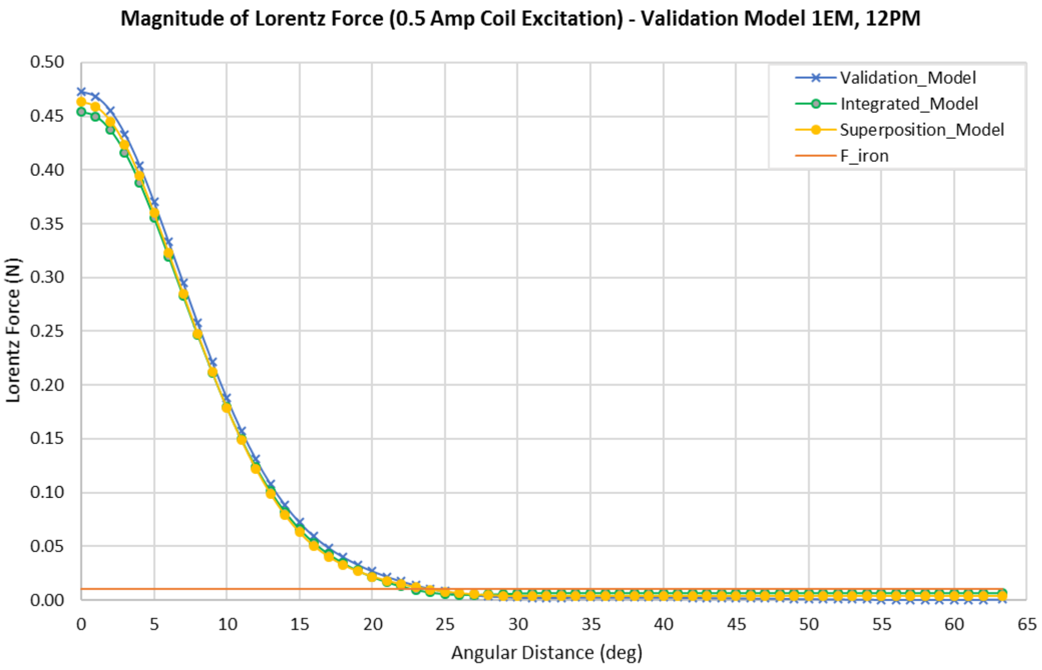

Figure 71: Forces for Generalized vs. Complete Rotor Assembly 2 Adjacent PM (0.5 Amp)

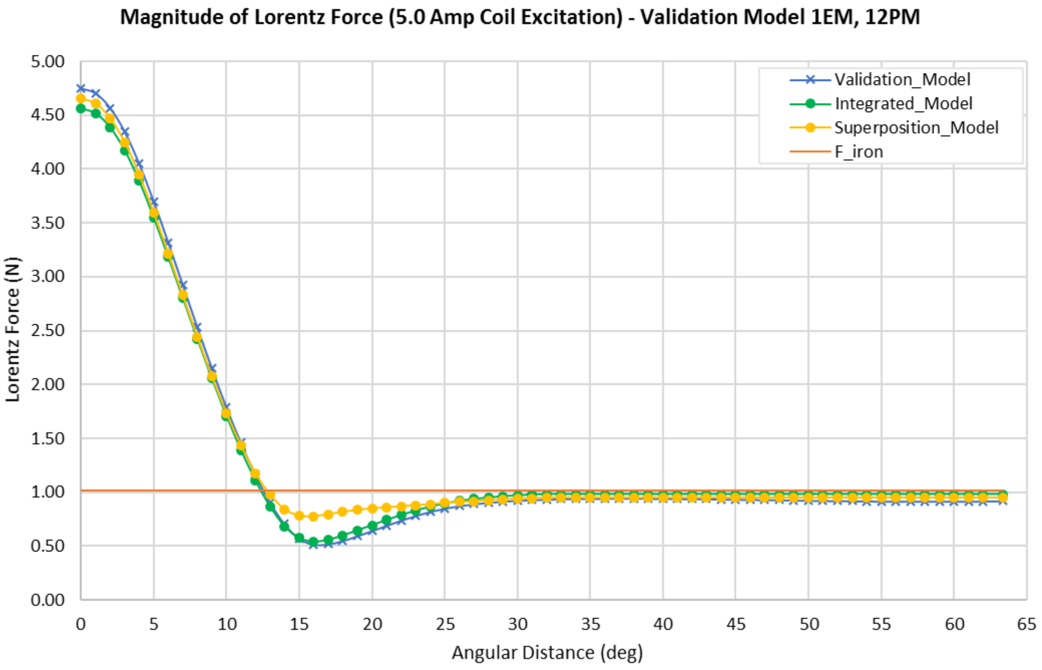

Figure 72: Forces for Generalized vs. Complete Rotor Assembly 2 Adjacent PMs (5 Amp)

5.5.10 Computation of Force and Torque

The magnetic forces are computed by COMSOL® using the Lorentz Force. The constitutive relation of which is given by equation (120), where J is the current density in the electromagnet volume and B is the magnetic field.

$$\vec{F}_L = \hat{J} \times \hat{B} \tag{120}$$

The advantage of using the Lorentz force calculate the magnetic forces, rather than the Maxwell Stress-Tensor, is because it is produces highly accurate results for current carrying, non-magnetic domains, and is less sensitive to surface mesh density than the Maxwell Stress Tensor method (COMSOL, 2019). The force computed by COMSOL® represents the net force acting on the EM. The force acting on the EM is equal and opposite to the force acting on the sphere in accordance with Newtons third law. Consequently, the forces predicated by COMSOL® must be reversed in the dynamic model in order to represent the forces acting on the spherical rotor.

The torques are computed by COMSOL® using equation (123), where r_O is a point on the origin of the axis of rotation (specified at the origin of the coordinate system for all simulations), r is the distance to the point of action, n_1 is the normal vector pointing outward from the domain containing material 1, and T_2 is the stress tensor in material 2. In this case material 1 is the copper coil and material 2 is the air surrounding the coil. The torque is calculated as a boundary integral of the stress tensor on the outside of the coil (COMSOL, 2019).

$$M_O = \oint_{\partial\Omega_1} (r - r_O) \times (n_1 T_2)\, dS \tag{121}$$

For air, the stress tensor is calculated by COMSOL® using equation (122), where p is the air pressure, I is the identity 3-by-3 matrix, and E and B are 3-by-1 vectors representing the electric field and magnetic field respectively. Treating air as a vacuum ($p = 0$) the expression becomes the Maxwell stress tensor (COMSOL, 2019).

$$T_2 = -pI - \left(\frac{\epsilon_0}{2} E \cdot E + \frac{1}{2\mu_0} B \cdot B\right) I + \epsilon_0 E E^T + \frac{1}{\mu_0} B B^T \tag{122}$$

Note that none of the methods described above can used to compute or visualize the force distribution inside a domain. The relations only compute the total force and total torque in situations where the device is surrounded by a nonsolid medium (COMSOL, 2019).

5.5.11 Meshing and Convergence

The model mesh was controlled by the physics module and biased toward evaluation of the magnetic field. The fineness of the mesh was selected based on the results of a convergence study that compared the Lorentz forces output by COMSOL for each of the built-in physics-based refinements. The Lorentz forces were scaled against the coarsest physics-based mesh available in COMSOL®, which is called “coarser”. The results are tabulated and plotted in Figure 73. The results show that in all cases the forces predicted by the “ultra-fine” mesh differed from the “coarser” mesh by less than four percent. The “ultra-fine” mesh was used for all simulations because sufficient computational resources were available to solve the models using the finest mesh in a reasonable amount of time.

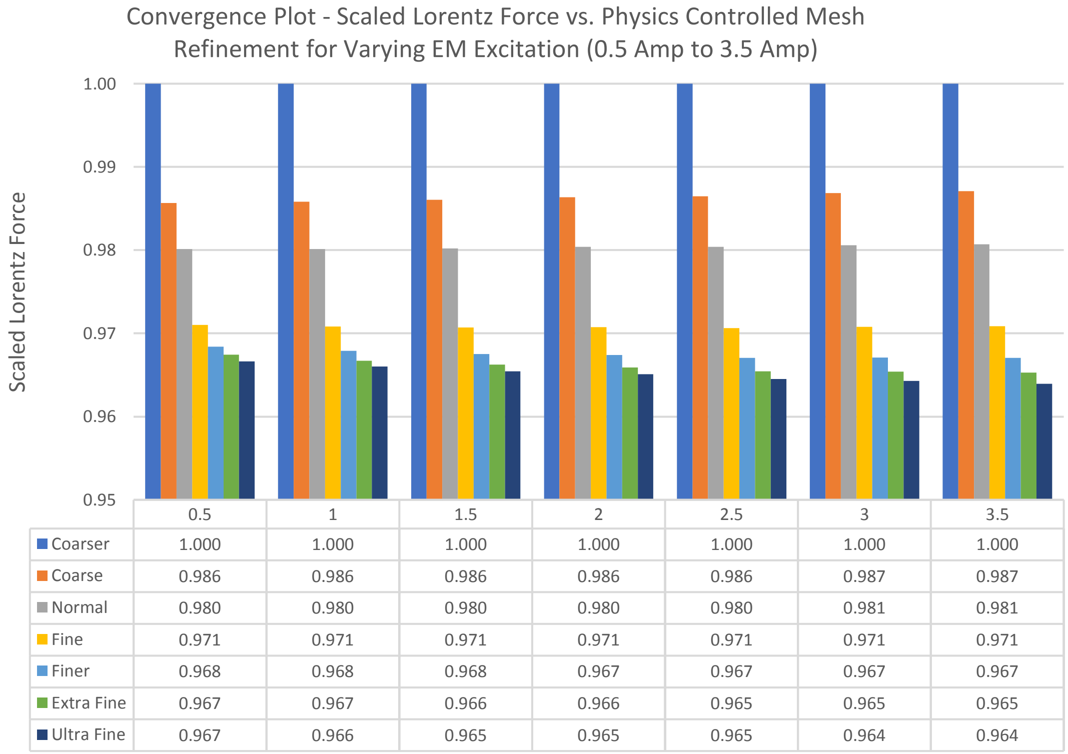

	0.5	1	1.5	2	2.5	3	3.5
■ Coarser	1.000	1.000	1.000	1.000	1.000	1.000	1.000
■ Coarse	0.986	0.986	0.986	0.986	0.986	0.987	0.987
■ Normal	0.980	0.980	0.980	0.980	0.980	0.981	0.981
■ Fine	0.971	0.971	0.971	0.971	0.971	0.971	0.971
■ Finer	0.968	0.968	0.968	0.967	0.967	0.967	0.967
■ Extra Fine	0.967	0.967	0.966	0.966	0.965	0.965	0.965
■ Ultra Fine	0.967	0.966	0.965	0.965	0.965	0.964	0.964

Figure 73: Convergence: Normalized Force vs Varying Current & Mesh Refinement

An Infinite Element Domain (IED) was incorporated into the mesh in order to model the system as an unbounded domain. The IED applies a real-valued coordinate scaling to a layer of virtual domains surrounding the physical region of interest (COMSOL®, 2015), and is advantageous because it removes the ambiguity associated with sizing the physical domain in the problem, such that the external boundaries do not interfere with the fields in or on the model domains. Additionally, the IED eliminates the need to specify a boundary condition for the problem (Frei, 2016). The end effect of the IED is that the domain behaves as if it were of infinite extent. The meshes of the two generalized models are depicted in Figure 74 and Figure 75. The IED is not shown in the PM model for clarity.

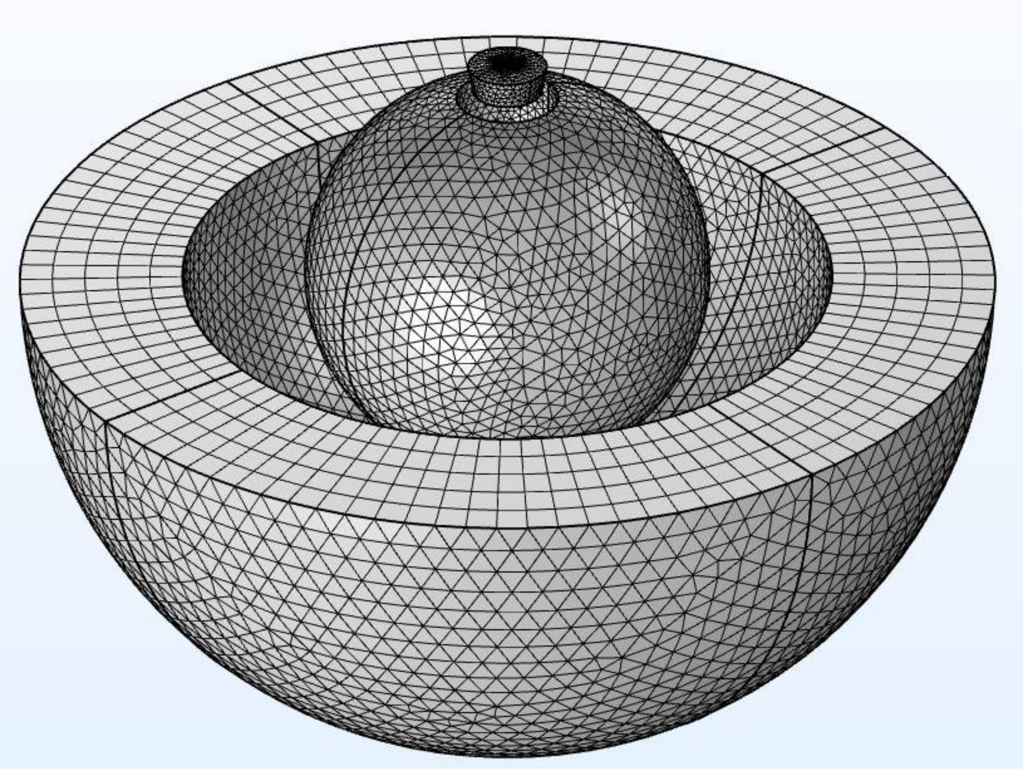

Figure 74: Mesh of the Generalized EM and Sphere Model

Figure 75: Mesh of the Generalized EM and PM Model

5.6 Relations for Forces and Torques

The forces and torques acting on the rotor assembly are computed off-line from the Simulink® dynamic model, using simulation data obtained from the generalized superposition FEM model of the NGCRS, as presented in Section 0. The applicable data is provided in Appendix A.

Based on the results of the FEM simulations, the magnetic forces between the EMs and the rotor iron and rotor PMs were divided into two distinct regions. In the first region, henceforth referred to as the "*Iron"* region, the force between the EM and the rotor iron is dominant and the PM field interactions with the EM are neglected. And the second region, henceforth referred to as the "*Iron +PM"* region is where the magnetic field interactions between the EM and PM cannot be neglected. The threshold for these two regions is determined from the scalar distance between the EM and PM, where the forces predicted by the *Iron* region and *Iron + PM* region are equal. An illustration of the two regions is provided in Figure 78 for a coil excitation of 5 amperes. The threshold distance is dependent only on the coil excitation current. This of course would not be true for a 6-DOF model, in which case the force would be dependent upon the EM current and the magnetic airgap.

A fit equation was derived to relate the EM current to the threshold distance. The equation was obtained by calculating the magnitude of the magnetic forces predicted by the generalized superposition model for each coil excitation simulated, and converting the angular distances to scalar distances using equation (123). From there, a curve was fit to each force vs distance data set using the MATLAB® curve fitting toolbox. The equations for each curve fit were input into a MATLAB script as an equality set equal to force the EM exerts on the iron rotor (e.g. force in the Iron region) for the applicable current level. The equality was solved numerically to determine the point of intersection, thus obtaining the threshold distance. This process was repeated for every coil excitation simulated. The resulting curve fit for the current vs threshold distance data is shown in Figure 77, and Figure 76 illustrates the procedure and threshold distance for a coil excitation of 5 amperes. The data, fit curves, and scripts used to derive the threshold distance relation are provided in Appendix B.

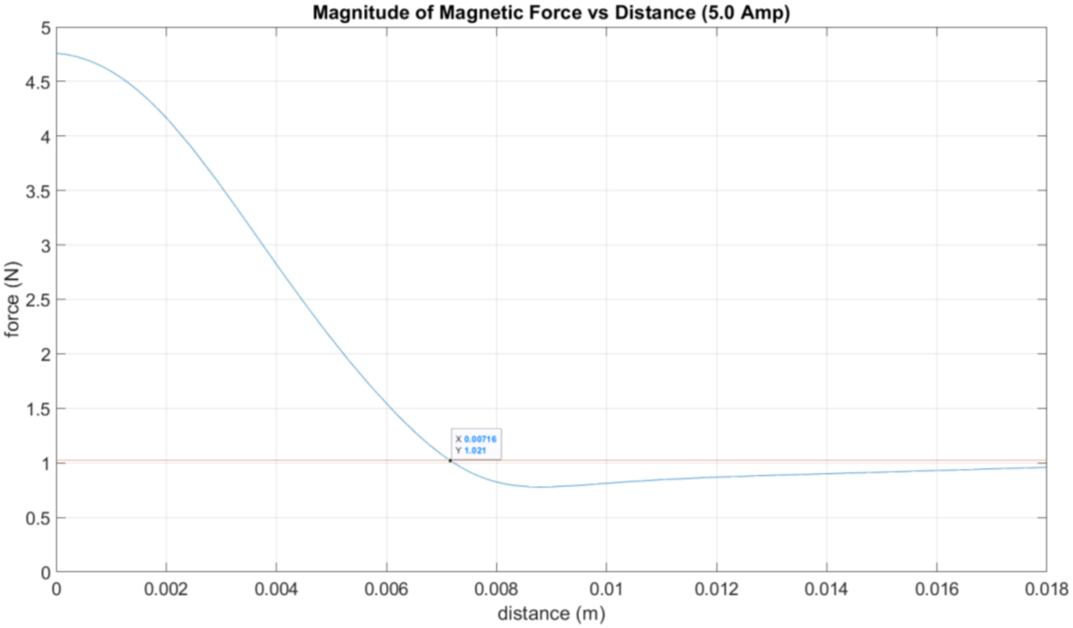

Figure 76: Distance where Regions of Force are Equal (5 Amps)

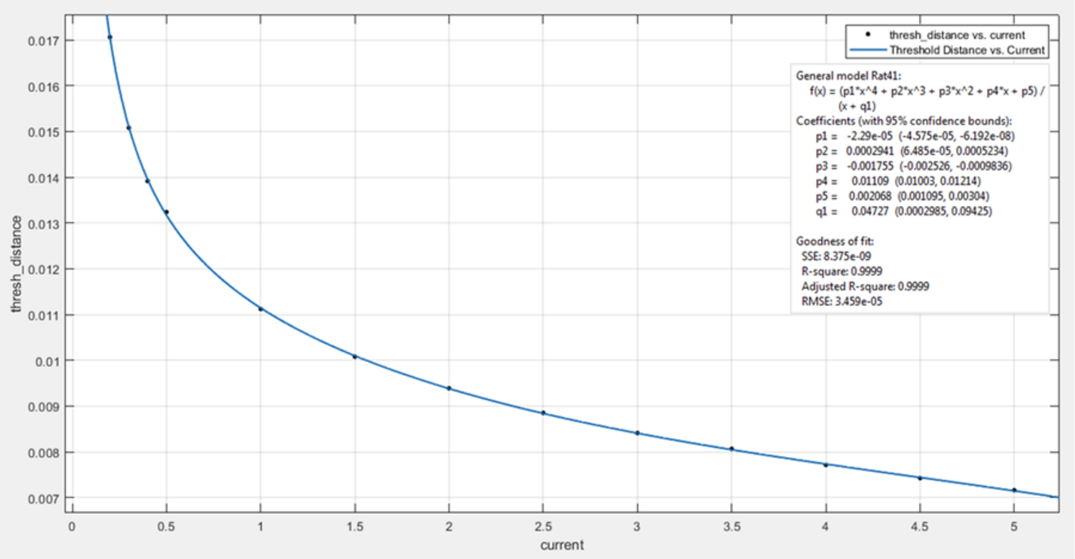

```
General model Rat41:
   f(x) = (p1*x^4 + p2*x^3 + p3*x^2 + p4*x + p5) /
          (x + q1)
Coefficients (with 95% confidence bounds):
     p1 =   -2.29e-05  (-4.575e-05, -6.192e-08)
     p2 =   0.0002941  (6.485e-05, 0.0005234)
     p3 =   -0.001755  (-0.002526, -0.0009836)
     p4 =     0.01109  (0.01003, 0.01214)
     p5 =    0.002068  (0.001095, 0.00304)
     q1 =     0.04727  (0.0002985, 0.09425)

Goodness of fit:
  SSE: 8.375e-09
  R-square: 0.9999
  Adjusted R-square: 0.9999
  RMSE: 3.459e-05
```

Figure 77: Threshold Distance of Regions of Force as a Function of Current

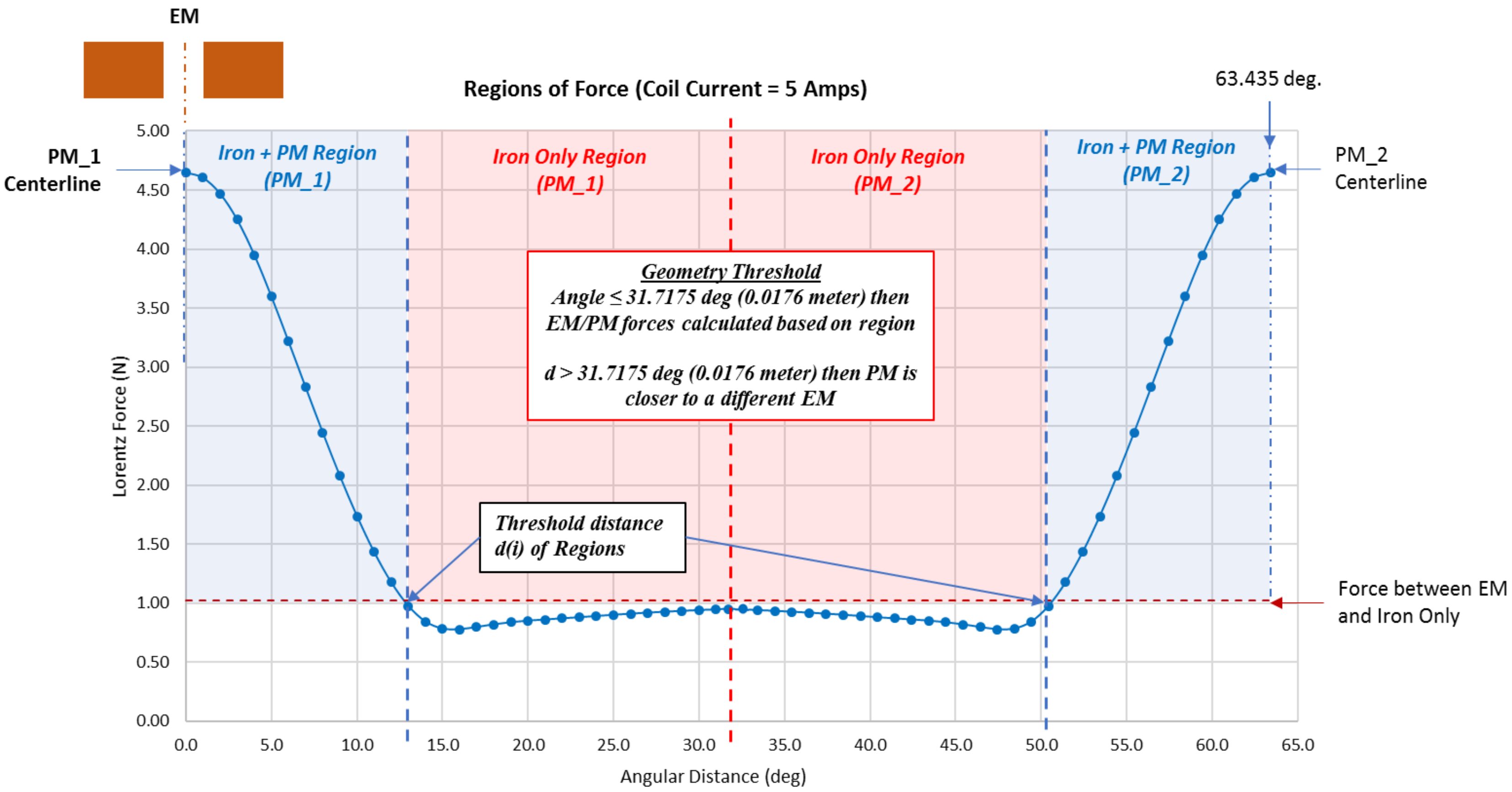

Figure 78: Threshold Distance for Iron Only and Iron + PM Forces

An algorithm was implemented in MATLAB Simulink® to calculate the net force and torque acting on the rotor assembly for any arbitrary orientation. A functional description of the algorithm is provided in the Section 5.6.1.

The COMSOL® simulation data is output in terms of the angular distance between the EM and PM. The angles were converted to scalar distances using the law of cosines given by equation (123), where r is the radius of the sphere, and θ is the angular distance between the centerlines of the EM and PM. The conversion was performed outside the algorithm to reduce the computation time. All fit curves in Appendix B were fit to the linear distance d.

$$d = \sqrt{r_{EM}^2 + r_s^2 - 2\, r_{EM}\, r_s \cos(\theta)} \tag{123}$$

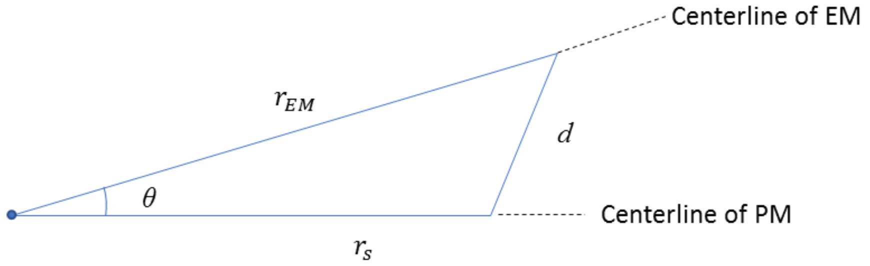

Figure 79: Conversion of Angular Distance to Linear Distance

5.6.1 Force and Torque Computation Algorithm

The force and torque algorithm is applicable to a 3-DOF problem with the rotor fixed translationally at the origin (e.g. fixed radial airgap). However, this algorithm could be extended to a 6-DOF model with modification. A high-level logic flow diagram of the algorithm is depicted Figure 80. Note that the logic is applied to each EM relative to every rotor PM.

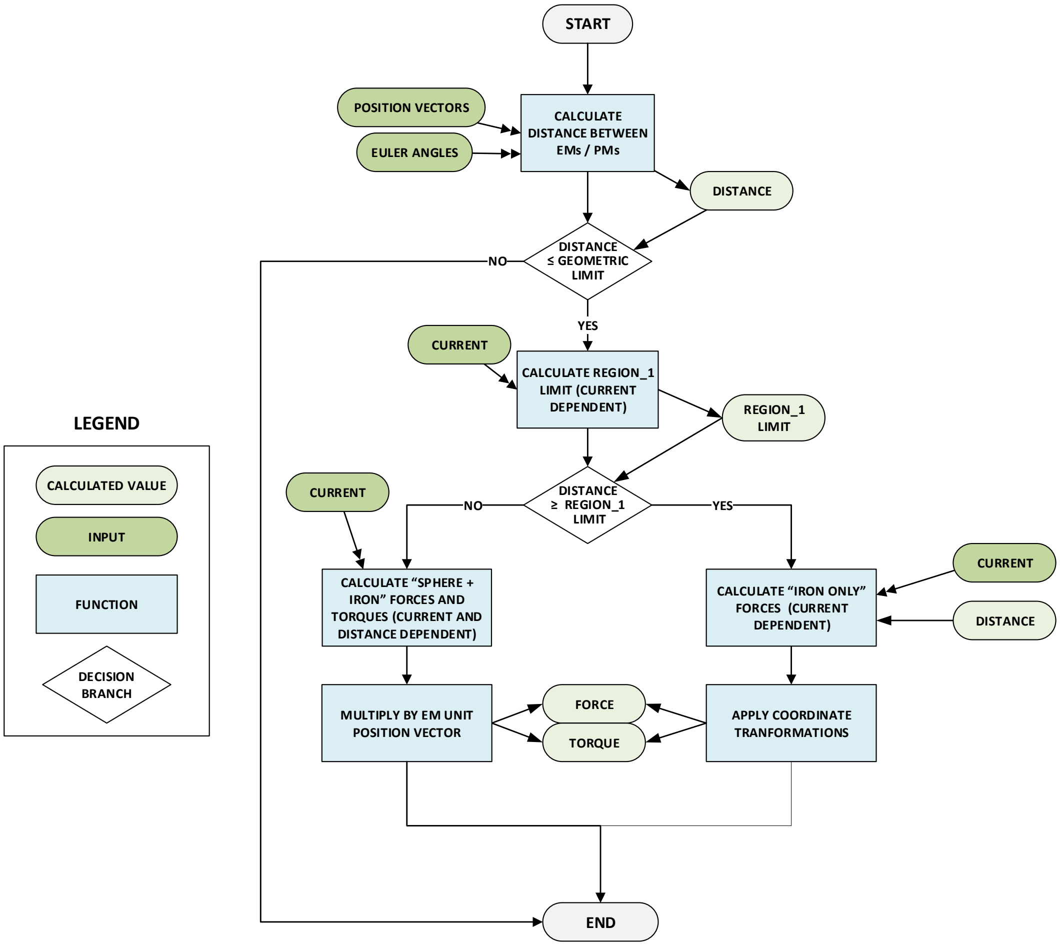

Figure 80: Logic Flow Diagram for Calculation of Forces and Torques

The first step of the algorithm is to apply the ZYX Euler Angle rotations to each PM position vector and calculate the rotated PM position vector coordinates in terms of the basis vectors ($\hat{\imath}$, $\hat{\jmath}$, $\hat{k}$) in the (fixed) stator coordinate system. Next, the scalar distance between each fixed EM position vector and each instantaneous (rotated) PM position vector is calculated, yielding a total of 72 distances (6 EMs x 12 PMs). The scalar distance d is simply the formula for the magnitude of the distance between two points.

$$d\left(\vec{E}_M,\vec{P}_M\right) = \left\|\vec{E}_M - \vec{P}_M\right\| = \sqrt{(E_{Mx}-P_{Mx})^2\hat{\imath} + \left(E_{My}-P_{My}\right)^2\hat{\jmath} + (E_{Mz}-P_{Mz})^2\hat{k}} \qquad (124)$$

The resulting distance is always positive, and therefore it is obvious which PM and EM are interacting because the RS inner and outer geometries preclude more than one PM from interacting with an EM for any orientation. Figure 81 provides an illustration of the scalar distance between an EM and PM.

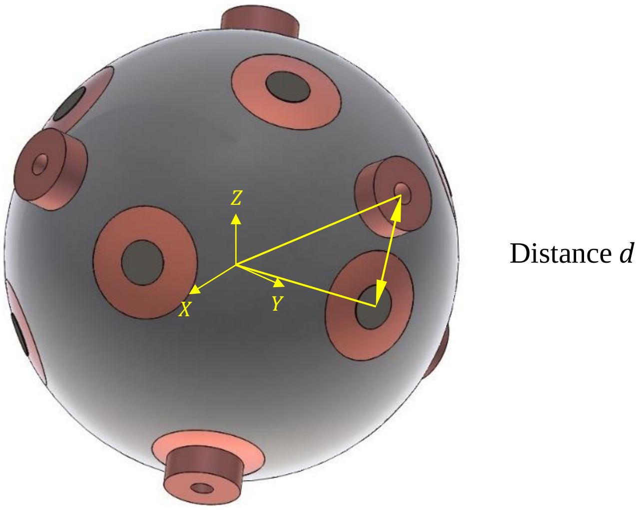

Figure 81: Euclidean Distance between a Single EM and PM

Subsequent to this, the algorithm identifies the PM in closest proximity to each EM which in turn permits identification of the specific EM-PM pairs. The minimum distances for the EM-PM pairs are then compared to threshold distances calculated from the equation of the fit curve shown in Figure 76 using the instantaneous EM current. From there, the relations describing the force in each region are used to calculate the net force and torque acting on the rotor assembly. The relations describing the magnetic force in the Iron region and the Iron + PM region are discussed in detail in Sections 5.5.2 and 5.5.4. Note that if the EM is equi-distant to more than one PM, then the force is considered to be in iron region as can be discerned from Figure 78.

5.6.2 Forces in the Iron Region

In this region, the EM is a sufficient distance from the PM so that the field interaction between the EM and the rotor iron is dominant, and the effect of the PM field is neglected as was illustrated in Figure 78. Moreover, the magnetic force acts on the rotor through its center of mass and tends to attract rotor toward the EM along the central axis of the EM as illustrated in the free body diagram (FBD) in Figure 82, where F_{iron} is the attractive force between the stator housing and the rotor iron, and F_{mr} and F_{ms} are the inertia forces of the rotor and stator masses respectively. The complete FBD of the rotor is shown in Figure 83

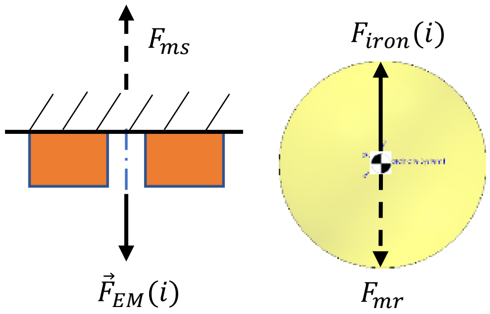

Figure 82: FBD of Forces Acting on a Single EM and Rotor

$$\vec{F}_{EM}(i) = F_{iron}(i)\frac{\vec{P}_{EM}}{r} = F_{iron}(i)\left(\frac{P_x}{r}\hat{\imath} + \frac{P_y}{r}\hat{\jmath} + \frac{P_z}{r}\hat{k}\right) = F_x\hat{\imath} + F_y\hat{\jmath} + F_z\hat{k} \qquad (125)$$

The COMSOL® simulation outputs the magnetic forces in x, y, z components, and from there the magnitude of the force is calculated off-line from the algorithm, permitting implementation of a single fit curve into the algorithm rather than a fit curve for each force component. The magnitude of the force is resolved in terms of x, y, z force components for each stator EM, simply by multiplying the magnitude of the force $F_{iron}(i)$ by the EM unit position vector $\frac{\vec{P}_{EM}}{r}$ as shown in equation (125). This result was verified by COMSOL® simulation and is discussed in Chapter 6

The forces acting on the rotor are treated as a linear combination of forces and thus may be summed to obtain the net force as given by equation (126), where n represents EMs one through six, i represents the instantaneous coil current, m_r is the mass of the rotor, and a represents rotor acceleration.

$$\sum_{n=1}^{6} \vec{F}_{EMn}\,(i_n) = \sum_{n=1}^{6} F_{xn}(i_n)\hat{\imath} + \sum_{n=1}^{6} F_{yn}\,(i_n)\hat{\jmath} + \sum_{n=1}^{6} F_{zn}\,(i_n)\hat{k} = m_r\left(a_x\hat{\imath} + a_y\hat{\jmath} + a_z\hat{k}\right) \quad (126)$$

Since the rotor and stator are fixed translationally, the resultant accelerations are zero.

$$m_r\left(a_x\hat{\imath} + a_y\hat{\jmath} + a_z\hat{k}\right) = 0 \quad (127)$$

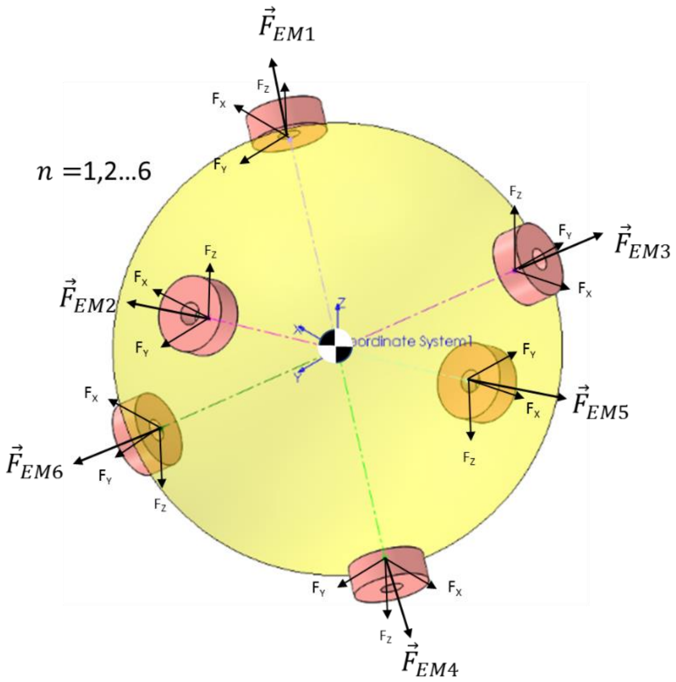

Figure 83: FBD of Magnetic Forces acting on Rotor in Iron Region

The magnitude of the magnetic force in this region is estimated by a second order polynomial fit equation which is given below and the quality of the fit and values of the coefficients a and b are shown in Figure 84. The data points in the fit curves represent the magnitude of the magnetic force the EM exerts on the iron rotor or a given current level, with the influence of the PM magnetic field excluded from the model.

$$F_{mag}(i) = F_{iron}(i) = \mathrm{a}i^{b} = 0.04082\,i^{2} \quad (128)$$

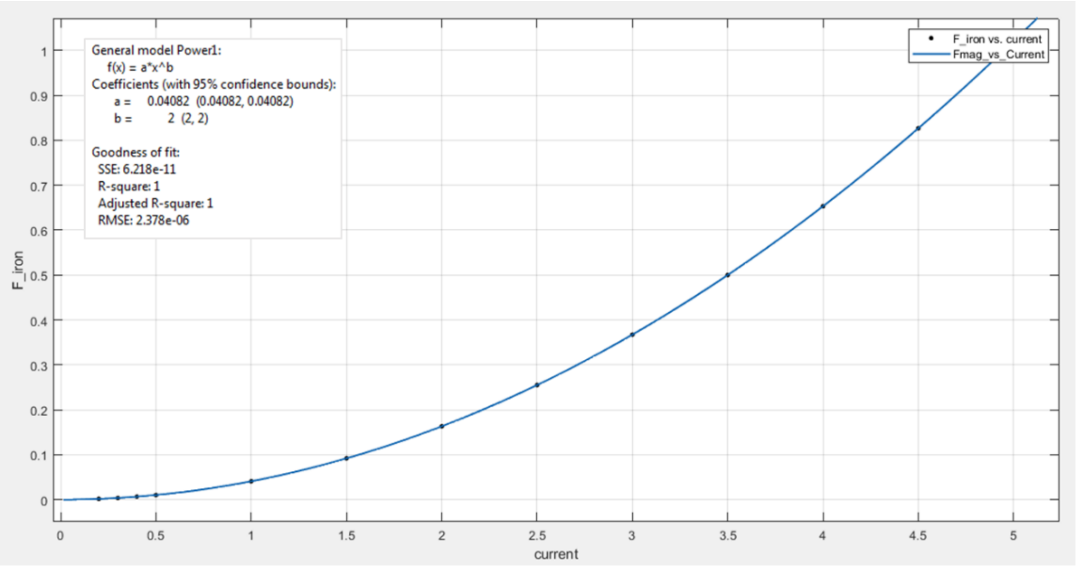

Figure 84: Fit Curve of Magnitude of Iron Only Force vs. Current

The inverse model is also evaluated so the ensuing controller can determine the appropriate current to develop the desired force. The inverse model fit curve is provided in Figure 85:

$$i\left(F_{mag}\right) = \mathrm{a}F^{b} = 4.949\, F_{mag}{}^{1/2} \tag{129}$$

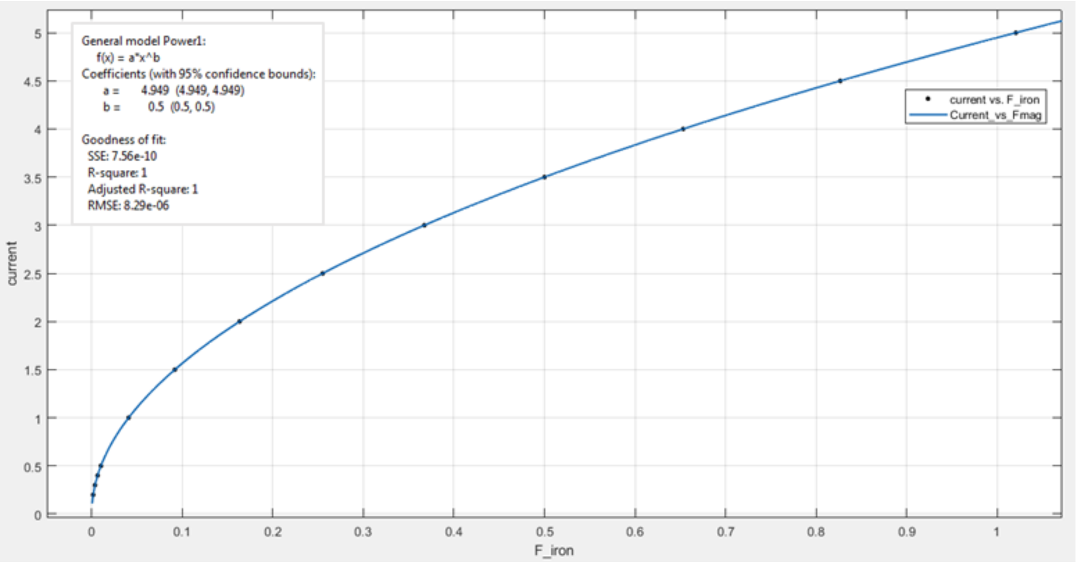

Figure 85: Fit Curve of Inverse Model: Current vs. Magnitude of Iron Only Force

5.6.3 Torque in the Iron Region

Torque in the Iron Region is equal to zero because the line of action of the resultant magnetic force induced by each EM acts through the rotor center of mass. The EM position vector and resultant force vectors are collinear as shown in Figure 86.

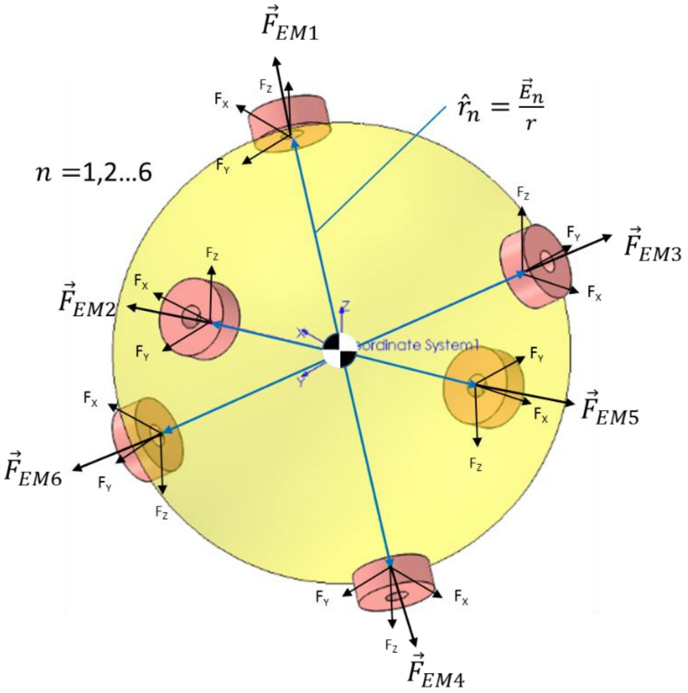

Figure 86: Evaluation of Torques in the Iron Region

This can be verified by evaluating the cross product as shown below, where $\hat{r}_n$ is the EM unit position vector, and F_{EMn} is the force exerted on the rotor by the EM, thus the sum of the torques in the iron region are zero.

$$\sum_{n=1}^{6} \vec{\tau}_n = \sum_{n=1}^{6} \hat{r}_n \times \vec{F}_{EMn} = 0 \tag{130}$$

This result is true only for a translationally fixed 3-DOF model. If the rotor is free to translate in the *x*, *y*, *z* axis this would cause the rotor center of mass to be eccentric to the line of action of the EM forces.

5.6.4 Calculation of Force in Iron + PM Region

Calculation of force in this region is more difficult because the force vector does not act through the center of mass unless the centerline of the EM and PM are coincident. Simply multiplying the magnitude of the force by the EM unit position vector by will not yield the correct resultant force. The individual force components output by the generalized (superposition) FEM model must be transformed into the correct force components for each EM. The necessary transformation is achieved by a series of coordinate frame rotations and is discussed in the subsequent paragraphs. The example and illustrations that follow consider P_{EMU2} as an example (EM position 2 in upper hemisphere of the stator), and all rotations follow the right-hand rule.

The magnetic force data was generated by rotating a single EM about the X-Axis, relative to a fixed PM, by a positive angle starting from 0 degrees (centerlines of PM and EM coincident on the Z-axis) up to 31.7175 degrees (half the distance between adjacent PM). Figure 87 shows that the axis of the EM and PM are located on the ZY Plane, and consequently, COMSOL outputs only z and y force components. However, in the RS, the EMs are fixed and the PMs rotate and can be in any position relative to the EM. Therefore, the first rotation transforms the COMSOL force vector to represent a fixed EM and a rotating PM. Rotation is about the x-axis by the angle ϕ_1 which is determined from the scalar distance between the EM and PM. The end result is the EM is coincident with the Z axis as illustrated in Figure 87.

$$\phi_1 = 2\pi - \cos^{-1}\left(-\frac{d^2 - r_{EM}^2 - r_s^2}{2r_{EM}r_s}\right) = 2\pi - \cos^{-1}\left(\frac{r_{EM}^2 + r_s^2 - d^2}{2r_{EM}r_s}\right) \tag{131}$$

The rotation matrix is:

$$[R_{x1}]\begin{bmatrix} x_1 \\ y_1 \\ z_1 \end{bmatrix} = \begin{bmatrix} 1 & 0 & 0 \\ 0 & cos(\phi_1) & -sin(\phi_1) \\ 0 & sin(\phi_1) & cos(\phi_1) \end{bmatrix}\begin{bmatrix} x_1 \\ y_1 \\ z_1 \end{bmatrix} = \begin{bmatrix} x'_1 \\ y'_1 \\ z'_1 \end{bmatrix} \tag{132}$$

And the transformed force vector $\vec{F}_{tr}$ is given by the equation below, where $\vec{F}_{sim}$ is the force vector given by COMSOL and expressed as a column vector. The effect of the rotation is illustrated in Figure 87 for an arbitrary angle ϕ_1.

$$\vec{F}_{tr} = [R_{x1}]\vec{F}_{sim} = [0 \quad F_y \quad F_z]^T \tag{133}$$

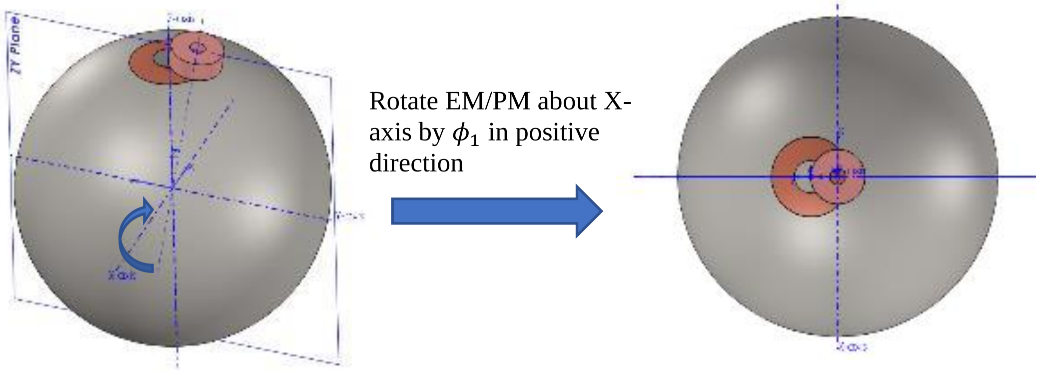

Figure 87: Transformation from Moving EM to Fixed EM with Moving PM

Next, the EM / PM pair is rotated into the stator EM coordinates. These rotations are specific to the coordinates of each EM and are fixed values. The values are given in Table 2.

Table 2: EM Rotation Angles

EM Position	**Rotation about Z-axis (radians)**	**Rotation about X-axis (radians)**
EM_{U1}	$\psi_1 = 0$	$\phi_2 = -\cos^{-1}\left(\frac{1}{\sqrt{3}}\right)$
EM_{U2}	$\psi_1 = {}^{5\pi}/_{3}$	$\phi_2 = \cos^{-1}\left(\frac{1}{\sqrt{3}}\right)$
EM_{U3}	$\psi_1 = {}^{\pi}/_{3}$	$\phi_2 = \cos^{-1}\left(\frac{1}{\sqrt{3}}\right)$
EM_{L1}	$\psi_1 = 0$	$\phi_2 = \pi - \cos^{-1}\left(\frac{1}{\sqrt{3}}\right)$
EM_{L2}	$\psi_1 = {}^{2\pi}/_{3}$	$\phi_2 = \pi - \cos^{-1}\left(\frac{1}{\sqrt{3}}\right)$
EM_{L3}	$\psi_1 = {}^{4\pi}/_{3}$	$\phi_2 = \pi - \cos^{-1}\left(\frac{1}{\sqrt{3}}\right)$

The rotation matrix for the Z-axis rotation is:

$$[R_{z1}]\begin{bmatrix}x_1\\y_1\\z_1\end{bmatrix}=\begin{bmatrix}cos(\psi_1) & -sin(\psi_1) & 0\\ sin(\psi_1) & cos(\psi_1) & 0\\ 0 & 0 & 1\end{bmatrix}\begin{bmatrix}x_1\\y_1\\z_1\end{bmatrix}=\begin{bmatrix}x'_1\\y'_1\\z'_1\end{bmatrix} \tag{134}$$

And the rotation matrix for the subsequent X-axis rotation is:

$$[R_{x2}]\begin{bmatrix}x'_1\\y'_1\\z'_1\end{bmatrix}=\begin{bmatrix}1 & 0 & 0\\ 0 & cos(\phi_2) & -sin(\phi_2)\\ 0 & sin(\phi_2) & cos(\phi_2)\end{bmatrix}\begin{bmatrix}x'_1\\y'_1\\z'_1\end{bmatrix}=\begin{bmatrix}x''_1\\y''_1\\z''_1\end{bmatrix} \tag{135}$$

The resulting orientation of the EM and PM is shown in Figure 88. The rotated PM position vector still does not align with the instantaneous PM position vector. Another rotation must be applied to align the PM position vectors.

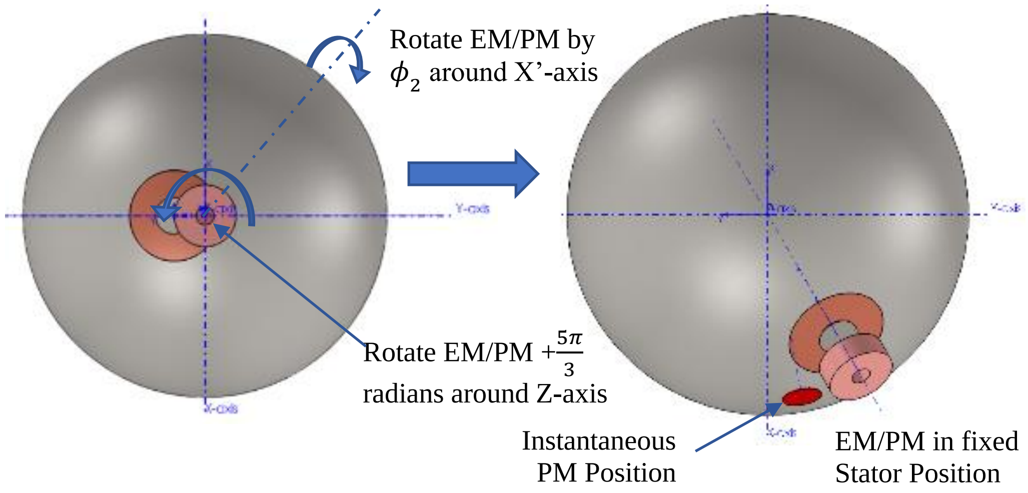

Figure 88: Rotation from COMSOL Coordinates to Stator Coordinates (EM_{U2})

The necessary rotation angle ψ_2 is obtained by pre-multiplying the instantaneous PM position vector by the inverse matrix, which for a rotation matrix is simply the transpose.

$$([R_{Z1}][R_{x2}])^{-1}\,\vec{P}_{PM}=([R_{Z1}][R_{x2}])^{T}\,\vec{P}_{PM} \tag{136}$$

Note that R_{Z1} and R_{x2} are proper rotation matrices and therefore have a determinant equal to one, and is verified by computing the determinants of the rotation matrices for the angles listed in Table 2. And because the determinants of R_{Z1} and R_{x2} are non-zero, both matrices are invertible (Strang, 1980).

This transforms the instantaneous PM position vector into the COMSOL® simulation coordinate frame. From there, the rotation angle ψ_2 is determined from the arctangent of the x, y components of the simulation PM position denoted by subscript s, and the instantaneous PM position denoted by subscript i rotated into original coordinate system. The angles are measured from the positive X-axis as shown in Figure 89. The MATLAB® code utilizes the *atan2* function to calculate the angle for two reasons. Firstly, it has the capability to identify the quadrant for the inverse tangent, and secondly it increases the computation efficiency.

$$\psi_s = atan_2(y_s, x_s) \tag{137}$$

$$\psi_i = atan_2(y_i, x_i) \tag{138}$$

$$\psi_2 = \psi_s - \psi_i \tag{139}$$

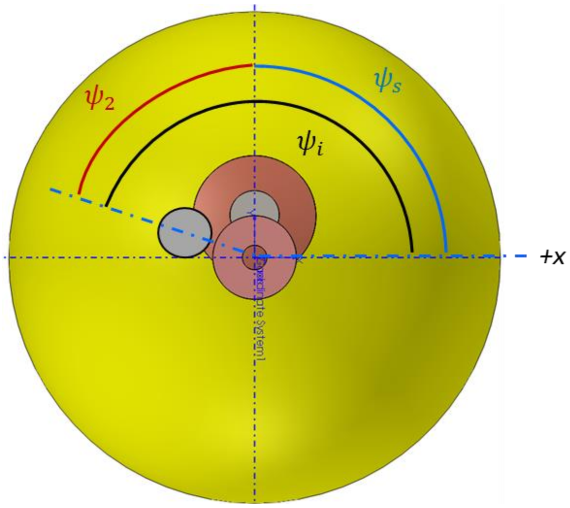

Figure 89: Determination of Final Transformation Rotation Angle

The final rotation matrix is given below:

$$[R_{z2}]\begin{bmatrix}x''_1\\y''_1\\z''_1\end{bmatrix}=\begin{bmatrix}cos(\psi_2) & -sin(\psi_2) & 0\\sin(\psi_2) & cos(\psi_2) & 0\\0 & 0 & 1\end{bmatrix}\begin{bmatrix}x''_1\\y''_1\\z''_1\end{bmatrix}=\begin{bmatrix}x\\y\\z\end{bmatrix} \tag{140}$$

Finally, the transformed force components for any arbitrary orientation of the PM relative to each EM can be determined by pre-multiplying the force vector $\vec{F}_{tr}$ by the rotation matrices in the order in which the rotations were applied, as shown in the equation below. The resulting force vector $\vec{F}_{EM}$ is expressed as a column vector for each EM with a PM within the threshold distance.

$$\vec{F}_{EM}=[R_{Z1}][R_{x2}][R_{Z2}]\,\vec{F}_{tr} \tag{141}$$

The transformations presented in this section were validated for each EM position by performing COMSOL® simulations, the results of which are discussed in Section 6.2.

The y and z components of the magnetic forces in the Iron + PM region are functions of both current and the distance between the EM and PM. The forces are estimated by a fifth order polynomial in the distance dependent variable and a second order polynomial in the current dependent variable and are of the form given by equation (130). A high-quality fit could not be achieved over the full range of distance, so two plots were created by dividing the distance in half. The y-components of force plotted in Figure 90 and Figure 91, and the z-components are plotted in Figure 92 and Figure 93.

$$\vec{F}_{y,z}(d,i)=p_0+p_1d+p_2i+p_3d^2+p_4di+p_5y^2+p_6x^3+p_7d^2i+p_8di^2+ \\ p_9d^4+p_{10}d^3i+p_{11}d^2i^2+p_{12}d^5+p_{13}d^4i+p_{14}d^3i^2 \tag{142}$$

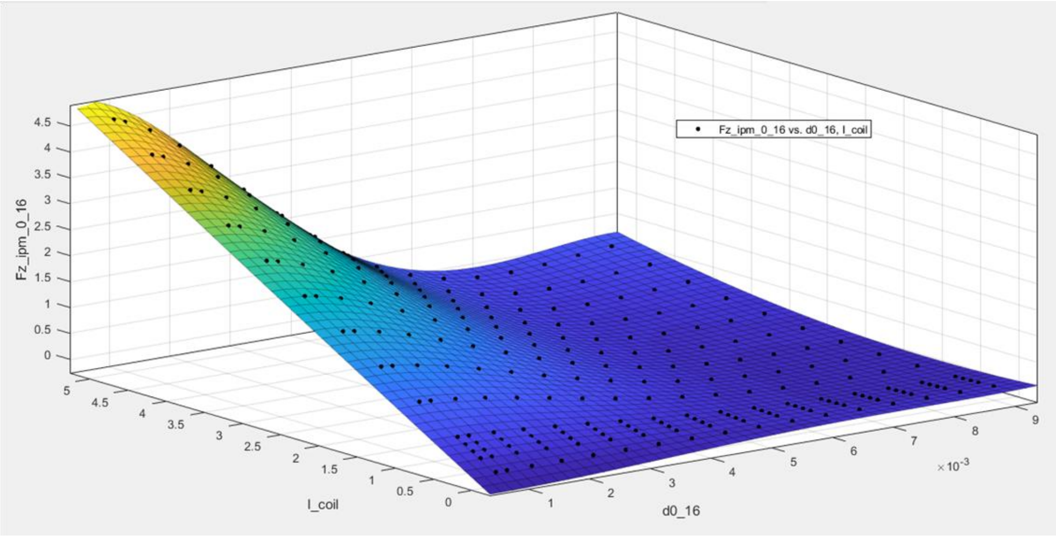

Figure 90: Y Component of Lorentz Force vs Current vs Distance: Iron + PM Region

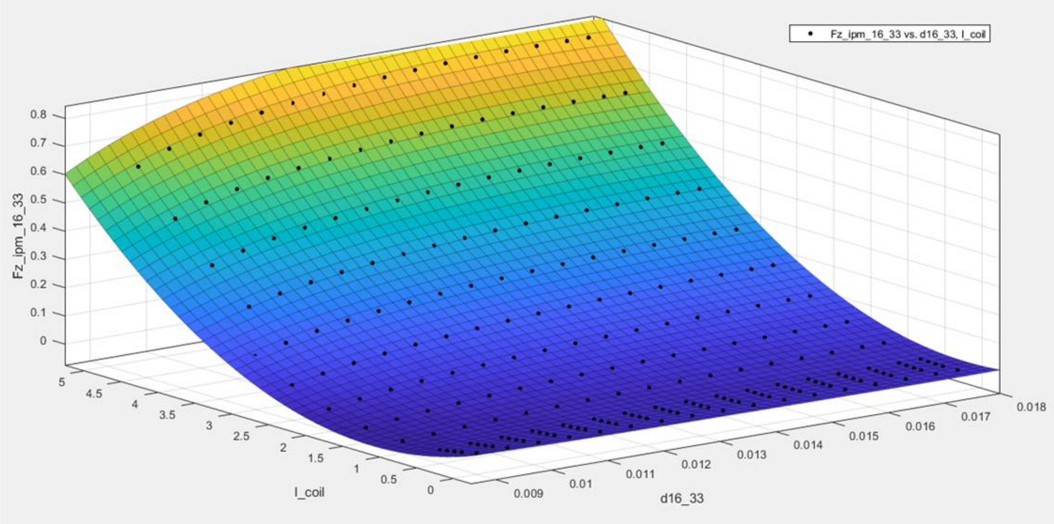

Figure 91: Y Component of Lorentz Force vs Current vs Distance: Iron + PM Region

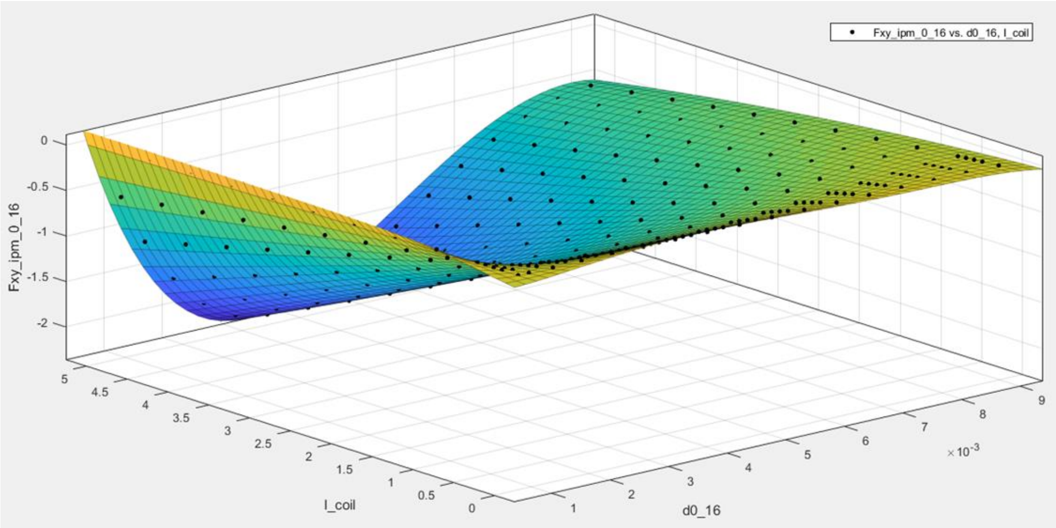

Figure 92: Z Component of Lorentz Force vs Current vs Distance: Iron + PM Region

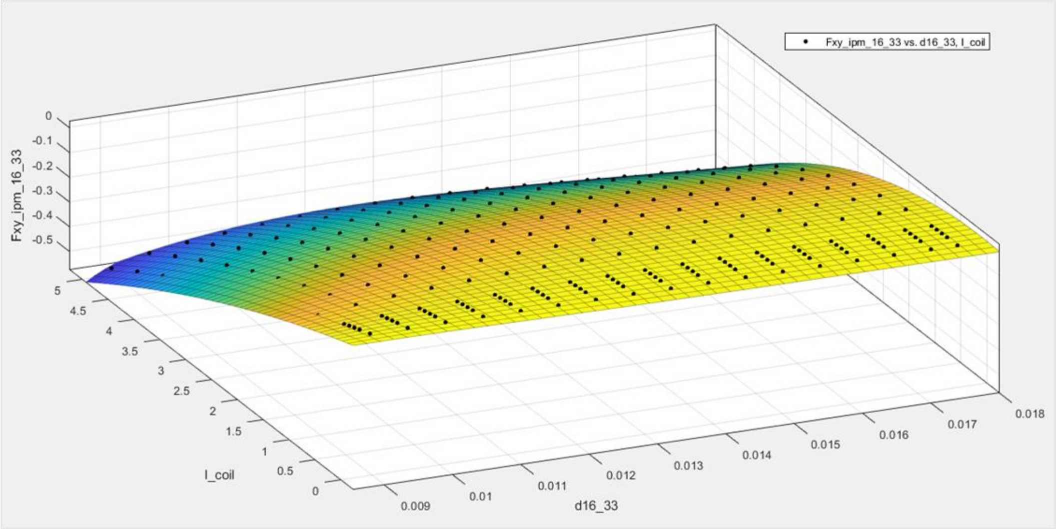

Figure 93: Z Component of Lorentz Force vs Current vs Distance: Iron + PM Region

The inverse models are also evaluated so the ensuing controller can determine the appropriate current level to develop the desired force for a given distance. The inverse relations were determined by symbolically solving equation (130) in terms of the current. The symbolic solver output two possible solutions. The correct solution is identified by inputting validation data into both equations and comparing against the current value associated with the distance and force input into the equation. The raw data, residuals plots, and the equations of the surfaces are provided in Appendix B.

5.6.5 Torque in the Iron + PM Region

Torque in the Iron + PM region is not zero because the line of action of the magnetic forces do not act through the rotor center of mass. The total external torques acting on the rotor, due to the magnetic forces, is given below in terms of basis vectors of the body-fixed stator coordinate system, where $\vec{r}$ is the position vector of the PM.

$$\sum_{n=1}^{6} \vec{\tau}_n = \sum_{n=1}^{6} \left(\vec{r}_n \times \vec{F}_n\right) = \begin{bmatrix} \hat{\boldsymbol{\imath}} & \hat{\boldsymbol{\jmath}} & \widehat{\boldsymbol{k}} \\ r_{xn} & r_{yn} & r_{zn} \\ F_{xn} & F_{yn} & F_{zn} \end{bmatrix} \tag{143}$$

$$\sum_{n=1}^{6} \vec{\tau}_n = \sum_{n=1}^{6} \left(r_{yn}F_{zn} - r_{zn}F_{yn}\right) \hat{\boldsymbol{\imath}} - \sum_{n=1}^{6} (r_{xn}F_{zn} - r_{zn}F_{xn})\, \hat{\boldsymbol{\jmath}} + \sum_{n=1}^{6} \left(r_{xn}F_{yn} - r_{yn}F_{xn}\right) \widehat{\boldsymbol{k}} \tag{144}$$

The torques are only summed for the EM-PM pairs that are within the Iron + PM region as defined in Section 5.6.4. If the EM-PM pair is within the Iron region, then the torque is equal to zero for the reasons discussed in Section 5.6.3. Note that as discussed in section 5.5.10, the forces calculated by COMSOL® represent the total force acting on a domain, and a singular value of r, representing perpendicular distance to the line of action for the total force, cannot be obtained from the model. As a consequence of this, the point of action of the total force is considered to coincide with the PM position vector, and the moment arm $\vec{r}$ is the position vector of the PM.

5.7 Equations of Motion

5.7.1 Mass Moment of Inertia

The inertial properties of a rigid body can be characterized by an inertia tensor of the rotor moment and products of inertia as shown below (Hibbeler, 2007).

$$I_{rotor} = \begin{bmatrix} I_{xx} & -I_{xy} & -I_{xz} \\ -I_{yx} & I_{yy} & -I_{yz} \\ -I_{zy} & -I_{zy} & I_{zz} \end{bmatrix} \tag{145}$$

And, in the case of a homogenous sphere with its center of mass located at the origin of the reference frame axes, the *y*-*z*, *x*-*z*, and *x*-*y* planes are all planes of symmetry. Therefore, all of the products of inertia are zero ($I_{xy} = I_{yx} = I_{xz} = I_{zx} = I_{yz} = I_{zy} = 0$) (Hibbeler, 2007) and the inertia tensor is reduced to the principal moments of inertia, where $I_{xx} = I_x,\ I_{yy} = I_y,\ I_{zz} = I_z$.

$$I_{rotor} = \begin{bmatrix} I_x & 0 & 0 \\ 0 & I_y & 0 \\ 0 & 0 & I_z \end{bmatrix} \tag{146}$$

The principal moments of inertia are all equal for a homogeneous sphere ($I_x = I_y = I_z$), and are calculated below for an iron sphere of a radius equal to 0.03175m, or 1.25 inches.

$$\begin{aligned} I_s = \frac{2}{5} m_s {r_s}^2 &= \frac{2}{5}(1.0551022\ kg) \cdot (0.03175m)^2 \\ &= 4.2544 \cdot 10^{-4}\ kg \cdot m^2 \end{aligned} \tag{147}$$

The NGCRS rotor assembly is a composite body comprising an iron rotor, copper (or polymer) inserts, and PMs, and so is not perfectly symmetrical or homogenous. However, its principle moments of inertia are closely approximated by that of the homogenous sphere. This is verified by computing the inertia tensor using Solidworks® version 2015, in terms of the coordinate system used to derive the PM position vectors.

$$I_{rotor} = \begin{bmatrix} 4.3945 \cdot 10^{-4} & -1.0542 \cdot 10^{-13} & -5.3007 \cdot 10^{-12} \\ -1.0542 \cdot 10^{-13} & 4.3945 \cdot 10^{-4} & 2.5688 \cdot 10^{-13} \\ -5.3007 \cdot 10^{-12} & 2.5688 \cdot 10^{-13} & 4.3945 \cdot 10^{-4} \end{bmatrix} kg \cdot m^2 \tag{148}$$

The principal moments of inertia of the rotor assembly calculated using Solidworks® version 2015 are provided below. Comparison of the results homogeneous sphere and the NGCRS rotor assembly are in close agreement (≈ 3.2% difference). The Simulink® dynamic model use the values calculated by Solidworks®.

$$I_{rotor} = \begin{bmatrix} I_x & 0 & 0 \\ 0 & I_y & 0 \\ 0 & 0 & I_z \end{bmatrix} = \begin{bmatrix} 4.3945 \cdot 10^{-4} & 0 & 0 \\ 0 & 4.3945 \cdot 10^{-4} & 0 \\ 0 & 0 & 4.3945 \cdot 10^{-4} \end{bmatrix} kg \cdot m^2 \tag{149}$$

The inertia tensor above assumes a uniform density throughout the sphere. If the density is not uniform, then the inertias along the principal axes are not equal.

5.7.2 Euler Equations of Motion

The motion of the rotor assembly is considered as rigid body motion. A body-fixed reference frame (X, Y, Z) is defined with its origin located at the center of mass of the RS. The orientation is as described in Section 5.4. The motion of the rotor is considered using fixed body axes, with the xyz axes oriented along the principal axes of the rotor. Using this arrangement, the products of inertia will be zero (Greenwood, 2003). The equations of motion for the body-fixed frame are given below, and are known as the Euler equations of motion because they were first formulated by the mathematician Leonhard Euler in the 18th century. These equations are a set of three first-order, non-linear, coupled set of differential equations. Note, however, that if the inertias along the principal axis are equal, the second term on the right-hand side of each equation vanishes, and the equations reduce to a set of second order ordinary differential equations. If the principal moments of inertia are not equal, then the non-linear set of equations would need to be analyzed carefully to study the existence of solutions.

$$\tau_x = I_x \dot{\omega}_x + \left(I_z - I_y\right)\omega_y \omega_z \tag{150}$$

$$\tau_y = I_y \dot{\omega}_y + (I_x - I_z)\omega_z \omega_x \tag{151}$$

$$\tau_z = I_z \dot{\omega}_z + \left(I_y - I_x\right)\omega_x \omega_y \tag{152}$$

The body-axes components of the externally applied moments τ_x, τ_y, τ_z are calculated using the force and torque relations presented in Section 5.6. The angular velocity components (ω) are obtained by integrating the differential equations with respect to time, the Euler angle rates are then obtained from the angular velocity components using the kinematic relations defined in Section 5.4.2, and the Euler angles (orientation) of the rotor is obtained by integrating the Euler angle rates with respect to time. These calculations are performed in the Simulink® model.

5.8 Simulink Model

The dynamics of the reactions sphere are implemented in a MATLAB Simulink® model using the relations and methods presented herein.

5.8.1 Electromagnet Model

Each levitation electromagnet is modeled in Simulink® using the relations presented in Section 5.1.2, and both the inductance and resistance values are considered constant in this model. The EM parameters are listed in Table 3, and the Simulink model of the EM is shown in Figure 94. The resistance listed in the table was approximated using the relation below, where R_i is the nominal ohmic resistance per inch of 32 AWG copper wire (ANSI NEMA 1000-2011, 2011), N is the number of turns, and d_m is the mean diameter of the coil.

$$R = R_i N \pi d_m = \frac{0.013675\ ohm}{in} 360 \cdot \pi \cdot 0.2858 in = 4.419 \text{ ohms} \tag{153}$$

The approximated coil resistance is in close agreement with the value of 4.276 ohms predicted by COMSOL®. The values predicted by COMSOL® are used in the Simulink® model. The EM is modeled using equation (33). The applicable modeling parameters are listed in Table 3.

Table 3: Solenoid Modeling Parameters

Parameter	Value	Units
L	$5.271 \cdot 10^{-4}$	Henries
N	360	turns
l_c	$4.318 \cdot 10^{-3}$	m
r_m	$3.630 \cdot 10^{-3}$	m
r_o	$5.715 \cdot 10^{-3}$	m
r_i	$1.524 \cdot 10^{-3}$	m
R	4.276	Ohms

The input into the EM is voltage and the output is current. The model presented herein uses a step function for the voltage, but in future implementations the controller algorithm will provide the excitation signals.

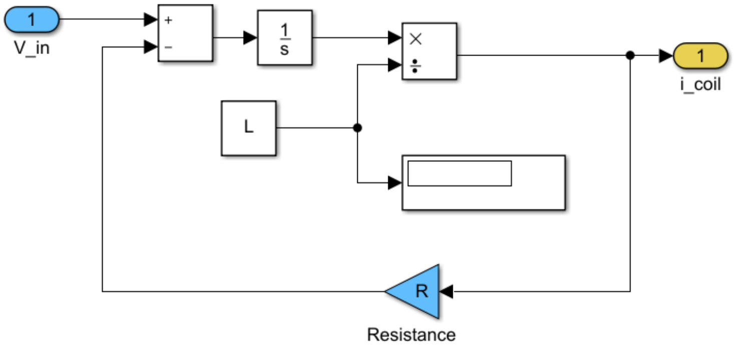

Figure 94: Simulink Electromagnet Model

5.8.2 Reaction Sphere Model

The instantaneous EM currents and the instantaneous Euler angles are inputs into the reaction sphere model. The forces and torques acting on the reaction sphere are computed using the force and torque relations described in Section 5.6 and the motion of the rotor is modeled using the equations of motion presented in Section 5.7. The force and torque relations are integrated in a MATLAB® Level 2 S-function. The source code for the S-function is provided in Appendix D.

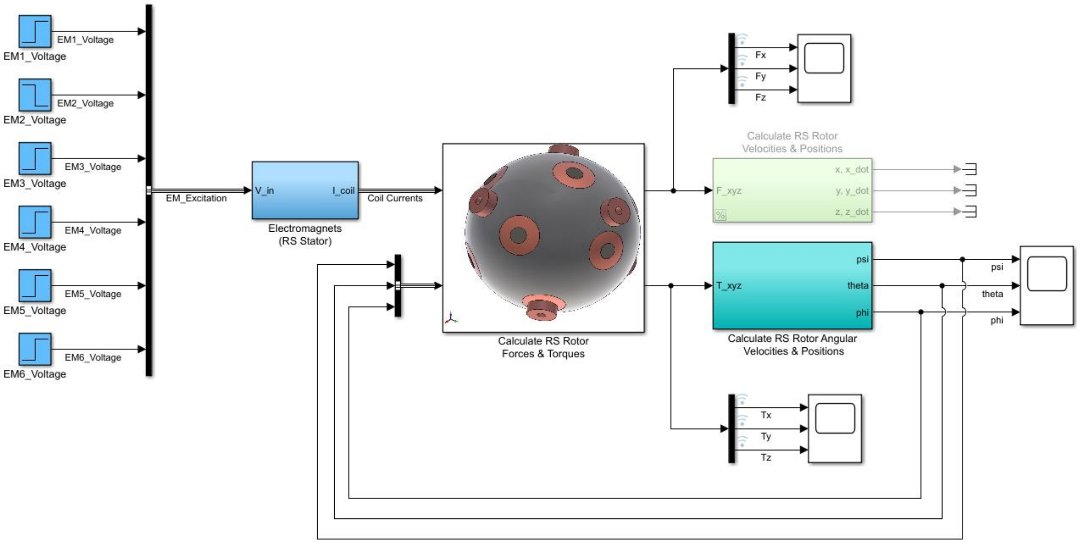

Figure 95: 3 DOF Simulink Reaction Sphere Model

Plots of the force and torque outputs are provided in the figures below. Figure 96 shows the force and torque output by the model with one EM active within the iron-only region. As expected, the force is constant and no torque is applied to the rotor and no rotation occurs.

Figure 97 shows a plot of the model output for 1 EM located in the excited with 5 amperes Force, Torque and Angular Velocity for 1 EM initially positioned in the Iron-Only region and 1 EM initially positioned in the iron + PM Region. As expected, the force is constant when the active EM-PM pairs are in the iron region and force changes with the distance between the EM-PM pairs in the iron + PM region and torque is applied.

And Figure 98 shows the system response to all 6 EMs energized and de-energized at random times and varying levels of current. The plots illustrate the complex behavior of the system.

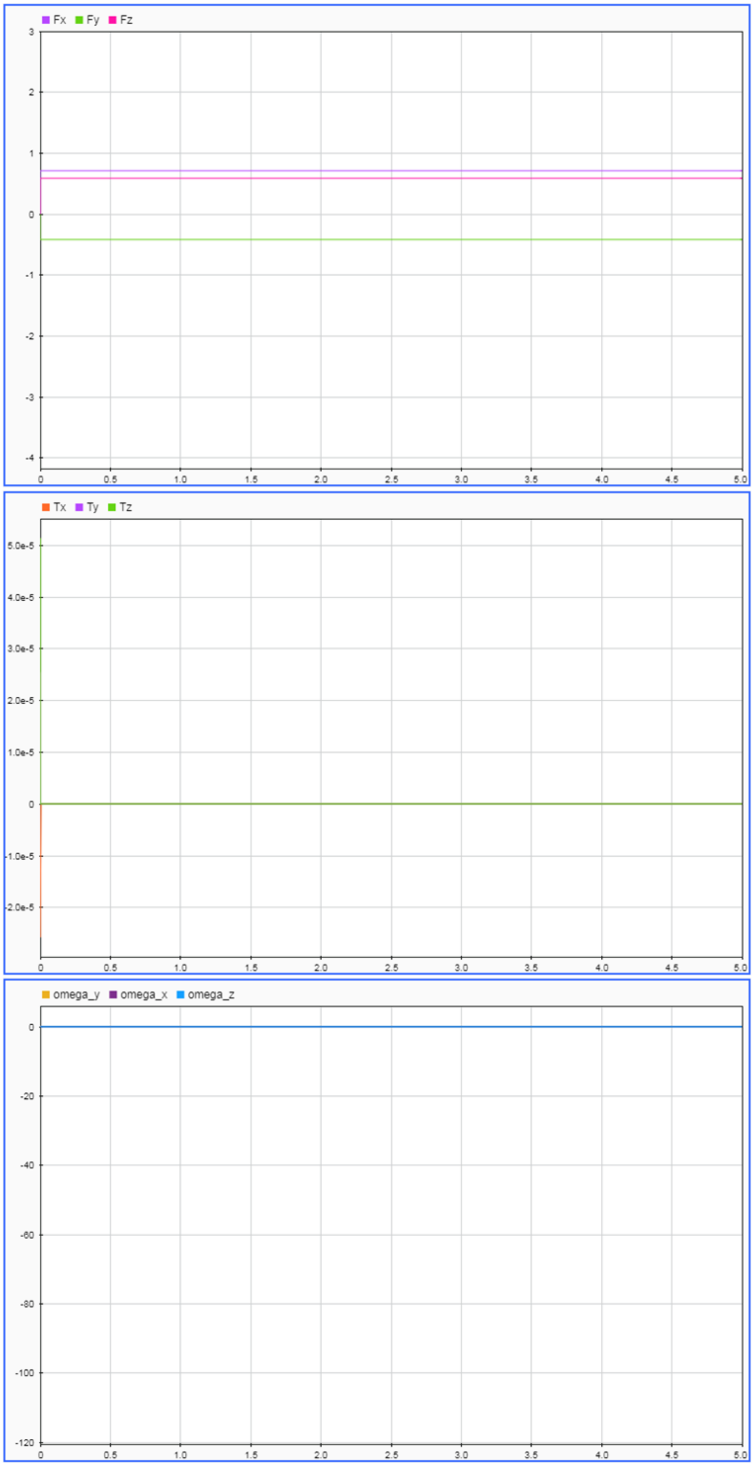

Figure 96: Model Force, Torque and Angular Velocities for 1 EM in Iron-Only Region

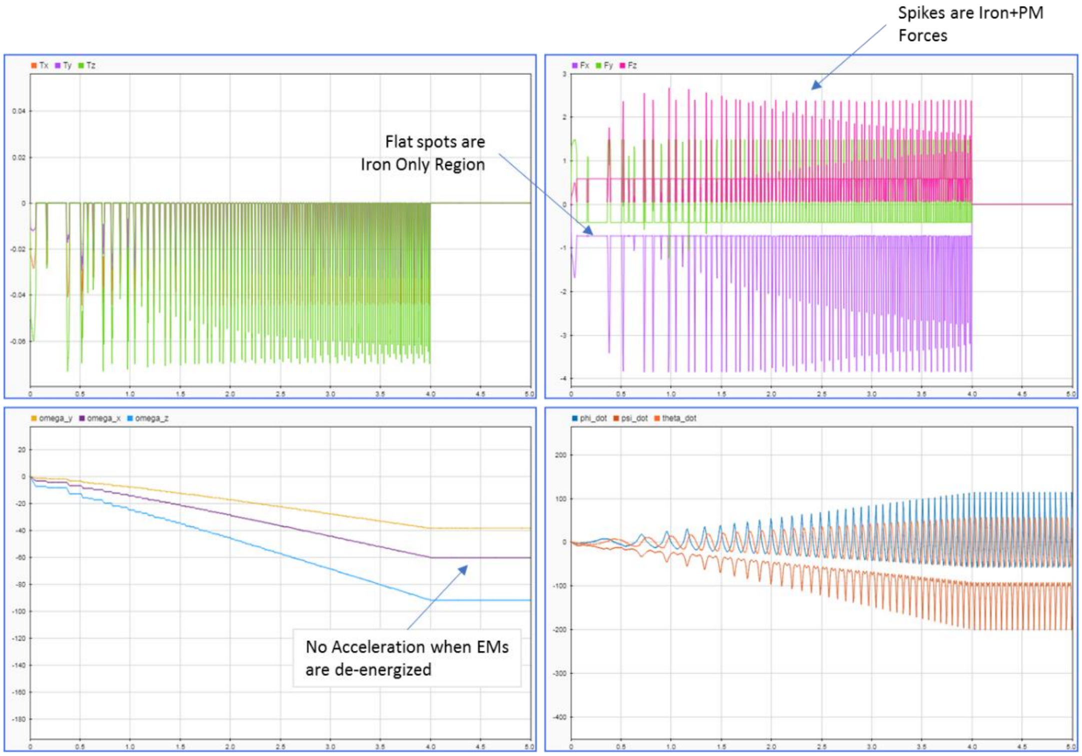
Spikes are Iron+PM Forces

Flat spots are Iron Only Region

No Acceleration when EMs are de-energized

Figure 97: Force, Torque and Angular Velocity for 1 EM in Iron-Only and 1 EM in Iron + PM Region

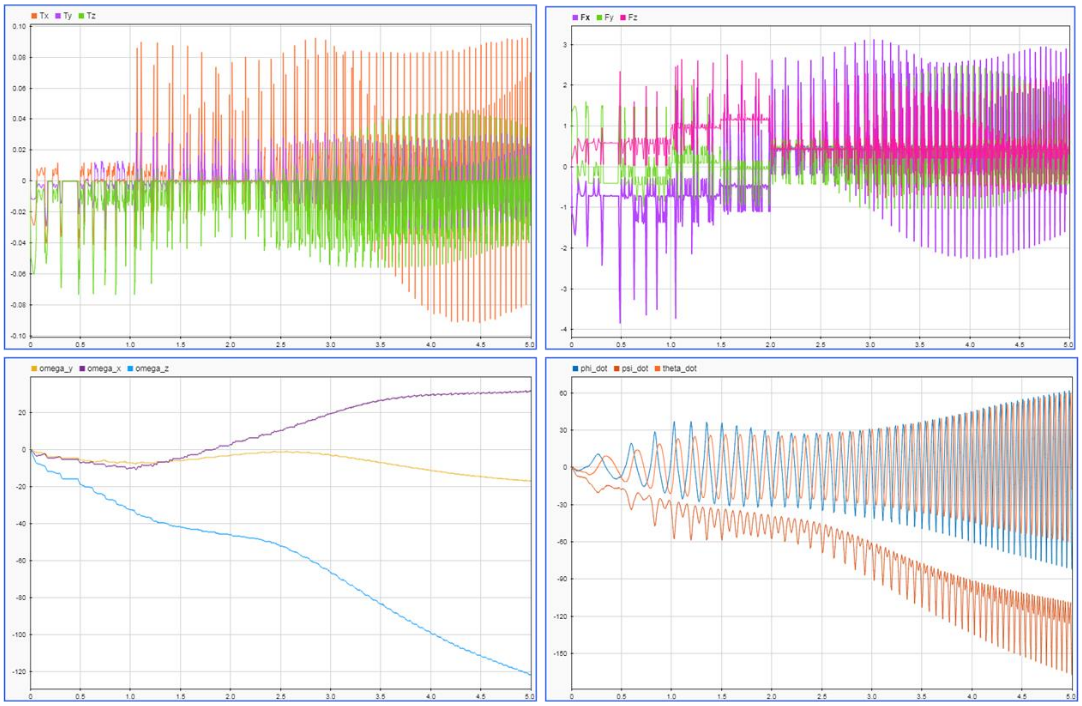

Figure 98: Model Output for all 6 EMs Activated and De-energized Randomly

Chapter 6 Testing and Model Validation

6.1 Validation of Magnetic Forces

The scope of thesis project precluded the fabrication of a prototype for model verification. In lieu of this, the forces predicted by COMSOL® FEM model were compared against the forces predicted by an analytical model which treated the EM and PM as a magnetic dipole pair. The analytical approach is described in the subsequent paragraphs and includes comparisons of magnetic forces predicted by the FEM models.

6.1.1 Magnetic Dipoles

The magnetic forces predicted by the FEM model were compared against forces computed from an analytic model of the PM and EM treated as magnetic dipoles. The formula for the force between two closed circuits is given by equation (154) where μ_0 is the magnetic constant, equal to $4\pi 10^{-7}\, N/A^{-2}$, I_E the current of circuit E, I_P the current of circuit P, $\vec{d}_E$ the path increment vector along the circuit representing the EM, $\vec{d}_P$ the path increment vector along the circuit representing the PM, and $\vec{R}$ is the vector from circuit path element $\vec{d}_P$ to circuit path element $\vec{d}_E$ (Lorrain, et al., 1988).

$$\vec{F}_{PE} = \frac{\mu_0}{4\pi} I_P I_E \oint_P \oint_E \frac{\vec{d}_E \times \left(\vec{d}_P \times \vec{R}\right)}{R^3} \tag{154}$$

Yung et. al, 1998, derived the expression for the force $\vec{F}_{PE}$ of a magnetic dipole pair given by equation (155), where r is the magnitude of the separation distance, $\hat{r}$ is the unit separation vector, $\vec{m}_E$ and $\vec{m}_P$ are the magnetic dipole moment vectors of the EM and PM, respectively. Note that equation (155) provides the force of the PM acting on the EM, however it can be re-arranged to provide the force the EM exerts on the PM. The first term of the equation (on the left side of the minus sign) represents the component of force parallel to each dipole moment vector, while the second term (on right hand side of minus sign) represents the component of force projected on the separation vector $\hat{r}$ (Yung, et al., 1998).

$$\vec{F}_{PE} = \frac{3\mu_0}{4\pi r^4}\big((\hat{r}\times\vec{m}_P)\times\vec{m}_E + (\hat{r}\times\vec{m}_E)\times\vec{m}_P - 2\hat{r}(\vec{m}_P\cdot\vec{m}_E) + 5\hat{r}((\hat{r}\times\vec{m}_P)\cdot(\hat{r}\times\vec{m}_E))\big) \tag{155}$$

The magnetic dipoles are considered as circular circuits with planar surface area, where the dipole moment vector $\vec{m}$ is normal to the surface area. The geometry of a generic magnetic dipole is shown in Figure 99.

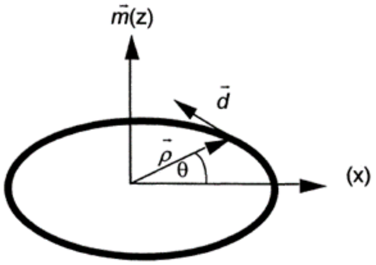

Figure 99: Geometry of a Magnetic Dipole Moment Circuit (Yung, 1998)

The expression for an electrical circuit represented as a magnetic dipole is given by equation (156), where m is the magnitude of the magnetic moment, $\hat{m}$ is the unit vector in the direction of the dipole, $\hat{\rho}$ is the directional unit vector from origin to position of $\hat{d}$ the path increment unit vector which is tangent to the circle, I_e is the electrical current in the circuit, and N is the number of turns. The cross product of these two vectors results in a magnetic moment vector normal to the planar circuit and located at its center (Young, et al., 1998). Note that in this analysis, the EM dipole vector is rotated about the x-axis in the same manner as the FEM model.

$$\begin{gathered}\vec{m}_E = m_E\hat{m}_E = (NI_E\pi\rho^2)\big(\hat{\rho}\times\hat{d}\big) \\ \vec{m}_E = NI_E\pi\big(r_o^2 - r_i^2\big)[0 \quad sin(2\pi-\theta) \quad cos(2\pi-\theta)]\end{gathered} \tag{156}$$

The expression for the magnetic dipole of a PM is given by equation (157), where M is the magnetization of the PM, V is the volume of the cylindrical PM, A_p is the sectional area of the PM and L_p is the length of the PM. The position of the PM is fixed along the z-axis so its magnetic moment unit vector is simply one in the z-coordinate.

$$\vec{m}_P = m_P\hat{m}_P = (MV)\left(\hat{\rho}\times\hat{d}\right) = \left(MA_pL_p\right)[0 \quad 0 \quad 1] \tag{157}$$

The magnetization of the PM was determined from the remnant flux density and magnetization relations given in equation (158). The external field due to the EM is small relative to the magnetization of the PM and is therefore neglected to simplify the analysis. The magnetization of the PM is obtained from the Arnold Magnetics® data sheet for an N52 PM, and is set equal to the intrinsic coercivity value of 875,000 A/m. The dipole moments are located on the plane that bisects the lengths of the PM and EM as shown in Figure 100.

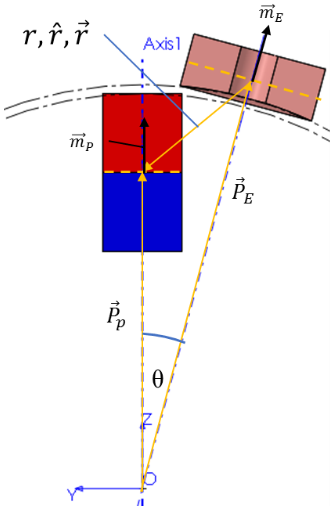

Figure 100: Location of EM Dipole Moment

Therefore, the scalar distance between the dipole centers can be obtained by equation (158).

$$r = \left\|\vec{P}_E - \vec{P}_P\right\| = \sqrt{(P_{Ex} - P_{Mx})^2 + \left(P_{Ey} - P_{My}\right)^2 + (P_{Ez} - P_{Mz})^2} \tag{158}$$

The directional vector $\vec{r}$ from the EM and PM dipole centers is obtained from vector subtraction:

$$\vec{r} = \vec{P}_E - \vec{P}_P \tag{159}$$

The unit vector $\hat{r}$ is the unit vector along $\vec{r}$ is obtained by:

$$\hat{r} = \frac{\vec{r}}{r} = \frac{\vec{P}_E - \vec{P}_P}{\left\|\vec{P}_E - \vec{P}_P\right\|} \tag{160}$$

The generalized RS modeled as two magnetic dipole moments is shown in Figure 101. The foregoing relations were input into MATLAB® and the magnetic forces computed for varying current levels and angular distances (θ). The forces were compared against the forces predicted by COMSOL® and showed close agreement.

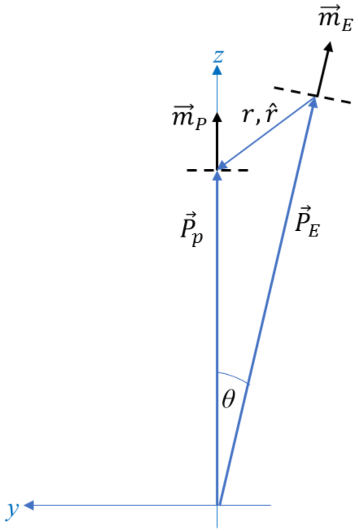

Figure 101: Magnetic Dipole Moment Model of Generalized RS

Figure 102 compares the magnitude of magnetic forces as a function of angular distance for the COMSOL and Magnetic Dipole analytic model. Similarly, Figure 103 compares the y and z components of force. The plots show that the forces predicted by the magnetic dipole analysis trend with the COMSOL values fairly closely, but the dipole method overpredicted the forces. The MATLAB script used to calculate the forces between the two magnetic dipoles is provided in Appendix E.

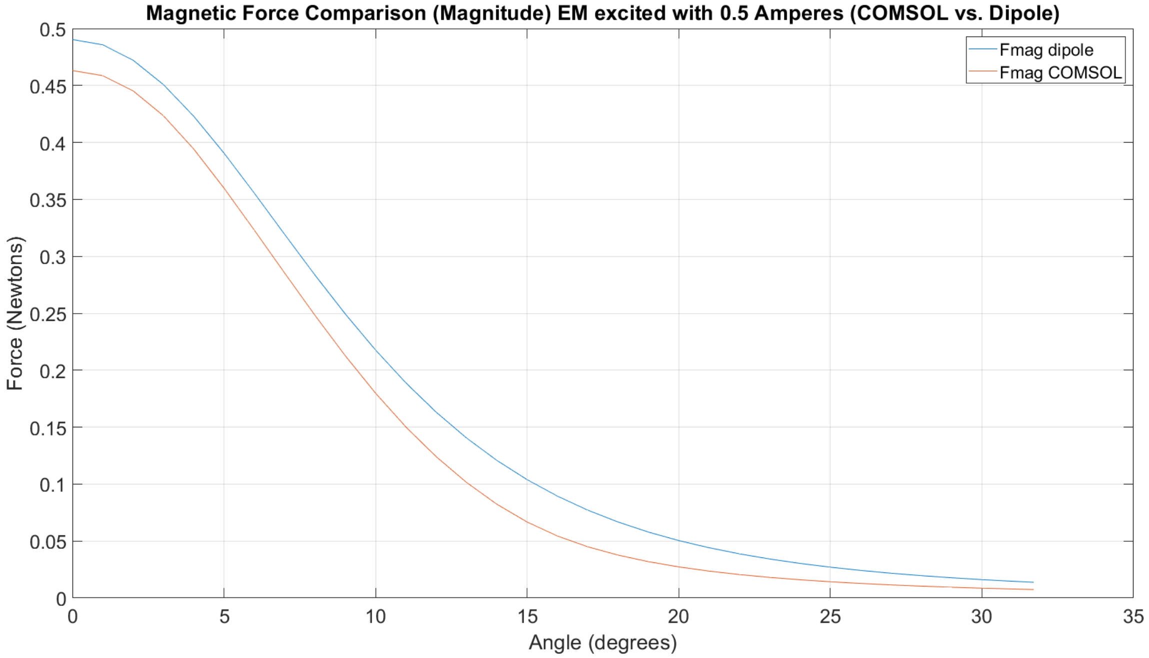

Figure 102: Magnitude of Magnetic Force: COMSOL vs. Dipole Moment (0.5 Amp)

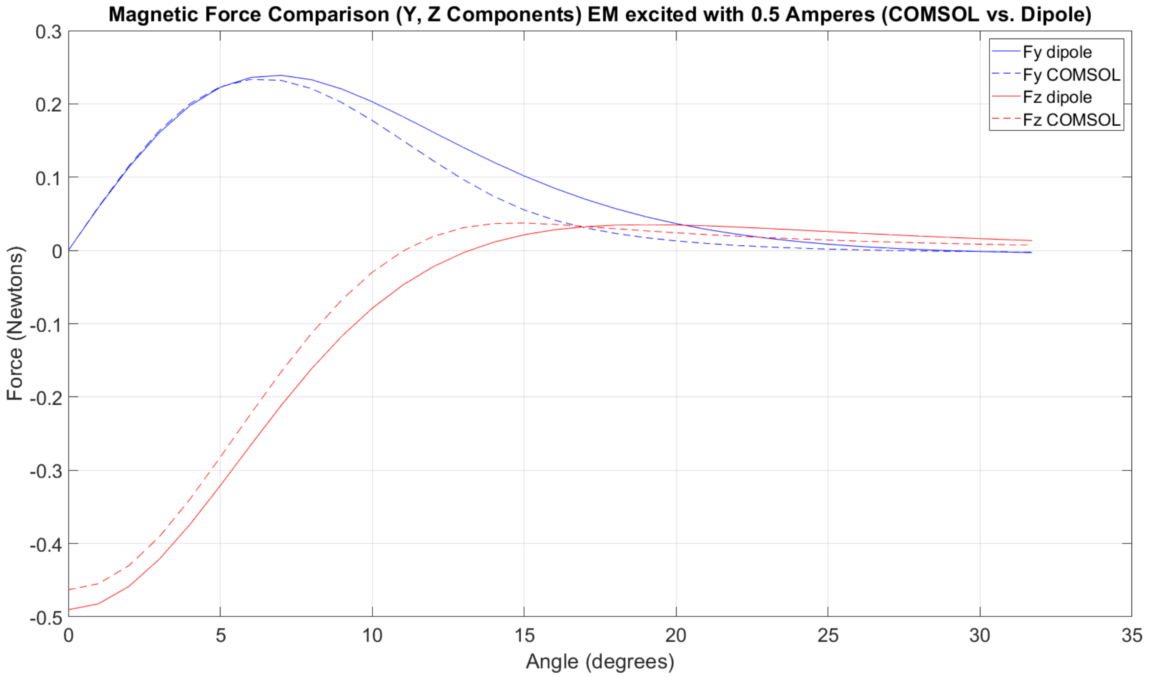

Figure 103: Y, Z Comp. of Magnetic Force: COMSOL vs. Dipole Moment (0.5 Amp)

Additional simulations were performed using COMSOL® and FEMM 4.2 to further assess the magnetic dipole analysis. Simulations were performed for the 0.5-inch-long PM in the RS coordinates (no shift) and for distances between the EM and PM of 0.25-inch to a 1-inch in 0.25-inch increments. The centerline of the EM and PM were coincident and the angle between them was not changed. The angle could not be altered because FEMM 4.2 is only capable of solving axisymmetric problems in 3-dimensions. The problem setup is illustrated in Figure 104.

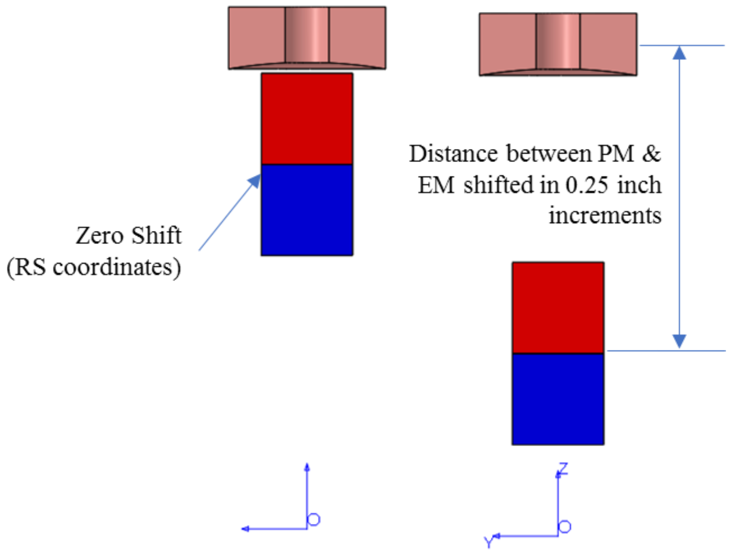

Figure 104: Configuration of EM / PM for Magnetic Dipole Simulations

The forces predicted by each model are presented in Figure 105 and are scaled against the forces predicted by COMSOL®. The COMSOL® and FEMM 4.2 models showed close and consistent agreement for the different configurations, however, the dipole calculation increased in error as the distance increased.

An article by Y. Zhang, et.al, 2020 assessed the accuracy of magnetic force calculations between PMs with various geometries using magnetic charge, magnetizing current, and magnetic dipole methods. They found that the magnetic dipole method was the least accurate for the distances they tested, with the exception of the spherical PMs, which agreed closely with measurements. Future work should investigate the methods discussed by Zhang, et al., or derive an analytical model using the Lorentz Force Law.

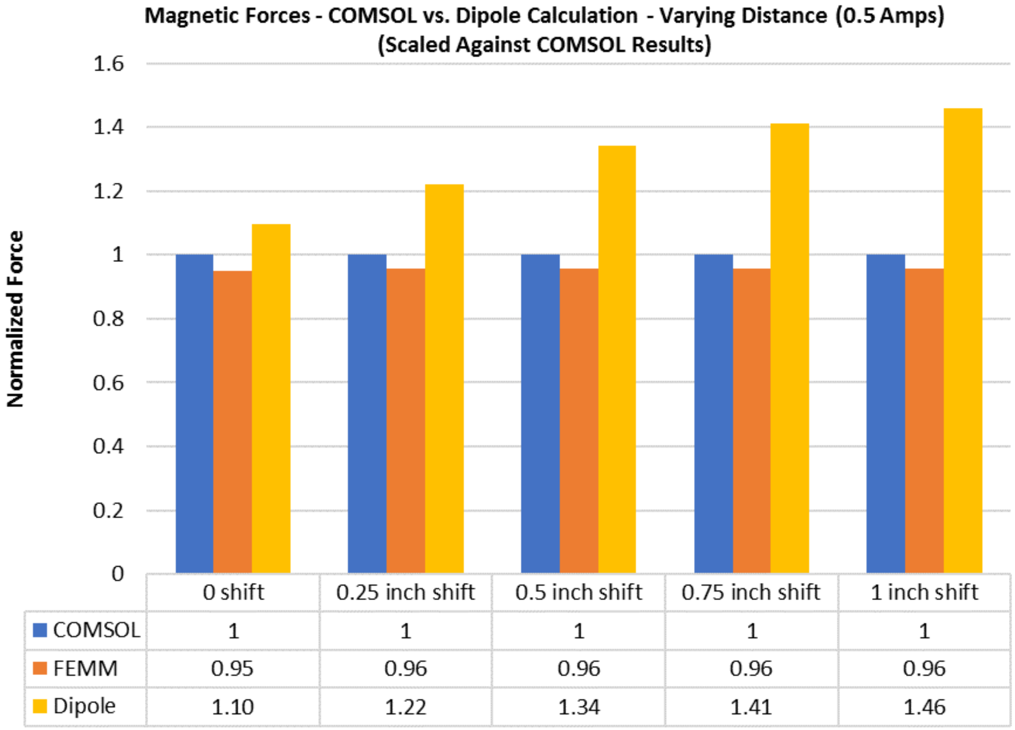

	0 shift	0.25 inch shift	0.5 inch shift	0.75 inch shift	1 inch shift
🟦 COMSOL	1	1	1	1	1
🟧 FEMM	0.95	0.96	0.96	0.96	0.96
🟨 Dipole	1.10	1.22	1.34	1.41	1.46

Figure 105: Comparison of Forces Predicted by COMSOL, FEMM, and Dipole Model

6.2 Validation of Coordinate Transformations

The coordinate transformations defined in Section 5.6.4 were validated by performing additional COMSOL simulations of the generalized EM / PM superposition model. The coordinate transformations were verified for each of the six levitation EMs positioned in their respective stator coordinates.

6.2.1 Validation of Transformation of Forces

The PM was offset from the EM centerline by a fixed value of 10 degrees and for four positions around the EM, with each position incremented by 90 degrees, as illustrated by Figure 106. All simulations were performed with a fixed coil excitation of 0.5 ampere. The transformed forces and torques agreed with the COMSOL® simulation for every case. The validation data is tabulated in Appendix C.

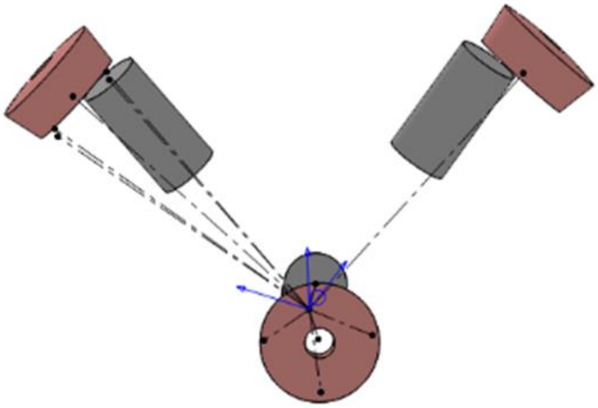

Figure 106: Validation of Magnetic Force Coordinate Transformations

6.3 Validation of Euler Angle Calculations

The Euler Angle calculations were verified by using the MATLAB® Simulink® robotics system design and analysis toolbox which includes a utility to perform various coordinate transformations conversion, such as conversion from a set of Euler Angles a to a rotation matrix and vice versa. The rotation matrix for an arbitrary set of Euler angles, following the ZYX sequence laid out in in Section 5.4.1, was calculated in the MATLAB workspace and then applied to the permanent magnet coordinates. The computed values for rotation matrix and the rotated PM coordinates were compared against values computed using the Coordinate Transformation Conversion (CTC) utility. Note that the CTC tool outputs the rotation matrices as a column vector, which requires transposing the workspace rotation matrix in order to make a proper comparison. A sample comparison is provided in Figure 107 and shows the same rotation matrix and rotated coordinates are obtained.

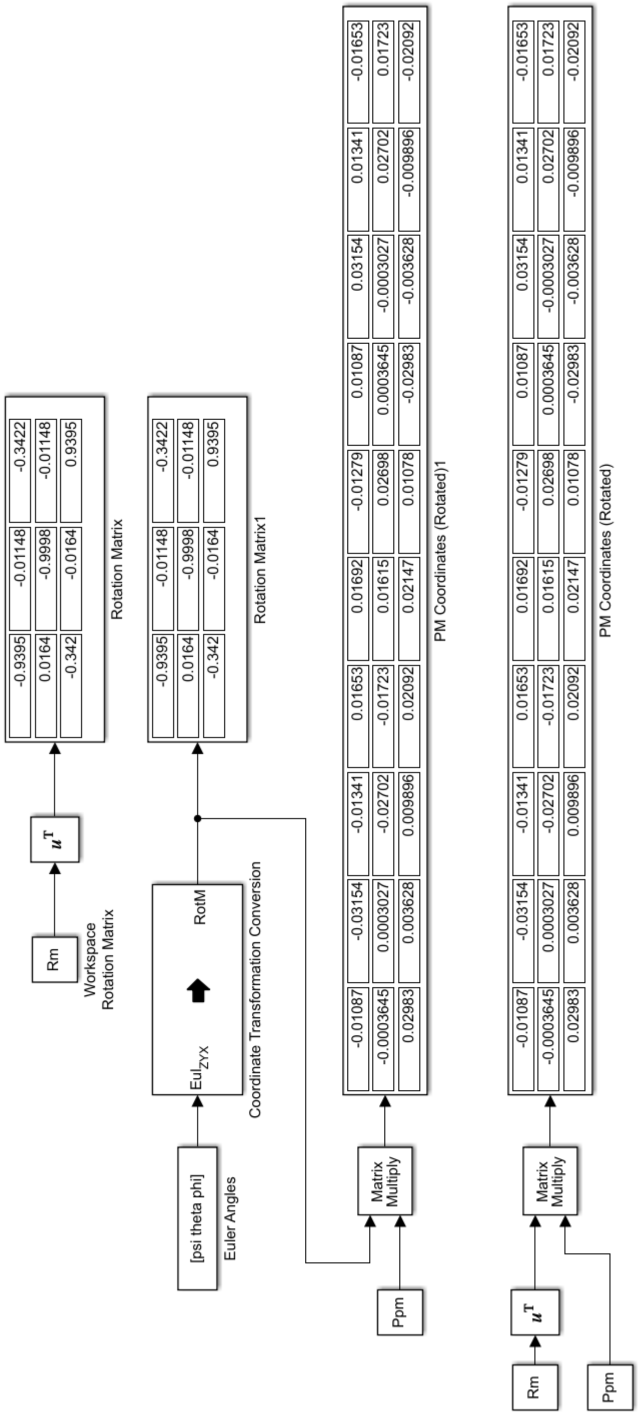

Figure 107: Euler Angle Validation using Simulink®

Chapter 7 Results

7.1 Conclusions

In summary, this thesis demonstrates that the methods presented herein, provide a means to model the dynamics of a 3-DOF model of a reaction sphere by computing the magnetic force relations from FEM models, off-line from the Simulink® dynamic model. Moreover, the objectives of this thesis, outlined in Chapter 4 , were met as follows:

1. Levitation EMs with sufficiently fast response times can be integrated into the NGCRS
2. The FEM modeling demonstrated that the EM and PM field interactions are limited to a single EM-PM pair
3. A generalized set of force and relations can be derived from the FEM models, allowing the force and torque for any arbitrary orientation of the rotor/stator, and for any EM-PM pair.
4. An algorithm was implemented in MATLAB to determine the appropriate force and torque relations to use for any instantaneous rotor / stator orientation and levitation coil current
5. A 3-DOF rotational dynamic model was developed using the methodologies presented herein

7.2 Recommendations and Future Work

7.2.1 Model Fidelity

The fidelity of the reaction sphere model should be increased to include the translational degrees of freedom so that all six degrees of freedom are modeled. The 3-DOF model considers the rotor to be fixed translationally. Therefore, the forces within the “iron only” region act along the center of mass of the rotor, and thus will not induce a torque. However, if the rotor is free to move translationally, then the foregoing statement is false, and an additional disturbance torque will be applied to the rotor assembly. Additional simulations must be performed to account for translation of the rotor within the stator, which alters the airgap, and consequently the magnetic forces and torques. The effect of the rotor being eccentric to the stator EMs must also be considered. The methodologies presented herein could be used as a starting point, namely, dividing the regions of force into the Iron only and Iron + PM. The region would be determined based on current and the magnetic airgap, and possibly the rotor eccentricity. The degree of coupling between the EM and PM could again be evaluated using the integrated and superposition models.

The model should also be updated to include the eight (8) electromagnetics that apply torque to the reaction sphere. As a starting point, the force and torque relations describing the levitation EMs could be used until a more representative model of the drive EMs is available. The position vectors of the drive EMs are given in Section 5.3.2, equation (88) which is expressed in terms of the fixed RS stator coordinate system.

The dynamic model herein does not account for the disturbance forces and torques that would be induced by eddy-currents that form in the rotor iron as it rotates past an active electromagnet. Furthermore, the electromagnet model does not account for the back emf that would be generated as the PM rotates past the EM. Taking into account these factors will further improve the fidelity of the reaction sphere model.

7.2.2 Validation of the FEM Model

The results of the FEM model should be validated with experimental results. A test bench model should be developed to verify the magnetic forces and torques predicted by the FEM model. However, the earths gravitational acceleration presents a significant challenge to completely validating the model because the levitation and drive coils are sized to operate in a zero gravity or near zero gravity environment. The only feasible solution would be to test a prototype on NASA’s Reduced Gravity Aircraft, commonly referred to as the “Vomit Comet”. The aircraft performs parabolic maneuvers which provides approximately 25 seconds of weightlessness. This of course would not be done until development of a complete 6-DOF model, and levitation and spacecraft attitude control algorithms are integrated.

7.2.3 Electromagnet Optimization Study

The characteristic parameters of the electromagnet, namely the number of turns, overall conductor length, and the geometric aspect ratios should be further investigated and optimized to provide the maximum force output for a given power level. Numerous electromagnet optimization studies have been published, such as (Haignere, et al., 1976) who studied optimal shapes and sizes of electromagnets to optimize the magnetic field at a constant power level, and another by (Yuan, et al., 2014) who researched optimization of electromagnetic efficiency by considering the geometric factors and thermal condition of the coil as coupled.

References

Stagmer, E. (2016). Reaction Sphere for Stabilization and Control in Three Axes. *U.S. Patent No. 9,475,592 B2.* Washington, D. C.: U.S. Patent and Trademark Office.

Rossini, L., (2014). *Electromagnetic Modeling and Control Aspects of a Reaction Sphere for Satellite Attitude Control*. (Unpublished Doctoral Thesis). École Polytechnique Fédérale de Lausanne, Lausanne, Switzerland.

Rossini, L., Chételat, O., Onillon, E., & Perriard, Y., (2011). Analytical and Experimental Investigation on the Force and Torque of a Reaction Sphere for Satellite Attitude Control. *IEEE/ASME International Conference on Advanced Intelligent Mechatronics,* Pages 487-492.

Rossini, L., Chételat, O., Onillon, E., & Perriard, Y., (2013). Force and Torque Analytical Models of a Reaction Sphere Actuator Based on Spherical Harmonic Rotation and Decomposition. *IEEE/ASME Transactions on Mechatronics, vol. 18, no. 3,* Pages 1006-1018.

Rossini, L., Onillon, E., Boletis, A., Mingard, S., Wawrzaszek, R., Serin, J., & Ortega, C., (2015). Development and Closed-Loop Experimental Results of a Reaction Sphere Elegant Breadboard. *European Space Mechanisms and Tribology Symposium (ESMATS)*.

CORDIS, (2014, November 30). *European Levitated Spherical Actuator Project*. https://cordis.europa.eu/project/id/283223

CORDIS, (2014, November 30). *Final Report Summary – ELSA* (*European Levitated Spherical Actuator)*. (https://cordis.europa.eu/project/id/283223/reporting

Bong, B., (2004). Singularity Analysis and Visualization for Single-Gimbal Control Moment Gyro Systems. *Journal of Guidance, Control, and Dynamics, vol. 27, no. 2,* Pages 271-282.

Sidi, M. J., (2000). *Spacecraft Dynamics and Control: A Practical Engineering Approach*. Cambridge: Cambridge University Press, 2000.

Ruiter, A., Damaren, C. J., & Forbes J. (2013). *Spacecraft Dynamics and Controls, An Introduction*. Wiley & Sons; West Sussex, United Kingdom.

Coxeter, H.S.M., (1961). *Introduction to Geometry*, John Wiley and Sons Inc.

Uchino, K., (1997). Piezoelectric Ultrasonic Motors: Overview, *Smart Materials and Structures*, *Volume 7,* Pages 273-285.

Toyama, S., Hatae, S., & Nonaka, M., (1991). Development of Multi-Degree of Freedom Spherical Ultrasonic Motor, *Fifth International Conference on Advanced Robotics 'Robots in Unstructured Environments, Volume 1 (doi: 10.1109/ICAR.1991.240476),* Pages. 55-60.

Zhou, L., (2014). Magnetically Suspended Reaction Sphere with One-axis Hysteresis Drive (Unpublished Masters Thesis). Massachusetts Institute of Technology, Cambridge, MA.

Zhou, L., Mohammad, I. N., & Trumper, D. L., (2017). One-Axis Hysteresis Motor Driven Magnetically Suspended Reaction Sphere. *Mechatronics, Volume 42*, Pages 69-80.

Zhu, L., Guo, J., & Gill, E., (2016). Reaction Sphere for Microsatellite Attitude Control. *Proceedings of 67th International Astronautical Congress*, (September 26-30, 2016), Pages 1-7.

Iwakura, A., Tsuda, S., & Tsuda, Y., (2008). Feasibility Study on Three-Dimensional Reaction Wheel. *Proceedings of School of Engineering, Tokai University, Tokyo, Japan, Volume XXXIII*, Pages 51-57.

Kim, D., Yoon, H., Kang, W., Kim, Y., & Choi, H., (2014). Development of a Spherical Reaction Wheel Actuator Using Electromagnetic Induction, *Aerospace Science and Technology 39,* Pages 86-94.

Yuan, L., Zhang, J., Chen, Si-Lu., Liang, Y., 1, Chen, J., 1, Zhang C., & Yang, G., (2019). Design and Optimization of a Magnetically Levitated Inductive Reaction Sphere for Spacecraft Attitude Control. *Energies (2019, 12, 1553).*

COMSOL® (2019). AC / DC Module User Guide, Version 5.4. Burlington, MA: COMSOL®.

Frei, W. (2016, March 22). *How to Choose Between Boundary Conditions for Coil Modeling*. COMSOL Blogs. https://www.comsol.com/blogs/how-to-choose-between-boundary-conditions-for-coil-modeling/

Tozzo, C. (2018, January 23). *Modeling Ferromagnetic Materials in COMSOL Multiphysics*®. COMSOL Blogs. https://www.comsol.com/blogs/modeling-ferromagnetic-materials-in-comsol-multiphysics/

COMSOL® *Self-demagnetization of a Cylindrical AlNiCo magnet*. Application ID: 57891. https://www.comsol.com/model/self-demagnetization-of-a-cylindrical-alnico-magnet-57891

Markley, F. L., & Crassidis, L. J., (2014). *Fundamental of Spacecraft Attitude Determination and Control*. (2014). Springer Science and Business Media, New York.

Greenwood, T. D., (1965). *Principles of Dynamics*. Prentice Hall Inc. (1965), Upper Saddle River, New Jersey.

Greenwood, T. D., (2003). *Advanced Dynamics*. Cambridge University Press (2003), New York.

Hibbeler, R. C., (2010). Engineering Mechanics: Statics, 12th edition. Prentice Hall Inc. (2010), Upper Saddle River, New Jersey.

Hibbeler, R. C., (2007). Engineering Mechanics: Dynamics, 11th edition. Prentice Hall Inc. (2007), Upper Saddle River, New Jersey.

Wheeler, H. A., (1928). *Simple Inductance Formulas for Radio Coils*, Proceedings of the Institute of Radio Engineers, October 1928, pp. 1398-1400.

Eclipse Magnetics Ltd. *Sintered Neodymium Iron Boron (NdFeB) Magnets*

National Electrical Manufacturers Association. (2011). American National Standard, Magnet Wire (Standard No. ANSI/NEMA MW 1000-2011).

Meeker, D. (2007, April 5). *Magnetic Circuit Derivation of Energy Stored in a Permanent Magnet*. femm wiki page. https://www.femm.info/wiki/PMEnergy#

Meeker, D. (2007, September 27). *Circuit model of a uniformly magnetized cylindrical permanent magnet*. femm wiki page. https://www.femm.info/Archives/misc/BarMagnet.pdf

Meeker, D. (2018, January 30). *Finite Element Method Magnetics Version 4.2 User Manual*. https://www.femm.info/Archives/doc/manual42.pdf

Magnetic Materials Producers Association (MMPA). (December 1998). *Permanent Magnet Guidelines*. Chicago, Illinois.

Sen, P. C., (1996). *Principles of Electric Machines and Power Electronics, Second Edition*. (1996). John Wiley & Sons, Inc., Somerset, New Jersey.

Roters, H. C., (1941). *Electromagnetic Devices, First Edition.* (1941). John Wily & Sons, Inc., New York.

Hambley, A. R., (2005). *Electrical Engineering, Principles and Applications, Third Edition*. (2005). Pearson Education Inc., Upper Saddle River, New Jersey.

Lorrain, P., Corson, D., (1988). *Electromagnetic Fields and Waves Including Electric Circuits, Third Edition* (1988). W. H. Freeman and Company, New York.

Zhang, Y., Leng, Y., Zhang, H., Su, X., Sun, S., Chen, X., and Xu, J., (2020). Comparative study on equivalent models calculating magnetic force between permanent magnets. *Journal of Intelligent Manufacturing and Special Equipment, vol. 1, no. 1, Pages 43-65.*

Yuan, A., He, J., Pan, Y., Yin, X., Luo, C., and Chen, S., (2014). Research on electromagnetic efficiency optimization in the design of air-core coils. *International Transactions on Electrical Energy Systems, no., 25, Pages 789-798.*

Haignere, E., and Potter, W., (1976). Optimizing the Shape and Size of a Uniform-Current-Density Magnet to Maximize the Field at Constant Power. *Journal of Applied Physics, vol. 47, no., 4 1657.*

Gutierrez, H., (2020). *Attitude Control of Spacecraft by Correlated Electromagnetic Levitated Actuator (CELA).* Mothly Report and Status Update. (August 2020). Unpublished Work. Florida Institute of Technology.

Strang, G., (1980). *Linear Algebra and Its Application, Second Edition.* Academic Press Inc., New York, New York.

Appendix A

COMSOL Simulation Data – Magnetic Forces

Table 4: Magnitude of Magnetic Force for Varying Distance and Current (0-0.5 Amp)

		Coil Current				
Angle (deg)	**Distance (m)**	**0**	**0.2**	**0.3**	**0.4**	**0.5**
0.000	7.62000E-04	0.0E+00	1.79054E-01	2.68600E-01	3.58164E-01	4.63185E-01
1.000	9.46086E-04	0.0E+00	1.77325E-01	2.66007E-01	3.54705E-01	4.58709E-01
2.000	1.35584E-03	0.0E+00	1.72169E-01	2.58276E-01	3.44398E-01	4.45383E-01
3.000	1.84661E-03	0.0E+00	1.63734E-01	2.45615E-01	3.27507E-01	4.23529E-01
4.000	2.36848E-03	0.0E+00	1.52421E-01	2.28645E-01	3.04872E-01	3.94244E-01
5.000	2.90461E-03	0.0E+00	1.39123E-01	2.08677E-01	2.78233E-01	3.59783E-01
6.000	3.44823E-03	0.0E+00	1.24826E-01	1.87223E-01	2.49607E-01	3.22739E-01
7.000	3.99615E-03	0.0E+00	1.10252E-01	1.65342E-01	2.20414E-01	2.84970E-01
8.000	4.54668E-03	0.0E+00	9.58802E-02	1.43761E-01	1.91609E-01	2.47701E-01
9.000	5.09884E-03	0.0E+00	8.21149E-02	1.23092E-01	1.64006E-01	2.11967E-01
10.000	5.65201E-03	0.0E+00	6.93429E-02	1.03892E-01	1.38363E-01	1.78748E-01
11.000	6.20577E-03	0.0E+00	5.78147E-02	8.65503E-02	1.15174E-01	1.48700E-01
12.000	6.75982E-03	0.0E+00	4.76244E-02	7.12018E-02	9.46309E-02	1.22049E-01
13.000	7.31396E-03	0.0E+00	3.87849E-02	5.78673E-02	7.67574E-02	9.88404E-02
14.000	7.86800E-03	0.0E+00	3.12793E-02	4.65315E-02	6.15461E-02	7.90727E-02
15.000	8.42183E-03	0.0E+00	2.51183E-02	3.72191E-02	4.90437E-02	6.28232E-02
16.000	8.97532E-03	0.0E+00	2.02783E-02	2.99007E-02	3.92216E-02	5.00659E-02
17.000	9.52838E-03	0.0E+00	1.65495E-02	2.42637E-02	3.16602E-02	4.02554E-02
18.000	1.00809E-02	0.0E+00	1.36537E-02	1.98831E-02	2.57849E-02	3.26394E-02
19.000	1.06329E-02	0.0E+00	1.13688E-02	1.64215E-02	2.11425E-02	2.66247E-02
20.000	1.11842E-02	0.0E+00	9.53746E-03	1.36424E-02	1.74095E-02	2.17896E-02
21.000	1.17348E-02	0.0E+00	8.04840E-03	1.13757E-02	1.43626E-02	1.78456E-02
22.000	1.22846E-02	0.0E+00	6.82250E-03	9.50475E-03	1.18440E-02	1.45939E-02
23.000	1.28335E-02	0.0E+00	5.80262E-03	7.94442E-03	9.74638E-03	1.18992E-02
24.000	1.33816E-02	0.0E+00	4.94630E-03	6.63270E-03	7.98953E-03	9.66765E-03
25.000	1.39287E-02	0.0E+00	4.22228E-03	5.52354E-03	6.51663E-03	7.83372E-03
26.000	1.44749E-02	0.0E+00	3.60534E-03	4.57975E-03	5.28116E-03	6.35000E-03
27.000	1.50200E-02	0.0E+00	3.07571E-03	3.77194E-03	4.25025E-03	5.18868E-03
28.000	1.55640E-02	0.0E+00	2.61764E-03	3.07709E-03	3.40297E-03	4.34109E-03
29.000	1.61068E-02	0.0E+00	2.21948E-03	2.47862E-03	2.73266E-03	3.80523E-03
30.000	1.66485E-02	0.0E+00	1.87108E-03	1.96408E-03	2.24580E-03	3.56603E-03
31.000	1.71890E-02	0.0E+00	1.56469E-03	1.52589E-03	1.95444E-03	3.57130E-03
31.7175	1.75760E-02	0.0E+00	1.36718E-03	1.25820E-03	1.86765E-03	3.68591E-03

Table 5: Magnitude of Magnetic Force for Varying Distance and Current (1-2.5 amp)

		Coil Current			
Angle (deg)	**Distance (m)**	**1.0**	**1.5**	**2.0**	**2.5**
0.000	7.62000E-04	9.26808E-01	1.39086E+00	1.85535E+00	2.32031E+00
1.000	9.46086E-04	9.17846E-01	1.37744E+00	1.83740E+00	2.29782E+00
2.000	1.35584E-03	8.91131E-01	1.33730E+00	1.78381E+00	2.23065E+00
3.000	1.84661E-03	8.47353E-01	1.27142E+00	1.69583E+00	2.12060E+00
4.000	2.36848E-03	7.88633E-01	1.18315E+00	1.57788E+00	1.97278E+00
5.000	2.90461E-03	7.19534E-01	1.07924E+00	1.43889E+00	1.79854E+00
6.000	3.44823E-03	6.45209E-01	9.67409E-01	1.28935E+00	1.61106E+00
7.000	3.99615E-03	5.69377E-01	8.53257E-01	1.13664E+00	1.41954E+00
8.000	4.54668E-03	4.94510E-01	7.40489E-01	9.85713E-01	1.23026E+00
9.000	5.09884E-03	4.22622E-01	6.32094E-01	8.40531E-01	1.04806E+00
10.000	5.65201E-03	3.55651E-01	5.30948E-01	7.04913E-01	8.77804E-01
11.000	6.20577E-03	2.94844E-01	4.38916E-01	5.81414E-01	7.22855E-01
12.000	6.75982E-03	2.40707E-01	3.56821E-01	4.71290E-01	5.85024E-01
13.000	7.31396E-03	1.93392E-01	2.85046E-01	3.75324E-01	4.65802E-01
14.000	7.86800E-03	1.53017E-01	2.24058E-01	2.94653E-01	3.67368E-01
15.000	8.42183E-03	1.19963E-01	1.74846E-01	2.31306E-01	2.93208E-01
16.000	8.97532E-03	9.43372E-02	1.37874E-01	1.86257E-01	2.44618E-01
17.000	9.52838E-03	7.50056E-02	1.11340E-01	1.56623E-01	2.16449E-01
18.000	1.00809E-02	6.03534E-02	9.25357E-02	1.37856E-01	2.01220E-01
19.000	1.06329E-02	4.91135E-02	7.92952E-02	1.26213E-01	1.93263E-01
20.000	1.11842E-02	4.04379E-02	7.01600E-02	1.19283E-01	1.89457E-01
21.000	1.17348E-02	3.37851E-02	6.41562E-02	1.15546E-01	1.88191E-01
22.000	1.22846E-02	2.88590E-02	6.06628E-02	1.14197E-01	1.88854E-01
23.000	1.28335E-02	2.54748E-02	5.91483E-02	1.14615E-01	1.91001E-01
24.000	1.33816E-02	2.34414E-02	5.90640E-02	1.16221E-01	1.94106E-01
25.000	1.39287E-02	2.25175E-02	5.99309E-02	1.18548E-01	1.97768E-01
26.000	1.44749E-02	2.23802E-02	6.12956E-02	1.21126E-01	2.01487E-01
27.000	1.50200E-02	2.27723E-02	6.29339E-02	1.23818E-01	2.05182E-01
28.000	1.55640E-02	2.34740E-02	6.46666E-02	1.26455E-01	2.08706E-01
29.000	1.61068E-02	2.43362E-02	6.63929E-02	1.28979E-01	2.11994E-01
30.000	1.66485E-02	2.52702E-02	6.80724E-02	1.31350E-01	2.15064E-01
31.000	1.71890E-02	2.62161E-02	6.96654E-02	1.33569E-01	2.17900E-01
31.7175	1.75760E-02	2.68878E-02	7.07582E-02	1.35071E-01	2.19812E-01

Table 6: Magnitude of Magnetic Force for Varying Distance and Current (3-5 amp)

		Coil Current				
Angle (deg)	**Distance (m)**	**3**	**3.5**	**4**	**4.5**	**5**
0.000	7.62000E-04	2.78564E+00	3.25144E+00	3.71771E+00	4.18445E+00	4.65156E+00
1.000	9.46086E-04	2.75859E+00	3.21982E+00	3.68151E+00	4.14356E+00	4.60606E+00
2.000	1.35584E-03	2.67791E+00	3.12559E+00	3.57360E+00	4.02194E+00	4.47078E+00
3.000	1.84661E-03	2.54554E+00	2.97083E+00	3.39637E+00	3.82228E+00	4.24848E+00
4.000	2.36848E-03	2.36780E+00	2.76300E+00	3.15832E+00	3.55391E+00	3.94960E+00
5.000	2.90461E-03	2.15825E+00	2.51783E+00	2.87752E+00	3.23710E+00	3.59670E+00
6.000	3.44823E-03	1.93256E+00	2.25375E+00	2.57478E+00	2.89567E+00	3.21629E+00
7.000	3.99615E-03	1.70199E+00	1.98408E+00	2.26569E+00	2.54695E+00	2.82787E+00
8.000	4.54668E-03	1.47409E+00	1.71746E+00	1.96018E+00	2.20255E+00	2.44453E+00
9.000	5.09884E-03	1.25478E+00	1.46090E+00	1.66646E+00	1.87170E+00	2.07674E+00
10.000	5.65201E-03	1.04986E+00	1.22145E+00	1.39285E+00	1.56424E+00	1.73589E+00
11.000	6.20577E-03	8.63743E-01	1.00461E+00	1.14596E+00	1.28842E+00	1.43241E+00
12.000	6.75982E-03	6.98963E-01	8.14057E-01	9.31267E-01	1.05153E+00	1.17565E+00
13.000	7.31396E-03	5.58074E-01	6.53739E-01	7.54312E-01	8.61236E-01	9.75809E-01
14.000	7.86800E-03	4.44738E-01	5.29127E-01	6.22622E-01	7.26957E-01	8.43512E-01
15.000	8.42183E-03	3.64069E-01	4.46731E-01	5.43271E-01	6.55121E-01	7.83154E-01
16.000	8.97532E-03	3.16783E-01	4.05202E-01	5.11174E-01	6.35365E-01	7.78057E-01
17.000	9.52838E-03	2.93929E-01	3.90405E-01	5.06367E-01	6.41902E-01	7.97024E-01
18.000	1.00809E-02	2.84417E-01	3.87840E-01	5.11514E-01	6.55330E-01	8.19235E-01
19.000	1.06329E-02	2.81025E-01	3.89422E-01	5.18305E-01	6.67539E-01	8.37063E-01
20.000	1.11842E-02	2.80563E-01	3.92331E-01	5.24622E-01	6.77314E-01	8.50359E-01
21.000	1.17348E-02	2.81682E-01	3.95760E-01	5.30295E-01	6.85224E-01	8.60491E-01
22.000	1.22846E-02	2.84206E-01	4.00055E-01	5.36306E-01	6.92923E-01	8.69855E-01
23.000	1.28335E-02	2.87959E-01	4.05343E-01	5.43117E-01	7.01222E-01	8.79654E-01
24.000	1.33816E-02	2.92480E-01	4.11258E-01	5.50410E-01	7.09915E-01	8.89755E-01
25.000	1.39287E-02	2.97444E-01	4.17520E-01	5.57974E-01	7.18793E-01	8.99962E-01
26.000	1.44749E-02	3.02281E-01	4.23469E-01	5.65036E-01	7.26992E-01	9.09303E-01
27.000	1.50200E-02	3.06975E-01	4.29159E-01	5.71745E-01	7.34721E-01	9.18080E-01
28.000	1.55640E-02	3.11368E-01	4.34449E-01	5.77926E-01	7.41805E-01	9.26070E-01
29.000	1.61068E-02	3.15444E-01	4.39289E-01	5.83550E-01	7.48219E-01	9.33285E-01
30.000	1.66485E-02	3.19197E-01	4.43745E-01	5.88703E-01	7.54071E-01	9.39851E-01
31.000	1.71890E-02	3.22639E-01	4.47801E-01	5.93383E-01	7.59375E-01	9.45779E-01
31.7175	1.75760E-02	3.24974E-01	4.50548E-01	5.96538E-01	7.62958E-01	9.49783E-01

Table 7: Z-Comp. of Magnetic Force for Varying Scalar Distance and Current (0-0.5 Amp)

	Fz Component for Varying Coil Current (Amp) and Distance (m)				
Distance (m)	**0**	**0.2**	**0.3**	**0.4**	**0.5**
7.620E-04	0.0000E+00	1.7905E-01	2.6860E-01	3.5816E-01	4.6318E-01
9.461E-04	0.0000E+00	1.7581E-01	2.6374E-01	3.5169E-01	4.5481E-01
1.356E-03	0.0000E+00	1.6627E-01	2.4943E-01	3.3261E-01	4.3015E-01
1.847E-03	0.0000E+00	1.5102E-01	2.2656E-01	3.0212E-01	3.9073E-01
2.368E-03	0.0000E+00	1.3134E-01	1.9705E-01	2.6278E-01	3.3986E-01
2.905E-03	0.0000E+00	1.0917E-01	1.6380E-01	2.1847E-01	2.8259E-01
3.448E-03	0.0000E+00	8.6380E-02	1.2966E-01	1.7299E-01	2.2381E-01
3.996E-03	0.0000E+00	6.4339E-02	9.6646E-02	1.2905E-01	1.6706E-01
4.547E-03	0.0000E+00	4.4072E-02	6.6322E-02	8.8714E-02	1.1503E-01
5.099E-03	0.0000E+00	2.6457E-02	4.0002E-02	5.3756E-02	6.9966E-02
5.652E-03	0.0000E+00	1.2100E-02	1.8588E-02	2.5367E-02	3.3429E-02
6.206E-03	0.0000E+00	1.1946E-03	2.3645E-03	3.9160E-03	5.8863E-03
6.760E-03	0.0000E+00	-6.3662E-03	-8.8398E-03	-1.0840E-02	-1.2997E-02
7.314E-03	0.0000E+00	-1.0896E-02	-1.5508E-02	-1.9562E-02	-2.4095E-02
7.868E-03	0.0000E+00	-1.2897E-02	-1.8400E-02	-2.3275E-02	-2.8742E-02
8.422E-03	0.0000E+00	-1.3068E-02	-1.8574E-02	-2.3393E-02	-2.8770E-02
8.975E-03	0.0000E+00	-1.2259E-02	-1.7297E-02	-2.1608E-02	-2.6373E-02
9.528E-03	0.0000E+00	-1.1115E-02	-1.5544E-02	-1.9220E-02	-2.3231E-02
1.008E-02	0.0000E+00	-9.9281E-03	-1.3746E-02	-1.6799E-02	-2.0077E-02
1.063E-02	0.0000E+00	-8.8011E-03	-1.2052E-02	-1.4537E-02	-1.7148E-02
1.118E-02	0.0000E+00	-7.7678E-03	-1.0508E-02	-1.2484E-02	-1.4499E-02
1.173E-02	0.0000E+00	-6.8351E-03	-9.1158E-03	-1.0640E-02	-1.2125E-02
1.228E-02	0.0000E+00	-5.9980E-03	-7.8687E-03	-8.9872E-03	-1.0001E-02
1.283E-02	0.0000E+00	-5.2497E-03	-6.7538E-03	-7.5106E-03	-8.1016E-03
1.338E-02	0.0000E+00	-4.5819E-03	-5.7591E-03	-6.1935E-03	-6.4093E-03
1.393E-02	0.0000E+00	-3.9873E-03	-4.8743E-03	-5.0236E-03	-4.9058E-03
1.447E-02	0.0000E+00	-3.4584E-03	-4.0889E-03	-3.9871E-03	-3.5777E-03
1.502E-02	0.0000E+00	-2.9874E-03	-3.3910E-03	-3.0679E-03	-2.4007E-03
1.556E-02	0.0000E+00	-2.5674E-03	-2.7703E-03	-2.2525E-03	-1.3600E-03
1.611E-02	0.0000E+00	-2.1930E-03	-2.2184E-03	-1.5296E-03	-4.3920E-04
1.665E-02	0.0000E+00	-1.8586E-03	-1.7271E-03	-8.8820E-04	3.7550E-04
1.719E-02	0.0000E+00	-1.5598E-03	-1.2895E-03	-3.1920E-04	1.0959E-03
1.758E-02	0.0000E+00	-1.3651E-03	-1.0053E-03	4.9300E-05	1.5613E-03

Table 8: Z-Comp. of Magnetic Force for Varying Scalar Distance and Current (1-3 Amp)

	Fz Component for Varying Coil Current (Amp) and Distance (m)				
Distance (m)	**1**	**1.5**	**2**	**2.5**	**3**
7.620E-04	9.2681E-01	1.3909E+00	1.8554E+00	2.3203E+00	2.7856E+00
9.461E-04	9.1007E-01	1.3658E+00	1.8219E+00	2.2785E+00	2.7355E+00
1.356E-03	8.6076E-01	1.2919E+00	1.7234E+00	2.1554E+00	2.5879E+00
1.847E-03	7.8199E-01	1.1737E+00	1.5661E+00	1.9590E+00	2.3523E+00
2.368E-03	6.8036E-01	1.0215E+00	1.3633E+00	1.7058E+00	2.0489E+00
2.905E-03	5.6610E-01	8.5050E-01	1.1358E+00	1.4220E+00	1.7092E+00
3.448E-03	4.4904E-01	6.7567E-01	9.0372E-01	1.1332E+00	1.3641E+00
3.996E-03	3.3640E-01	5.0802E-01	6.8192E-01	8.5809E-01	1.0365E+00
4.547E-03	2.3361E-01	3.5575E-01	4.8145E-01	6.1073E-01	7.4355E-01
5.099E-03	1.4519E-01	2.2567E-01	3.1140E-01	4.0239E-01	4.9864E-01
5.652E-03	7.4147E-02	1.2215E-01	1.7745E-01	2.4003E-01	3.0990E-01
6.206E-03	2.1315E-02	4.6285E-02	8.0799E-02	1.2485E-01	1.7846E-01
6.760E-03	-1.4169E-02	-3.5120E-03	1.8972E-02	5.3283E-02	9.9420E-02
7.314E-03	-3.4255E-02	-3.0480E-02	-1.2770E-02	1.8880E-02	6.4460E-02
7.868E-03	-4.1752E-02	-3.9033E-02	-2.0580E-02	1.3610E-02	6.3520E-02
8.422E-03	-4.0384E-02	-3.4842E-02	-1.2140E-02	2.7710E-02	8.4720E-02
8.975E-03	-3.4558E-02	-2.4559E-02	3.6300E-03	5.0010E-02	1.1458E-01
9.528E-03	-2.7644E-02	-1.3239E-02	1.9990E-02	7.2020E-02	1.4288E-01
1.008E-02	-2.1046E-02	-2.9090E-03	3.4330E-02	9.0680E-02	1.6614E-01
1.063E-02	-1.5139E-02	6.0240E-03	4.6340E-02	1.0582E-01	1.8444E-01
1.118E-02	-9.9210E-03	1.3732E-02	5.6460E-02	1.1826E-01	1.9915E-01
1.173E-02	-5.3110E-03	2.0443E-02	6.5136E-02	1.2877E-01	2.1135E-01
1.228E-02	-1.2000E-03	2.6402E-02	7.2809E-02	1.3801E-01	2.2202E-01
1.283E-02	2.4750E-03	3.1732E-02	7.9666E-02	1.4628E-01	2.3158E-01
1.338E-02	5.7450E-03	3.6460E-02	8.5740E-02	1.5358E-01	2.3998E-01
1.393E-02	8.6330E-03	4.0617E-02	9.1048E-02	1.5992E-01	2.4724E-01
1.447E-02	1.1156E-02	4.4201E-02	9.5553E-02	1.6522E-01	2.5320E-01
1.502E-02	1.3366E-02	4.7302E-02	9.9404E-02	1.6967E-01	2.5812E-01
1.556E-02	1.5295E-02	4.9964E-02	1.0264E-01	1.7335E-01	2.6205E-01
1.611E-02	1.6975E-02	5.2239E-02	1.0536E-01	1.7632E-01	2.6515E-01
1.665E-02	1.8432E-02	5.4170E-02	1.0758E-01	1.7869E-01	2.6747E-01
1.719E-02	1.9694E-02	5.5795E-02	1.0940E-01	1.8051E-01	2.6911E-01
1.758E-02	2.0494E-02	5.6798E-02	1.1047E-01	1.8152E-01	2.6994E-01

Table 9: Z-Comp. of Iron + PM Force for Varying Scalar Distance and Current (3.5-5 Amp)

	Fz Component for Varying Coil Current (Amp) and Distance (m)			
Distance (m)	**3.5**	**4**	**4.5**	**5**
7.620E-04	3.2514E+00	3.7177E+00	4.1845E+00	4.6516E+00
9.461E-04	3.1930E+00	3.6509E+00	4.1093E+00	4.5681E+00
1.356E-03	3.0209E+00	3.4544E+00	3.8882E+00	4.3227E+00
1.847E-03	2.7462E+00	3.1406E+00	3.5356E+00	3.9311E+00
2.368E-03	2.3927E+00	2.7371E+00	3.0823E+00	3.4279E+00
2.905E-03	1.9972E+00	2.2862E+00	2.5761E+00	2.8669E+00
3.448E-03	1.5963E+00	1.8300E+00	2.0652E+00	2.3017E+00
3.996E-03	1.2173E+00	1.4003E+00	1.5856E+00	1.7732E+00
4.547E-03	8.7994E-01	1.0199E+00	1.1634E+00	1.3105E+00
5.099E-03	6.0015E-01	7.0690E-01	8.1892E-01	9.3620E-01
5.652E-03	3.8706E-01	4.7151E-01	5.6325E-01	6.6227E-01
6.206E-03	2.4159E-01	3.1427E-01	3.9650E-01	4.8826E-01
6.760E-03	1.5738E-01	2.2718E-01	3.0880E-01	4.0225E-01
7.314E-03	1.2398E-01	1.9742E-01	2.8481E-01	3.8614E-01
7.868E-03	1.2916E-01	2.1054E-01	3.0765E-01	4.2049E-01
8.422E-03	1.5890E-01	2.5022E-01	3.5871E-01	4.8434E-01
8.975E-03	1.9735E-01	2.9830E-01	4.1743E-01	5.5475E-01
9.528E-03	2.3256E-01	3.4106E-01	4.6837E-01	6.1450E-01
1.008E-02	2.6070E-01	3.7437E-01	5.0714E-01	6.5902E-01
1.063E-02	2.8223E-01	3.9917E-01	5.3526E-01	6.9051E-01
1.118E-02	2.9910E-01	4.1814E-01	5.5624E-01	7.1343E-01
1.173E-02	3.1286E-01	4.3331E-01	5.7271E-01	7.3104E-01
1.228E-02	3.2483E-01	4.4644E-01	5.8686E-01	7.4607E-01
1.283E-02	3.3555E-01	4.5821E-01	5.9954E-01	7.5955E-01
1.338E-02	3.4494E-01	4.6847E-01	6.1057E-01	7.7123E-01
1.393E-02	3.5300E-01	4.7721E-01	6.1987E-01	7.8096E-01
1.447E-02	3.5949E-01	4.8408E-01	6.2700E-01	7.8821E-01
1.502E-02	3.6472E-01	4.8950E-01	6.3245E-01	7.9356E-01
1.556E-02	3.6879E-01	4.9353E-01	6.3629E-01	7.9705E-01
1.611E-02	3.7182E-01	4.9635E-01	6.3873E-01	7.9895E-01
1.665E-02	3.7393E-01	4.9808E-01	6.3990E-01	7.9940E-01
1.719E-02	3.7522E-01	4.9883E-01	6.3994E-01	7.9856E-01
1.758E-02	3.7573E-01	4.9888E-01	6.3942E-01	7.9732E-01

Table 10: Y-Comp. of Magnetic Force for Varying Distance & Current (0 - 0.5 amp)

	Fy Component for Varying Coil Current (Amp) and Distance (m)				
Distance (m)	**0**	**0.2**	**0.3**	**0.4**	**0.5**
7.620E-04	0.0000E+00	2.5297E-06	3.8452E-06	5.1944E-06	6.6477E-06
9.461E-04	0.0000E+00	-2.3095E-02	-3.4634E-02	-4.6168E-02	-5.9687E-02
1.356E-03	0.0000E+00	-4.4692E-02	-6.7019E-02	-8.9335E-02	-1.1549E-01
1.847E-03	0.0000E+00	-6.3251E-02	-9.4846E-02	-1.2642E-01	-1.6343E-01
2.368E-03	0.0000E+00	-7.7351E-02	-1.1597E-01	-1.5457E-01	-1.9981E-01
2.905E-03	0.0000E+00	-8.6241E-02	-1.2929E-01	-1.7229E-01	-2.2268E-01
3.448E-03	0.0000E+00	-9.0111E-02	-1.3506E-01	-1.7994E-01	-2.3253E-01
3.996E-03	0.0000E+00	-8.9532E-02	-1.3416E-01	-1.7869E-01	-2.3086E-01
4.547E-03	0.0000E+00	-8.5151E-02	-1.2755E-01	-1.6983E-01	-2.1937E-01
5.099E-03	0.0000E+00	-7.7736E-02	-1.1641E-01	-1.5495E-01	-2.0009E-01
5.652E-03	0.0000E+00	-6.8279E-02	-1.0222E-01	-1.3602E-01	-1.7559E-01
6.206E-03	0.0000E+00	-5.7802E-02	-8.6518E-02	-1.1511E-01	-1.4858E-01
6.760E-03	0.0000E+00	-4.7197E-02	-7.0651E-02	-9.4008E-02	-1.2135E-01
7.314E-03	0.0000E+00	-3.7223E-02	-5.5751E-02	-7.4223E-02	-9.5859E-02
7.868E-03	0.0000E+00	-2.8497E-02	-4.2739E-02	-5.6975E-02	-7.3664E-02
8.422E-03	0.0000E+00	-2.1451E-02	-3.2253E-02	-4.3105E-02	-5.5848E-02
8.975E-03	0.0000E+00	-1.6153E-02	-2.4390E-02	-3.2733E-02	-4.2557E-02
9.528E-03	0.0000E+00	-1.2261E-02	-1.8631E-02	-2.5159E-02	-3.2876E-02
1.008E-02	0.0000E+00	-9.3732E-03	-1.4366E-02	-1.9561E-02	-2.5734E-02
1.063E-02	0.0000E+00	-7.1965E-03	-1.1154E-02	-1.5352E-02	-2.0367E-02
1.118E-02	0.0000E+00	-5.5339E-03	-8.7010E-03	-1.2135E-02	-1.6266E-02
1.173E-02	0.0000E+00	-4.2495E-03	-6.8050E-03	-9.6475E-03	-1.3094E-02
1.228E-02	0.0000E+00	-3.2512E-03	-5.3314E-03	-7.7143E-03	-1.0628E-02
1.283E-02	0.0000E+00	-2.4721E-03	-4.1833E-03	-6.2115E-03	-8.7152E-03
1.338E-02	0.0000E+00	-1.8634E-03	-3.2902E-03	-5.0471E-03	-7.2377E-03
1.393E-02	0.0000E+00	-1.3889E-03	-2.5982E-03	-4.1509E-03	-6.1074E-03
1.447E-02	0.0000E+00	-1.0188E-03	-2.0628E-03	-3.4632E-03	-5.2462E-03
1.502E-02	0.0000E+00	-7.3175E-04	-1.6519E-03	-2.9415E-03	-4.5999E-03
1.556E-02	0.0000E+00	-5.1041E-04	-1.3394E-03	-2.5508E-03	-4.1226E-03
1.611E-02	0.0000E+00	-3.4182E-04	-1.1056E-03	-2.2645E-03	-3.7798E-03
1.665E-02	0.0000E+00	-2.1573E-04	-9.3528E-04	-2.0627E-03	-3.5462E-03
1.719E-02	0.0000E+00	-1.2361E-04	-8.1580E-04	-1.9282E-03	-3.3990E-03
1.758E-02	0.0000E+00	-7.5320E-05	-7.5660E-04	-1.8670E-03	-3.3389E-03

Table 11: Y-Comp. of Iron + PM Force for Varying Distance and Current (1 - 3 amps)

	Fy Component for Varying Coil Current (Amp) and Distance (m)				
Distance (m)	**1**	**1.5**	**2**	**2.5**	**3**
7.620E-04	1.4063E-05	2.2772E-05	3.1912E-05	4.1827E-05	5.2518E-05
9.461E-04	-1.1923E-01	-1.7863E-01	-2.3789E-01	-2.9700E-01	-3.5598E-01
1.356E-03	-2.3068E-01	-3.4557E-01	-4.6014E-01	-5.7441E-01	-6.8838E-01
1.847E-03	-3.2635E-01	-4.8875E-01	-6.5063E-01	-8.1201E-01	-9.7287E-01
2.368E-03	-3.9881E-01	-5.9700E-01	-7.9439E-01	-9.9099E-01	-1.1867E+00
2.905E-03	-4.4414E-01	-6.6439E-01	-8.8341E-01	-1.1012E+00	-1.3178E+00
3.448E-03	-4.6331E-01	-6.9235E-01	-9.1963E-01	-1.1452E+00	-1.3690E+00
3.996E-03	-4.5937E-01	-6.8554E-01	-9.0936E-01	-1.1308E+00	-1.3499E+00
4.547E-03	-4.3585E-01	-6.4944E-01	-8.6014E-01	-1.0680E+00	-1.2728E+00
5.099E-03	-3.9690E-01	-5.9044E-01	-7.8072E-01	-9.6774E-01	-1.1515E+00
5.652E-03	-3.4784E-01	-5.1671E-01	-6.8221E-01	-8.4435E-01	-1.0031E+00
6.206E-03	-2.9407E-01	-4.3647E-01	-5.7577E-01	-7.1199E-01	-8.4511E-01
6.760E-03	-2.4029E-01	-3.5680E-01	-4.7091E-01	-5.8259E-01	-6.9186E-01
7.314E-03	-1.9033E-01	-2.8341E-01	-3.7511E-01	-4.6542E-01	-5.5434E-01
7.868E-03	-1.4721E-01	-2.2063E-01	-2.9393E-01	-3.6712E-01	-4.4018E-01
8.422E-03	-1.1296E-01	-1.7134E-01	-2.3099E-01	-2.9190E-01	-3.5408E-01
8.975E-03	-8.7780E-02	-1.3567E-01	-1.8622E-01	-2.3945E-01	-2.9534E-01
9.528E-03	-6.9726E-02	-1.1055E-01	-1.5534E-01	-2.0412E-01	-2.5687E-01
1.008E-02	-5.6565E-02	-9.2490E-02	-1.3351E-01	-1.7963E-01	-2.3085E-01
1.063E-02	-4.6722E-02	-7.9066E-02	-1.1740E-01	-1.6172E-01	-2.1203E-01
1.118E-02	-3.9202E-02	-6.8803E-02	-1.0508E-01	-1.4802E-01	-1.9762E-01
1.173E-02	-3.3365E-02	-6.0812E-02	-9.5437E-02	-1.3724E-01	-1.8622E-01
1.228E-02	-2.8834E-02	-5.4616E-02	-8.7976E-02	-1.2891E-01	-1.7743E-01
1.283E-02	-2.5354E-02	-4.9916E-02	-8.2401E-02	-1.2281E-01	-1.7115E-01
1.338E-02	-2.2727E-02	-4.6467E-02	-7.8460E-02	-1.1870E-01	-1.6719E-01
1.393E-02	-2.0797E-02	-4.4068E-02	-7.5920E-02	-1.1636E-01	-1.6537E-01
1.447E-02	-1.9402E-02	-4.2467E-02	-7.4439E-02	-1.1532E-01	-1.6512E-01
1.502E-02	-1.8437E-02	-4.1511E-02	-7.3823E-02	-1.1537E-01	-1.6616E-01
1.556E-02	-1.7807E-02	-4.1053E-02	-7.3861E-02	-1.1623E-01	-1.6816E-01
1.611E-02	-1.7438E-02	-4.0977E-02	-7.4396E-02	-1.1769E-01	-1.7088E-01
1.665E-02	-1.7287E-02	-4.1225E-02	-7.5356E-02	-1.1968E-01	-1.7420E-01
1.719E-02	-1.7304E-02	-4.1716E-02	-7.6632E-02	-1.2206E-01	-1.7798E-01
1.758E-02	-1.7406E-02	-4.2199E-02	-7.7720E-02	-1.2397E-01	-1.8094E-01

Table 12: Y-Comp. of Magnetic Force for Varying Distance and Current (3.5 - 5 Amp)

	Fy Component for Varying Coil Current (Amp) and Distance (m)			
Distance (m)	**3.5**	**4**	**4.5**	**5**
7.620E-04	6.3985E-05	7.6227E-05	8.9247E-05	1.0304E-04
9.461E-04	-4.1481E-01	-4.7349E-01	-5.3203E-01	-5.9042E-01
1.356E-03	-8.0204E-01	-9.1540E-01	-1.0285E+00	-1.1412E+00
1.847E-03	-1.1332E+00	-1.2930E+00	-1.4523E+00	-1.6112E+00
2.368E-03	-1.3817E+00	-1.5758E+00	-1.7692E+00	-1.9618E+00
2.905E-03	-1.5332E+00	-1.7474E+00	-1.9602E+00	-2.1720E+00
3.448E-03	-1.5910E+00	-1.8112E+00	-2.0298E+00	-2.2465E+00
3.996E-03	-1.5668E+00	-1.7811E+00	-1.9932E+00	-2.2029E+00
4.547E-03	-1.4749E+00	-1.6740E+00	-1.8703E+00	-2.0636E+00
5.099E-03	-1.3319E+00	-1.5091E+00	-1.6830E+00	-1.8538E+00
5.652E-03	-1.1585E+00	-1.3106E+00	-1.4593E+00	-1.6046E+00
6.206E-03	-9.7513E-01	-1.1020E+00	-1.2259E+00	-1.3466E+00
6.760E-03	-7.9870E-01	-9.0313E-01	-1.0052E+00	-1.1047E+00
7.314E-03	-6.4188E-01	-7.2802E-01	-8.1278E-01	-8.9616E-01
7.868E-03	-5.1312E-01	-5.8594E-01	-6.5865E-01	-7.3123E-01
8.422E-03	-4.1752E-01	-4.8222E-01	-5.4819E-01	-6.1542E-01
8.975E-03	-3.5390E-01	-4.1511E-01	-4.7900E-01	-5.4555E-01
9.528E-03	-3.1358E-01	-3.7428E-01	-4.3894E-01	-5.0758E-01
1.008E-02	-2.8715E-01	-3.4856E-01	-4.1505E-01	-4.8666E-01
1.063E-02	-2.6832E-01	-3.3061E-01	-3.9888E-01	-4.7315E-01
1.118E-02	-2.5390E-01	-3.1684E-01	-3.8646E-01	-4.6274E-01
1.173E-02	-2.4237E-01	-3.0571E-01	-3.7621E-01	-4.5390E-01
1.228E-02	-2.3352E-01	-2.9718E-01	-3.6843E-01	-4.4724E-01
1.283E-02	-2.2740E-01	-2.9158E-01	-3.6368E-01	-4.4371E-01
1.338E-02	-2.2394E-01	-2.8894E-01	-3.6219E-01	-4.4370E-01
1.393E-02	-2.2297E-01	-2.8915E-01	-3.6390E-01	-4.4725E-01
1.447E-02	-2.2382E-01	-2.9143E-01	-3.6795E-01	-4.5338E-01
1.502E-02	-2.2617E-01	-2.9543E-01	-3.7393E-01	-4.6166E-01
1.556E-02	-2.2965E-01	-3.0071E-01	-3.8133E-01	-4.7150E-01
1.611E-02	-2.3393E-01	-3.0687E-01	-3.8969E-01	-4.8239E-01
1.665E-02	-2.3892E-01	-3.1383E-01	-3.9893E-01	-4.9424E-01
1.719E-02	-2.4442E-01	-3.2136E-01	-4.0881E-01	-5.0676E-01
1.758E-02	-2.4864E-01	-3.2707E-01	-4.1624E-01	-5.1611E-01

Appendix B

Curve and Surface Fit Plots and Threshold Distances

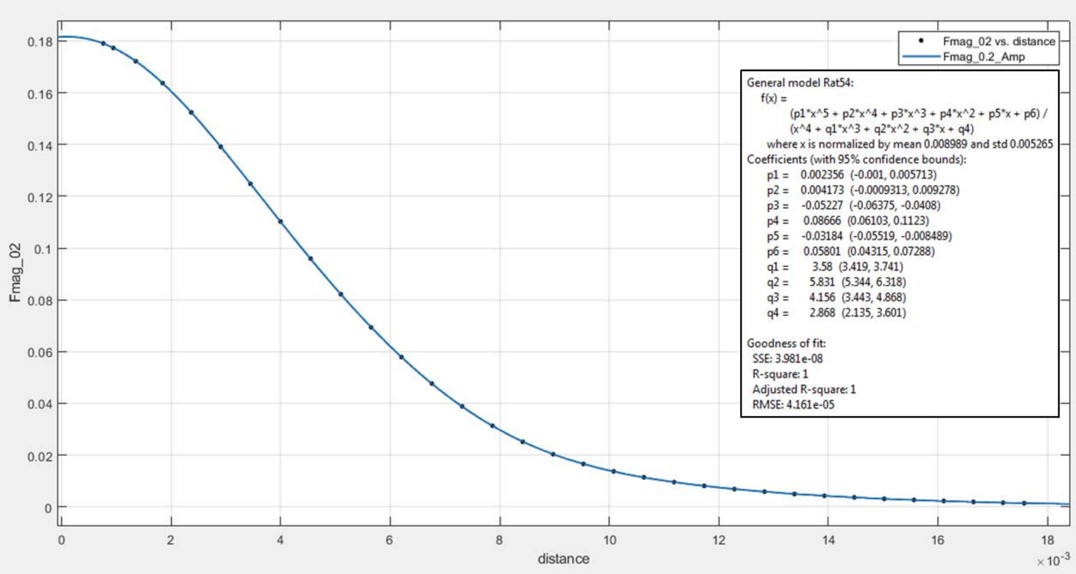

```
General model Rat54:
   f(x) =
          (p1*x^5 + p2*x^4 + p3*x^3 + p4*x^2 + p5*x + p6) /
          (x^4 + q1*x^3 + q2*x^2 + q3*x + q4)
     where x is normalized by mean 0.008989 and std 0.005265
Coefficients (with 95% confidence bounds):
     p1 =    0.002356  (-0.001, 0.005713)
     p2 =    0.004173  (-0.0009313, 0.009278)
     p3 =    -0.05227  (-0.06375, -0.0408)
     p4 =     0.08666  (0.06103, 0.1123)
     p5 =    -0.03184  (-0.05519, -0.008489)
     p6 =     0.05801  (0.04315, 0.07288)
     q1 =        3.58  (3.419, 3.741)
     q2 =       5.831  (5.344, 6.318)
     q3 =       4.156  (3.443, 4.868)
     q4 =       2.868  (2.135, 3.601)

Goodness of fit:
  SSE: 3.981e-08
  R-square: 1
  Adjusted R-square: 1
  RMSE: 4.161e-05
```

Figure 108: Curve Fit for Magnitude of Magnetic Force (N) vs. Distance (m) – 0.2 Amp Coil Excitation

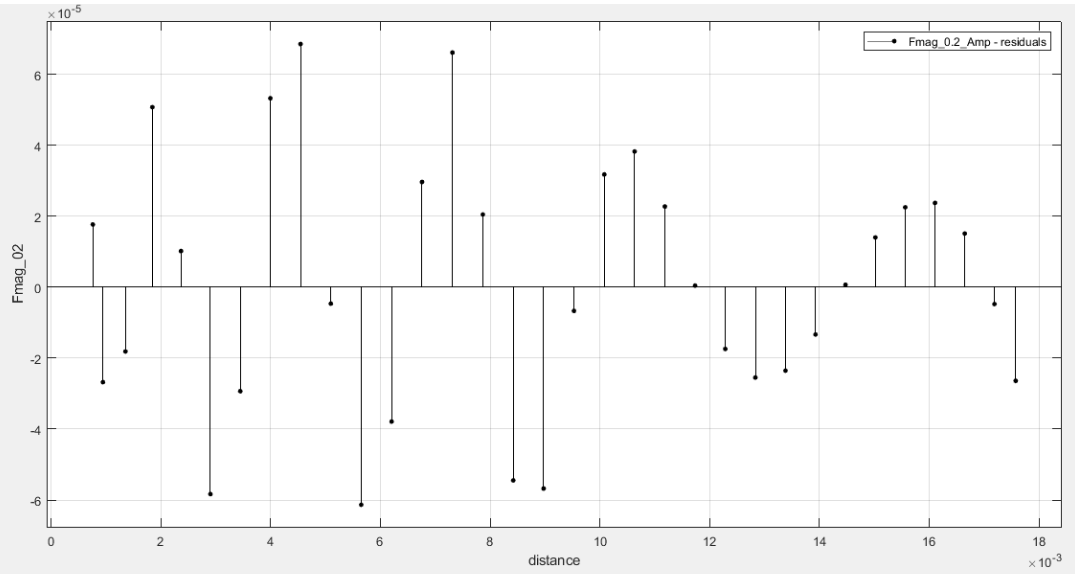

Figure 109: Residuals Plot for Magnitude of Magnetic Force (N) vs. Distance (m) – 0.2 Amp Coil Excitation

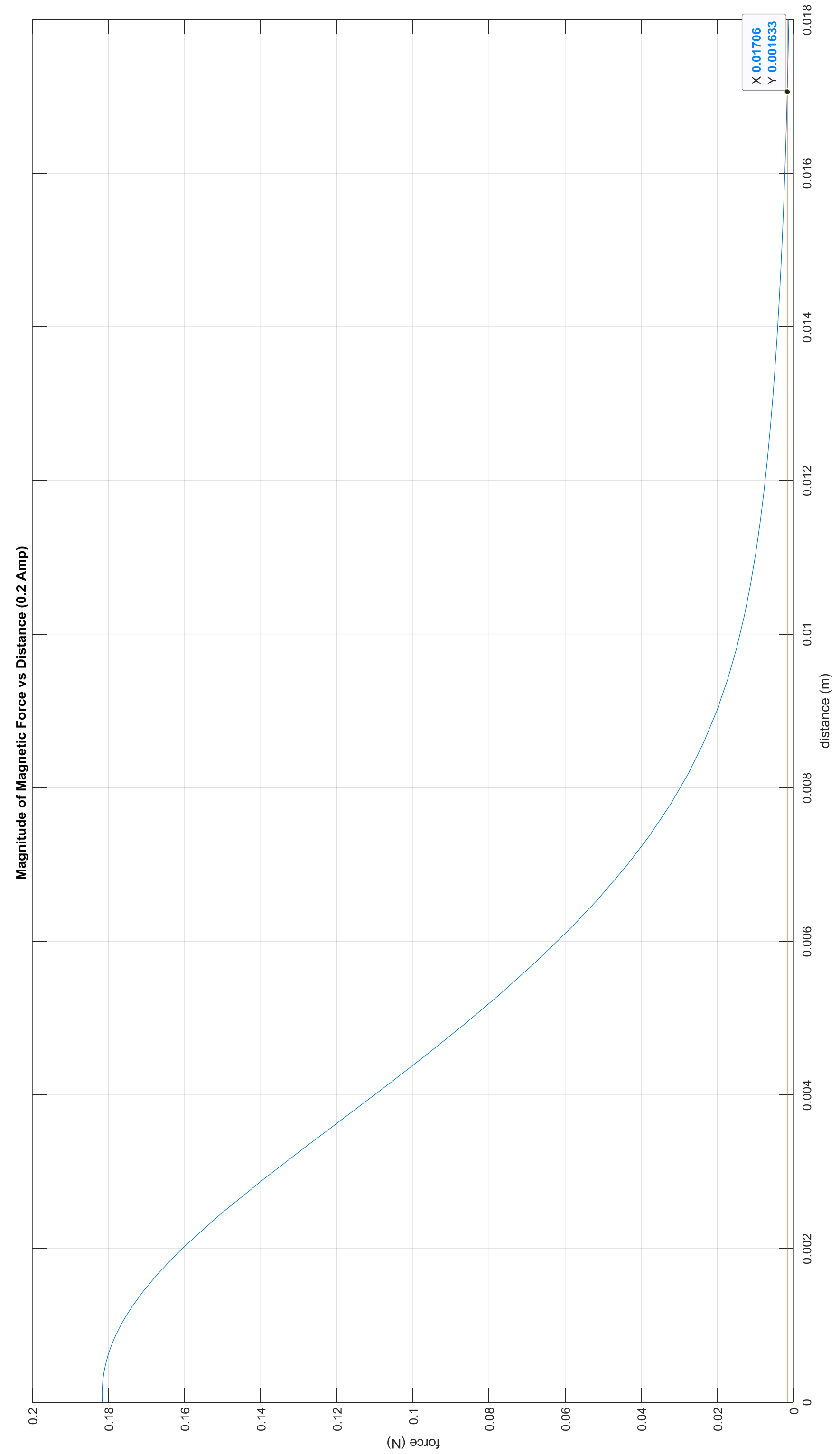

Figure 110: Threshold Distance where Iron and Iron + PM Forces are Equal (0.2 Amp)

MATLAB Source Code: Determination of Intersection Point of Iron Only Force and Iron + PM Force for 0.2 Ampere Coil Excitation

```
%% ==============  Fmag for 0.2 Amp of Current ================ %%
syms c x
%Coefficients (with 95% confidence bounds), where x is normalized
by mean
% 0.008989 and std 0.005265
    m1 = 0.008989;
    std1 = 0.005265;
F_sphere_02 = 0.00163283400972794;   % COMSOL prediction of EM
force on rotor
   c1 =  0.002356;  %(-0.001, 0.005713)
   c2 =  0.004173;  %(-0.0009313, 0.009278)
   c3 = -0.05227;   %(-0.06375, -0.0408)
   c4 =  0.08666;   %(0.06103, 0.1123)
   c5 = -0.03184;   %(-0.05519, -0.008489)
   c6 =  0.05801;   %(0.04315, 0.07288)
   c7 =  3.58;      %(3.419, 3.741)
   c8 =  5.831;     %(5.344, 6.318)
   c9 =  4.156;     %(3.443, 4.868)
  c10 =  2.868;     %(2.135, 3.601)
f02(x) = (c1*((x-m1)/std1)^5 + c2*((x-m1)/std1)^4 + c3*((x-
m1)/std1)^3 + c4*((x-m1)/std1)^2 + c5*((x-m1)/std1) + c6)/(((x-
m1)/std1)^4 + c7*((x-m1)/std1)^3 + c8*((x-m1)/std1)^2 + c9*((x-
m1)/std1) + c10);
eqn = (c1*c^5 + c2*c^4 + c3*c^3 + c4*c^2 + c5*c + c6)/(c^4 + c7*c^3
+ c8*c^2 + c9*c + c10) == F_sphere_02;
S = solve(eqn,c);
S1 = [vpa(S(1)); vpa(S(2)); vpa(S(3)); vpa(S(4)); vpa(S(5));];
S2 = std1*S1+m1;  %Point at which Iron+PM Force Intersects Iron
Only
Int_02 = S2(3);

fplot (f02)
hold on
fplot(F_sphere_02)
hold  on
plot(Int_02, F_sphere_02, 'r.')
xlim([0 0.018])
ylim([0 0.2])
grid on
xlabel('distance (m)')
ylabel('force (N)')
title('Magnitude of Magnetic Force vs Distance (0.2 Amp) ')
```

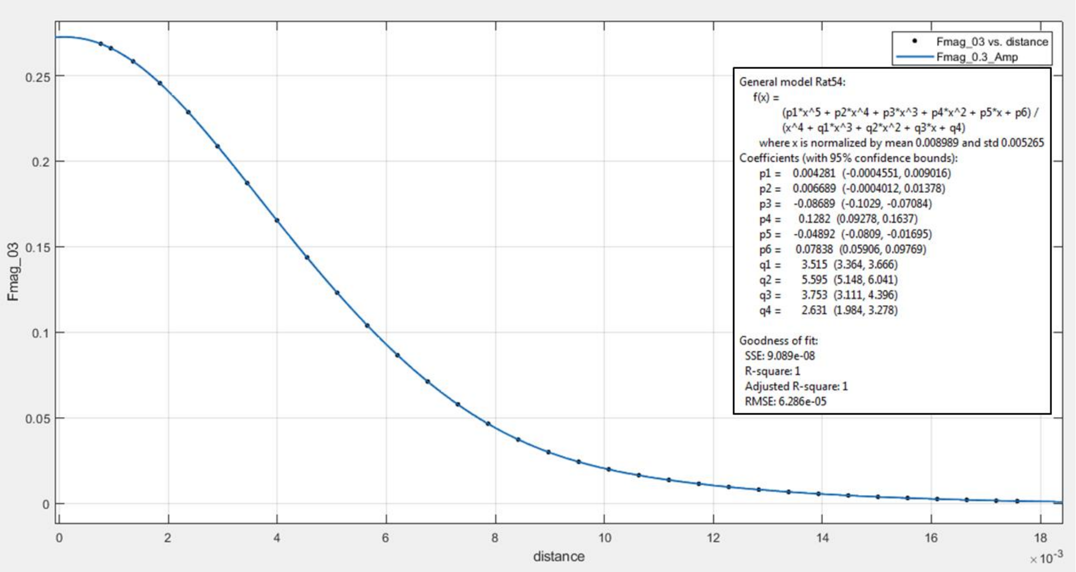

```
General model Rat54:
   f(x) =
         (p1*x^5 + p2*x^4 + p3*x^3 + p4*x^2 + p5*x + p6) /
         (x^4 + q1*x^3 + q2*x^2 + q3*x + q4)
    where x is normalized by mean 0.008989 and std 0.005265
Coefficients (with 95% confidence bounds):
    p1 =    0.004281  (-0.0004551, 0.009016)
    p2 =    0.006689  (-0.0004012, 0.01378)
    p3 =    -0.08689  (-0.1029, -0.07084)
    p4 =      0.1282  (0.09278, 0.1637)
    p5 =    -0.04892  (-0.0809, -0.01695)
    p6 =     0.07838  (0.05906, 0.09769)
    q1 =       3.515  (3.364, 3.666)
    q2 =       5.595  (5.148, 6.041)
    q3 =       3.753  (3.111, 4.396)
    q4 =       2.631  (1.984, 3.278)

Goodness of fit:
  SSE: 9.089e-08
  R-square: 1
  Adjusted R-square: 1
  RMSE: 6.286e-05
```

Figure 111: Curve Fit for Magnitude of Magnetic Force (N) vs. Distance (m) – 0.3 Amp Coil Excitation

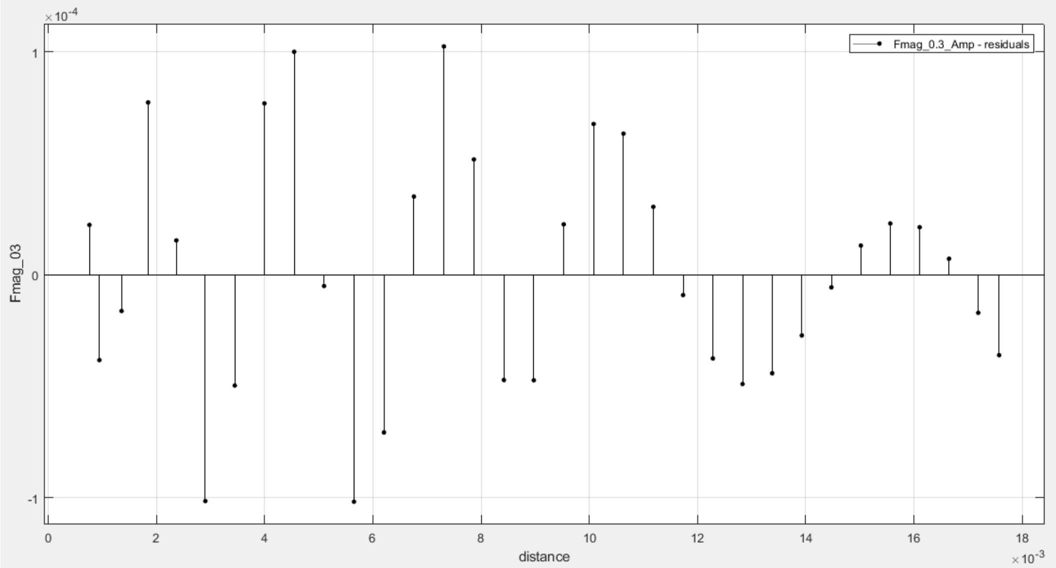

Figure 112: Residuals Plot for Magnitude of Magnetic Force (N) vs. Distance (m) – 0.3 Amp Coil Excitation

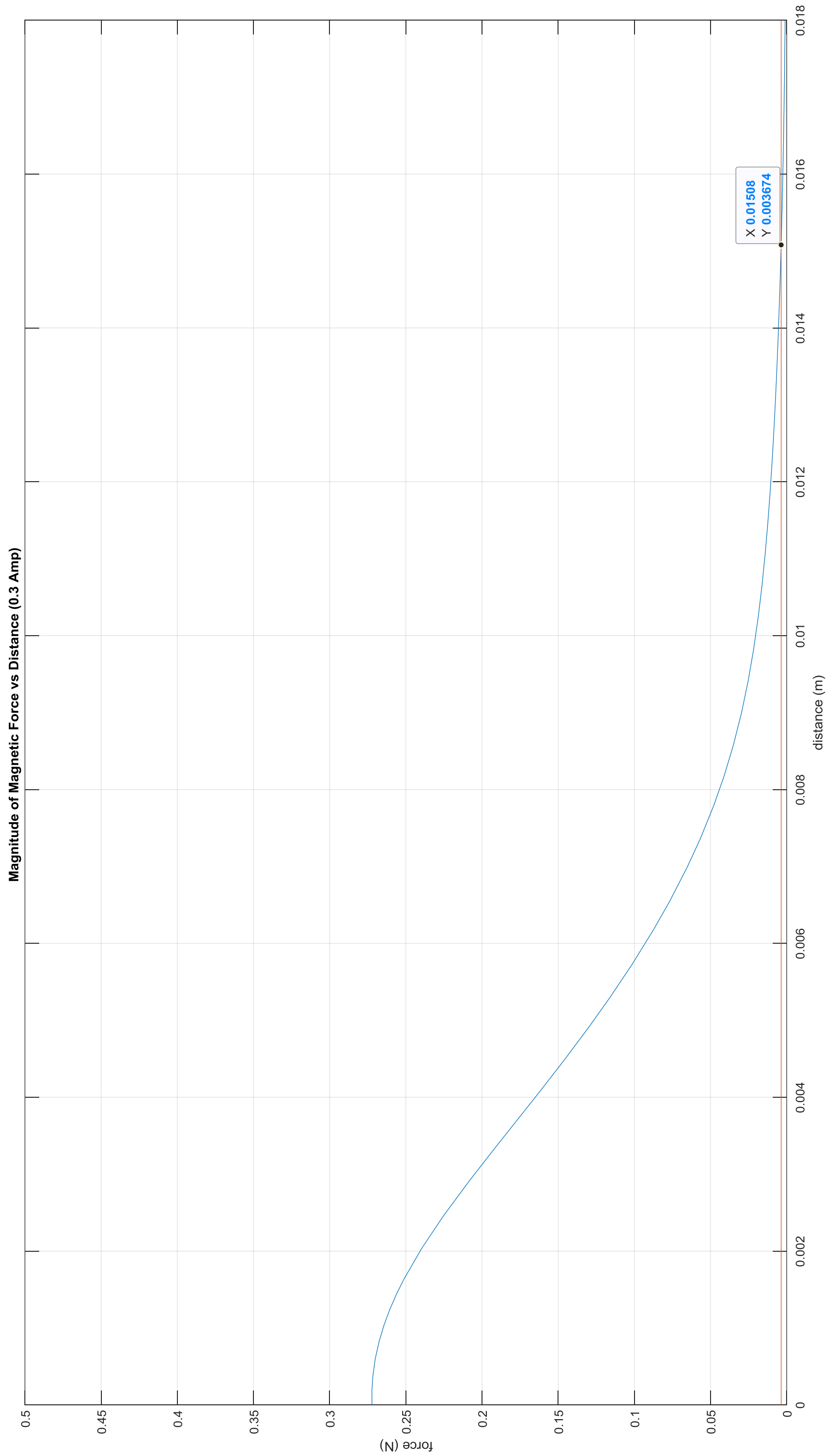

Figure 113: Threshold Distance where Iron and Iron + PM Forces are Equal (0.3Amp)

MATLAB Source Code: Determination of Intersection Point of Iron Only Force and Iron + PM Force for 0.3 Ampere Coil Excitation

```
%% 3  Fmag for 0.3 Amp of Current ================ %%
syms d x
%Coefficients (with 95% confidence bounds), where x is normalized
by mean
% 0.008989 and std 0.005265
    m1 = 0.008989;
    std1 = 0.005265;
F_sphere_03 = 0.00367395347096692;   % COMSOL prediction of EM
force on rotor
   d1 =  0.004281;   %(-0.0004551, 0.009016)
   d2 =  0.006689;   %(-0.0004012, 0.01378)
   d3 = -0.08689;    %(-0.1029, -0.07084)
   d4 =  0.1282;     %(0.09278, 0.1637)
   d5 = -0.04892;    %(-0.0809, -0.01695)
   d6 =  0.07838;    %(0.05906, 0.09769)
   d7 =  3.515;      %(3.364, 3.666)
   d8 =  5.595;      %(5.148, 6.041)
   d9 =  3.753;      %(3.111, 4.396)
  d10 =  2.631;      %(1.984, 3.278)
f03(x) = (d1*((x-m1)/std1)^5 + d2*((x-m1)/std1)^4 + d3*((x-
m1)/std1)^3 + d4*((x-m1)/std1)^2 + d5*((x-m1)/std1) + d6)/(((x-
m1)/std1)^4 + d7*((x-m1)/std1)^3 + d8*((x-m1)/std1)^2 + d9*((x-
m1)/std1) + d10);
eqn = (d1*d^5 + d2*d^4 + d3*d^3 + d4*d^2 + d5*d + d6)/(d^4 + d7*d^3
+ d8*d^2 + d9*d + d10) == F_sphere_03;
S = solve(eqn,d);
S1 = [vpa(S(1)); vpa(S(2)); vpa(S(3)); vpa(S(4)); vpa(S(5));];
S2 = std1*S1+m1;  %Point at which Iron+PM Force Intersects Iron
Only
Int_03 = S2(3);

fplot (f03)
hold on
fplot(F_sphere_03)
hold  on
plot(Int_03, F_sphere_03, 'r.')
xlim([0 0.018])
ylim([0 0.5])
grid on
xlabel('distance (m)')
ylabel('force (N)')
title('Magnitude of Magnetic Force vs Distance (0.3 Amp) ')
```

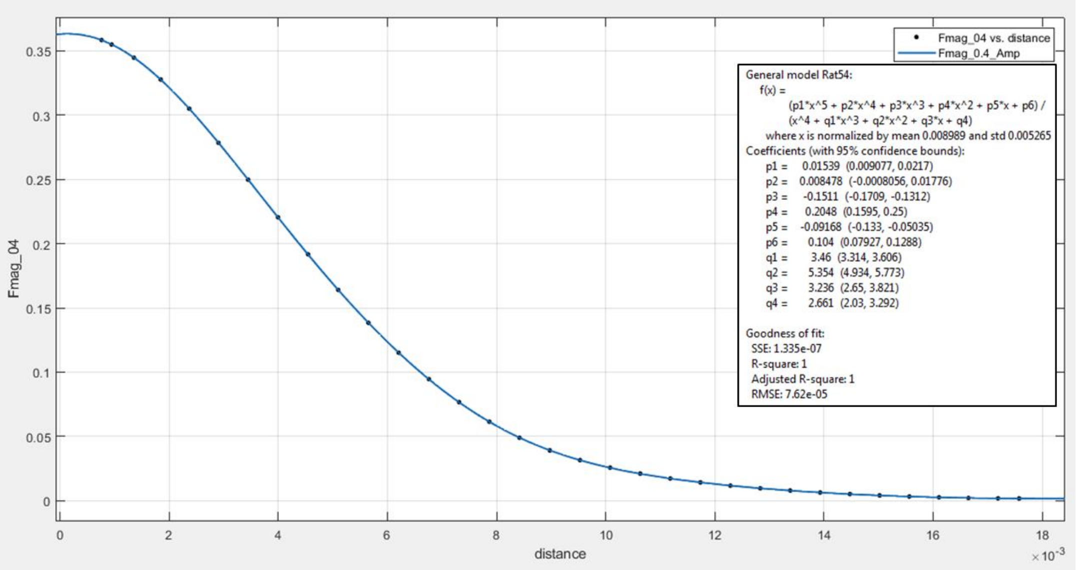

```
General model Rat54:
   f(x) =
        (p1*x^5 + p2*x^4 + p3*x^3 + p4*x^2 + p5*x + p6) /
        (x^4 + q1*x^3 + q2*x^2 + q3*x + q4)
     where x is normalized by mean 0.008989 and std 0.005265
Coefficients (with 95% confidence bounds):
     p1 =     0.01539  (0.009077, 0.0217)
     p2 =    0.008478  (-0.0008056, 0.01776)
     p3 =     -0.1511  (-0.1709, -0.1312)
     p4 =      0.2048  (0.1595, 0.25)
     p5 =    -0.09168  (-0.133, -0.05035)
     p6 =       0.104  (0.07927, 0.1288)
     q1 =        3.46  (3.314, 3.606)
     q2 =       5.354  (4.934, 5.773)
     q3 =       3.236  (2.65, 3.821)
     q4 =       2.661  (2.03, 3.292)

Goodness of fit:
  SSE: 1.335e-07
  R-square: 1
  Adjusted R-square: 1
  RMSE: 7.62e-05
```

Figure 114: Curve Fit for Magnitude of Magnetic Force (N) vs. Distance (m) – 0.4 Amp Coil Excitation

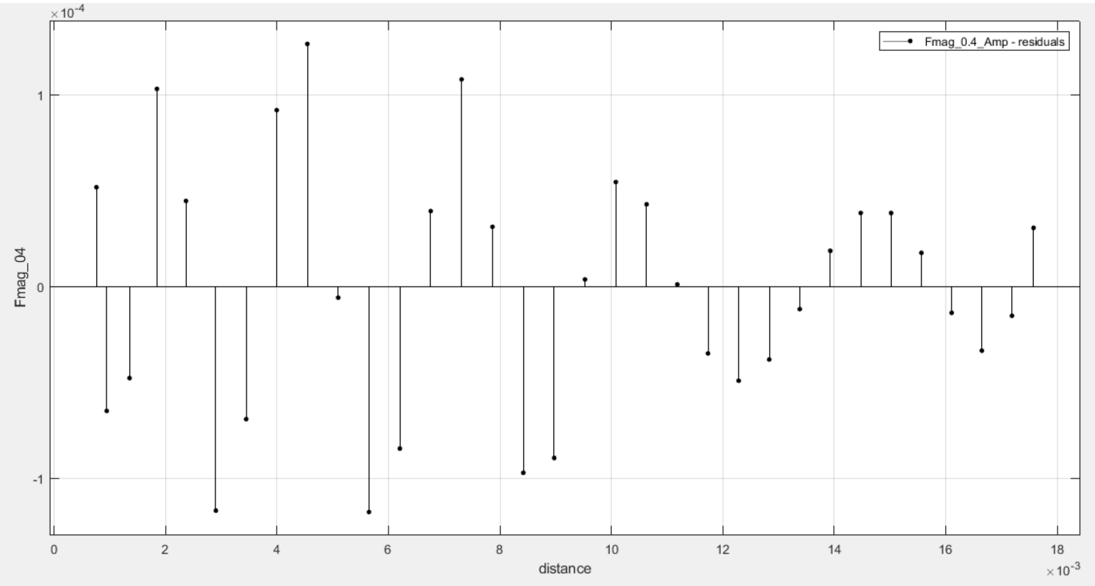

Figure 115: Residuals Plot for Magnitude of Magnetic Force (N) vs. Distance (m) – 0.4 Amp Coil Excitation

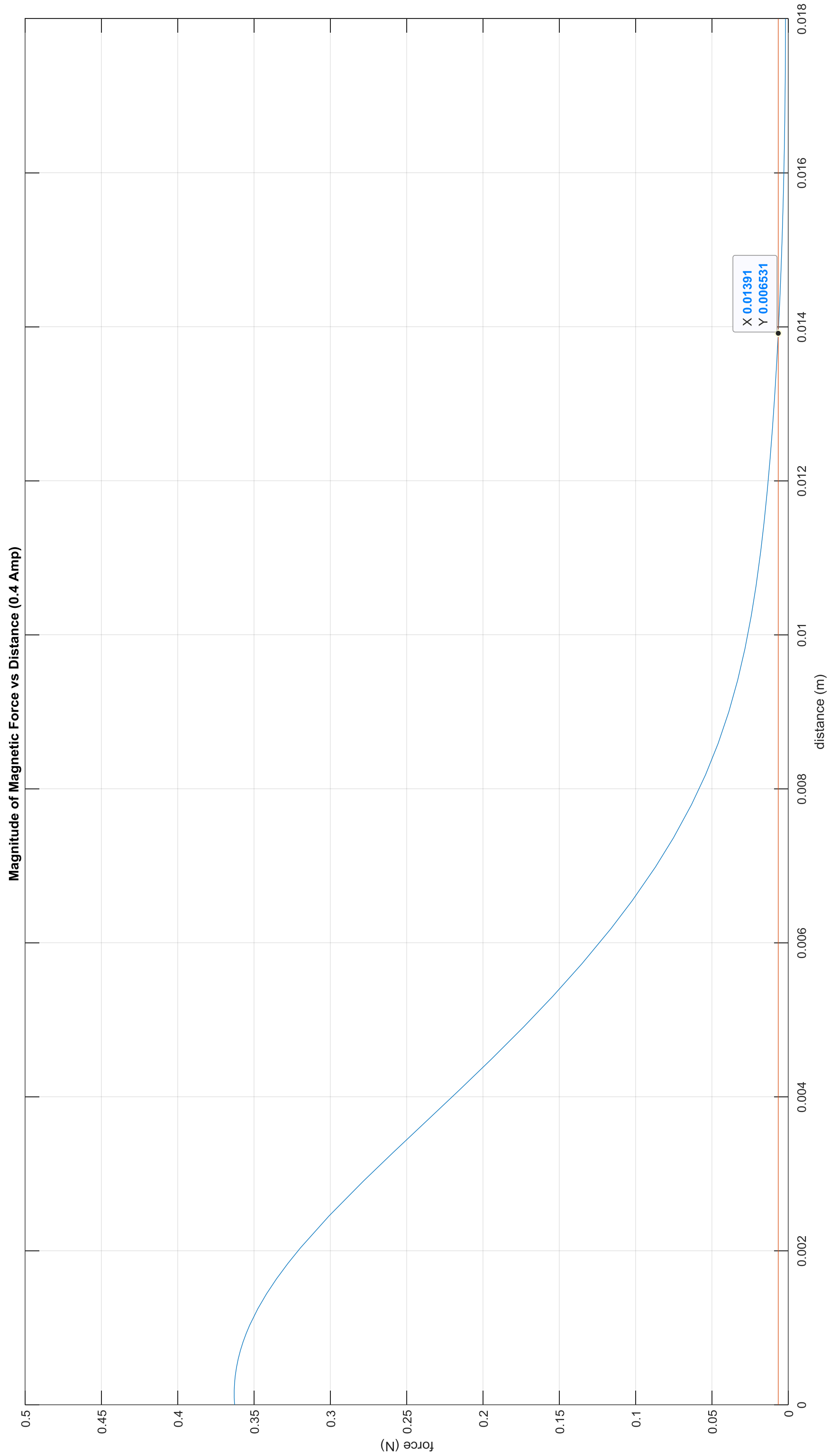

Figure 116: Threshold Distance where Iron and Iron + PM Forces are Equal (0.4 Amp)

MATLAB Source Code: Determination of Intersection Point of Iron Only Force and Iron + PM Force for 0.4 Ampere Coil Excitation

```
%% ==============  Fmag for 0.4 Amp of Current ================ %%
syms e x
%Coefficients (with 95% confidence bounds), where x is normalized
by mean
% 0.008989 and std 0.005265
    m1 = 0.008989;
    std1 = 0.005265;
F_sphere_04 = 0.00653142112431786;   % COMSOL prediction of EM
force on rotor
   e1 =  0.01539;  %(0.009077, 0.0217)
   e2 =  0.008478; %(-0.0008056, 0.01776)
   e3 = -0.1511;   %(-0.1709, -0.1312)
   e4 =  0.2048;   %(0.1595, 0.25)
   e5 = -0.09168;  %(-0.133, -0.05035)
   e6 =  0.104;    %(0.07927, 0.1288)
   e7 =  3.46;     %(3.314, 3.606)
   e8 =  5.354;    %(4.934, 5.773)
   e9 =  3.236;    %(2.65, 3.821)
  e10 =  2.661;    %(2.03, 3.292)
f04(x) = (e1*((x-m1)/std1)^5 + e2*((x-m1)/std1)^4 + e3*((x-
m1)/std1)^3 + e4*((x-m1)/std1)^2 + e5*((x-m1)/std1) + e6)/(((x-
m1)/std1)^4 + e7*((x-m1)/std1)^3 + e8*((x-m1)/std1)^2 + e9*((x-
m1)/std1) + e10);
eqn = (e1*e^5 + e2*e^4 + e3*e^3 + e4*e^2 + e5*e + e6)/(e^4 + e7*e^3
+ e8*e^2 + e9*e + e10) == F_sphere_04;
S = solve(eqn,e);
S1 = [vpa(S(1)); vpa(S(2)); vpa(S(3)); vpa(S(4)); vpa(S(5));];
S2 = std1*S1+m1;  %Point at which Iron+PM Force Intersects Iron
Only
Int_04 = S2(3);

fplot (f04)
hold on
fplot(F_sphere_04)
hold  on
plot(Int_04, F_sphere_04, 'r.')
xlim([0 0.018])
ylim([0 0.5])
grid on
xlabel('distance (m)')
ylabel('force (N)')
title('Magnitude of Magnetic Force vs Distance (0.4 Amp) ')
```

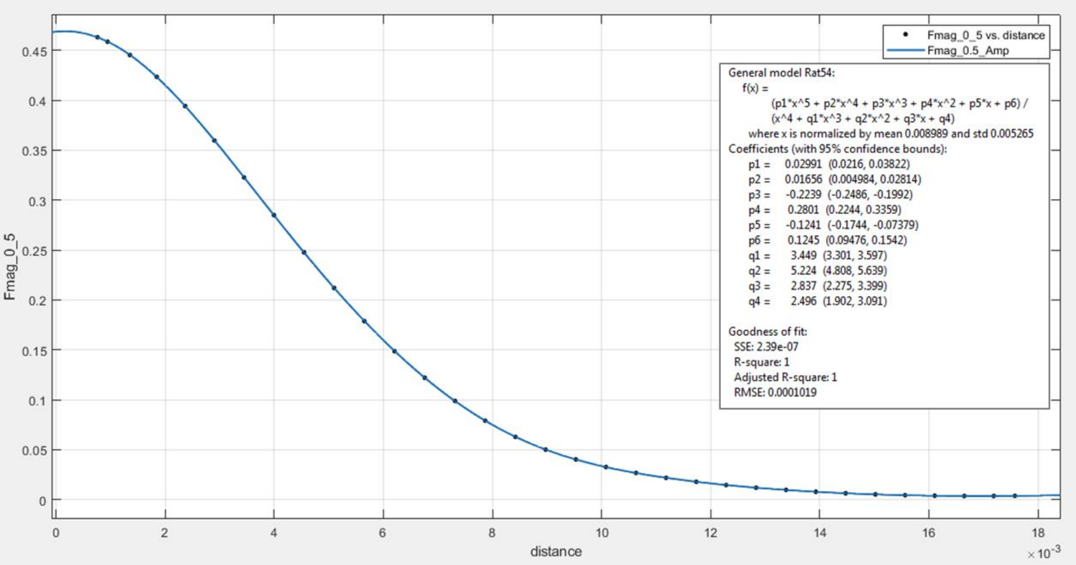

```
General model Rat54:
  f(x) =
        (p1*x^5 + p2*x^4 + p3*x^3 + p4*x^2 + p5*x + p6) /
        (x^4 + q1*x^3 + q2*x^2 + q3*x + q4)
    where x is normalized by mean 0.008989 and std 0.005265
Coefficients (with 95% confidence bounds):
    p1 =    0.02991  (0.0216, 0.03822)
    p2 =    0.01656  (0.004984, 0.02814)
    p3 =    -0.2239  (-0.2486, -0.1992)
    p4 =     0.2801  (0.2244, 0.3359)
    p5 =    -0.1241  (-0.1744, -0.07379)
    p6 =     0.1245  (0.09476, 0.1542)
    q1 =      3.449  (3.301, 3.597)
    q2 =      5.224  (4.808, 5.639)
    q3 =      2.837  (2.275, 3.399)
    q4 =      2.496  (1.902, 3.091)

Goodness of fit:
  SSE: 2.39e-07
  R-square: 1
  Adjusted R-square: 1
  RMSE: 0.0001019
```

Figure 117: Curve Fit for Magnitude of Magnetic Force (N) vs. Distance (m) – 0.5 Amp Coil Excitation

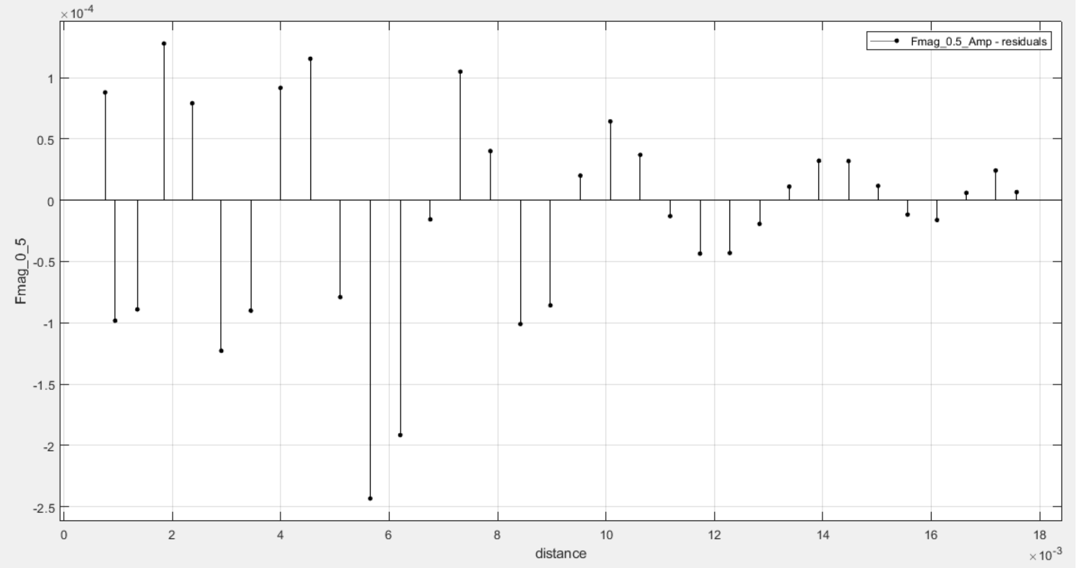

Figure 118: Residuals Plot for Magnitude of Magnetic Force (N) vs. Distance (m) – 0.5 Amp Coil Excitation

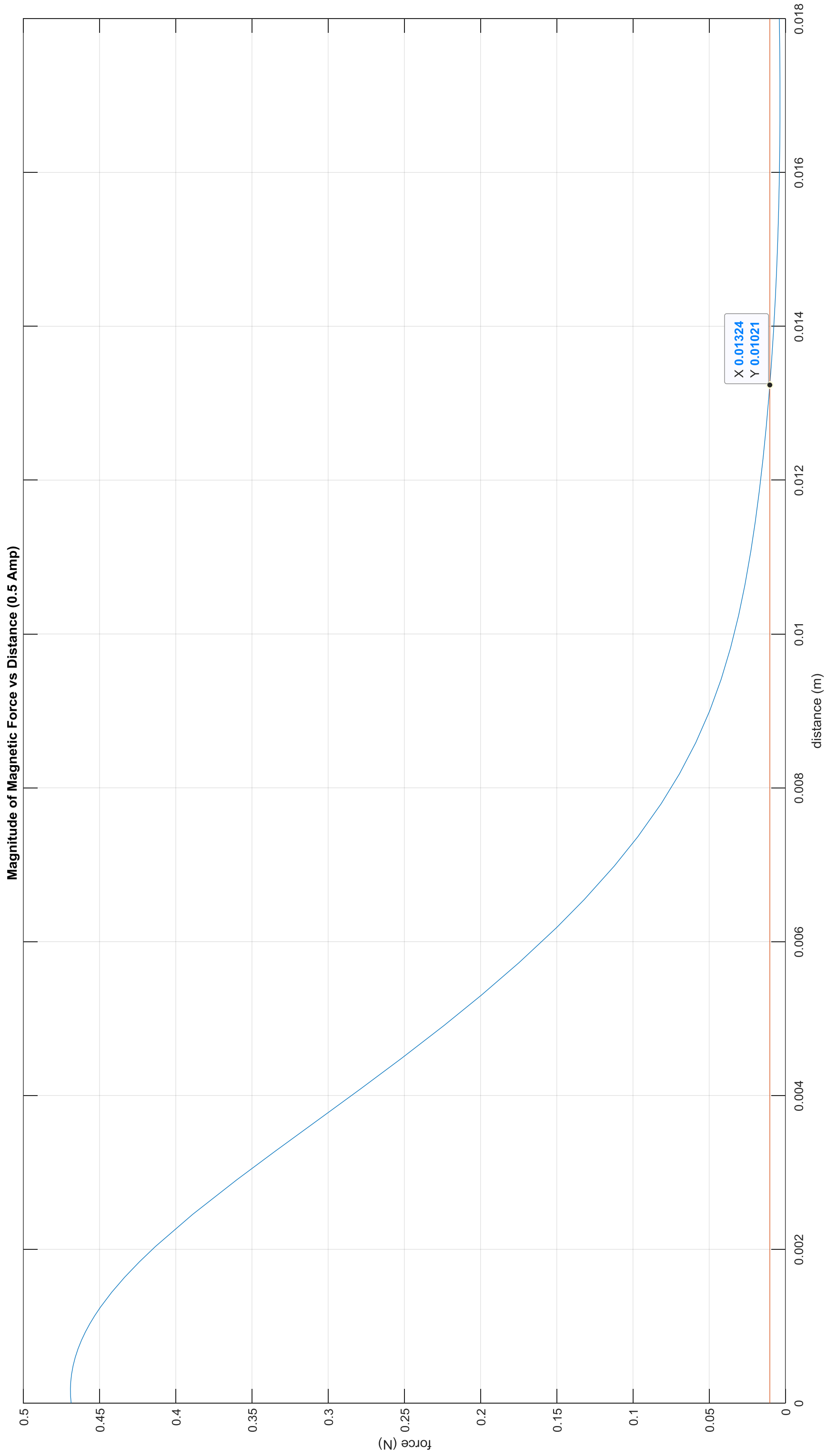

Figure 119: Threshold Distance where Iron and Iron + PM Forces are Equal (0.5 Amp)

MATLAB Source Code: Determination of Intersection Point of Iron Only Force and Iron + PM Force for 0.5 Ampere Coil Excitation

```
syms x
%Coefficients (with 95% confidence bounds), where x is normalized
by mean
% 0.008989 and std 0.005265
    m1 = 0.008989;
    std1 = 0.005265;
F_sphere_05 = 0.0102052895057943;   % COMSOL prediction of EM force
on rotor
   p1 =  0.02991;  %(0.0216, 0.03822)
   p2 =  0.01656;  %(0.004984, 0.02814)
   p3 = -0.2239;   %(-0.2486, -0.1992)
   p4 =  0.2801;   %(0.2244, 0.3359)
   p5 = -0.1241;   %(-0.1744, -0.07379)
   p6 =  0.1245;   %(0.09476, 0.1542)
   p7 =  3.449;    %(3.301, 3.597)
   p8 =  5.224;    %(4.808, 5.639)
   p9 =  2.837;    %(2.275, 3.399)
  p10 =  2.496;    %(1.902, 3.091)
f05(x) = (p1*((x-m1)/std1)^5 + p2*((x-m1)/std1)^4 + p3*((x-
m1)/std1)^3 + p4*((x-m1)/std1)^2 + p5*((x-m1)/std1) + p6)/(((x-
m1)/std1)^4 + p7*((x-m1)/std1)^3 + p8*((x-m1)/std1)^2 + p9*((x-
m1)/std1) + p10);
eqn = (p1*x^5 + p2*x^4 + p3*x^3 + p4*x^2 + p5*x + p6)/(x^4 + p7*x^3
+ p8*x^2 + p9*x + p10) == F_sphere_05;
S = solve(eqn,x);
S1 = [vpa(S(1)); vpa(S(2)); vpa(S(3)); vpa(S(4)); vpa(S(5));];
S2 = std1*S1+m1  %Point at which Iron+PM Force Intersects Magnitude
of Magnetic
Int_05 = S2(3);

fplot (f05)
hold on
fplot(F_sphere_05)
hold  on
plot(Int_05, F_sphere_05, 'r.')
xlim([0 0.018])
ylim([0 0.5])
grid on
xlabel('distance (m)')
ylabel('force (N)')
title('Magnitude of Magnetic Force vs Distance (0.5 Amp) ')
```

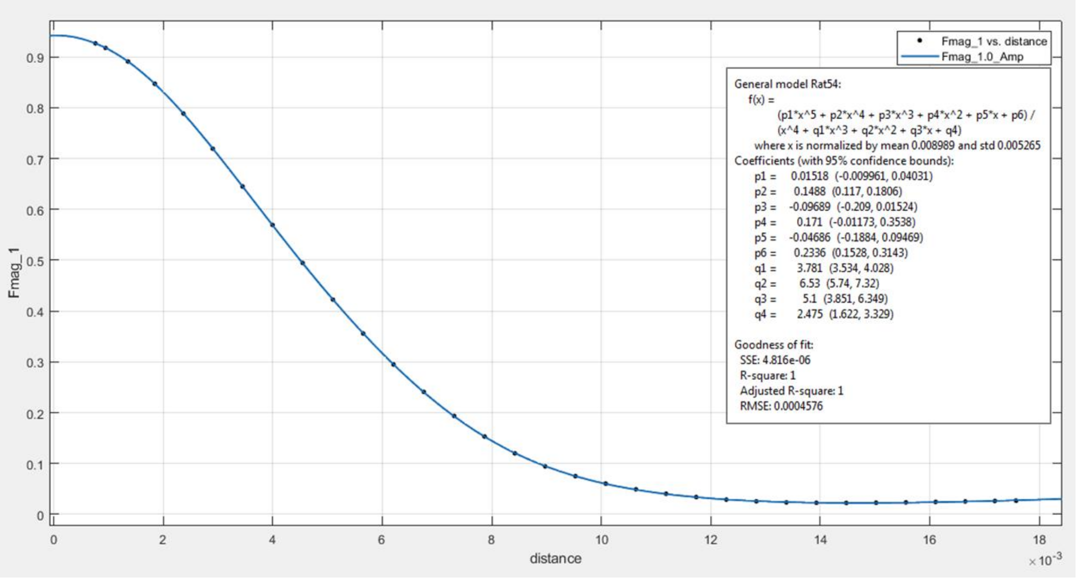

```
General model Rat54:
   f(x) =
          (p1*x^5 + p2*x^4 + p3*x^3 + p4*x^2 + p5*x + p6) /
          (x^4 + q1*x^3 + q2*x^2 + q3*x + q4)
     where x is normalized by mean 0.008989 and std 0.005265
Coefficients (with 95% confidence bounds):
     p1 =     0.01518  (-0.009961, 0.04031)
     p2 =      0.1488  (0.117, 0.1806)
     p3 =    -0.09689  (-0.209, 0.01524)
     p4 =       0.171  (-0.01173, 0.3538)
     p5 =    -0.04686  (-0.1884, 0.09469)
     p6 =      0.2336  (0.1528, 0.3143)
     q1 =       3.781  (3.534, 4.028)
     q2 =        6.53  (5.74, 7.32)
     q3 =         5.1  (3.851, 6.349)
     q4 =       2.475  (1.622, 3.329)

Goodness of fit:
  SSE: 4.816e-06
  R-square: 1
  Adjusted R-square: 1
  RMSE: 0.0004576
```

Figure 120: Curve Fit for Magnitude of Magnetic Force (N) vs. Distance (m) – 1.0 Amp Coil Excitation

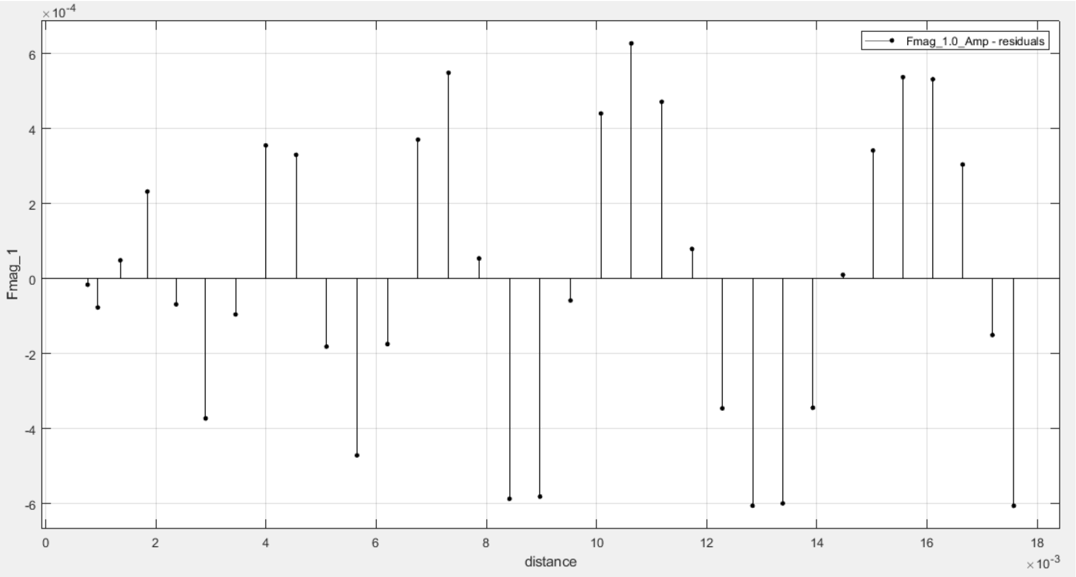

Figure 121: Residuals Plot for Magnitude of Magnetic Force (N) vs. Distance (m) – 1.0 Amp Coil Excitation

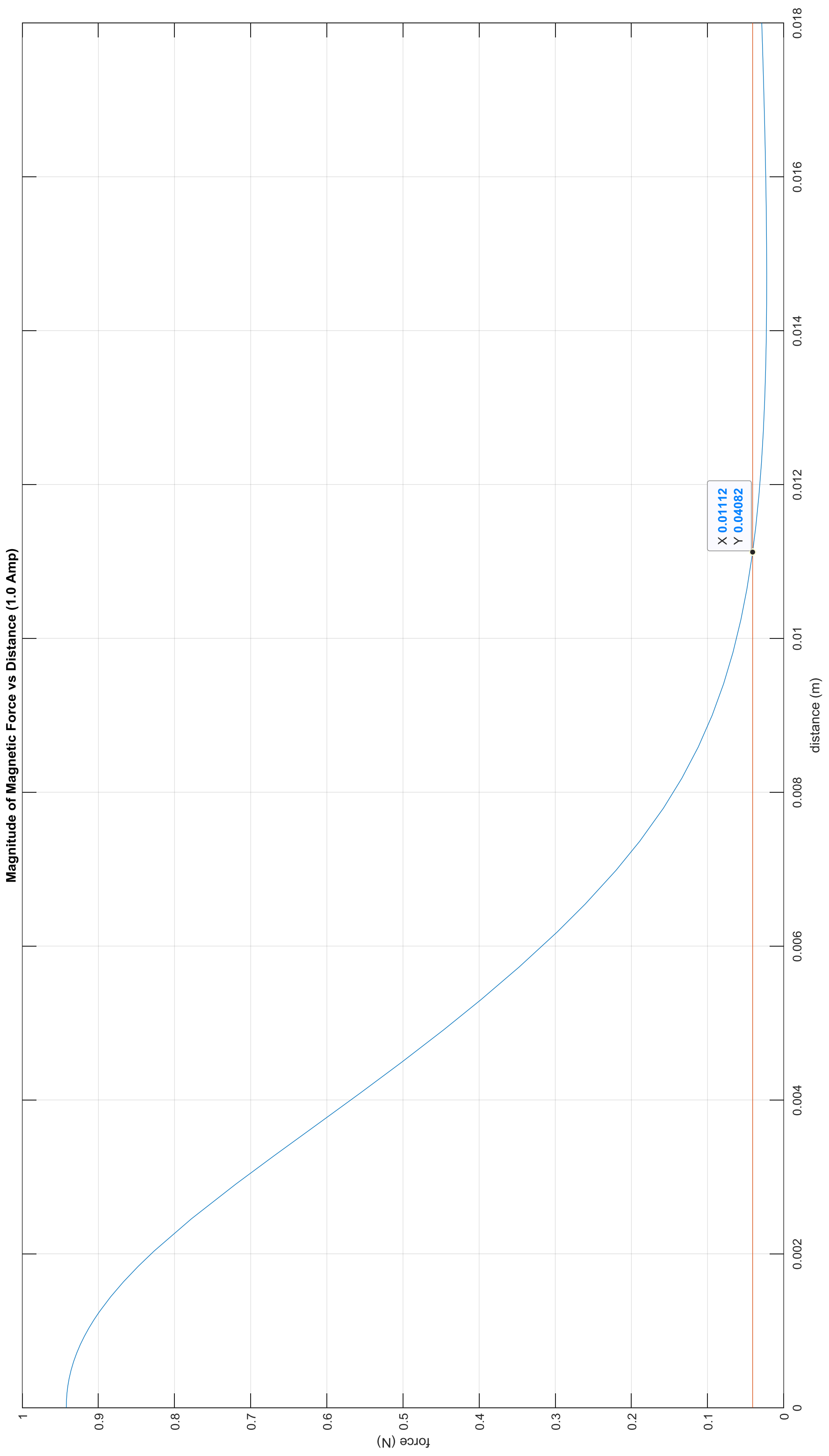

Figure 122: Threshold Distance where Iron and Iron + PM Forces are Equal (1.0 Amp)

MATLAB Source Code: Determination of Intersection Point of Iron Only Force and Iron + PM Force for 1.0 Ampere Coil Excitation

```
%% ==============  Fmag for 1.0 Amp of Current ================ %%
syms y x
% Coefficients with 95% confidence bounds, where x is normalized by
mean
% 0.008989 and std 0.005265
F_sphere_1 = 0.0408215383560347;
   q1 =  0.01518;  %(-0.009961, 0.04031)
   q2 =  0.1488;   %(0.117, 0.1806)
   q3 = -0.09689;  %(-0.209, 0.01524)
   q4 =  0.171;    %(-0.01173, 0.3538)
   q5 = -0.04686;  %(-0.1884, 0.09469)
   q6 =  0.2336;   %(0.1528, 0.3143)
   q7 =  3.781;    %(3.534, 4.028)
   q8 =  6.53;     %(5.74, 7.32)
   q9 =  5.1;      %(3.851, 6.349)
  q10 =  2.475;    %(1.622, 3.329)
eqn1 = (q1*y^5 + q2*y^4 + q3*y^3 + q4*y^2 + q5*y + q6)/(y^4 +
q7*y^3 + q8*y^2 + q9*y + q10) == F_sphere_1;
T = solve(eqn1,y);
T1 = [vpa(T(1)); vpa(T(2)); vpa(T(3)); vpa(T(4)); vpa(T(5));];
T2 = std1*T1+m1
Int_1 = T2(1);

f15(x) = (q1*((x-m1)/std1)^5 +q2*((x-m1)/std1)^4 + q3*((x-
m1)/std1)^3 + q4*((x-m1)/std1)^2 + q5*((x-m1)/std1) + q6)/(((x-
m1)/std1)^4 + q7*((x-m1)/std1)^3 + q8*((x-m1)/std1)^2 + q9*((x-
m1)/std1) + q10)
fplot (f15)
hold on
fplot(F_sphere_1)
hold on
plot(Int_1, F_sphere_1, 'r.')
xlim([0 0.018])
ylim([0 1])
grid on
xlabel('distance (m)')
ylabel('force (N)')
title('Magnitude of Magnetic Force vs Distance (1.0 Amp)')
```

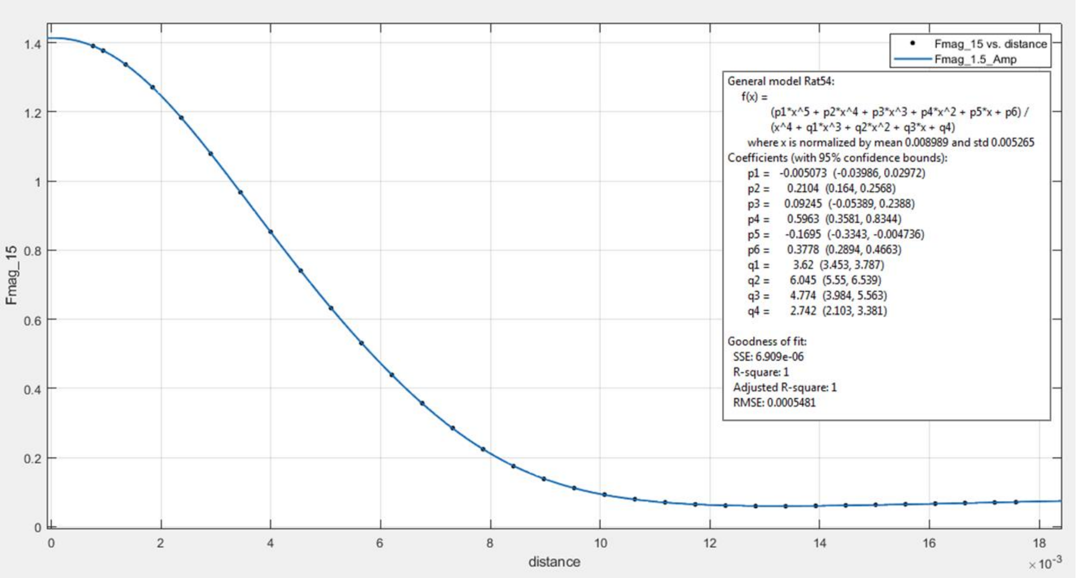

```
General model Rat54:
   f(x) =
         (p1*x^5 + p2*x^4 + p3*x^3 + p4*x^2 + p5*x + p6) /
         (x^4 + q1*x^3 + q2*x^2 + q3*x + q4)
     where x is normalized by mean 0.008989 and std 0.005265
Coefficients (with 95% confidence bounds):
     p1 =   -0.005073  (-0.03986, 0.02972)
     p2 =      0.2104  (0.164, 0.2568)
     p3 =     0.09245  (-0.05389, 0.2388)
     p4 =      0.5963  (0.3581, 0.8344)
     p5 =     -0.1695  (-0.3343, -0.004736)
     p6 =      0.3778  (0.2894, 0.4663)
     q1 =        3.62  (3.453, 3.787)
     q2 =       6.045  (5.55, 6.539)
     q3 =       4.774  (3.984, 5.563)
     q4 =       2.742  (2.103, 3.381)

Goodness of fit:
  SSE: 6.909e-06
  R-square: 1
  Adjusted R-square: 1
  RMSE: 0.0005481
```

Figure 123: Curve Fit for Magnitude of Magnetic Force (N) vs. Distance (m) – 1.5 Amps Coil Excitation

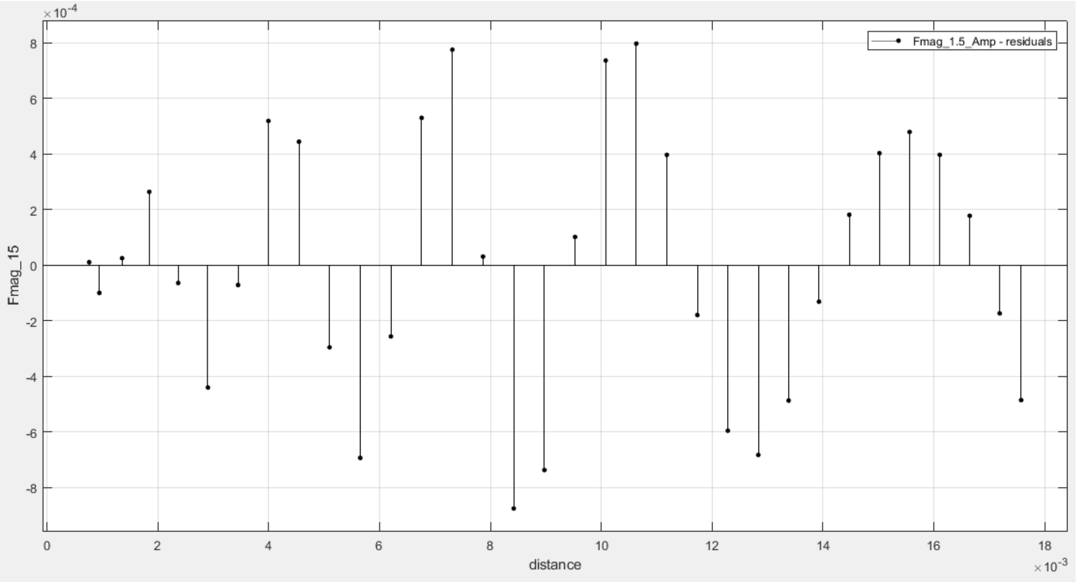

Figure 124: Residuals Plot for Magnitude of Magnetic Force (N) vs. Distance (m) – 1.5 Amps Coil Excitation

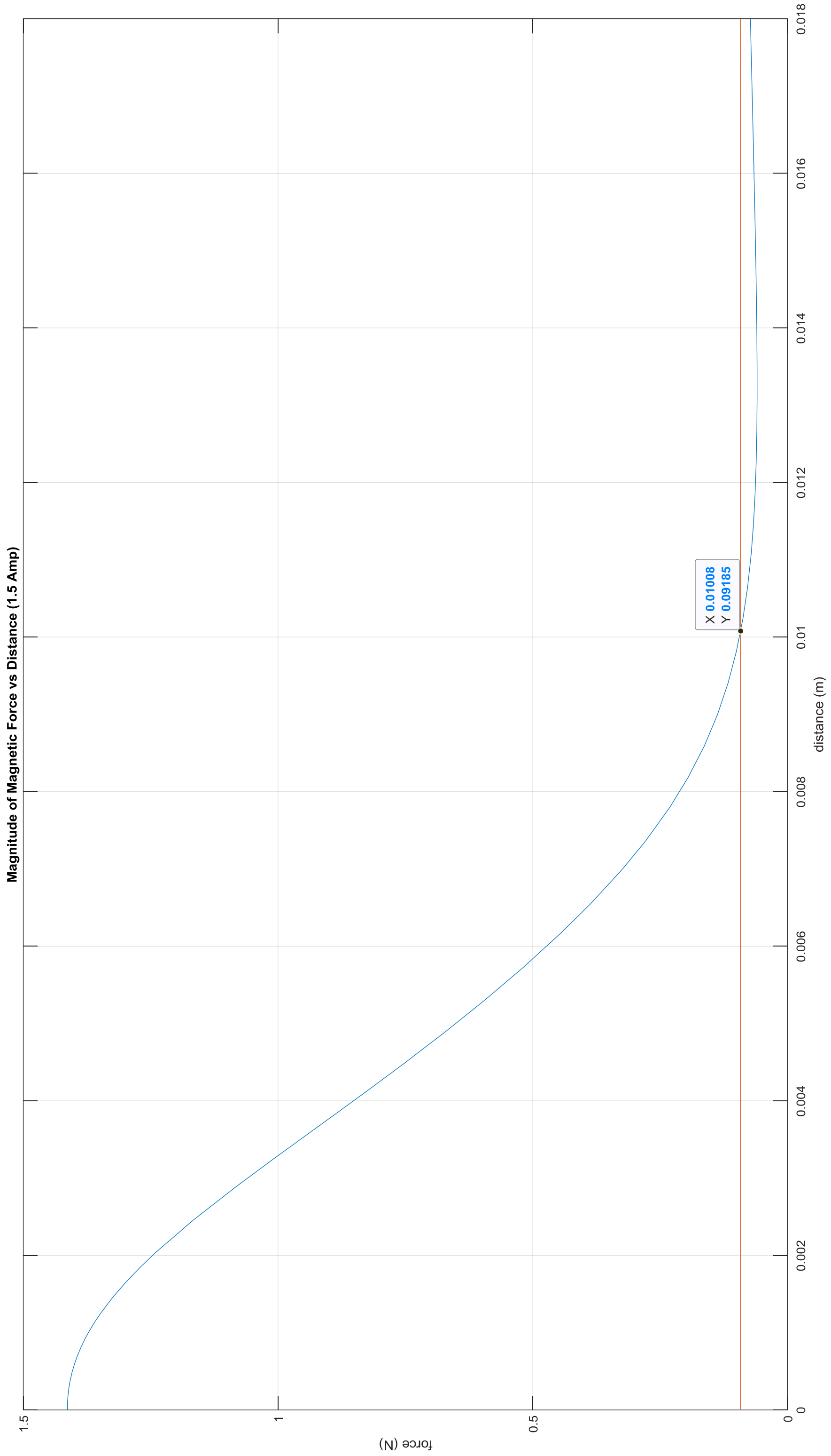

Figure 125: Threshold Distance where Iron and Iron + PM Forces are Equal (1.5 Amp)

MATLAB Source Code: Determination of Intersection Point of Iron Only Force and Iron + PM Force for 1.5 Ampere Coil Excitation

```
%% ======  Fmag for 1.5 Amp of Current ======= %%
syms z x
% Coefficients with 95% confidence bounds, where x is normalized by
mean
% 0.008989 and std 0.005265
F_sphere_15 = 0.0918477231825212;
   r1 = -0.005073;    %(-0.03986, 0.02972)
   r2 =  0.2104;      %(0.164, 0.2568)
   r3 =  0.09245;     %(-0.05389, 0.2388)
   r4 =  0.5963;      %(0.3581, 0.8344)
   r5 = -0.1695;      %(-0.3343, -0.004736)
   r6 =  0.3778;      %(0.2894, 0.4663)
   r7 =  3.62;        %(3.453, 3.787)
   r8 =  6.045;       %(5.55, 6.539)
   r9 =  4.774;       %(3.984, 5.563)
  r10 =  2.742;       %(2.103, 3.381)
eqn15 = (r1*z^5 + r2*z^4 + r3*z^3 + r4*z^2 + r5*z +r6)/(z^4 +
r7*z^3 + r8*z^2 + r9*z + r10) == F_sphere_15;
U = solve(eqn15,z);
U1 = [vpa(U(1)); vpa(U(2)); vpa(U(3)); vpa(U(4)); vpa(U(5));];
U2 = std1*U1+m1
Int_15 = U2(1);

f15(x)  = (r1*((x-m1)/std1)^5 +r2*((x-m1)/std1)^4 + r3*((x-
m1)/std1)^3 + r4*((x-m1)/std1)^2 + r5*((x-m1)/std1) + r6)/(((x-
m1)/std1)^4 + r7*((x-m1)/std1)^3 + r8*((x-m1)/std1)^2 + r9*((x-
m1)/std1) + r10)
fplot (f15)
hold on
fplot(F_sphere_15)
hold on
plot(Int_15, F_sphere_15, 'r.')
xlim([0 0.018])
ylim([0 1.5])
grid on
xlabel('distance (m)')
ylabel('force (N)')
title('Magnitude of Magnetic Force vs Distance (1.5 Amp)')
```

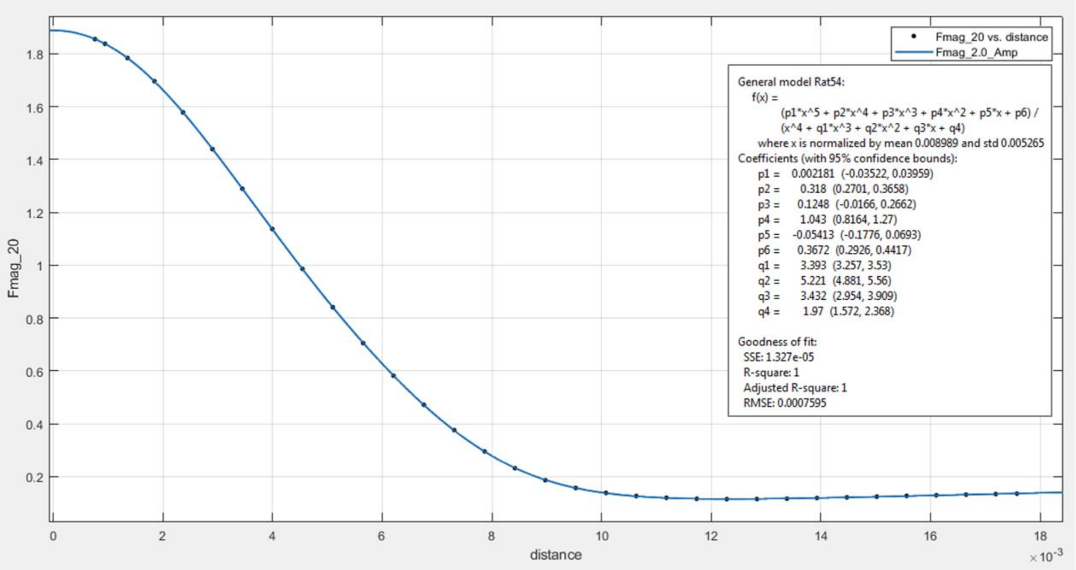

```
General model Rat54:
  f(x) =
        (p1*x^5 + p2*x^4 + p3*x^3 + p4*x^2 + p5*x + p6) /
        (x^4 + q1*x^3 + q2*x^2 + q3*x + q4)
    where x is normalized by mean 0.008989 and std 0.005265
Coefficients (with 95% confidence bounds):
    p1 =   0.002181  (-0.03522, 0.03959)
    p2 =      0.318  (0.2701, 0.3658)
    p3 =     0.1248  (-0.0166, 0.2662)
    p4 =      1.043  (0.8164, 1.27)
    p5 =   -0.05413  (-0.1776, 0.0693)
    p6 =     0.3672  (0.2926, 0.4417)
    q1 =      3.393  (3.257, 3.53)
    q2 =      5.221  (4.881, 5.56)
    q3 =      3.432  (2.954, 3.909)
    q4 =       1.97  (1.572, 2.368)

Goodness of fit:
  SSE: 1.327e-05
  R-square: 1
  Adjusted R-square: 1
  RMSE: 0.0007595
```

Figure 126: Curve Fit for Magnitude of Magnetic Force (N) vs. Distance (m) – 2.0 Amps Coil Excitation

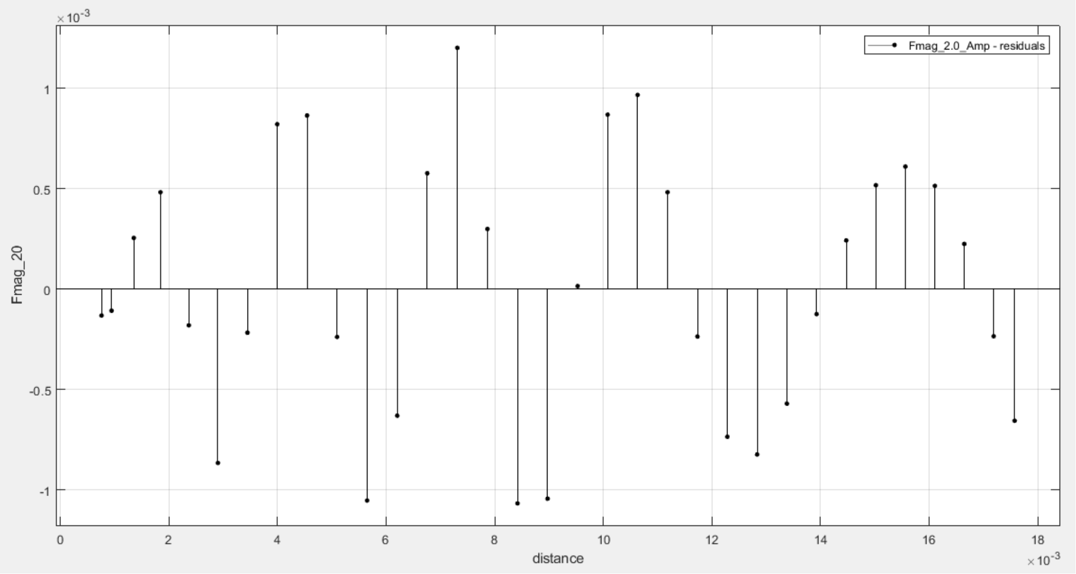

Figure 127: Residuals Plot for Magnitude of Magnetic Force (N) vs. Distance (m) – 2.0 Amps Coil Excitation

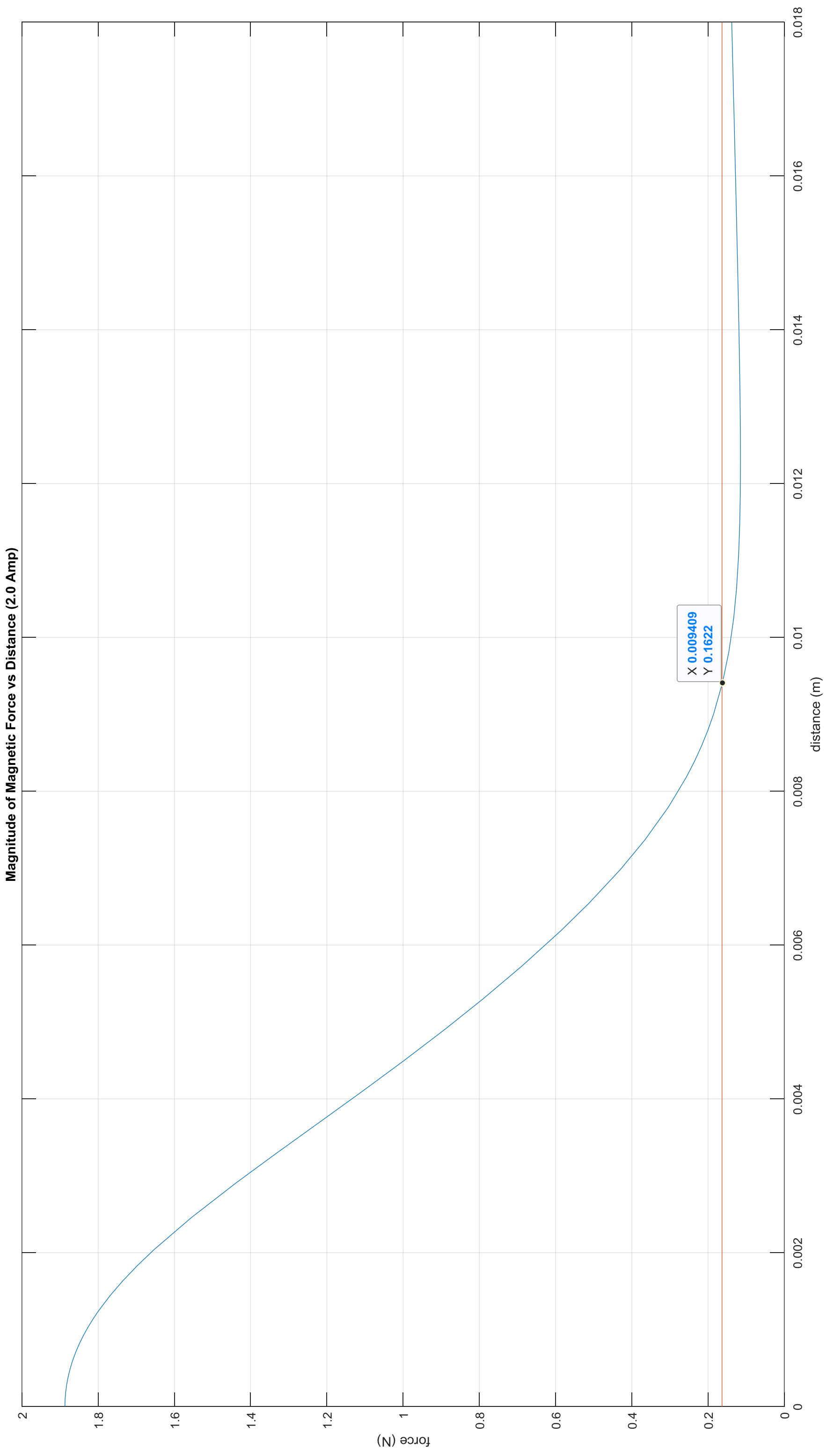

Figure 128: Threshold Distance where Iron and Iron + PM Forces are Equal (2.0 Amp)

MATLAB Source Code: Determination of Intersection Point of Iron Only Force and Iron + PM Force for 2.0 Ampere Coil Excitation

```
%% ======  Fmag for 2.0 Amp of Current ======= %%
syms a x
% Coefficients with 95% confidence bounds, where x is normalized by
mean
% 0.008989 and std 0.005265
F_sphere_20 = 0.16328392631564;
   s1 =  0.002181;  %(-0.03522, 0.03959)
   s2 =  0.318;     %(0.2701, 0.3658)
   s3 =  0.1248;    %(-0.0166, 0.2662)
   s4 =  1.043;     %(0.8164, 1.27)
   s5 = -0.05413;   %(-0.1776, 0.0693)
   s6 =  0.3672;    %(0.2926, 0.4417)
   s7 =  3.393;     %(3.257, 3.53)
   s8 =  5.221;     %(4.881, 5.56)
   s9 =  3.432;     %(2.954, 3.909)
  s10 =  1.97;      %(1.572, 2.368)
eqn20 = (s1*a^5 + s2*a^4 + s3*a^3 + s4*a^2 + s5*a + s6)/(a^4 +
s7*a^3 + s8*a^2 + s9*a +s10) == F_sphere_20;
V = solve(eqn20,a);
V1 = [vpa(V(1)); vpa(V(2)); vpa(V(3)); vpa(V(4)); vpa(V(5));];
V2 = std1*V1+m1
Int_2 = V2(1);

f2(x) = (s1*((x-m1)/std1)^5 +s2*((x-m1)/std1)^4 + s3*((x-
m1)/std1)^3 + s4*((x-m1)/std1)^2 + s5*((x-m1)/std1) + s6)/(((x-
m1)/std1)^4 + s7*((x-m1)/std1)^3 + s8*((x-m1)/std1)^2 + s9*((x-
m1)/std1) + s10)
fplot (f2)
hold on
fplot(F_sphere_20)
hold on
plot(Int_2, F_sphere_20, 'r.')
xlim([0 0.018])
ylim([0 2])
grid on
xlabel('distance (m)')
ylabel('force (N)')
title('Magnitude of Magnetic Force vs Distance (2.0 Amp)')
```

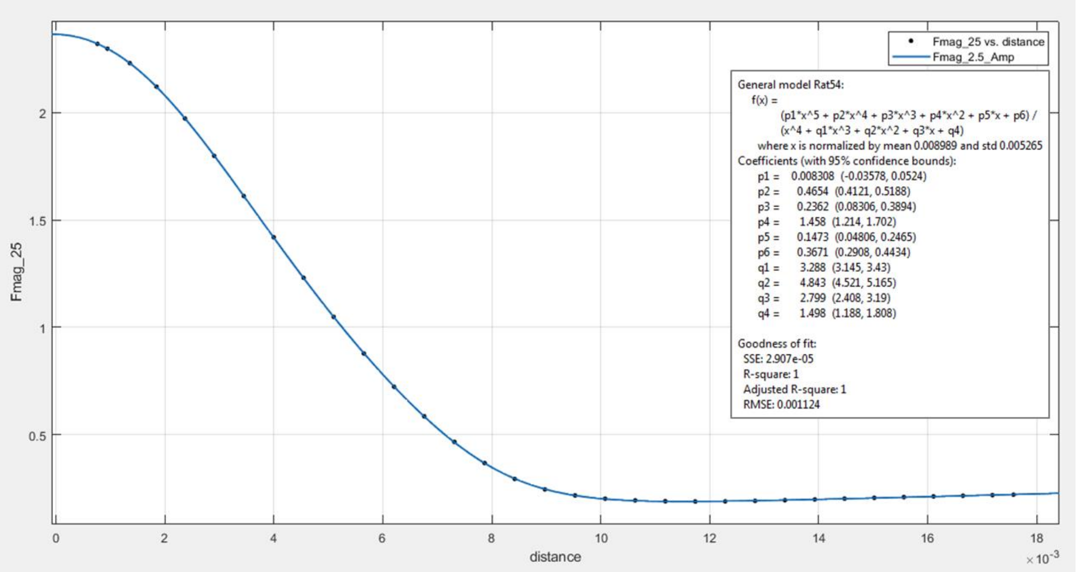

```
General model Rat54:
   f(x) =
         (p1*x^5 + p2*x^4 + p3*x^3 + p4*x^2 + p5*x + p6) /
         (x^4 + q1*x^3 + q2*x^2 + q3*x + q4)
     where x is normalized by mean 0.008989 and std 0.005265
Coefficients (with 95% confidence bounds):
     p1 =   0.008308  (-0.03578, 0.0524)
     p2 =     0.4654  (0.4121, 0.5188)
     p3 =     0.2362  (0.08306, 0.3894)
     p4 =      1.458  (1.214, 1.702)
     p5 =     0.1473  (0.04806, 0.2465)
     p6 =     0.3671  (0.2908, 0.4434)
     q1 =      3.288  (3.145, 3.43)
     q2 =      4.843  (4.521, 5.165)
     q3 =      2.799  (2.408, 3.19)
     q4 =      1.498  (1.188, 1.808)

Goodness of fit:
  SSE: 2.907e-05
  R-square: 1
  Adjusted R-square: 1
  RMSE: 0.001124
```

Figure 129: Curve Fit for Magnitude of Magnetic Force (N) vs. Distance (m) – 2.5 Amps Coil Excitation

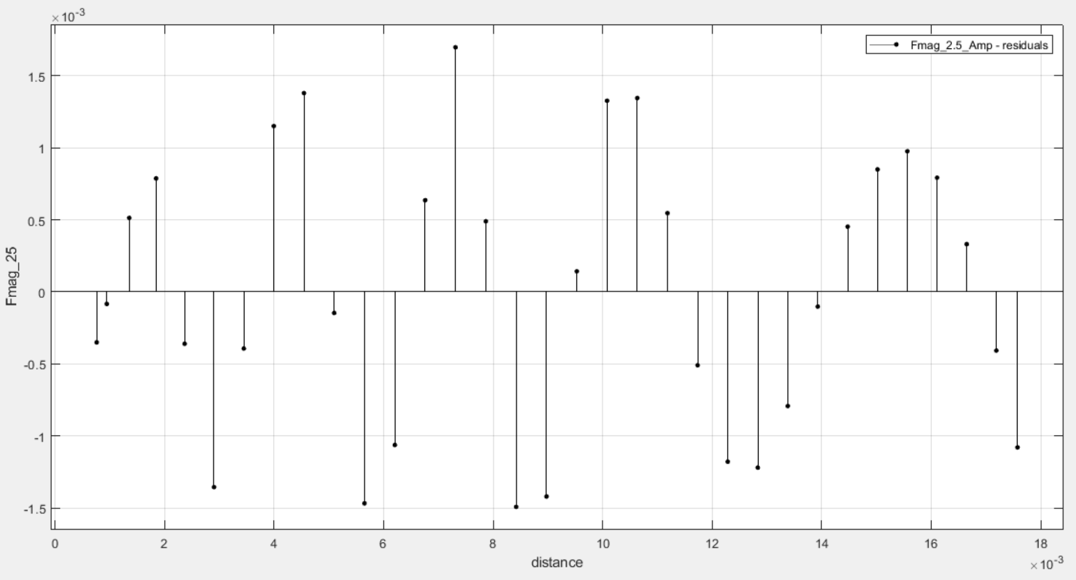

Figure 130: Residuals Plot for Magnitude of Magnetic Force (N) vs. Distance (m) – 2.5 Amps Coil Excitation

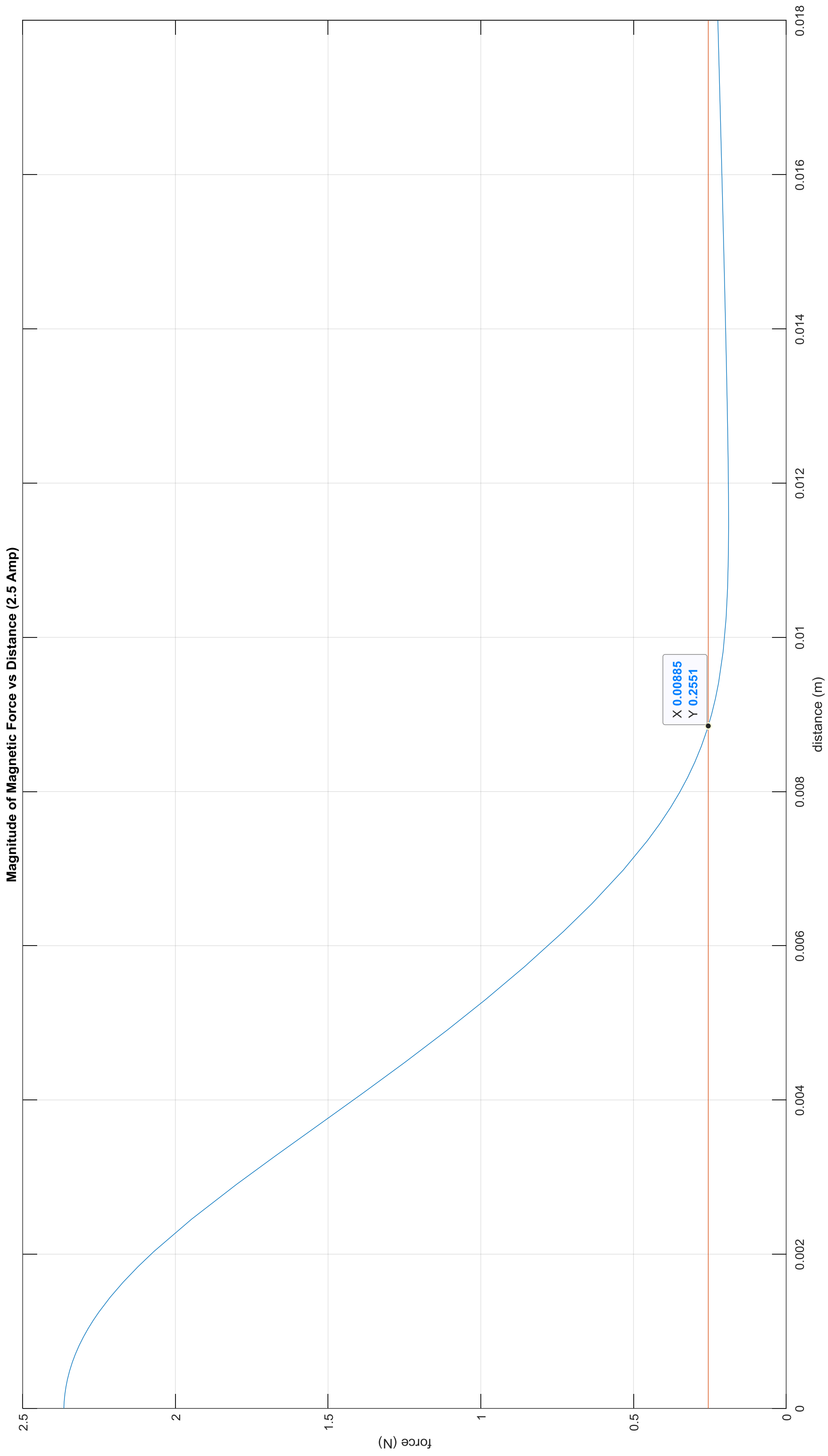

Figure 131: Threshold Distance where Iron and Iron + PM Forces are Equal (2.5 Amp)

MATLAB Source Code: Determination of Intersection Point of Iron Only Force and Iron + PM Force for 2.5 Ampere Coil Excitation

```
%% ======  Fmag for 2.5 Amp of Current ======= %%
syms b x
% Coefficients with 95% confidence bounds, where x is normalized by
mean
% 0.008989 and std 0.005265
F_sphere_25 = 0.255133551163744;
   t1 =  0.008308; %(-0.03578, 0.0524)
   t2 =  0.4654;   %(0.4121, 0.5188)
   t3 =  0.2362;   %(0.08306, 0.3894)
   t4 =  1.458;    %(1.214, 1.702)
   t5 =  0.1473;   %(0.04806, 0.2465)
   t6 =  0.3671;   %(0.2908, 0.4434)
   t7 =  3.288;    %(3.145, 3.43)
   t8 =  4.843;    %(4.521, 5.165)
   t9 =  2.799;    %(2.408, 3.19)
  t10 =  1.498;    %(1.188, 1.808)
eqn25 = (t1*b^5 + t2*b^4 + t3*b^3 + t4*b^2 + t5*b + t6)/(b^4 +
t7*b^3 + t8*b^2 + t9*b + t10) == F_sphere_25;
W = solve(eqn25,b);
W1 = [vpa(W(1)); vpa(W(2)); vpa(W(3)); vpa(W(4)); vpa(W(5));];
W2 = std1*W1+m1
Int_25 = W2(1);

f25(x) = (t1*((x-m1)/std1)^5 +t2*((x-m1)/std1)^4 + t3*((x-
m1)/std1)^3 + t4*((x-m1)/std1)^2 + t5*((x-m1)/std1) + t6)/(((x-
m1)/std1)^4 + t7*((x-m1)/std1)^3 + t8*((x-m1)/std1)^2 + t9*((x-
m1)/std1) + t10)
fplot (f25)
hold on
fplot(F_sphere_25)
hold on
plot(Int_25, F_sphere_25, 'r.')
xlim([0 0.018])
ylim([0 2.5])
grid on
xlabel('distance (m)')
ylabel('force (N)')
title('Magnitude of Magnetic Force vs Distance (2.5 Amp)')
```

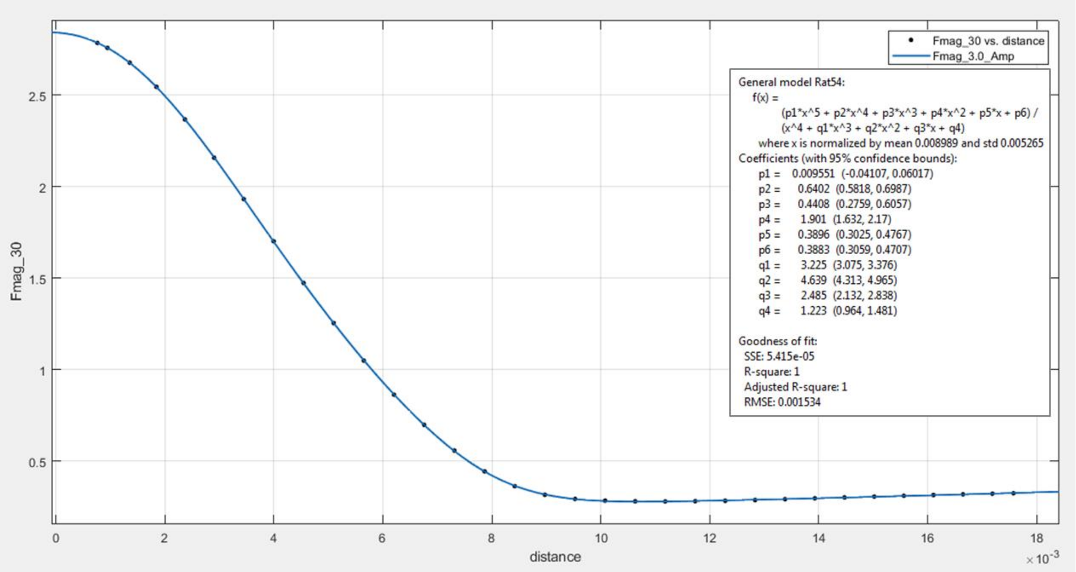

```
General model Rat54:
   f(x) =
         (p1*x^5 + p2*x^4 + p3*x^3 + p4*x^2 + p5*x + p6) /
         (x^4 + q1*x^3 + q2*x^2 + q3*x + q4)
     where x is normalized by mean 0.008989 and std 0.005265
Coefficients (with 95% confidence bounds):
     p1 =   0.009551  (-0.04107, 0.06017)
     p2 =     0.6402  (0.5818, 0.6987)
     p3 =     0.4408  (0.2759, 0.6057)
     p4 =      1.901  (1.632, 2.17)
     p5 =     0.3896  (0.3025, 0.4767)
     p6 =     0.3883  (0.3059, 0.4707)
     q1 =      3.225  (3.075, 3.376)
     q2 =      4.639  (4.313, 4.965)
     q3 =      2.485  (2.132, 2.838)
     q4 =      1.223  (0.964, 1.481)

Goodness of fit:
  SSE: 5.415e-05
  R-square: 1
  Adjusted R-square: 1
  RMSE: 0.001534
```

Figure 132: Curve Fit for Magnitude of Magnetic Force (N) vs. Distance (m) – 3.0 Amps Coil Excitation

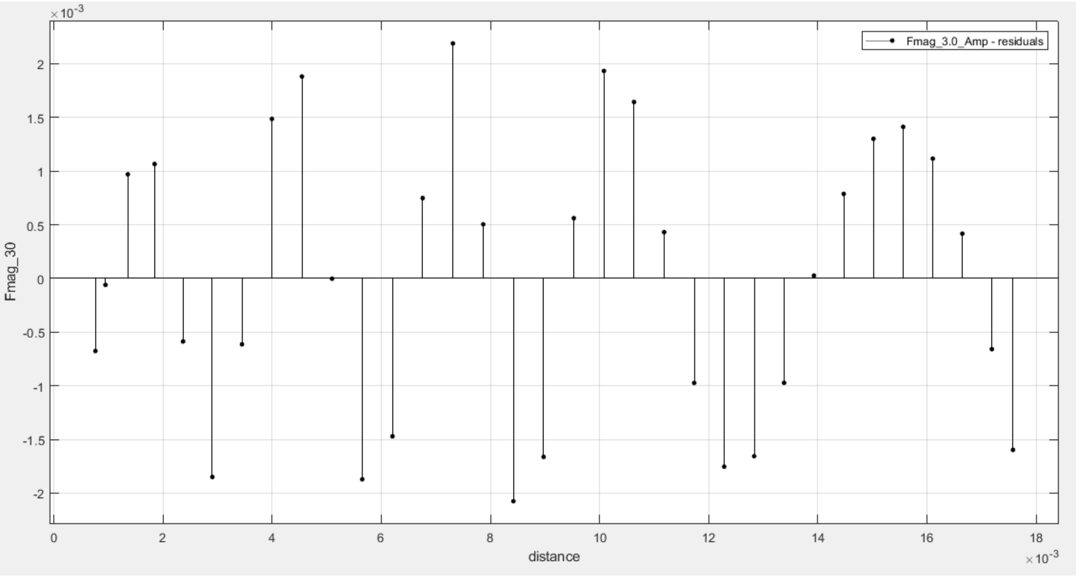

Figure 133: Residuals Plot for Magnitude of Magnetic Force (N) vs. Distance (m) – 3.0 Amps Coil Excitation

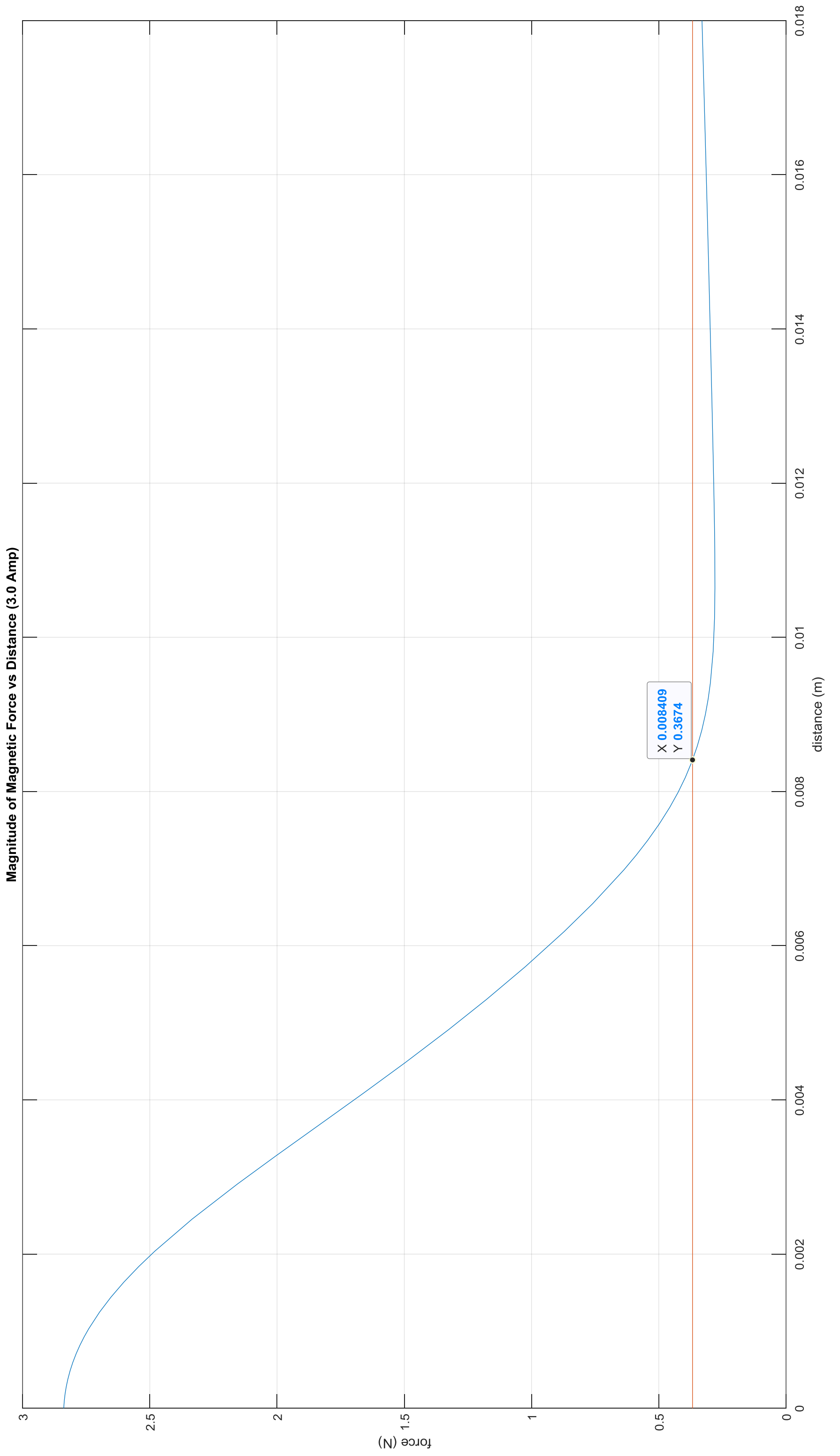

Figure 134: Threshold Distance where Iron and Iron + PM Forces are Equal (3.0 Amp)

MATLAB Source Code: Determination of Intersection Point of Iron Only Force and Iron + PM Force for 3.0 Ampere Coil Excitation

```
%% ======  Fmag for 3.0 Amp of Current ======= %%
syms c x
% Coefficients with 95% confidence bounds, where x is normalized by
mean
% 0.008989 and std 0.005265
F_sphere_30 = 0.367395346950679;
   u1 =  0.009551;  %(-0.04107, 0.06017)
   u2 =  0.6402;    %(0.5818, 0.6987)
   u3 =  0.4408;    %(0.2759, 0.6057)
   u4 =  1.901;     %(1.632, 2.17)
   u5 =  0.3896;    %(0.3025, 0.4767)
   u6 =  0.3883;    %(0.3059, 0.4707)
   u7 =  3.225;     %(3.075, 3.376)
   u8 =  4.639;     %(4.313, 4.965)
   u9 =  2.485;     %(2.132, 2.838)
  u10 =  1.223;     %(0.964, 1.481)
eqn30 = (u1*c^5 + u2*c^4 + u3*c^3 + u4*c^2 + u5*c + u6)/(c^4 +
u7*c^3 + u8*c^2 + u9*c +u10) == F_sphere_30;
Y = solve(eqn30,c);
Y1 = [vpa(Y(1)); vpa(Y(2)); vpa(Y(3)); vpa(Y(4)); vpa(Y(5));];
Y2 = std1*Y1+m1
Int_30 = Y2(1);

f30(x) = (u1*((x-m1)/std1)^5 +u2*((x-m1)/std1)^4 + u3*((x-
m1)/std1)^3 + u4*((x-m1)/std1)^2 + u5*((x-m1)/std1) + u6)/(((x-
m1)/std1)^4 + u7*((x-m1)/std1)^3 + u8*((x-m1)/std1)^2 + u9*((x-
m1)/std1) + u10)
fplot (f30)
hold on
fplot(F_sphere_30)
hold on
plot(Int_30, F_sphere_30, 'r.')
xlim([0 0.018])
ylim([0 3.0])
grid on
xlabel('distance (m)')
ylabel('force (N)')
title('Magnitude of Magnetic Force vs Distance (3.0 Amp)')
```

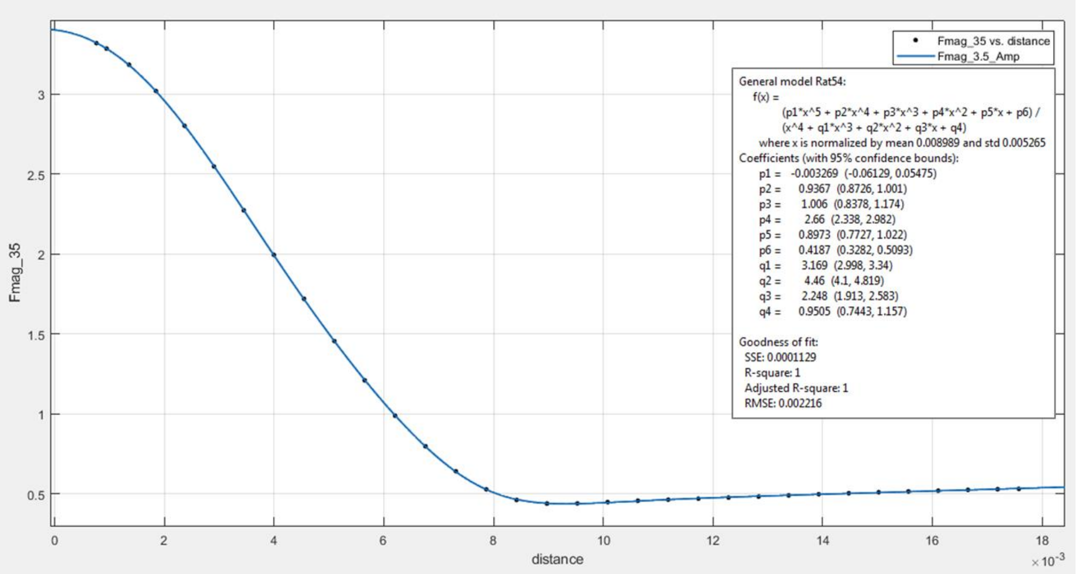

```
General model Rat54:
  f(x) =
        (p1*x^5 + p2*x^4 + p3*x^3 + p4*x^2 + p5*x + p6) /
        (x^4 + q1*x^3 + q2*x^2 + q3*x + q4)
    where x is normalized by mean 0.008989 and std 0.005265
Coefficients (with 95% confidence bounds):
    p1 =   -0.003269  (-0.06129, 0.05475)
    p2 =      0.9367  (0.8726, 1.001)
    p3 =       1.006  (0.8378, 1.174)
    p4 =        2.66  (2.338, 2.982)
    p5 =      0.8973  (0.7727, 1.022)
    p6 =      0.4187  (0.3282, 0.5093)
    q1 =       3.169  (2.998, 3.34)
    q2 =        4.46  (4.1, 4.819)
    q3 =       2.248  (1.913, 2.583)
    q4 =      0.9505  (0.7443, 1.157)

Goodness of fit:
  SSE: 0.0001129
  R-square: 1
  Adjusted R-square: 1
  RMSE: 0.002216
```

Figure 135: Curve Fit for Magnitude of Magnetic Force (N) vs. Distance (m) – 3.5 Amps Coil Excitation

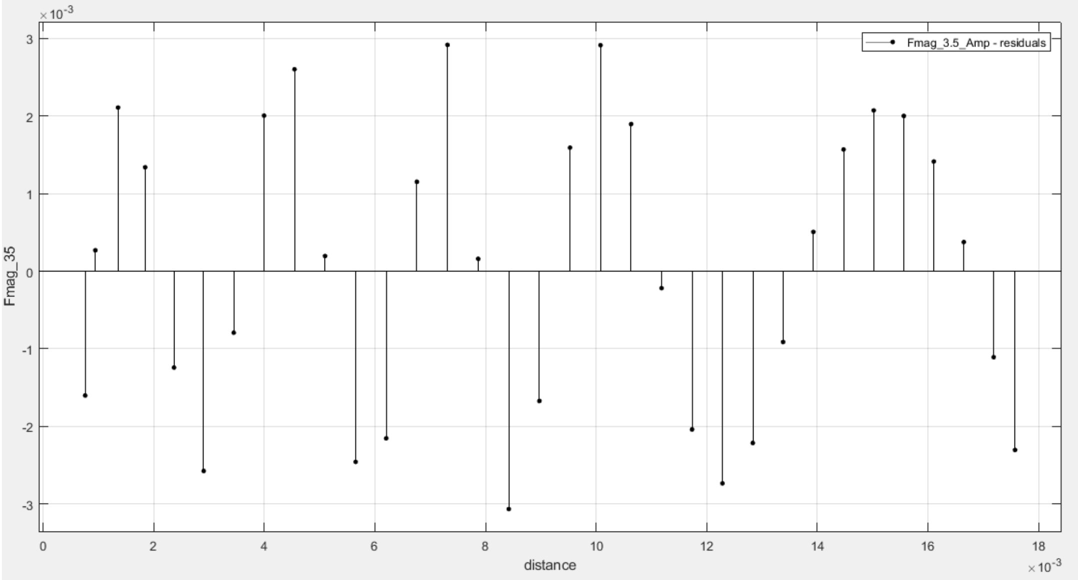

Figure 136: Residuals Plot for Magnitude of Magnetic Force (N) vs. Distance (m) – 3.5 Amps Coil Excitation

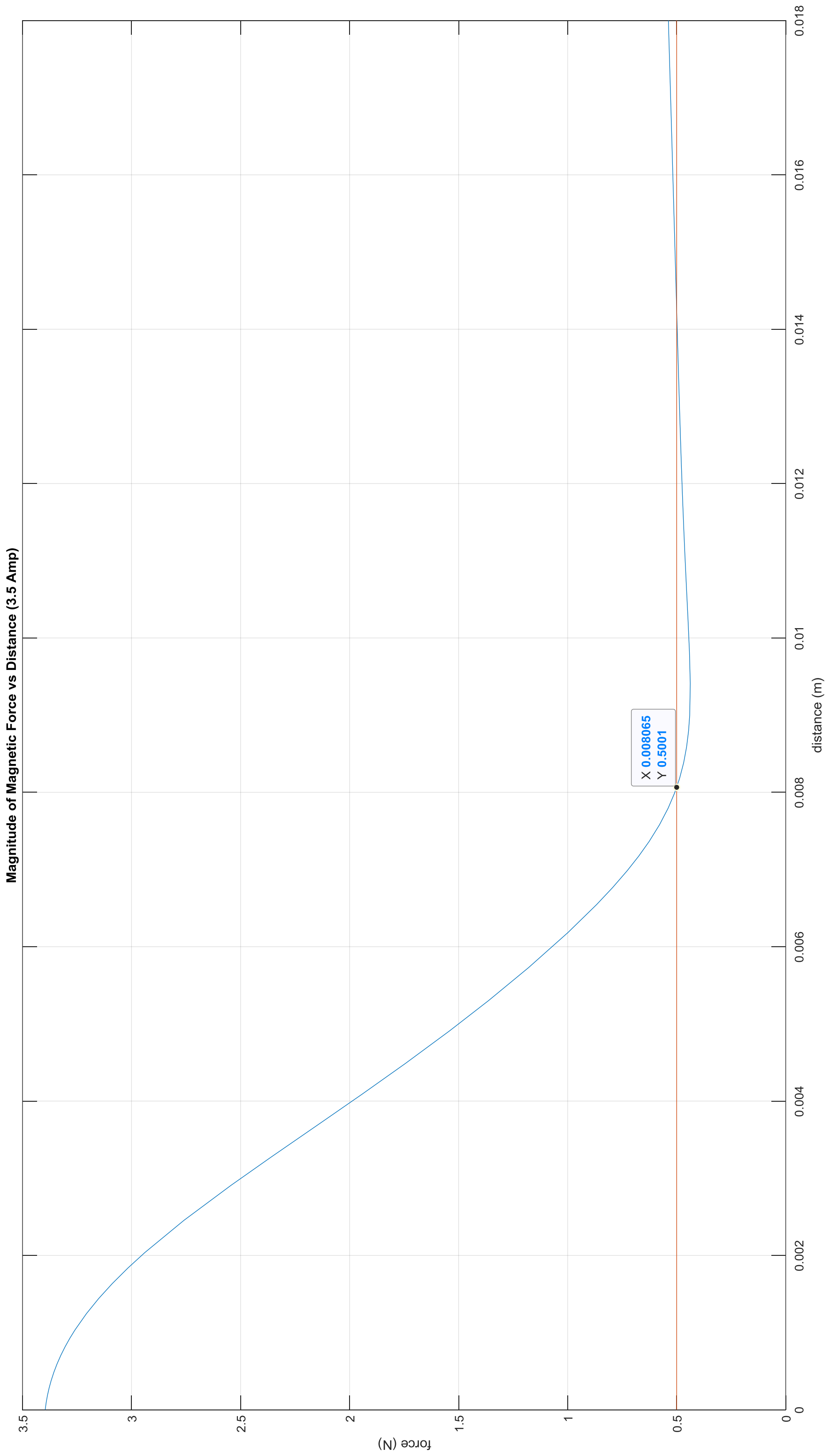

Figure 137: Threshold Distance where Iron and Iron + PM Forces are Equal (3.5 Amp)

MATLAB Source Code: Determination of Intersection Point of Iron Only Force and Iron + PM Force for 3.5 Ampere Coil Excitation

```
%% ======  Fmag for 3.5 Amp of Current ======= %%
syms d x
% % Coefficients with 95% confidence bounds, where x is normalized
by mean
% 0.008989 and std 0.005265
F_sphere_35 = 0.500060279779388;
   v1 = -0.003269;  %(-0.06129, 0.05475)
   v2 =  0.9367;    %(0.8726, 1.001)
   v3 =  1.006;     %(0.8378, 1.174)
   v4 =  2.66;      %(2.338, 2.982)
   v5 =  0.8973;    %(0.7727, 1.022)
   v6 =  0.4187;    %(0.3282, 0.5093)
   v7 =  3.169;     %(2.998, 3.34)
   v8 =  4.46;      %(4.1, 4.819)
   v9 =  2.248;     %(1.913, 2.583)
  v10 =  0.9505;    %(0.7443, 1.157)
eqn35 = (v1*d^5 + v2*d^4 + v3*d^3 + v4*d^2 + v5*d + v6)/(d^4 +
v7*d^3 + v8*d^2 + v9*d + v10) == F_sphere_35;
Z = solve(eqn35,d);
Z1 = [vpa(Z(1)); vpa(Z(2)); vpa(Z(3)); vpa(Z(4)); vpa(Z(5));];
Z2 = std1*Z1+m1
Int_35 = Z2(1);

f35(x)  = (v1*((x-m1)/std1)^5 +v2*((x-m1)/std1)^4 + v3*((x-
m1)/std1)^3 + v4*((x-m1)/std1)^2 + v5*((x-m1)/std1) + v6)/(((x-
m1)/std1)^4 + v7*((x-m1)/std1)^3 + v8*((x-m1)/std1)^2 + v9*((x-
m1)/std1) + v10)
fplot (f35)
hold on
fplot(F_sphere_35)
hold on
plot(Int_35, F_sphere_35, 'r.')
xlim([0 0.018])
ylim([0 3.5])
grid on
xlabel('distance (m)')
ylabel('force (N)')
title('Magnitude of Magnetic Force vs Distance (3.5 Amp)')
```

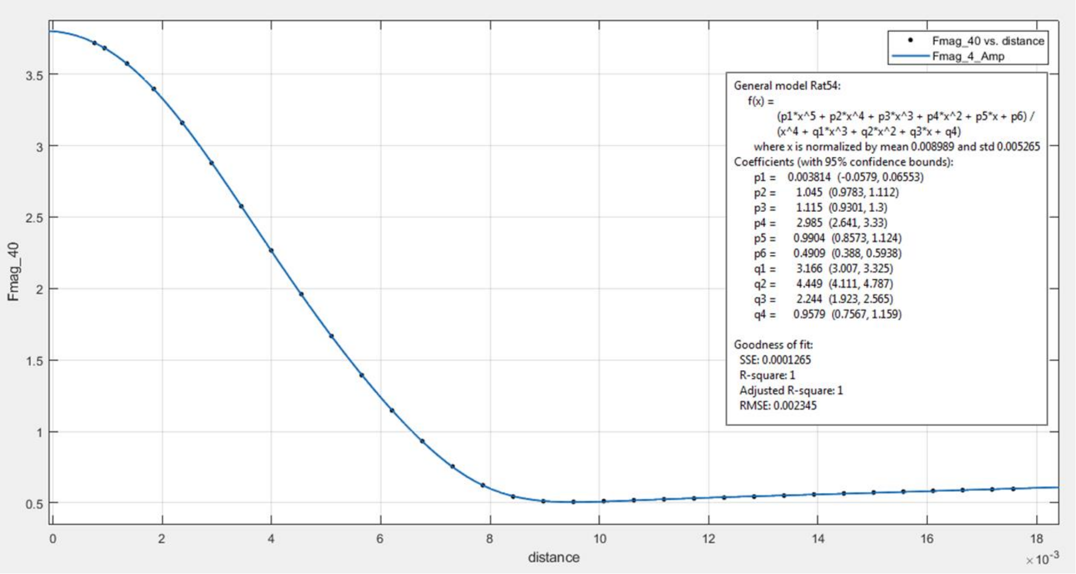

```
General model Rat54:
   f(x) =
            (p1*x^5 + p2*x^4 + p3*x^3 + p4*x^2 + p5*x + p6) /
            (x^4 + q1*x^3 + q2*x^2 + q3*x + q4)
     where x is normalized by mean 0.008989 and std 0.005265
Coefficients (with 95% confidence bounds):
     p1 =   0.003814  (-0.0579, 0.06553)
     p2 =      1.045  (0.9783, 1.112)
     p3 =      1.115  (0.9301, 1.3)
     p4 =      2.985  (2.641, 3.33)
     p5 =     0.9904  (0.8573, 1.124)
     p6 =     0.4909  (0.388, 0.5938)
     q1 =      3.166  (3.007, 3.325)
     q2 =      4.449  (4.111, 4.787)
     q3 =      2.244  (1.923, 2.565)
     q4 =     0.9579  (0.7567, 1.159)

Goodness of fit:
  SSE: 0.0001265
  R-square: 1
  Adjusted R-square: 1
  RMSE: 0.002345
```

Figure 138: Curve Fit for Magnitude of Magnetic Force (N) vs. Distance (m) – 4.0 Amps Coil Excitation

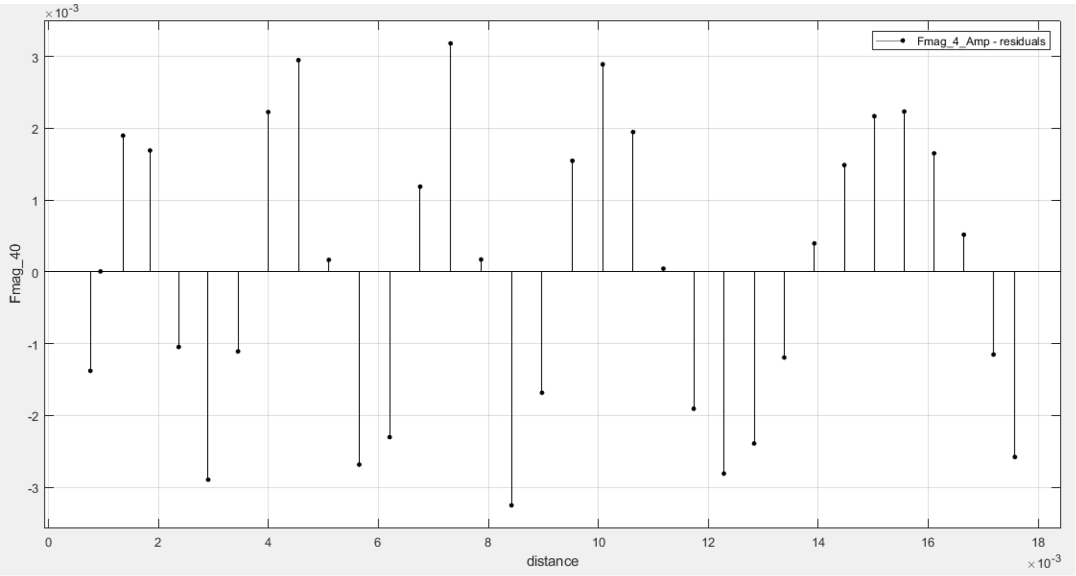

Figure 139: Residuals Plot for Magnitude of Magnetic Force (N) vs. Distance (m) – 4.0 Amps Coil Excitation

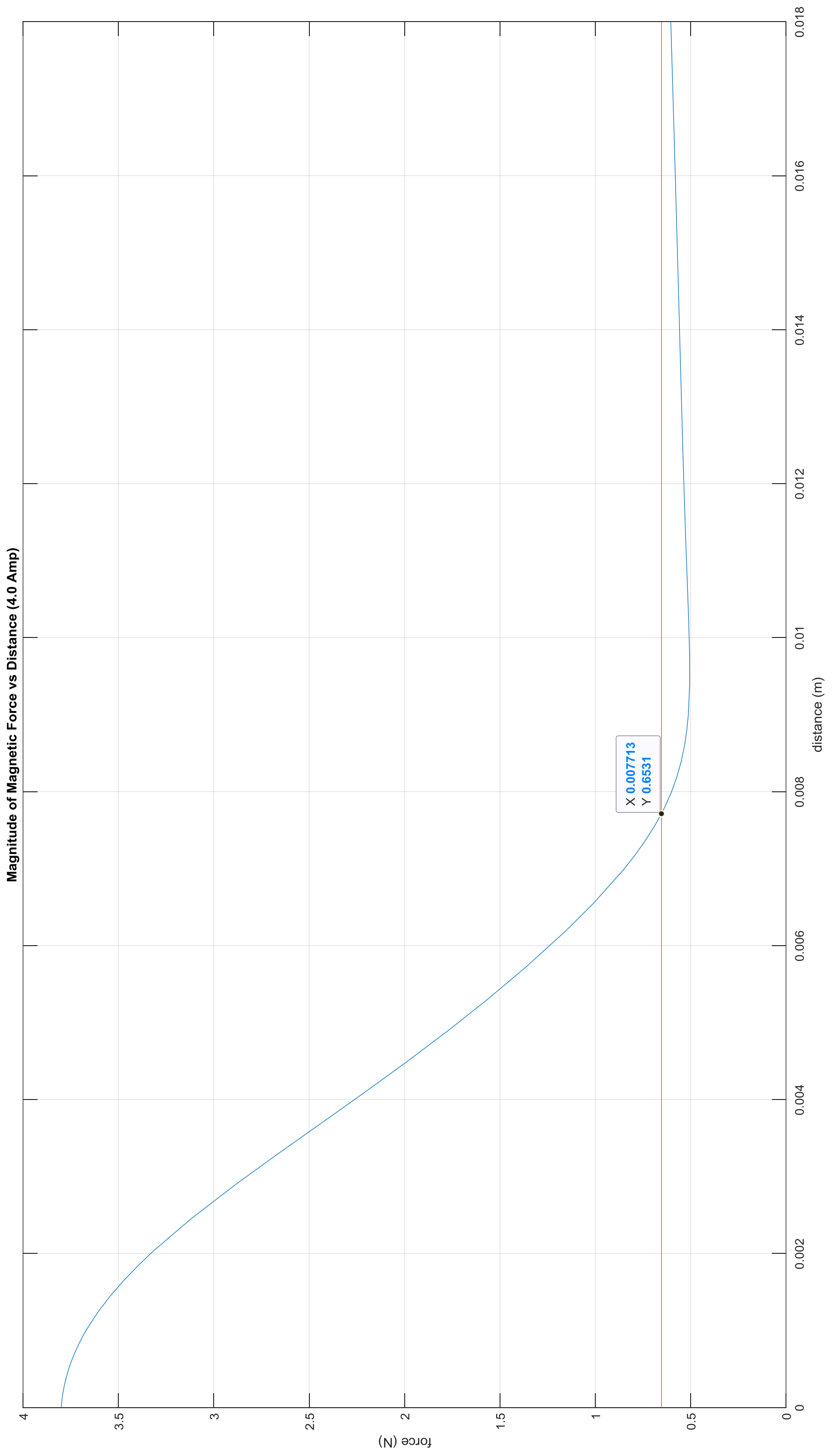

Figure 140: Threshold Distance where Iron and Iron + PM Forces are Equal (4.0 Amp)

MATLAB Source Code: Determination of Intersection Point of Iron Only Force and Iron + PM Force for 4.0 Ampere Coil Excitation

```
%% ======================  Fmag for 4.0 Amp of Current
=============== %%
syms e x
%  Coefficients with 95% confidence bounds, where x is normalized
by mean
%  0.008989 and std 0.005265
F_sphere_40 = 0.653133603631616;
   w1 =  0.003814;  %(-0.0579, 0.06553)
   w2 =  1.045;     %(0.9783, 1.112)
   w3 =  1.115;     %(0.9301, 1.3)
   w4 =  2.985;     %(2.641, 3.33)
   w5 =  0.9904;    %(0.8573, 1.124)
   w6 =  0.4909;    %(0.388, 0.5938)
   w7 =  3.166;     %(3.007, 3.325)
   w8 =  4.449;     %(4.111, 4.787)
   w9 =  2.244;     %(1.923, 2.565)
  w10 =  0.9579;    %(0.7567, 1.159)
eqn40 = (w1*e^5 + w2*e^4 + w3*e^3 + w4*e^2 + w5*e + w6)/(e^4 +
w7*e^3 + w8*e^2 + w9*e + w10) == F_sphere_40;
G = solve(eqn40,e);
G1 = [vpa(G(1)); vpa(G(2)); vpa(G(3)); vpa(G(4)); vpa(G(5));];
G2 = std1*G1+m1
Int_40 = G2(1);

f40(x) = (w1*((x-m1)/std1)^5 +w2*((x-m1)/std1)^4 + w3*((x-
m1)/std1)^3 + w4*((x-m1)/std1)^2 + w5*((x-m1)/std1) + w6)/(((x-
m1)/std1)^4 + w7*((x-m1)/std1)^3 + w8*((x-m1)/std1)^2 + w9*((x-
m1)/std1) + w10)
fplot (f40)
hold on
fplot(F_sphere_40)
hold on
plot(Int_40, F_sphere_40, 'r.')
xlim([0 0.018])
ylim([0 4])
grid on
xlabel('distance (m)')
ylabel('force (N)')
title('Magnitude of Magnetic Force vs Distance (4.0 Amp)')
```

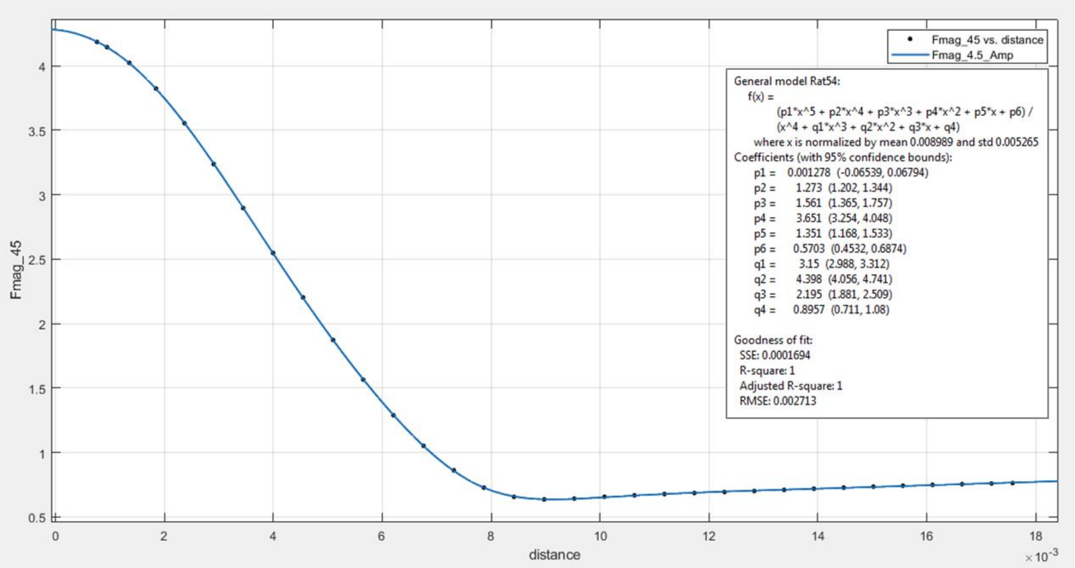

```
General model Rat54:
  f(x) =
        (p1*x^5 + p2*x^4 + p3*x^3 + p4*x^2 + p5*x + p6) /
        (x^4 + q1*x^3 + q2*x^2 + q3*x + q4)
    where x is normalized by mean 0.008989 and std 0.005265
Coefficients (with 95% confidence bounds):
    p1 =    0.001278  (-0.06539, 0.06794)
    p2 =       1.273  (1.202, 1.344)
    p3 =       1.561  (1.365, 1.757)
    p4 =       3.651  (3.254, 4.048)
    p5 =       1.351  (1.168, 1.533)
    p6 =      0.5703  (0.4532, 0.6874)
    q1 =        3.15  (2.988, 3.312)
    q2 =       4.398  (4.056, 4.741)
    q3 =       2.195  (1.881, 2.509)
    q4 =      0.8957  (0.711, 1.08)

Goodness of fit:
  SSE: 0.0001694
  R-square: 1
  Adjusted R-square: 1
  RMSE: 0.002713
```

Figure 141: Curve Fit for Magnitude of Magnetic Force (N) vs. Distance (m) – 4.5 Amps Coil Excitation

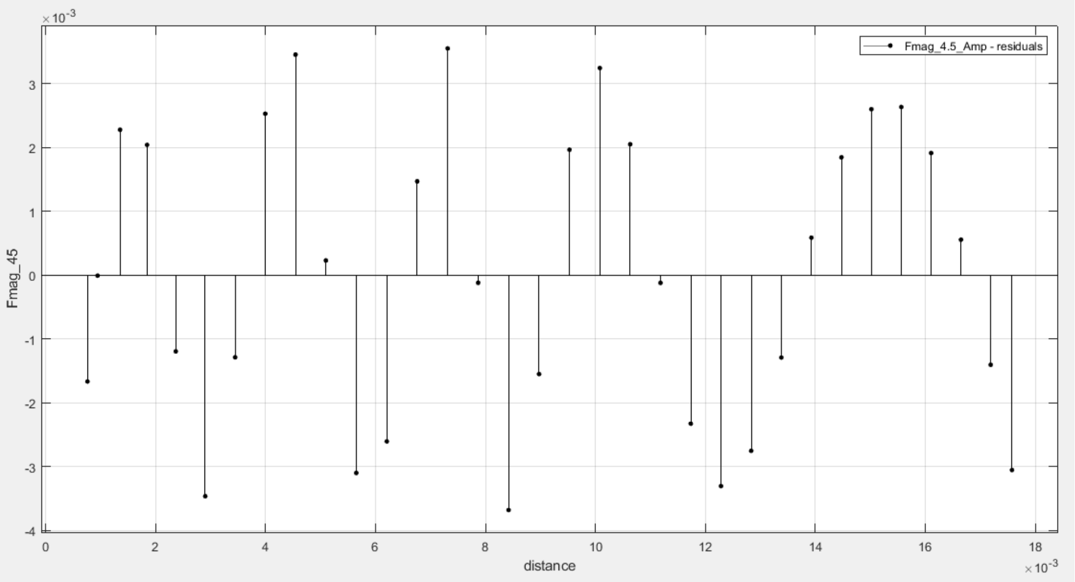

Figure 142: Residuals Plot for Magnitude of Magnetic Force (N) vs. Distance (m) – 4.5 Amps Coil Excitation

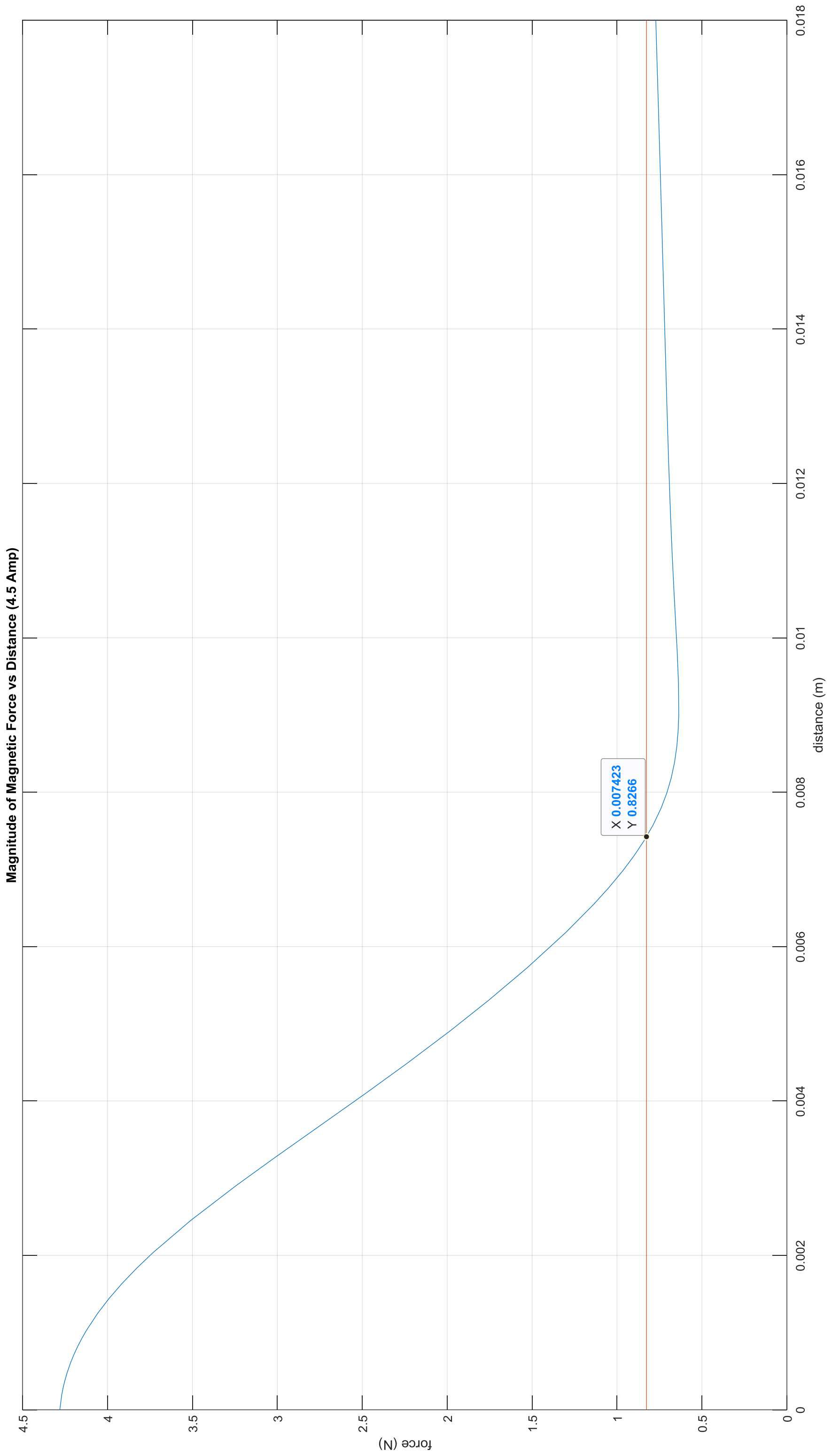

Figure 143: Threshold Distance where Iron and Iron + PM Forces are Equal (4.5 Amp)

MATLAB Source Code: Determination of Intersection Point of Iron Only Force and Iron + PM Force for 4.5 Ampere Coil Excitation

```
%% ======  Fmag for 4.5 Amp of Current ======= %%
syms f x
% Coefficients with 95% confidence bounds, where x is normalized by
mean
% 0.008989 and std 0.005265
F_sphere_45 = 0.826632335629862;
   x1 =  0.001278;   %(-0.06539, 0.06794)
   x2 =  1.273;      %(1.202, 1.344)
   x3 =  1.561;      %(1.365, 1.757)
   x4 =  3.651;      %(3.254, 4.048)
   x5 =  1.351;      %(1.168, 1.533)
   x6 =  0.5703;     %(0.4532, 0.6874)
   x7 =  3.15;       %(2.988, 3.312)
   x8 =  4.398;      %(4.056, 4.741)
   x9 =  2.195;      %(1.881, 2.509)
  x10 =  0.8957;     %(0.711, 1.08)
eqn45 = (x1*f^5 + x2*f^4 + x3*f^3 + x4*f^2 + x5*f +x6)/(f^4 +
x7*f^3 + x8*f^2 + x9*f + x10) == F_sphere_45;
H = solve(eqn45,f);
H1 = [vpa(H(1)); vpa(H(2)); vpa(H(3)); vpa(H(4)); vpa(H(5));];
H2 = std1*H1+m1
Int_45 = H2(1);

f45(x) = (x1*((x-m1)/std1)^5 +x2*((x-m1)/std1)^4 + x3*((x-
m1)/std1)^3 + x4*((x-m1)/std1)^2 + x5*((x-m1)/std1) + x6)/(((x-
m1)/std1)^4 + x7*((x-m1)/std1)^3 + x8*((x-m1)/std1)^2 + x9*((x-
m1)/std1) + x10)
fplot (f45)
hold on
fplot(F_sphere_45)
hold on
plot(Int_45, F_sphere_45, 'r.')
xlim([0 0.018])
ylim([0 4.5])
grid on
xlabel('distance (m)')
ylabel('force (N)')
title('Magnitude of Magnetic Force vs Distance (4.5 Amp)')
```

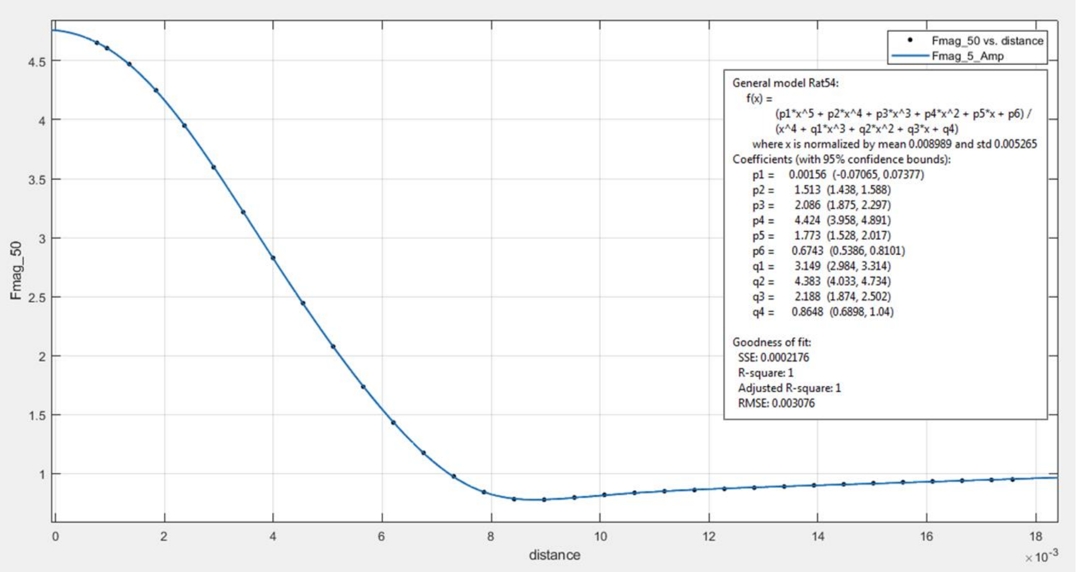

```
General model Rat54:
   f(x) =
            (p1*x^5 + p2*x^4 + p3*x^3 + p4*x^2 + p5*x + p6) /
            (x^4 + q1*x^3 + q2*x^2 + q3*x + q4)
     where x is normalized by mean 0.008989 and std 0.005265
Coefficients (with 95% confidence bounds):
     p1 =    0.00156  (-0.07065, 0.07377)
     p2 =      1.513  (1.438, 1.588)
     p3 =      2.086  (1.875, 2.297)
     p4 =      4.424  (3.958, 4.891)
     p5 =      1.773  (1.528, 2.017)
     p6 =     0.6743  (0.5386, 0.8101)
     q1 =      3.149  (2.984, 3.314)
     q2 =      4.383  (4.033, 4.734)
     q3 =      2.188  (1.874, 2.502)
     q4 =     0.8648  (0.6898, 1.04)

Goodness of fit:
  SSE: 0.0002176
  R-square: 1
  Adjusted R-square: 1
  RMSE: 0.003076
```

Figure 144: Curve Fit for Magnitude of Magnetic Force (N) vs. Distance (m) – 5.0 Amps Coil Excitation

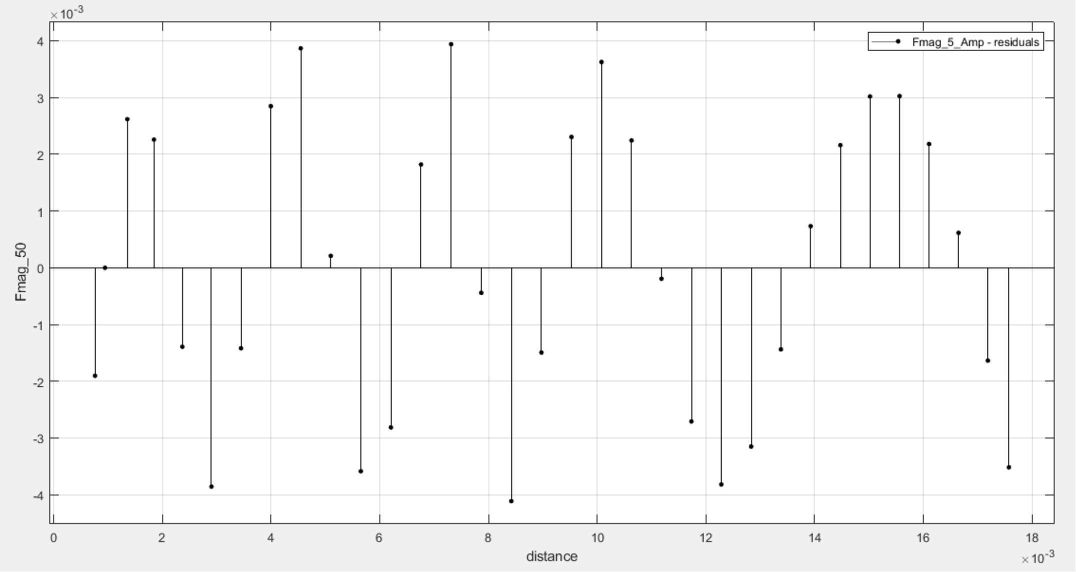

Figure 145: Residuals Plot for Magnitude of Magnetic Force (N) vs. Distance (m) – 5.0 Amps Coil Excitation

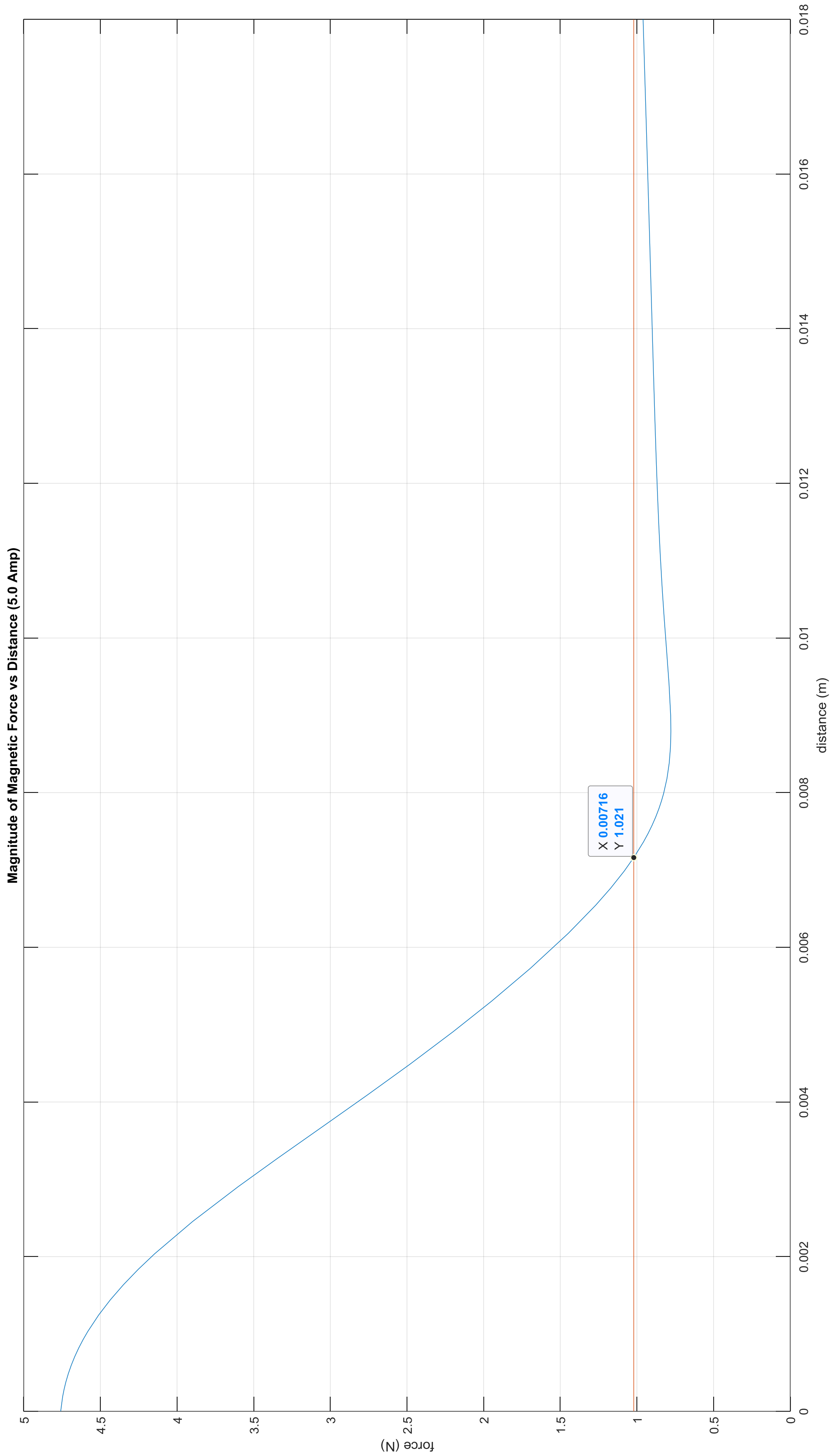

Figure 146: Threshold Distance where Iron and Iron + PM Forces are Equal (5.0 Amp)

MATLAB Source Code: Determination of Intersection Point of Iron Only Force and Iron + PM Force for 5.0 Ampere Coil Excitation

```
%% ======  Fmag for 5.0 Amp of Current ======= %%
syms k x
% Coefficients with 95% confidence bounds, where x is normalized by
mean
% 0.008989 and std 0.005265
F_sphere_50 = 1.02052895057943;
   y1 = 0.00156;  %(-0.07065, 0.07377)
   y2 = 1.513;    %(1.438, 1.588)
   y3 = 2.086;    %(1.875, 2.297)
   y4 = 4.424;    %(3.958, 4.891)
   y5 = 1.773;    %(1.528, 2.017)
   y6 = 0.6743;   %(0.5386, 0.8101)
   y7 = 3.149;    %(2.984, 3.314)
   y8 = 4.383;    %(4.033, 4.734)
   y9 = 2.188;    %(1.874, 2.502)
  y10 = 0.8648;   %(0.6898, 1.04)
eqn50 = (y1*k^5 + y2*k^4 + y3*k^3 + y4*k^2 + y5*k + y6)/(k^4 +
y7*k^3 + y8*k^2 + y9*k + y10) == F_sphere_50;
J = solve(eqn50,k);
J1 = [vpa(J(1)); vpa(J(2)); vpa(J(3)); vpa(J(4)); vpa(J(5));];
J2 = std1*J1+m1
Int_50 = J2(1);

f50(x) = (y1*((x-m1)/std1)^5 +y2*((x-m1)/std1)^4 + y3*((x-
m1)/std1)^3 + y4*((x-m1)/std1)^2 + y5*((x-m1)/std1) + y6)/(((x-
m1)/std1)^4 + y7*((x-m1)/std1)^3 + y8*((x-m1)/std1)^2 + y9*((x-
m1)/std1) + y10)
fplot (f50)
hold on
fplot(F_sphere_50)
hold on
plot(Int_50, F_sphere_50, 'r.')
xlim([0 0.018])
ylim([0 5.0])
grid on
xlabel('distance (m)')
ylabel('force (N)')
title('Magnitude of Magnetic Force vs Distance (5.0 Amp)')
```

Table 13: Fit Data –Distance where Magnitude of Magnetic Force equals Iron + PM Force vs. Coil Excitation

Intersection Distance and Angle of Iron Only & Iron+PM Force vs. Icoil			
Angle (deg)	**Distance (m)**	**Force (N)**	**Current (A)**
3.07617E+01	1.70603E-02	1.63283E-03	0.2
2.71089E+01	1.50792E-02	3.67395E-03	0.3
2.49748E+01	1.39149E-02	6.53142E-03	0.4
2.37363E+01	1.32371E-02	1.02053E-02	0.5
1.98854E+01	1.11210E-02	4.08215E-02	1.0
1.79955E+01	1.00784E-02	9.18477E-02	1.5
1.67440E+01	9.38687E-03	1.63284E-01	2.0
1.57742E+01	8.85037E-03	2.55134E-01	2.5
1.49777E+01	8.40947E-03	3.67395E-01	3.0
1.43552E+01	8.06477E-03	5.00060E-01	3.5
1.37202E+01	7.71302E-03	6.53134E-01	4.0
1.31972E+01	7.42324E-03	8.26632E-01	4.5
1.27226E+01	7.16025E-03	1.02053E+00	5.0

Table 14: Fit Data for Magnitude of Iron Only Force (N) vs. Coil Excitation (A)

Current (Amps)	Force (N)
0	0
0.2	1.63283E-03
0.3	3.67395E-03
0.4	6.53142E-03
0.5	1.02053E-02
1.0	4.08215E-02
1.5	9.18477E-02
2.0	1.63284E-01
2.5	2.55134E-01
3.0	3.67395E-01
3.5	5.00060E-01
4.0	6.53134E-01
4.5	8.26632E-01
5.0	1.02053E+00

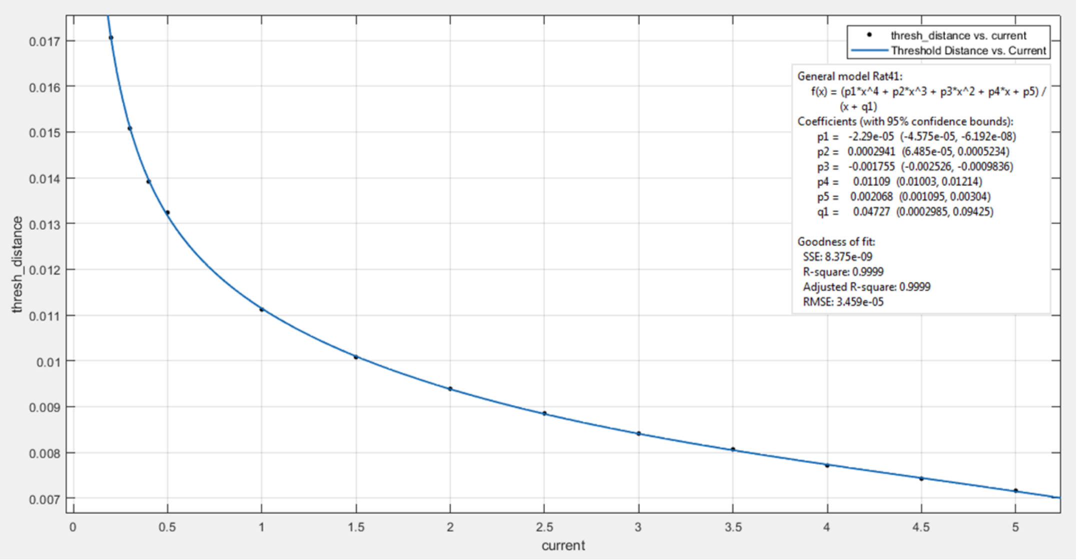

```
General model Rat41:
  f(x) = (p1*x^4 + p2*x^3 + p3*x^2 + p4*x + p5) /
         (x + q1)
Coefficients (with 95% confidence bounds):
    p1 =   -2.29e-05  (-4.575e-05, -6.192e-08)
    p2 =   0.0002941  (6.485e-05, 0.0005234)
    p3 =   -0.001755  (-0.002526, -0.0009836)
    p4 =     0.01109  (0.01003, 0.01214)
    p5 =    0.002068  (0.001095, 0.00304)
    q1 =     0.04727  (0.0002985, 0.09425)

Goodness of fit:
  SSE: 8.375e-09
  R-square: 0.9999
  Adjusted R-square: 0.9999
  RMSE: 3.459e-05
```

Figure 147: Curve Fit for Iron Only / Iron + PM Threshold Distance (m) vs. Coil Excitation (Amp)

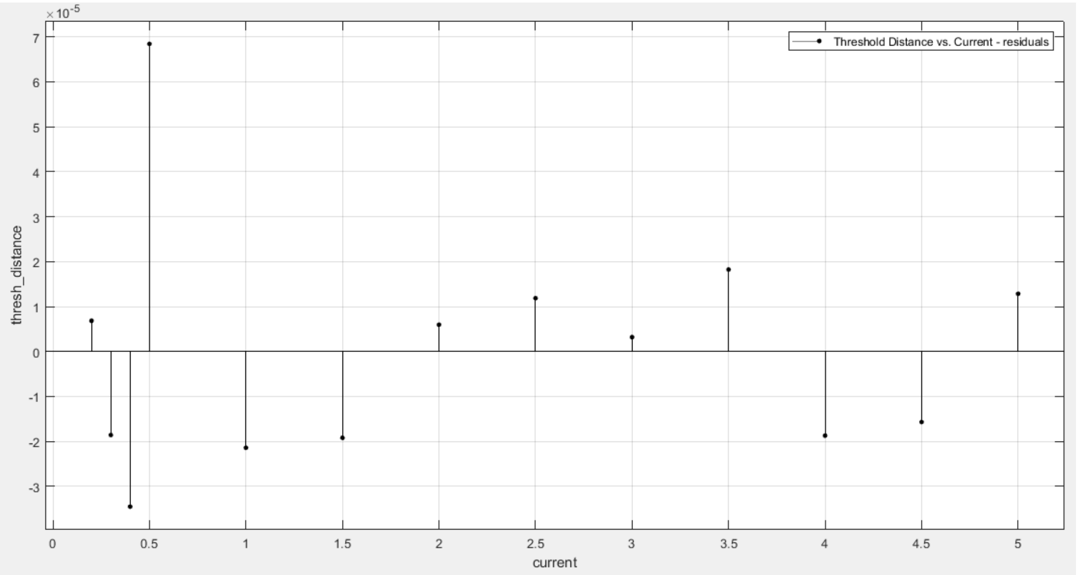

Figure 148: Residuals Plot for Iron Only / Iron + PM Threshold Distance (m) vs. Coil Excitation (Amp)

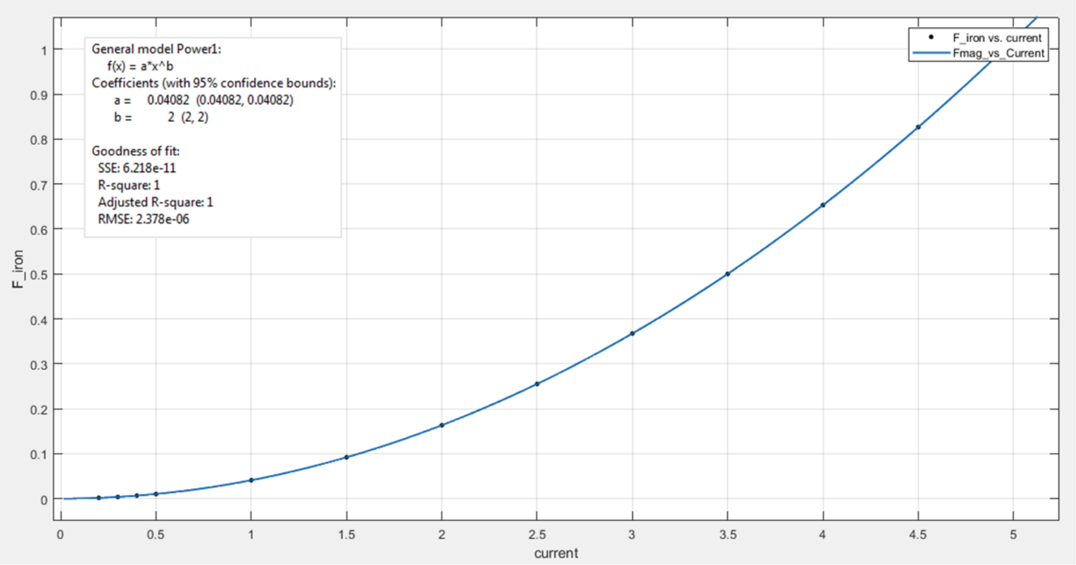

Figure 149: Curve Fit for Magnitude of Iron Only Force (N) vs. Coil Excitation (A)

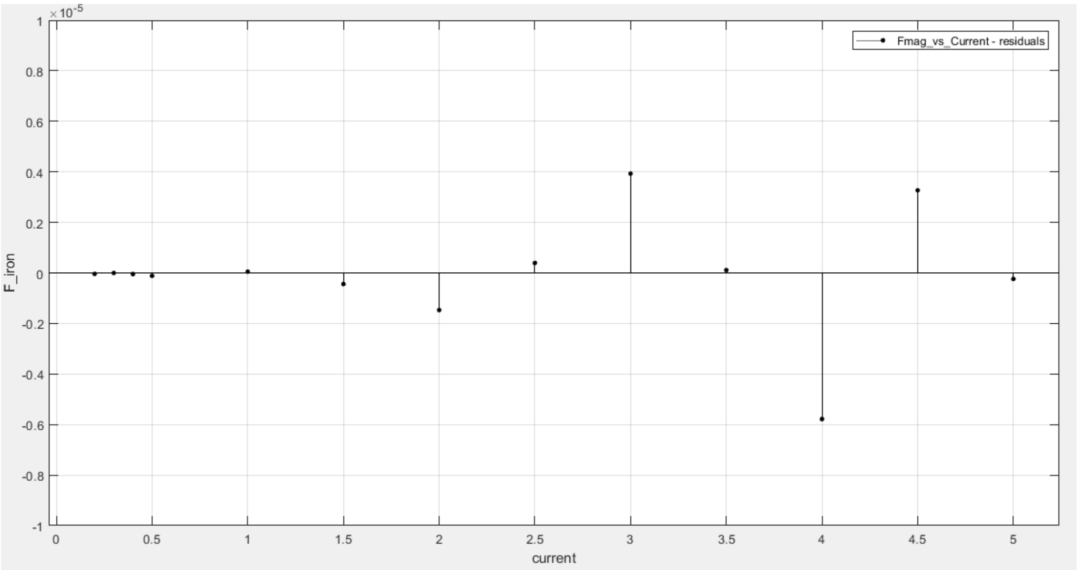

Figure 150: Residuals Plot for Magnitude of Iron Only Force (N) vs. Coil Excitation (A)

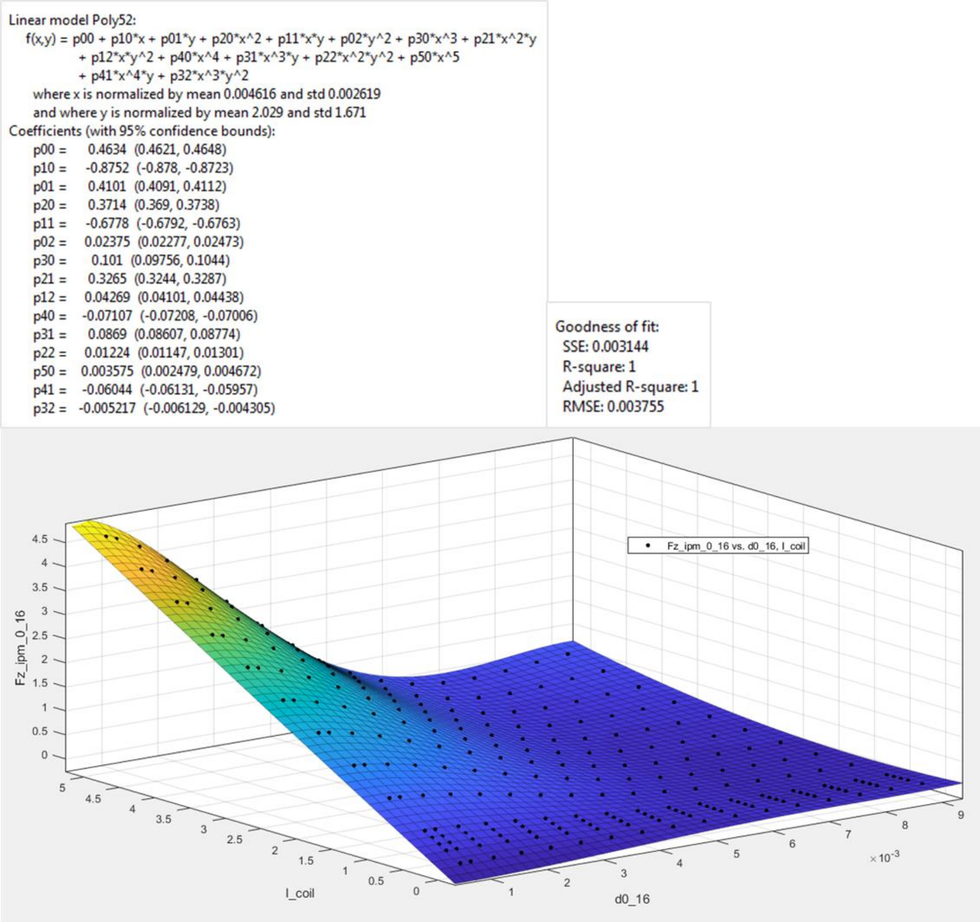

Linear model Poly52:

f(x,y) = p00 + p10*x + p01*y + p20*x^2 + p11*x*y + p02*y^2 + p30*x^3 + p21*x^2*y
+ p12*x*y^2 + p40*x^4 + p31*x^3*y + p22*x^2*y^2 + p50*x^5
+ p41*x^4*y + p32*x^3*y^2

where x is normalized by mean 0.004616 and std 0.002619
and where y is normalized by mean 2.029 and std 1.671

Coefficients (with 95% confidence bounds):

p00 = 0.4634 (0.4621, 0.4648)
p10 = -0.8752 (-0.878, -0.8723)
p01 = 0.4101 (0.4091, 0.4112)
p20 = 0.3714 (0.369, 0.3738)
p11 = -0.6778 (-0.6792, -0.6763)
p02 = 0.02375 (0.02277, 0.02473)
p30 = 0.101 (0.09756, 0.1044)
p21 = 0.3265 (0.3244, 0.3287)
p12 = 0.04269 (0.04101, 0.04438)
p40 = -0.07107 (-0.07208, -0.07006)
p31 = 0.0869 (0.08607, 0.08774)
p22 = 0.01224 (0.01147, 0.01301)
p50 = 0.003575 (0.002479, 0.004672)
p41 = -0.06044 (-0.06131, -0.05957)
p32 = -0.005217 (-0.006129, -0.004305)

Goodness of fit:
SSE: 0.003144
R-square: 1
Adjusted R-square: 1
RMSE: 0.003755

Figure 151: Surface Fit: Magnetic Force Z-comp vs. Coil Excitation (A) vs. Distance (m)

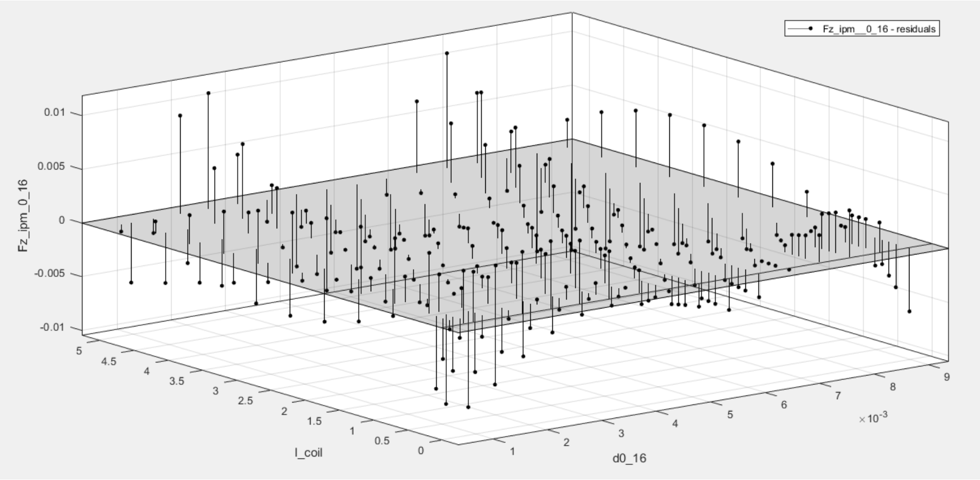

Figure 152: Residuals Plot: Magnetic Force Z-comp vs. Coil Current (A) vs. Distance (m)

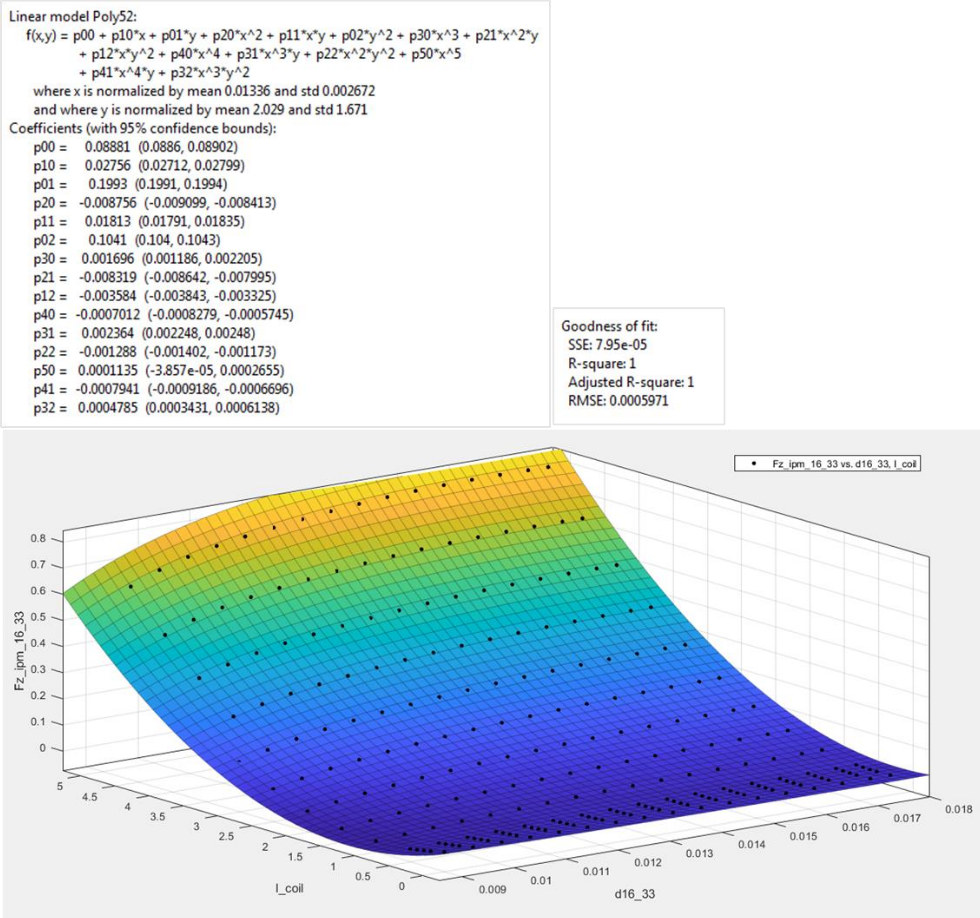

```
Linear model Poly52:
    f(x,y) = p00 + p10*x + p01*y + p20*x^2 + p11*x*y + p02*y^2 + p30*x^3 + p21*x^2*y
                  + p12*x*y^2 + p40*x^4 + p31*x^3*y + p22*x^2*y^2 + p50*x^5
                  + p41*x^4*y + p32*x^3*y^2
      where x is normalized by mean 0.01336 and std 0.002672
      and where y is normalized by mean 2.029 and std 1.671
Coefficients (with 95% confidence bounds):
      p00 =     0.08881  (0.0886, 0.08902)
      p10 =     0.02756  (0.02712, 0.02799)
      p01 =      0.1993  (0.1991, 0.1994)
      p20 =   -0.008756  (-0.009099, -0.008413)
      p11 =     0.01813  (0.01791, 0.01835)
      p02 =      0.1041  (0.104, 0.1043)
      p30 =    0.001696  (0.001186, 0.002205)
      p21 =   -0.008319  (-0.008642, -0.007995)
      p12 =   -0.003584  (-0.003843, -0.003325)
      p40 =  -0.0007012  (-0.0008279, -0.0005745)
      p31 =    0.002364  (0.002248, 0.00248)
      p22 =   -0.001288  (-0.001402, -0.001173)
      p50 =   0.0001135  (-3.857e-05, 0.0002655)
      p41 =  -0.0007941  (-0.0009186, -0.0006696)
      p32 =   0.0004785  (0.0003431, 0.0006138)
```

```
Goodness of fit:
  SSE: 7.95e-05
  R-square: 1
  Adjusted R-square: 1
  RMSE: 0.0005971
```

Figure 153: Surface Fit: Magnetic Force Z-comp vs. Coil Current (A) vs. Distance (m)

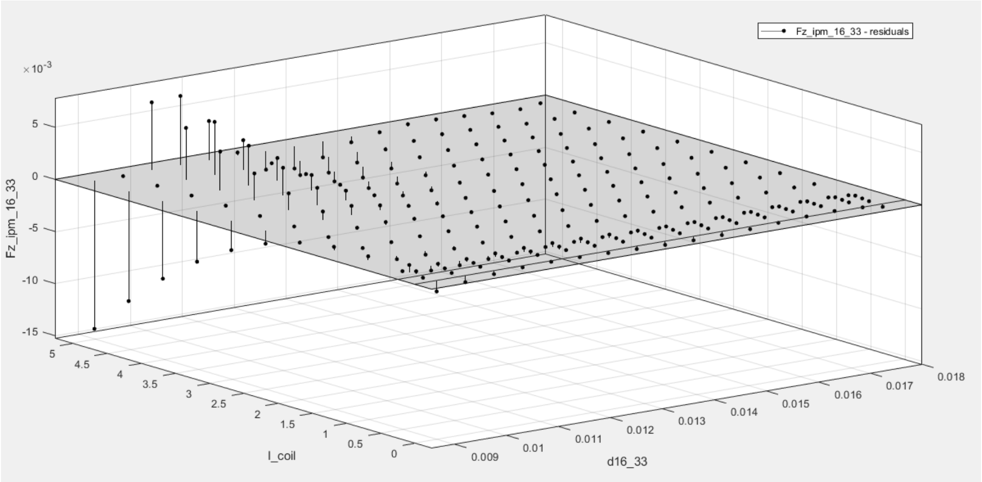

Figure 154: Residuals Plot: Magnetic Force Z-comp vs. Coil Current (A) vs. Distance (m)

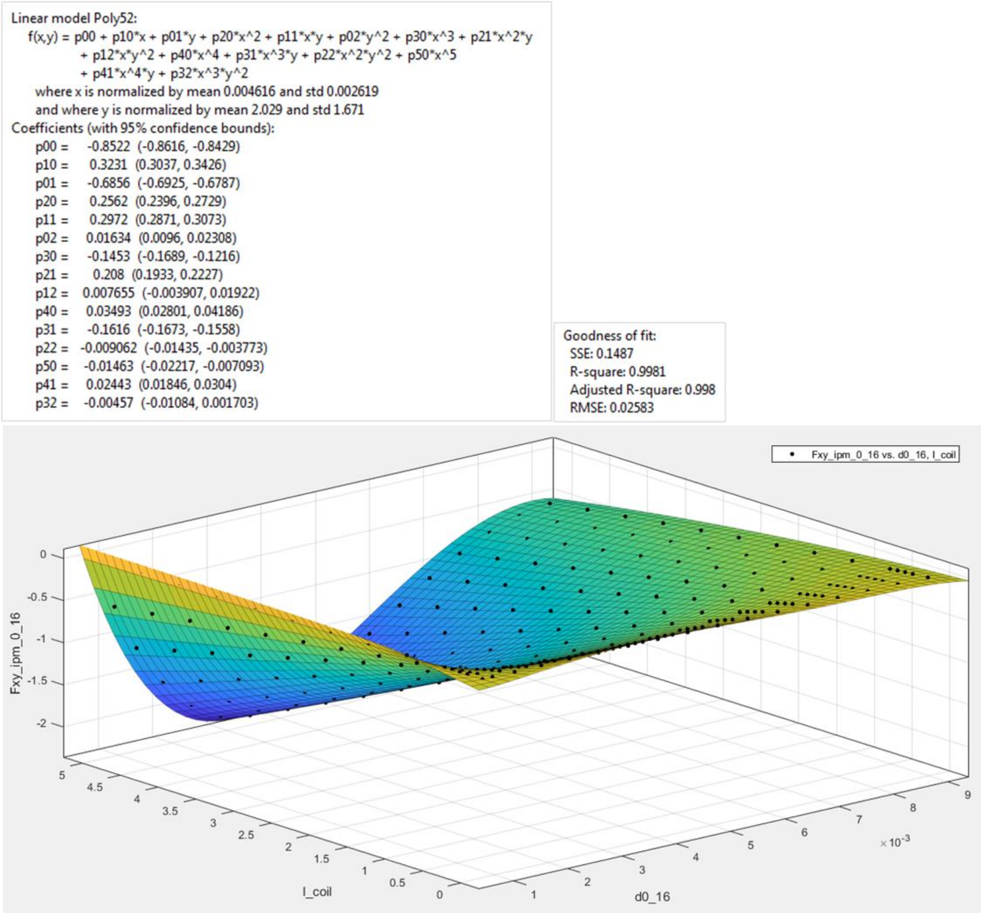

```
Linear model Poly52:
    f(x,y) = p00 + p10*x + p01*y + p20*x^2 + p11*x*y + p02*y^2 + p30*x^3 + p21*x^2*y
                  + p12*x*y^2 + p40*x^4 + p31*x^3*y + p22*x^2*y^2 + p50*x^5
                  + p41*x^4*y + p32*x^3*y^2
      where x is normalized by mean 0.004616 and std 0.002619
      and where y is normalized by mean 2.029 and std 1.671
Coefficients (with 95% confidence bounds):
      p00 =     -0.8522  (-0.8616, -0.8429)
      p10 =      0.3231  (0.3037, 0.3426)
      p01 =     -0.6856  (-0.6925, -0.6787)
      p20 =      0.2562  (0.2396, 0.2729)
      p11 =      0.2972  (0.2871, 0.3073)
      p02 =     0.01634  (0.0096, 0.02308)
      p30 =     -0.1453  (-0.1689, -0.1216)
      p21 =       0.208  (0.1933, 0.2227)
      p12 =    0.007655  (-0.003907, 0.01922)
      p40 =     0.03493  (0.02801, 0.04186)
      p31 =     -0.1616  (-0.1673, -0.1558)
      p22 =   -0.009062  (-0.01435, -0.003773)
      p50 =    -0.01463  (-0.02217, -0.007093)
      p41 =     0.02443  (0.01846, 0.0304)
      p32 =    -0.00457  (-0.01084, 0.001703)
```

```
Goodness of fit:
  SSE: 0.1487
  R-square: 0.9981
  Adjusted R-square: 0.998
  RMSE: 0.02583
```

Figure 155: Surface Fit: Magnetic Force Y-comp vs. Coil Current (A) vs. Distance (m)

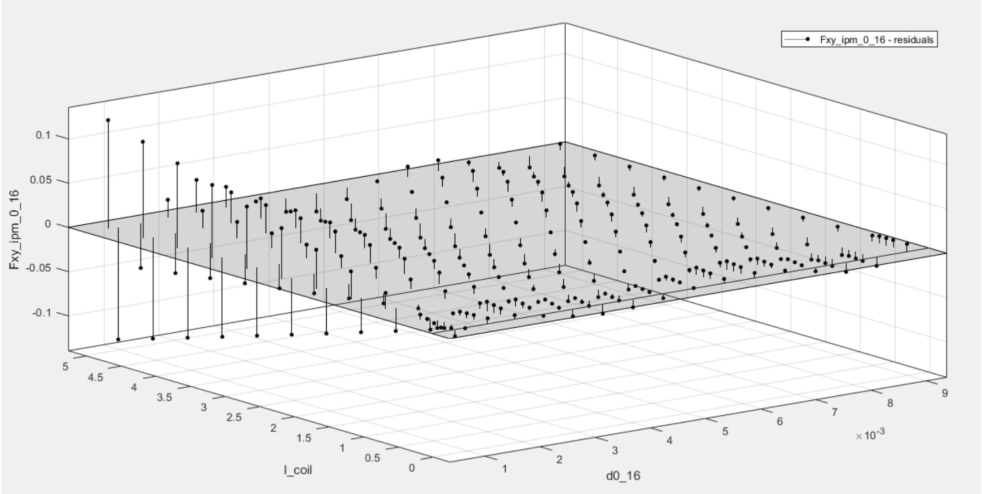

Figure 156: Residuals Plot: Magnetic Force Y-comp vs. Coil Current (A) vs. Distance (m)

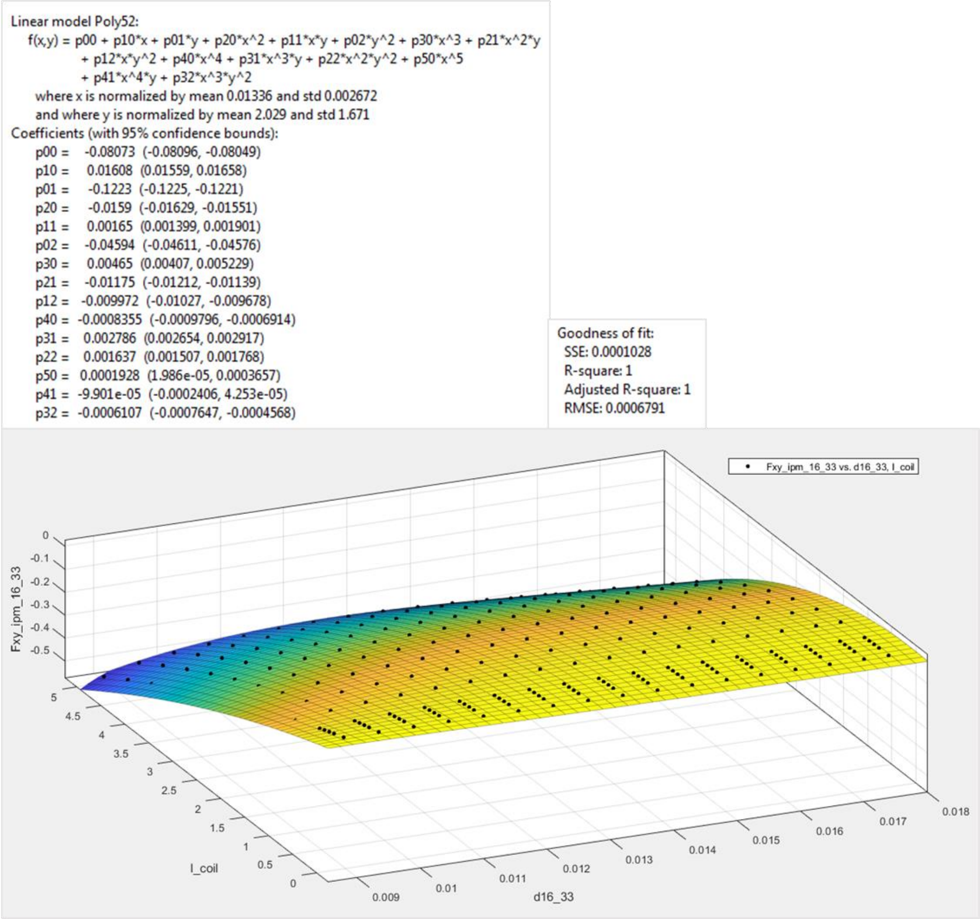

Linear model Poly52:
f(x,y) = p00 + p10*x + p01*y + p20*x^2 + p11*x*y + p02*y^2 + p30*x^3 + p21*x^2*y
+ p12*x*y^2 + p40*x^4 + p31*x^3*y + p22*x^2*y^2 + p50*x^5
+ p41*x^4*y + p32*x^3*y^2
where x is normalized by mean 0.01336 and std 0.002672
and where y is normalized by mean 2.029 and std 1.671

Coefficients (with 95% confidence bounds):

p00 =	-0.08073	(-0.08096, -0.08049)
p10 =	0.01608	(0.01559, 0.01658)
p01 =	-0.1223	(-0.1225, -0.1221)
p20 =	-0.0159	(-0.01629, -0.01551)
p11 =	0.00165	(0.001399, 0.001901)
p02 =	-0.04594	(-0.04611, -0.04576)
p30 =	0.00465	(0.00407, 0.005229)
p21 =	-0.01175	(-0.01212, -0.01139)
p12 =	-0.009972	(-0.01027, -0.009678)
p40 =	-0.0008355	(-0.0009796, -0.0006914)
p31 =	0.002786	(0.002654, 0.002917)
p22 =	0.001637	(0.001507, 0.001768)
p50 =	0.0001928	(1.986e-05, 0.0003657)
p41 =	-9.901e-05	(-0.0002406, 4.253e-05)
p32 =	-0.0006107	(-0.0007647, -0.0004568)

Goodness of fit:
SSE: 0.0001028
R-square: 1
Adjusted R-square: 1
RMSE: 0.0006791

Figure 157: Surface Fit: Iron+PM Force Y-comp vs. Coil Current (A) vs Distance (m)

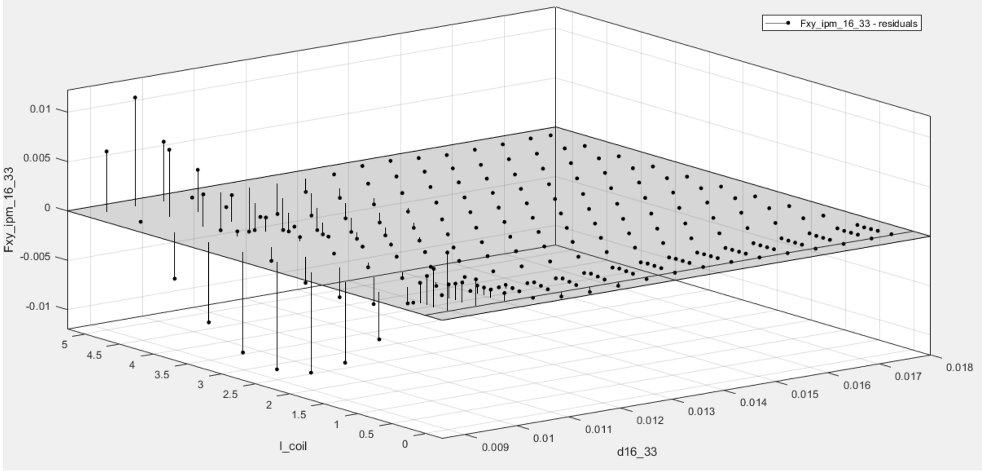

Figure 158: Surface Fit: Iron+PM Force Y-comp (N) vs Coil Current (A) vs Distance (m)

Appendix C

Validation Data: Transformation of Magnetic Forces and Torques

Table 15: Validation Data for Coordinate Transformation of Forces

	EM_1 Force Validation Data - 0.5 Amps of Coil Excitation							
	COMSOL Lorentz Force				**Coordinate Transformation Forces**			
PM Position	**Fx**	**Fy**	**Fz**	**Fmag**	**Fx**	**Fy**	**Fz**	**Fmag**
1	-4.0828E-06	-1.4203E-01	1.0017E-01	1.7380E-01	-3.6500E-06	-1.4204E-01	1.0016E-01	1.7380E-01
2	-1.6379E-01	-4.7474E-02	-3.3565E-02	1.7380E-01	-1.6378E-01	-4.7480E-02	-3.3569E-02	1.7380E-01
3	-4.0020E-06	4.7084E-02	-1.6730E-01	1.7380E-01	-3.6500E-06	4.7082E-02	-1.6730E-01	1.7380E-01
4	1.6379E-01	-4.7480E-02	-3.3569E-02	1.7381E-01	1.6378E-01	-4.7475E-02	-3.3574E-02	1.7380E-01

	EM_2 Force Validation Data - 0.5 Amps of Coil Excitation							
	COMSOL Validation Data				**Coordinate Transformation Forces**			
PM Position	**Fx**	**Fy**	**Fz**	**Fmag**	**Fx**	**Fy**	**Fz**	**Fmag**
1	1.2301E-01	7.1023E-02	1.0016E-01	1.7380E-01	1.2301E-01	7.1021E-02	1.0016E-01	1.7380E-01
2	1.2301E-01	-1.1810E-01	-3.3575E-02	1.7380E-01	1.2301E-01	-1.1810E-01	-3.3569E-02	1.7380E-01
3	-4.0785E-02	-2.3543E-02	-1.6730E-01	1.7380E-01	-4.0772E-02	-2.3544E-02	-1.6730E-01	1.7380E-01
4	-4.0785E-02	1.6558E-01	-3.3571E-02	1.7380E-01	-4.0776E-02	1.6558E-01	-3.3574E-02	1.7380E-01

	EM_3 Force Validation Data - 0.5 Amps of Coil Excitation							
	COMSOL Validation Data				**Coordinate Transformation Forces**			
PM Position	**Fx**	**Fy**	**Fz**	**Fmag**	**Fx**	**Fy**	**Fz**	**Fmag**
1	-1.2301E-01	7.1014E-02	1.0017E-01	1.7381E-01	-1.2301E-01	7.1015E-02	1.0016E-01	1.7380E-01
2	4.0774E-02	1.6558E-01	-3.3569E-02	1.7380E-01	4.0772E-02	1.6558E-01	-3.3568E-02	1.7380E-01
3	4.0774E-02	-2.3546E-02	-1.6730E-01	1.7380E-01	4.0776E-02	-2.3538E-02	-1.6730E-01	1.7380E-01
4	-1.2301E-01	-1.1811E-01	-3.3565E-02	1.7380E-01	-1.2301E-01	-1.1810E-01	-3.3575E-02	1.7380E-01

	EM_4 Force Validation Data - 0.5 Amps of Coil Excitation							
	COMSOL Validation Data				**Coordinate Transformation Forces**			
PM Position	**Fx**	**Fy**	**Fz**	**Fmag**	**Fx**	**Fy**	**Fz**	**Fmag**
1	-3.6553E-06	-4.7092E-02	1.6730E-01	1.7380E-01	-3.6500E-06	-4.7082E-02	1.6730E-01	1.7380E-01
2	1.6379E-01	4.7476E-02	3.3574E-02	1.7381E-01	1.6378E-01	4.7475E-02	3.3574E-02	1.7380E-01
3	-4.0577E-06	1.4204E-01	-1.0016E-01	1.7380E-01	3.6500E-06	1.4204E-01	-1.0016E-01	1.7380E-01
4	-1.6379E-01	4.7470E-02	3.3571E-02	1.7380E-01	-1.6378E-01	4.7480E-02	3.3569E-02	1.7380E-01

	EM_5 Force Validation Data - 0.5 Amps of Coil Excitation							
	COMSOL Validation Data				**Coordinate Transformation Forces**			
PM Position	**Fx**	**Fy**	**Fz**	**Fmag**	**Fx**	**Fy**	**Fz**	**Fmag**
1	4.0774E-02	2.3545E-02	1.6730E-01	1.7380E-01	4.0776E-02	2.3538E-02	1.6730E-01	1.7380E-01
2	-1.2301E-01	1.1811E-01	3.3564E-02	1.7380E-01	-1.2301E-01	1.1810E-01	3.3575E-02	1.7380E-01
3	-1.2301E-01	-7.1015E-02	-1.0017E-01	1.7381E-01	-1.2301E-01	-7.1015E-02	-1.0016E-01	1.7380E-01
4	4.0773E-02	-1.6558E-01	3.3568E-02	1.7380E-01	4.0772E-02	-1.6558E-01	3.3568E-02	1.7380E-01

	EM_6 Force Validation Data - 0.5 Amps of Coil Excitation							
	COMSOL Validation Data				**Coordinate Transformation Forces**			
PM Position	**Fx**	**Fy**	**Fz**	**Fmag**	**Fx**	**Fy**	**Fz**	**Fmag**
1	-4.0785E-02	2.3543E-02	1.6730E-01	1.7380E-01	-4.0772E-02	2.3544E-02	1.6730E-01	1.7380E-01
2	-4.0785E-02	-1.6558E-01	3.3571E-02	1.7380E-01	-4.0776E-02	-1.6558E-01	3.3574E-02	1.7380E-01
3	1.2301E-01	-7.1023E-02	-1.0016E-01	1.7380E-01	1.2301E-01	-7.1021E-02	-1.0016E-01	1.7380E-01
4	1.2301E-01	1.1811E-01	3.3575E-02	1.7381E-01	1.2301E-01	1.1810E-01	3.3569E-02	1.7380E-01

Notes:

- All forces are in Newtons
- Discrepancies between COMSOL validation data and the transformed simulation data are due to rounding errors.

Table 16: Validation Data for Torques from Transformed Magnetic Forces

	EM_1 Torque Validation Data - 0.5 Amps of Coil Excitation (N/m)					
	COMSOL Torque (EM)			**Coord. Transformation Torque (EM)**		
PM Position	**Tx**	**Ty**	**Tz**	**Tx**	**Ty**	**Tz**
1	5.2329E-03	2.6079E-06	-5.7585E-06	5.3251E-03	-7.6637E-08	1.0838E-07
2	-1.8222E-05	-3.0212E-03	4.2702E-03	1.1112E-07	-3.0745E-03	4.3480E-03
3	-5.2204E-03	-6.2930E-06	1.9009E-05	-5.3249E-03	-7.5121E-08	1.0624E-07
4	-4.7234E-05	3.0693E-03	-4.3293E-03	1.1756E-07	3.0745E-03	-4.3480E-03

	EM_2 Torque Validation Data - 0.5 Amps of Coil Excitation (N/m)					
	COMSOL Torque (EM)			**Coord. Transformation Torque (EM)**		
PM Position	**Tx**	**Ty**	**Tz**	**Tx**	**Ty**	**Tz**
1	-2.59980E-03	4.56860E-03	3.34700E-05	-2.6626E-03	4.6116E-03	-7.2338E-08
2	2.62780E-03	1.51810E-03	4.28720E-03	2.6625E-03	1.5371E-03	4.3478E-03
3	2.60660E-03	-4.48930E-03	1.66120E-05	2.6625E-03	-4.6117E-03	-9.7238E-08
4	-2.57280E-03	-1.55270E-03	-4.23840E-03	-2.6625E-03	-1.5373E-03	-4.3479E-03

	EM_3 Torque Validation Data - 0.5 Amps of Coil Excitation (N/m)					
	COMSOL Torque (EM)			**Coord. Transformation Torque (EM)**		
PM Position	**Tx**	**Ty**	**Tz**	**Tx**	**Ty**	**Tz**
1	-2.5640E-03	-4.4846E-03	-2.3266E-05	-2.6625E-03	-4.6119E-03	-1.3457E-07
2	-2.6084E-03	1.5118E-03	4.2631E-03	-2.6625E-03	1.5371E-03	4.3478E-03
3	2.5814E-03	4.4920E-03	1.4395E-05	2.6625E-03	4.6115E-03	-1.1773E-07
4	2.6328E-03	-1.4889E-03	-4.2721E-03	2.6625E-03	-1.5374E-03	-4.3480E-03

	EM_4 Torque Validation Data - 0.5 Amps of Coil Excitation (N/m)					
	COMSOL Torque (EM)			**Coord. Transformation Torque (EM)**		
PM Position	**Tx**	**Ty**	**Tz**	**Tx**	**Ty**	**Tz**
1	-5.2374E-03	-2.2749E-05	4.6668E-05	-5.3251E-03	6.8613E-08	-9.7033E-08
2	1.6354E-05	-3.0183E-03	4.2737E-03	-9.0249E-08	-3.0745E-03	4.3480E-03
3	5.2609E-03	1.3516E-05	-1.5052E-05	5.3250E-03	7.6166E-08	-1.0772E-07
4	1.5890E-05	3.0427E-03	-4.3135E-03	-1.2324E-07	3.0745E-03	-4.3480E-03

	EM_5 Torque Validation Data - 0.5 Amps of Coil Excitation (N/m)					
	COMSOL Torque (EM)			**Coord. Transformation Torque (EM)**		
PM Position	**Tx**	**Ty**	**Tz**	**Tx**	**Ty**	**Tz**
1	2.6185E-03	-4.5350E-03	-6.4552E-06	2.6625E-03	-4.6115E-03	9.4744E-08
2	2.5706E-03	1.4699E-03	4.1865E-03	2.6625E-03	1.5374E-03	4.3480E-03
3	-2.5992E-03	4.5323E-03	1.5795E-05	-2.6626E-03	4.6119E-03	1.1158E-07
4	-2.6121E-03	-1.5189E-03	-4.2745E-03	-2.6625E-03	-1.5371E-03	-4.3478E-03

	EM_6 Torque Validation Data - 0.5 Amps of Coil Excitation (N/m)					
	COMSOL Torque (EM)			**Coord. Transformation Torque (EM)**		
PM Position	**Tx**	**Ty**	**Tz**	**Tx**	**Ty**	**Tz**
1	2.6214E-03	4.4953E-03	-4.4398E-05	2.6625E-03	4.6117E-03	9.7238E-08
2	-2.5820E-03	1.4878E-03	4.2142E-03	-2.6625E-03	1.5373E-03	4.3479E-03
3	-2.5841E-03	-4.5027E-03	-1.8639E-05	-2.6626E-03	-4.6116E-03	7.2338E-08
4	2.6158E-03	-1.5021E-03	-4.2629E-03	2.6627E-03	-1.5371E-03	-4.3480E-03

Note:

- All torques are in Newton-meters. Discrepancies between COMSOL validation data and the transformed simulation data are due to rounding errors and because the line of action associated with the torque is not provided by COMSOL.

Appendix D

MATLAB Code: Force and Torque Computation Algorithm

```
%MSFUNTMPL_BASIC A Template for a Level-2 MATLAB S-Function
% The MATLAB S-function is written as a MATLAB function with the
same name as the S-function. Replace 'msfuntmpl_basic' with the
name of your S-function. It should be noted that the MATLAB S-
function is very similar to Level-2 C-Mex S-functions. You should
be able to get more information for each of the block methods by
referring to the documentation for C-Mex S-functions. Copyright
2003-2010 The MathWorks, Inc.

function MagLev_Final(block);
% J.Byron - Master's Thesis - Dynamic Modeling of a 3-DOF Reaction
Sphere. This MATLAB Level 2 S-function calculates the scalar
distance between each EM and PM, and determines which EM / PM pair
are interacting. Due to the geometry of the PMs on the sphere, only
one PM can interact with one EM at any given position. The EM
positions are fixed relative to a global coordinate system located
at the center of stator. The EM position vectors are integrated
into this S-function and given in Cartesian coordinates to make use
of various vector operations. After calculating the distance, the
instantaneous current each EM is used to calculate the EM/PM
distance where the Iron Only force equals the Iron+PM force. This
distance "dt" will then be used as a threshold to logically
determine which force is dominate. The output of this function are
the forces and torques acting on rotor (sphere) and the
corresponding reactions on the stator (EMs).

%========== UNITS =============%
% Length ==> meters  (m)
% Force  ==> Newtons (N)
% Mass   ==> Kilograms (kg)
% Moment of Inertia ==> kg*m^2
% Torque ==> Newton-meter (Nm)
% Curent ==> Amperes (A)
% Angle  ==> Radians (rad)

setup(block);
%end function

function setup(block);
  %% Register number of ports
  block.NumInputPorts  = 2;
  block.NumOutputPorts = 2;

  %% Setup port properties to be inherited or dynamic
  block.SetPreCompInpPortInfoToDynamic;
  block.SetPreCompOutPortInfoToDynamic;

  %% Setup port properties (datatype id = 0 ==> Double

  % Input Port 1 ==> Array Coil Currents
  block.InputPort(1).Dimensions   = [1 6];
  block.InputPort(1).DataTypeId   = 0;
```

```
  block.InputPort(1).Complexity   = 'Real';
  block.InputPort(1).DirectFeedthrough = true;

  % Input Port 2 ==> Euler Angles
  block.InputPort(2).Dimensions   = [1 3];
  block.InputPort(2).DataTypeId   = 0;
  block.InputPort(2).Complexity   = 'Real';
  block.InputPort(2).DirectFeedthrough = true;

  % Output Port ==> Forces
  block.OutputPort(1).Dimensions   = [3 1];
  block.OutputPort(1).DataTypeId   = 0;
  block.OutputPort(1).Complexity   = 'Real';

  % Output Port ==> Torques
  block.OutputPort(2).Dimensions   = [3 1];
  block.OutputPort(2).DataTypeId   = 0;
  block.OutputPort(2).Complexity   = 'Real';

  % Register parameters
  block.NumDialogPrms = 0;

  % Ccontinuous states for derivatives
  % block.NumContStates = 6;

  % Register sample times:[0 offset]: Continuous
  block.SampleTimes = [0 0];

  % Specify if Accelerator should use TLC or call back to the
MATLAB file
  block.SetAccelRunOnTLC(false);

  % Specify the block simStateCompliance:'DefaultSimState', Same
sim state as a built-in block
  block.SimStateCompliance = 'DefaultSimState';

  %% Register methods
  block.RegBlockMethod('SetInputPortSamplingMode',
@SetInputPortFrameData);
  %block.RegBlockMethod('InitializeConditions',
@InitializeConditions);
  block.RegBlockMethod('Outputs', @Outputs);     % Required
  block.RegBlockMethod('Terminate', @Terminate); % Required
%end function

% NOTE: If more than one instance of this block is used within a
Simulink
% model, then a Dwork vector must be defined to prevent the S-
function
% instances from overwriting one another.
```

```
function SetInputPortFrameData(block, idx, fd)

  block.InputPort(idx).SamplingMode = fd;
  block.OutputPort(idx).SamplingMode  = fd;
 %end function

function Outputs(block)
%=============== ASSIGN INPUTS AND SIMULATION PARAMETERS
================%

 i_coil = block.InputPort(1).Data;    % EM_1 current
    psi = block.InputPort(2).Data(1); % Rotation Angle of Z axis
  theta = block.InputPort(2).Data(2); % Rotation Angle of Y' axis
    phi = block.InputPort(2).Data(3); % Rotation Angle of X'' axis

% Mass properties obtained from Solidworks CAD model:
Rotor_NGC_RS_V2.assy

rs = 0.03175;             % Radius of Sphere (m) ==> 1.25 inch
rem = 0.032512;           % Radius of inner sphere rs + airgap
m = 1.092;                % Mass of rotor (sphere, inserts, PMs)
I = [4.3955e-04 0 0;      % Inertia Tensor of Sphere
     0 4.3955e-04 0;
     0 0 4.3955e-04;];
dh = 0.00842182786076174; % Distance where Iron + PM force function
changes

% Pre-allocating arrays increases computation speed %
    ds = zeros(6,12);  % Distance between Rotated PMs and each EM
    dm = zeros(6,1);   % Distance between EM - PM in closest
proximity
    d = zeros(6,2);     % Adjusted distance (dm) for fit surface of
Force (centered/scaled) for X,Y,Z
    id_pm = zeros(6,1);  % Identity of PM closest to each EM
    fgen  = zeros(3,6);  % Force components in predicted by
generalized model
    fcan = zeros(3,6);   % Force components in canonical form (EM
fixed)
    fcomp = zeros(3,6);  % Force components transformed to EM
coordinates
    tcomp = zeros(3,6);  % Torque components of each EM
    Ptpm  = zeros(3,6);  % Transposed PM coordinates

 %========== POSITION VECTORS OF ELECTROMAGNETS (EMs) ============%
 % Columns 1-3 are upper hemisphere EM position vectors and columns
 % 4-6 are lower hemisphere EM position vectors

  Pem = rem.*[0 -sqrt(2)/2 sqrt(2)/2 0 sqrt(2)/2 -sqrt(2)/2;
       sqrt(2)/sqrt(3) -sqrt(2)/(2*sqrt(3)) -sqrt(2)/(2*sqrt(3)) -
sqrt(2)/sqrt(3) sqrt(2)/(2*sqrt(3)) sqrt(2)/(2*sqrt(3));
       1/sqrt(3) 1/sqrt(3) 1/sqrt(3) -1/sqrt(3) -1/sqrt(3) -
1/sqrt(3);];
```

```
 ru = Pem/rem;  % Convert EM position vectors into unit vectors

%========== POSITION VECTORS OF PERMANENT MAGNETS (PMs) ==========%
% Columns 1-6 are upper hemisphere PM position vectors and columns
6-12 are lower hemisphere PM position vectors

 Ppm = rs.*[0 2/sqrt(5) (5-sqrt(5))/10 (-5-sqrt(5))/10 (-5-
sqrt(5))/10 (5-sqrt(5))/10 0 -2/sqrt(5) -(5-sqrt(5))/10 -(-5-
sqrt(5))/10 -(-5-sqrt(5))/10 -(5-sqrt(5))/10;
        0 0 sqrt((5+sqrt(5))/10) sqrt((5-sqrt(5))/10) -sqrt((5-
sqrt(5))/10) -sqrt((5+sqrt(5))/10) 0 0 -sqrt((5+sqrt(5))/10) -
sqrt((5-sqrt(5))/10) sqrt((5-sqrt(5))/10) sqrt((5+sqrt(5))/10);
        1 1/sqrt(5) 1/sqrt(5) 1/sqrt(5) 1/sqrt(5) 1/sqrt(5) -1 -
1/sqrt(5) -1/sqrt(5) -1/sqrt(5) -1/sqrt(5) -1/sqrt(5);];

%================ EULER ROTATION MATRIX ====================%
 Rm = [cos(psi)*cos(theta),  sin(psi)*cos(theta),   -sin(theta);
     -sin(psi)*cos(phi)+cos(psi)*sin(theta)*sin(phi),
cos(psi)*cos(phi)+sin(psi)*sin(theta)*sin(phi),
cos(theta)*sin(phi);
      sin(psi)*sin(phi)+cos(psi)*sin(theta)*cos(phi), -
cos(psi)*sin(phi)+sin(psi)*sin(theta)*cos(phi),
cos(theta)*cos(phi)];

 %============ CALCULATE COORDINATES OF ROTATED PMs ===========%
%Note: since the position vectors of the PMs are given as column
vectors the rotation matrix must be transposed and pre-multiplies
the position vectors

    Prpm = transpose(Rm)*Ppm;

%============ CALCULATE FORCE IN IRON ONLY REGION ==============%
 % Equation calculates the magnitude of magnetic force (Newtons)
between an EM and the iron rotor as a function of current
(Calculated for each EM). PM field is neglected in this region.

    p1 =  0.04082;
    p2 =  2;

    fio = p1.*i_coil.^p2;

 %== COEFFICIENTS OF POLYNOMIAL THAT CALCULATES IRON+PM" FORCE ===%
 % column_1 is applicable for dh <= 0.00842182786076174 and i =
0..5 and column_2 is applicable for dh  > 0.00842182786076174 and i
= 0..5

    dmean = [0.004616  0.01336];
    dstd  =  [0.002619 0.002672];
    imean = 2.029;
    istd  =  1.671;
```

```
 % Coefficients for Z-Component
    z00 = [0.4634      0.08881];
    z10 = [-0.8752     0.02756];
    z01 = [0.4101      0.1993];
    z20 = [0.3714     -0.008756];
    z11 = [-0.6778     0.01813];
    z02 = [0.02375     0.1041];
    z30 = [0.101       0.001696];
    z21 = [0.3265     -0.008319];
    z12 = [0.04269    -0.003584];
    z40 = [-0.07107   -0.0007012];
    z31 = [0.0869      0.002364];
    z22 = [0.01224    -0.001288];
    z50 = [0.003575    0.0001135];
    z41 = [-0.06044   -0.0007941];
    z32 = [-0.005217   0.0004785];

 % Coefficients for XY-Components
    a00 =  [-0.8522    -0.08073];
    a10 =  [0.3231      0.01608];
    a01 =  [-0.6856    -0.1223];
    a20 =  [0.2562     -0.0159];
    a11 =  [0.2972      0.00165];
    a02 =  [0.01634    -0.04594];
    a30 =  [-0.1453     0.00465];
    a21 =  [0.208      -0.01175];
    a12 =  [0.007655   -0.009972];
    a40 =  [0.03493    -0.0008355];
    a31 =  [-0.1616     0.002786];
    a22 =  [-0.009062   0.001637];
    a50 =  [-0.01463    0.0001928];
    a41 =  [0.02443    -9.901e-05];
    a32 =  [-0.00457   -0.0006107];

 %====== CALCULATE THRESHOLD DISTANCE FOR PM INTERACTION =========%
 % Equation outputs the the distance "dio" (meters) where the "Iron
Only" force is equal to the "Iron + PM force" for a given EM
current

    a1 = -2.29e-05;
    a2 =  0.0002941;
    a3 = -0.001755;
    a4 =  0.01109;
    a5 =  0.002068;
    a6 =  0.04727;

    dio = (a1.*i_coil.^4 + a2.*i_coil.^3 + a3.*i_coil.^2 +
a4.*i_coil + a5)./(i_coil + a6);

 %==== CALCULATE SCALAR DISTANCE BETWEEN EMs AND ROTATED PMs =====%
```

```
 % This for-loop calculates the distance between all 12 PMs
relative to each EM for a total of 72 distances. i denotes the
number of PMs and j denotes number of EMs. For example row 1,
columns 1-12 correspond to distances of all PMs relative to EM_1.
Column 1, rows 1-6 are the distances between each EM relative to
PM_1.

    for k = 1:12
        for j = 1:6
            ds(j,k) = norm(Pem(:,j)-Prpm(:,k));
        end
    end

 %============ DETERMINE MINIMUM DISTANCE BETWEEN EM / PM =========%
 % This for loop identifies and outputs the PM number (id) and
distance (dm)
 % of the closest PM to each EM

    for j = 1:6
        [dm(j,:), id_pm(j,:)] = min(ds(j,:));
    end

%========= COORDINATE TRANSFORMATIONS - FORCE VECTORS ===========%
% The rotation matrices to perform the coordinate transformations
is:
   1.) Rotation about x-axis by instantaneous angle between EM/PM
(phi_in)
   2.) Rotation about z-axis to the applicable stator position
(psi_em)
%   3.) Rotation about x'-axis to EM Stator position

% Note: the instantaneous value in step 1 transforms the rotating
EM in the generalized model to the dynamic model where where the EM
is fixed.

% phi_in  ==> rotation matrix moves EM to canonical position in
generalized model (canonical position is coincident with Z-axis)
% psi_em  ==> rotation matrix moves EM from canonical position to
stator coordinates
% phi2_em ==> rotation matrix moves EM from canonical position to
stator coordinates

   phi_in = acos(((dm.^2)-rem^2 - rs^2)/(-2*rem*rs));
   psi_em = [0 (5*pi/3) (pi/3) 0 (2*pi/3) (4*pi/3)];
  phi2_em = [-acos(1/sqrt(3)) acos(1/sqrt(3)) acos(1/sqrt(3)) pi-
acos(1/sqrt(3)) pi-acos(1/sqrt(3)) pi-acos(1/sqrt(3))];


%============== CALCULATE FORCES AND TORQUES =====================%
% The "Iron Only" force acts along the axis of the EM position
vector and acts to pull the sphere toward the electromagnet
```

```
(direction of minimum reluctance). Therefore, multiplying the
magnitude of the force by the EM position vector will give the
force components with the correct direction. (x,y,z) and sign (+/-
). Calculation of this force is performed in the first "if"
statement.

% The "Iron + PM" force does not act thru the center of mass of the
rotor. Therefore a moment will be generated. Calculation of the
forces and  torques in Iron + PM Region are performed in the
remaining "else if" statements. Note: the functions that calculate
the fy and fz components in this region are separated into 2 fit
equations to improve accuracy of the computed force.

% Adjust input for fit curves and surfaces (centered/scaled)

 i = (i_coil-imean)./istd;

    for n = 1:2
        d(:,n) = (dm-dmean(n))./dstd(n);
    end

%The logic in this for loop is in accordance with the logic
discussed in the thesis document, section 5.5
    for j = 1:6
         if(ge(dm(j), dio(j)))
                fcomp(:,j) = fio(j)*ru(:,j);
                tcomp(:,j) = cross(ru(:,j),fcomp(:,j));
         elseif((lt(dm(j), dio(j))) & (le(dm(j), dh)))
                     fx = 0;
                     fy = a00(1)+ a10(1)*d(j,1)  + a20(2)*d(j,1)^2 +
a30(1)*d(j,1)^3 + a40(1)*d(j,1)^4 + a50(1)*d(j,1)^5 + a01(1)*i(j) +
a02(1)*i(j)^2 + a11(1)*d(j,1)*i(:,j) + a21(1)*d(j,1)^2*i(j) +
a12(1)*d(j,1)*i(j)^2 + a31(1)*d(j,1)^3*i(j) +
a22(1)*d(j,1)^2*i(j)^2 + a41(1)*d(j,1)^4*i(j) +
a32(1)*d(j,1)^3*i(j)^2;
                     fz = z00(1)+ z10(1)*d(j,1)  + z20(1)*d(j,1)^2 +
z30(1)*d(j,1)^3 + z40(1)*d(j,1)^4 + z50(1)*d(j,1)^5 + z01(1)*i(j) +
z02(1)*i(j)^2 + z11(1)*d(j,1)*i(:,j) + z21(1)*d(j,1)^2*i(j) +
z12(1)*d(j,1)*i(j)^2 + z31(1)*d(j,1)^3*i(j) +
z22(1)*d(j,1)^2*i(j)^2 + z41(1)*d(j,1)^4*i(j) +
z32(1)*d(j,1)^3*i(j)^2;
              fgen(:,j) = [fx; fy; fz]; % Components from
Generalized RS model
                 Rx_gen = [1 0 0;  0 cos(phi_in(j)) -
sin(phi_in(j));  0  sin(phi_in(j))  cos(phi_in(j))];
              fcan(:,j) = Rx_gen*fgen(:,j);
                  Rz_em = [cos(psi_em(j)) -sin(psi_em(j)) 0;
sin(psi_em(j)) cos(psi_em(j)) 0; 0 0 1];
                 Rx2_em = [1 0 0; 0 cos(phi2_em(j)) -
sin(phi2_em(j)); 0 sin(phi2_em(j)) cos(phi2_em(j))];
              Ptpm(:,j) = transpose(Rz_em*Rx2_em)*Prpm(:,id_pm(j));
                    vpn = [0 abs(sin(phi_in(j)))
abs(cos(phi_in(j)))];
```

```
                     gc = atan2(vpn(2),vpn(1));
                     gp = atan2(Ptpm(2),Ptpm(1));
                 psi_tr = gp-gc;
                 Rz2_em = [cos(psi_tr) -sin(psi_tr) 0; sin(psi_tr)
cos(psi_tr) 0; 0  0  1];
             fcomp(:,j) = Rz_em*Rx2_em*Rz2_em*fcan(:,j);
             tcomp(:,j) = cross(Prpm(:,id_pm(j)),fcomp(:,j));
         elseif((lt(dm(j), dio(j))) & (gt(dm(j), dh)))
                     fx = 0;
                     fy = a00(2)+ a10(2)*d(j,2)  + a20(2)*d(j,2)^2 +
a30(2)*d(j,2)^3 + a40(2)*d(j,2)^4 + a50(2)*d(j,2)^5 + a01(2)*i(j) +
a02(2)*i(j)^2 + a11(2)*d(j,2)*i(:,j) + a21(2)*d(j,2)^2*i(j) +
a12(2)*d(j,2)*i(j)^2 + a31(2)*d(j,2)^3*i(j) +
a22(2)*d(j,2)^2*i(j)^2 + a41(2)*d(j,2)^4*i(j) +
a32(2)*d(j,2)^3*i(j)^2;
                     fz = z00(2)+ z10(2)*d(j,2)  + z20(2)*d(j,2)^2 +
z30(2)*d(j,2)^3 + z40(2)*d(j,2)^4 + z50(2)*d(j,2)^5 + z01(2)*i(j) +
z02(2)*i(j)^2 + z11(2)*d(j,2)*i(:,j) + z21(2)*d(j,2)^2*i(j) +
z12(2)*d(j,2)*i(j)^2 + z31(2)*d(j,2)^3*i(j) +
z22(2)*d(j,2)^2*i(j)^2 + z41(2)*d(j,2)^4*i(j) +
z32(2)*d(j,2)^3*i(j)^2;
              fgen(:,j) = [fx; fy; fz];
                 Rx_gen = [1 0 0;  0 cos(phi_in(j)) -
sin(phi_in(j));  0  sin(phi_in(j))  cos(phi_in(j))];
              fcan(:,j) = Rx_gen*fgen(:,j);
                  Rz_em = [cos(psi_em(j)) -sin(psi_em(j)) 0;
sin(psi_em(j)) cos(psi_em(j)) 0; 0 0 1];
                 Rx2_em = [1 0 0; 0 cos(phi2_em(j)) -
sin(phi2_em(j)); 0 sin(phi2_em(j)) cos(phi2_em(j))];
              Ptpm(:,j) = transpose(Rz_em*Rx2_em)*Prpm(:,id_pm(j));
                    vpn = [0 abs(sin(phi_in(j)))
abs(cos(phi_in(j)))];
                     gc = atan2(vpn(2),vpn(1));
                     gp = atan2(Ptpm(2),Ptpm(1));
                 psi_tr = gp-gc;
                 Rz2_em = [cos(psi_tr) -sin(psi_tr) 0; sin(psi_tr)
cos(psi_tr) 0; 0  0  1];
             fcomp(:,j) = Rz_em*Rx2_em*Rz2_em*fcan(:,j);
             tcomp(:,j) = cross(Prpm(:,id_pm(j)),fcomp(:,j));
         else
              fcomp(:,j) = [0; 0; 0];
              tcomp(:,j) = [0; 0; 0];
         end
    end
    % Net force and torque acting on the rotor assembly
    fnet = sum(fcomp,2);
    tnet = sum(tcomp,2);

 % Define outputs as net force and net torque
 block.OutputPort(1).Data = fnet;
 block.OutputPort(2).Data = tnet;


 function Terminate(block)
```

Appendix E

MATLAB® Script for Magnetic Dipole Analytical Model

```
% FORCES ACTING ON MAGNETIC DIPOLES %
cf  = 0.0254;          % conversion factor from inch to meter
theta = [0:32];        % Angle between dipole vectors (degrees)
theta(33) = 31.715;
mu0 = 4*pi*10^-7;      % permeability of free space (N/Amp^2)
mur = 1.05;            % relative permeability PM
mu = mu0*mur;          % permeability of PM
N = 360;               % Number of turns in EM
Ie = 0.5;              % Current in EM (Ampere)

rs = 1.25*cf;          % Radius of Sphere
di = 0.12*cf;          % Inner Diameter of EM
do = 0.45*cf;          % Outer Diameter of EM
dp = 0.25*cf;          % diameter of PM
Lp = 0.50*cf;          % Length of the PM
Lg = 0.03*cf;          % Length of airgap
Le = 0.17*cf;          % Length from base of EM coil

Ae = (pi/4)*(do^2-di^2);    % Sectional Area of EM (in XY Plane)
Ap = (pi/4)*dp^2;           % Sectional Area of PM (in XY Plane)
Vp = Ap*Lp;                 % Volume of PM

rp  = rs - (Lp/2) - (cf*0); % distance of PM dipole moment from
origin (dipole located at mid-plane of PM)
re  = rs + Lg + Le/2;       % distance of EM dipole moment from
origin (dipole located at mid-plane of EM)

Pe  = re.*[zeros(1,33); sind(360-theta); cosd(360-theta)];  % EM
position vector as a function of theta
Pp  = rp.*[zeros(1,33); zeros(1,33); ones(1,33)];           % PM
position vector (fixed)

% =================== N52 Magnetization Curve =================== %
B = [1.450  1.400   1.379   1.293   1.209   1.125   1.041   0.956
0.871   0.787   0.663   0.572   0.487   0.404   0.317   0.222
0.125   0.000];
H = [0  -37661  -53928  -120801 -185866 -250932 -315997 -381063 -
446354 -511194 -605178 -672954 -734405 -789530 -834714 -860741 -
869958 -875000];

for k = 1:33
     r(k) = norm(Pe(:,k)-Pp(:,k));  % scalar distance between EM/PM
end

ru  = (Pe-Pp)./r;   % unit vector along separation distance vector

me  = N*Ie*Ae;      % Magnitude of Magnetic Dipole moment of EM
meu = [zeros(1,33); sind(360-theta); cosd(360-theta)]; % unit
vector along EM dipole
mev = me.*meu;      % Magnetic Dipole Moment Vector
```

```
M  = 875000;     % Magnetization of PM
mp  = M*Ap*Lp;  % Magnitude of Magnetic Dipole moment of PM
mpu = [zeros(1,33); zeros(1,33); ones(1,33)]; % unit vector along
PM dipole
mpv = mp.*mpu;   % Magnetic Dipole Moment Vector of PM (fixed)

% Fpe = force of PM on EM and Fep = force of EM on PM
Fpe = transpose((3*mu0./(4*pi*r.^4)).*(cross(cross(ru,mpv),mev) +
cross(cross(ru,mev),mpv)-
2.*ru.*dot(mpv,mev)+5.*ru.*dot(cross(ru,mpv),cross(ru,mev))));
% Fep = transpose((3*mu./(4*pi*r.^4)).*(cross(cross(ru,mev),mpv) +
cross(cross(ru,mpv),mev)-
2.*ru.*dot(mev,mpv)+5.*ru.*dot(cross(ru,mev),cross(ru,mpv))));

% COMSOL Simulation Data Force on EM for PM only (0.5 Ampere
Excitation) %
Fy_COMSOL = [-0.0000064 0.0597670   0.1156600   0.1637100
0.2002400   0.2233200   0.2334400   0.2320700   0.2208500
0.2017500   0.1773000   0.1501500   0.1225800   0.0965650
0.0737340   0.0552230   0.0412290   0.0308930   0.0231900
0.0173760   0.0129340   0.0095071   0.0068415   0.0047556
0.0031131   0.0018182   0.0007926   -0.0000173  -0.0006566  -
0.0011587  -0.0015497  -0.0018525  -0.0020230];
Fz_COMSOL = [-0.4631000 -0.4547200  -0.4300400  -0.3905800  -
0.3396400  -0.2822300  -0.2231800  -0.1659900  -0.1133000  -
0.0673780  -0.0298160  -0.0011378  0.0188950   0.0310510
0.0365990   0.0373420   0.0354620   0.0326360   0.0296260
0.0267220   0.0240330   0.0215920   0.0193990   0.0174380
0.0156880   0.0141250   0.0127310   0.0114820   0.0103640
0.0093621   0.0084622   0.0076527   0.0071219];
Fmag_COMSOL = [0.4631000    0.4586310   0.4453219   0.4235017
0.3942732   0.3598966   0.3229606   0.2853229   0.2482169
0.2127037   0.1797896   0.1501543   0.1240277   0.1014345
0.0823176   0.0666634   0.0543818   0.0449387   0.0376228
0.0318746   0.0272924   0.0235924   0.0205701   0.0180748
0.0159939   0.0142415   0.0127556   0.0114820   0.0103848
0.0094335   0.0086029   0.0078737   0.0074036];

Fy_dipole = transpose(Fpe(:,2));
Fz_dipole = transpose(Fpe(:,3));

for i = 1:33
     Fmag_dipole(i) = norm(Fpe(i,:));  % magnitude of dipole force
end

figure
plot (theta,Fy_dipole,'b', theta,Fy_COMSOL,'b--',
theta,Fz_dipole,'r',  theta,Fz_COMSOL,'r--')
grid on
title('Magnetic Force Comparison (Y, Z Components) EM excited with
0.5 Amperes (COMSOL vs. Dipole)')
xlabel('Angle (degrees)')
```

```
ylabel('Force (Newtons)')
legend('Fy dipole','Fy COMSOL', 'Fz dipole','Fz COMSOL')

figure
plot (theta,Fmag_dipole, theta, Fmag_COMSOL)
grid on
legend('Fmag dipole','Fmag COMSOL')
title('Magnetic Force Comparison (Magnitude) EM excited with 0.5
Amperes (COMSOL vs. Dipole)')
xlabel('Angle (degrees)')
ylabel('Force (Newtons)')
```